

**DYNAMIC SIMULATION OF DROPS BY THE PARTICLE FINITE ELEMENT
METHOD**

by

Elaf Naeem Mahrous

A dissertation submitted to the Faculty of the University of Delaware in partial fulfillment of the requirements for the degree of Doctor of Philosophy in Mechanical Engineering

Summer 2021

© 2021 Elaf Naeem Mahrous
All Rights Reserved

**DYNAMIC SIMULATION OF DROPS BY THE PARTICLE FINITE ELEMENT
METHOD**

by

Elaf Naeem Mahrous

Approved: _____
Ajay Prasad, Ph.D.
Chair of the Department of Mechanical Engineering

Approved: _____
Levi T. Thompson, Ph.D.
Dean of the College of Engineering

Approved: _____
Louis F. Rossi, Ph.D.
Vice Provost for Graduate and Professional Education and
Dean of the Graduate College

I certify that I have read this dissertation and that in my opinion it meets the academic and professional standard required by the University as a dissertation for the degree of Doctor of Philosophy.

Signed: _____

R. Valéry Roy, Ph.D.
Professor in charge of dissertation

I certify that I have read this dissertation and that in my opinion it meets the academic and professional standard required by the University as a dissertation for the degree of Doctor of Philosophy.

Signed: _____

Ajay Prasad, Ph.D.
Member of dissertation committee

I certify that I have read this dissertation and that in my opinion it meets the academic and professional standard required by the University as a dissertation for the degree of Doctor of Philosophy.

Signed: _____

Joseph Kuehl, Ph.D.
Member of dissertation committee

I certify that I have read this dissertation and that in my opinion it meets the academic and professional standard required by the University as a dissertation for the degree of Doctor of Philosophy.

Signed: _____

Marc Secanell, Ph.D.
Member of dissertation committee

ACKNOWLEDGEMENTS

First and foremost, all praise and glory to Almighty Allah, my Lord who guided and helped me to accomplish this dissertation. Peace and blessing of Allah be upon my prophet Muhammad, who urged people to seek and contribute in knowledge. I have then to thank my parents for their love and help throughout my life. I would like also to thank my wife and kids who have always been by my side.

I would like to convey my deepest appreciation and gratitude to my committee chair Professor R. Valéry Roy, who opened his doors, shared his valuable knowledge and expertise, and conveyed a spirit of adventure during my Ph.D. journey. Thanks to Professor Marc Secanell and Dr. Alex Jarauta, whom I started with and earned from this distinguished field of research. I would like also to thank my committee members, Professor Ajay Prasad, Professor Joseph Kuehl, and Professor Marc Secanell.

I thank the University of Delaware for giving their helping hand when I needed it the most. I would also like to thank Jubail University College and the Royal Commission for Jubail and Yanbu of Saudi Arabia for their scholarship and financial support.

I would not forget to thank Mr. Thomas Chan and Dr. Adam Weber at UC Berkeley, with the collaboration of Professor Marc Secanell, for their permission to utilize their unpublished experimental data and use it in chapter 5 of this dissertation. I am also thankful to Dr. Pavel Ryzhakov and Kratos-Multiphysics team for their support in implementing Kratos framework and Gid post-processing features.

Last but not least, thanks to my brothers, sisters, and friends for their encouragement in my many difficult moments, especially during the COVID-19 pandemic crisis.

TABLE OF CONTENTS

LIST OF TABLES	xi
LIST OF FIGURES	xiii
ABSTRACT	xxii

Chapter

1 MOTIVATION AND BACKGROUND	1
1.1 Physical phenomena and modeling challenges	3
1.1.1 Surface tension and partial wetting	3
1.1.2 Drop spreading	5
1.1.3 Drop sliding	6
1.2 Embedded two-phase flow	8
1.2.1 Polymer electrolyte membrane fuel cells	8
1.2.2 Evaporative cooling in wet cooling towers	12
1.2.3 Piezoelectric inkjet printing	13
1.2.4 Oil and gas processing	14
1.3 Numerical modeling	15
1.4 The Particle Finite Element Method (PFEM)	20
1.5 Goals and implementation methodology	22
1.6 Dissertation outline	22
2 A TWO-DIMENSIONAL NUMERICAL MODEL FOR DROP SPREADING DYNAMICS	25
2.1 Introduction	25
2.1.1 Disjoining pressure model	27

2.1.2	Dissipative and viscous force models	28
2.2	Physical model and governing equations	31
2.3	Boundary conditions at the liquid-vapor interface Γ_I	32
2.4	Curvature in 2D	33
2.5	Forces at the solid-liquid interface	34
2.5.1	Forces acting at the contact line, $\partial\Gamma$	35
2.5.2	Forces acting at the solid-liquid interface away from the contact line, Γ_S	38
2.6	Discretization technique	38
2.6.1	Introduction to the finite element method	39
2.6.2	Discretized governing equations	40
2.6.3	Monolithic approach	44
2.6.4	Solution algorithm	48
2.7	Mesh size and time step criteria	48
2.8	Mesh dependence study	50
2.9	Experimental validation	58
2.9.1	Case #1: spreading of a water drop on a hydrophobic triethoxysilane substrate	58
2.9.2	Case #2: spreading of a squalane (C30 H62) drop on a silica substrate	62
2.9.3	Cases #3 and #4: injection of water drops on teflon (hydrophobic) and kapton (hydrophillic) substrates	64
2.9.3.1	Kapton	67
2.9.3.2	PTFE	67
2.10	Conclusion	69
3	A TWO-DIMENSIONAL NUMERICAL MODEL FOR SLIDING MOTION OF LIQUID DROPS	73
3.1	Introduction	73
3.2	Physical model	76
3.2.1	Governing equations	76

3.2.2	Boundary conditions	76
3.2.2.1	Retention force	77
3.2.2.2	Total dissipative force acting at the contact line $\partial\Gamma$. . .	78
3.2.2.3	Forces acting at the solid-liquid interface away from the contact line, Γ_S	79
3.3	Discretized governing equations	79
3.4	Mesh size and time step criteria	80
3.5	Experimental validation	81
3.5.1	Cases #1 and #2: ethylene glycol drop on an omniphilic polycarbonate substrate	81
3.5.2	Mesh dependency analysis	88
3.5.3	Cases #3 and #4: water drop on a hydrophobic PTFE substrate . .	88
3.5.4	Case #5: water drop on a hydrophilic PMMA substrate with time-varying inclination	92
3.5.5	Case #6: viscous Newtonian drop on an omniphilic smooth glass .	95
3.6	Rolling viscous drops	97
3.7	Conclusion	100
4	DROP DYNAMICS IN 3D	103
4.1	Introduction	103
4.2	3D model for drop spreading dynamics	104
4.2.1	Physical model	104
4.2.1.1	Governing equations	104
4.2.1.2	Boundary conditions at the free-surface Γ_I	105
4.2.1.3	Curvature in 3D	106
4.2.1.4	Forces acting on the contact line, $\partial\Gamma$	108
4.2.1.5	Forces acting on the solid-liquid interface away from the contact line, Γ_S	110
4.2.2	Mesh size and time step criteria	111
4.2.3	Discretized governing equations	111
4.2.4	Numerical examples	113

4.2.5	Experimental validation	114
4.2.5.1	Cases #1 and #2: equilibrium configuration for viscous glycerol drops on smooth polyethylene terephthalate glycol surface	116
4.2.5.2	Case #3: water drop spreading on a hydrophobic triethoxysilane substrate	120
4.2.5.3	Case #4: water drop spreading on a hydrophilic kapton substrate	122
4.3	3D model for sliding liquid drops	122
4.3.1	Mesh size and time step criteria	125
4.3.2	Experimental validation	126
4.3.2.1	Case #1: ethylene glycol drop on an omniphilic polycarbonate substrate	126
4.3.2.2	Case #2: water drop on a hydrophobic PTFE substrate	127
4.3.2.3	Case #3: viscous Newtonian drop on an omniphilic smooth glass	130
4.4	Conclusion	135
5	AN EMBEDDED TWO-PHASE FLOW	137
5.1	Introduction	137
5.2	Physical model	140
5.2.1	Governing equations for the proposed embedded numerical model	140
5.2.2	Boundary and interface conditions	141
5.3	Finite element formulation for the gas phase	144
5.3.1	Monolithic approach	144
5.3.2	Fractional step approach	147
5.4	Finite element formulation for the liquid phase	149
5.5	Coupling strategy	150
5.5.1	Dirichlet boundary condition	151
5.5.2	Neumann boundary condition	153
5.6	Solution algorithm	154

5.7	Validating the Eulerian domain	155
5.8	Experimental validation for the embedded, two-phase flow, model	163
5.8.1	2D embedded simulation: water drop injection on kapton and PTFE substrates	163
5.8.2	3D embedded flow simulations: water drop ejection from a PEMFC channel	171
5.9	An embedded simulation for Reynolds number greater than 2300	173
5.10	Numerical experiments	181
5.11	Conclusion	186
6	CONCLUSION AND FUTURE WORK	187
6.1	Conclusion	187
6.2	Drop spreading dynamics	188
6.3	Drop sliding dynamics	189
6.4	3D drop dynamic model	190
6.5	Embedded, two-phase, flow model	191
6.6	Achievements and contributions	192
6.7	Future work	193
6.7.1	Rolling viscous drops simulations in 3D	194
6.7.2	Liquid injection simulations in 3D	194
6.7.3	Modeling heat transport	194
6.7.4	Effect of surface porosity	194
6.7.5	Effect of transitional and turbulent flow regimes	195
6.7.6	Drop breakup and coalescence simulations	195
6.7.7	Computational optimization	195
Appendix		
A	DELAUNAY TRIANGULATION AND ALPHA SHAPE METHOD	196
A.1	Delaunay triangulation/tetrahedralization	196
A.2	Alpha shape method	198
B	VISCOUS STRESS IMPLEMENTATION	199
B.1	Viscous stress implementation in 2D	199
B.2	Viscous stress implementation in 3D	201
C	ELEMENTAL CONTRIBUTION TO MATRIX ENTRIES OF THE 2D	

LIQUID DROP SLIDING MODEL	205
D SOLUTION ALGORITHM OF THE 2D LIQUID DROP SLIDING MODEL	206
E GEOMETRY OF SPHERICAL DROPS	207
F ELEMENTAL CONTRIBUTION TO MATRIX ENTRIES OF THE 3D LAGRANGIAN MODEL	209
G SOLUTION ALGORITHM OF THE 3D LAGRANGIAN MODEL	210
H PERMISSION	211
BIBLIOGRAPHY	213

LIST OF TABLES

2.1	Analyzing different slip coefficient parameters at the contact line and at the solid-liquid interface excluding the contact line, $\beta_{\partial\Gamma}$ and β_{Γ_s}	52
3.1	Physical properties of the liquids and substrate inclination angles.	82
3.2	Simulation parameters.	83
3.3	Numerical vs. experimental steady-state velocities (u_{ss}).	88
3.4	Parametric analysis for different k values.	90
4.1	Contact angles values obtained numerically (θ_{ave}) for water drops on kapton and PTFE substrates, and the corresponding error with respect to the prescribed equilibrium angle θ_e	116
4.2	Dimensions of glycerine drops at equilibrium configuration.	120
4.3	Comparison between numerical and experimental spreading evolution for a water drop of 0.82 radius spreading on a triethoxysilane substrate (based on Fig. 4.9).	120
4.4	Physical properties of the sliding liquid drops for different liquid/solid pairs.	127
4.5	Numerical vs. experimental steady-state velocities (u_{ss}) in 3D.	135
4.6	Numerical vs. experimental steady-state velocities (u_{ss}) in 2D.	135
5.1	U.S. DOE technical specifications and targets for automotive PEMFC [8, 43, 211].	138
5.2	L_{hy}^* criteria for a fully developed laminar flow inside a rectangular channel [91, 201].	157

5.3	Approximated value of f_D for developing laminar flow in a rectangular channel [56, 201].	159
5.4	Dynamic contact angle vs volume of injected drop, experimental vs. numerical, for water drop injected on kapton and PTFE substrates. ASA and RSA stand for advancing and receding sliding angles, respectively. .	169
5.5	Numerical parametric analysis for different values of inlet air velocity (v_{in}): horizontal channel of size 6.5 mm x 6.5 mm x 12 mm, and drop-to-channel height ratio of ~ 0.65	181

LIST OF FIGURES

1.1	Examples of water drops and surfaces with different wettabilities in the natural world (a) water drops travel through hydrophilic leaves downward towards the roots [33, 73, 183] and (b) water drops are formed on hydrophilic bumps and slides down on hydrophobic channels towards the mouth of a desert beetle, reproduced from [33, 169].	2
1.2	Example of surface wettability effects on blood drops, using two different titanium (Ti) base substrates: superhydrophobic (SHP) Ti and pure Ti foil. A blood drop rolls off the superhydrophobic substrate, leaving no stains. A blood drop slides down the pure Ti foil, leaving behind a blood. Figure is reproduced from reference [137].	3
1.3	Representation of (a) Young-Laplace equation, reproduced from [170] and (b) wetting of surfaces, reproduced from [246].	5
1.4	Cost analysis for automotive PEMFC systems [145, 211].	9
1.5	Schematic representation of the main components and processes of the PEMFC. Figure is reproduced from [13].	10
1.6	Example of two-phase flow applications in PEMFCs.	11
1.7	Schematic diagram of a cooling tower [35].	13
1.8	Fill zones: (a) two-phase flow inside the fill zone, reproduced from [36] and (b) fill arrangements inside the cooling tower, reproduced from [35].	13
1.9	Schematic diagram of a piezoelectric inkjet printer, reproduced from [235].	14
1.10	Schematic diagram of a fractional distillation, reproduced from [3]. . . .	16

1.11	Schematic representations of a) an Eulerian, front capturing, volume of fluid approach [90], b) an Eulerian, front capturing, level set approach: red color curve is the zero level set [6], c) an Eulerian, front tracking technique [110], and d) a Lagrangian approach [113].	17
1.12	Steps of the PFEM scheme: a) starting with an initial configuration of mesh nodes, i.e., particles where mathematical information and physical quantities are stored, b) generating mesh connectivity by Delaunay triangulation, c) recovering domain boundaries by the alpha shape method, d) updating the mesh after computations and, accordingly, e) updating the mesh nodes position. Figures are reproduced from [55]. . . .	21
2.1	Liquid profile in the vicinity of the apparent contact line: (1) bulk liquid, (2) liquid–air and liquid–solid interfaces, (3) region where surface forces boundary layers overlap, and (4) region of thin equilibrium film. The disjoining pressure is the dominating mechanism at regions (3) and (4). Figure is reproduced from [208].	28
2.2	Categories of commonly used modeling methods, and their corresponding length and time scales. Figure is reproduced from [222].	29
2.3	Schematic representation of the considered Lagrangian domain at the continuum level.	32
2.4	Changes in directions in discrete boundary [112, 114].	34
2.5	Schematic representation of the forces acting on a contact line of a sessile drop.	36
2.6	Initial and steady-state configuration for a sessile drop starting with an initial contact angle angle of 90° , and evolving with a spreading displacement of r	51
2.7	Evolution of (a) spreading displacement and (b) contact angle, for $\beta_{\partial\Gamma} = 0$ and $\beta_{\Gamma_s} = 0$; case 0 in table 2.1, using different mesh sizes.	53
2.8	Initial configuration of a sessile drop with a starting contact angle of 90° : a) coarse mesh of 1.25×10^{-5} m and b) fine mesh of 5×10^{-6} m.	53
2.9	Evolution of spreading displacement for constant $\beta_{\partial\Gamma}$ and β_{Γ_s} (a) and using eq. (2.5.7) and (2.5.13) (b). Contact angle evolution for constant $\beta_{\partial\Gamma}$ and β_{Γ_s} (c), and using eq. (2.5.7) and (2.5.13) (d), see table 2.1. Mesh size of $h = 1.25 \times 10^{-5}$ m (coarse mesh).	54

2.10	Evolution of spreading displacement for constant $\beta_{\partial\Gamma}$ and β_{Γ_S} (a) and using eq. (2.5.7) and (2.5.13) (b). Contact angle evolution for constant $\beta_{\partial\Gamma}$ and β_{Γ_S} (c), and using eq. (2.5.7) and (2.5.13) (d), see table 2.1. Mesh size of $h = 5 \times 10^{-6}$ m (fine mesh).	57
2.11	Mesh-independent results for (a) spreading displacement evolution, (b) contact angle temporal evolution, and (c) contact line velocity evolution, using our proposed boundary conditions and for two different triangular mesh sizes of $h = 1.25 \times 10^{-5}$ m (coarse mesh) and $h = 5 \times 10^{-6}$ m (fine mesh).	59
2.12	Initial and steady-state configuration for the sessile drop starting with an initial contact angle $\approx 180^\circ$, and evolving with a spreading displacement of r	60
2.13	Two different mesh sizes, $h = 8 \times 10^{-5}$ m and $h = 4 \times 10^{-5}$ m, representing the initial-stage of 0.001 m diameter drop.	60
2.14	Case #1: water drop spreading on Triethoxysilane, for $0 < t \leq 1.2$ ms, with a dominant capillary wave propagation at the contact line (a) experimentally, (reproduced with permission from J. Phys. Rev. Lett. 100, 234501 (2008). Copyright 2008 American Physical Society), and (b) numerically.	61
2.15	Case #1: water drop spreading rate on Triethoxysilane: (a) spreading displacement evolution (numerically vs. experimentally) and (b) contact line velocity evolution (numerically vs. experimentally).	63
2.16	Case #2: Squalane drop on silica: (a) contact angle evolution vs. contact line velocity (numerical vs. experimental), and (b) contact angle evolution vs. time (numerical vs. experimental).	65
2.17	Fuel cell channel and injection simulation: Illustration of the experimental setup. Reference: T. Chan. Validation of a Semi-Analytical Model for drop Dynamics in a PEMFC. Berkeley Lab.	66
2.18	Case #3: water-kapton injection analysis and comparison: (a), spreading displacement evolution, and (b) contact angle evolution.	68
2.19	Case #4: water-PTFE injection analysis and comparison: (a), spreading displacement evolution, and (b) contact angle evolution.	70

2.20	Initial and final sessile drop profiles, experimentally (in black color) vs numerically (in blue color), for: (a) water injected at flow rate of 5 $\mu\text{L/s}$ on kapton substrate, (b) water injected at flow rate of 5 $\mu\text{L/s}$ on PTFE substrate, and (c) water injected at flow rate of 10 $\mu\text{L/s}$ on PTFE substrate.	71
3.1	Sketch of a drop sliding down an inclined plane.	76
3.2	Cases #1 and #2: a 29.2 μL ethylene glycol drop sliding on an inclined plane of inclination angle α : (a) initial drop profile at $\alpha = 0^\circ$ and $t = 0$ s, (b,c) steady-state profiles at $\alpha = 11^\circ$ and 20° , respectively, and (d,e) drop velocity fields at $\alpha = 11^\circ$ and 20° , respectively.	85
3.3	Cases #1 and #2: a 29.2 μL ethylene glycol drop sliding on an inclined plane, with angle of inclination α : (a) contact angle evolution for $\alpha = 11^\circ$, (b) contact angle evolution for $\alpha = 20^\circ$	86
3.4	Cases #1 and #2: a 29.2 μL ethylene glycol drop sliding on an inclined plane, with angle of inclination α : (a) advancing and receding velocities for $\alpha = 11^\circ$, (b) advancing and receding velocities for $\alpha = 20^\circ$	87
3.5	Demonstration of mesh-independence for a 29.2 μL ethylene glycol drop sliding on an inclined plane of inclination angle $\alpha = 20^\circ$: (a) two different mesh sizes of $h = 2 \times 10^{-4}$ m and $h = 3 \times 10^{-4}$ m representing the initial configuration, (b) contact angle evolution, (c) advancing and receding velocities.	89
3.6	Cases #3 and #4: water drops sliding on PTFE substrate, inclined at angle $\alpha = 60^\circ$: (a,b) steady-state profile obtained experimentally for drop volumes of 7.5 μL and 10 μL , respectively [reproduced with permission from Annapragada <i>et al.</i> Int. J. Heat Mass Transf. 55 , 5-6 1466-1474 (2012). Copyright 2011 Elsevier Ltd.], (c,d) numerically obtained steady-state profiles for drop volumes of 7.5 μL and 10 μL , respectively, and (e,f) velocity fields for drop volumes of 7.5 μL and 10 μL , respectively.	93
3.7	Cases #3 and #4: water drops sliding on a PTFE substrate, inclined at angle $\alpha = 60^\circ$: (a) contact angle evolution, (b) advancing and receding velocities.	94

3.8	Case #5: a 30 μL water drop sliding on a rotating PMMA substrate: (a) sliding profile (experimentally)[reproduced with permission from Maurer <i>et al.</i> Proceedings of the 3rd Int. Conf. on FFHMT'16, 134 (2016). Copyright 2020, International ASET Inc.], (b) numerically obtained drop profile, and (c) comparison of the advancing and receding contact angle evolutions.	96
3.9	Case #6: a 100 μL PEG sessile drop sliding on smooth glass, inclined at $\alpha = 27^\circ$: (a) initial drop profile at $\alpha = 0^\circ$ and $t = 0$ s, (b) steady-state profile at $\alpha = 27^\circ$, (c) velocity fields.	98
3.10	Case #6: a 100 μL PEG sessile drop sliding on smooth glass, inclined at $\alpha = 27^\circ$: (a) contact angle evolution and (b) sliding advancing velocity evolution.	99
3.11	Descent rolling velocities for a 5 μL glycerol drop rolling on smooth PETG surface at $\alpha = 15^\circ$ and 20°	101
3.12	Velocity vector for a 5 μL rolling glycerol drop on smooth PETG surface at $\alpha = 15^\circ$	101
4.1	Schematic representation of the 3D Lagrangian domain.	104
4.2	(a) Normal curvature, and (b) principal directions in 3D [112].	107
4.3	(a) The shaded area representing the “one-ring neighborhood” of x_i node, (b) angles located opposite to an edge. Figures are reproduced from [112].	107
4.4	Initial and steady-state configurations for sessile drops starting with two different prismatic initial configurations.	114
4.5	Spreading evolution for two different initial geometries.	115
4.6	schematic representation of the initial configuration (dashed line) and the equilibrium configuration (solid line) of a viscous liquid drop [10].	117
4.7	Case #1: equilibrium configuration for a glycerol drop on smooth PETG surfaces of: (a) 1.35 mm radius, experimentally [10], (b) 1.1 mm radius, numerically in 2D and (c) 1.1 mm radius, numerically in 3D.	118
4.8	Case #2: equilibrium configuration for a glycerol drop on smooth PETG surfaces of: (a) 2.3 mm radius, experimentally [10], (b) 2.15 radius, numerically in 2D and (c) 2.15 radius, numerically in 3D.	119

4.9	Case #3: water drop of a radius 0.82 spreading on triethoxysilane, for $0 < t \leq 1.2$ ms, with a dominant capillary wave propagation at the contact line (a) experimentally [28], (reproduced with permission from J. Phys. Rev. Lett. 100, 234501 (2008). Copyright 2008 American Physical Society), and (b) numerically.	121
4.10	Case #4: spreading evolution for water drop on kapton substrate.	123
4.11	Spreading rate evolution for water drop on kapton substrate.	124
4.12	Case #1: sliding profiles for EG drop on an omniphilic polycarbonate substrate.	128
4.13	Case #1: contact angle and spreading rate evolution for EG drop sliding on polycarbonate substrate.	129
4.14	Case #2: sliding profiles for water drop sliding on PTFE substrate.	131
4.15	Case #2: contact angle and spreading rate evolution for water drop sliding on a hydrophobic PTFE substrate.	132
4.16	Case #3: sliding profiles for viscous Newtonian fluid on an omniphilic smooth glass.	133
4.17	Case #3: contact angle and spreading rate evolution for viscous Newtonian fluid.	134
5.1	Schematic graph for the embedded approach [115, 187].	142
5.2	Embedded schematic of a) real superimposed discretized Eulerian-PFEM domains, b) fictitious interface on the Eulerian mesh, and c) elements of the interface [112].	152
5.3	Coupling algorithm flowchart.	155
5.4	Mesh sizes for a 6.5 mm (H) x 6.5 mm (W) x 120 mm (L) channel: (a) a mesh size of 6×10^{-4} m, refined to 2.5×10^{-4} m at the center of the channel where the injection takes place, (b) a mesh size of 1×10^{-3} m.	160
5.5	Pressure drop along a 6.5 mm (H) x 6.5 mm (W) x 120 mm (L) channel, air inlet flow rate of 6 SLPM : (a) solution of the Eulerian domain in 2D, (b) solution of the Eulerian domain in 3D, and (c) pressure drop evolution both in 2D and 3D.	161

5.6	Pressure drop along a 6.5 mm (H) x 6.5 mm (W) x 120 mm (L) channel, air inlet flow rate of 10 SLPM : (a) solution of the Eulerian domain in 2D, (b) solution of the Eulerian domain in 3D, and (c) pressure drop evolution both in 2D and 3D.	162
5.7	Injection experiment: evolution of water drop injected on kapton substrate at flow rates of F6-Q15.	164
5.8	Injection simulation: evolution of water drop injected on kapton substrate at flow rates of F6-Q15.	165
5.9	Injection experiment: evolution of water drop injected on PTFE substrate at flow rates of F6-Q25.	166
5.10	Injection simulation: drop evolution of water drop injected on PTFE substrate at flow rate of F6-Q25.	167
5.11	Profiles of sliding water drops on PTFE substrate, driven by an inlet airflow of 6 SLPM: a) experimentally and b,c) numerically.	168
5.12	Dynamic contact angle vs volume of injected drop, experimental vs. numerical, for : (a) water injected on kapton at flow rates of F6-Q15 and (b) PTFE substrates at flow rates of F6-Q25.	169
5.13	Profiles of sliding water drops on PTFE substrate: a) a drop with drop-to-channel height ratio of 0.65 driven by airflow of 6 SLPM, and b) a drop with drop-to-channel height ratio of 0.53 driven by airflow of 10 SLPM.	172
5.14	Numerical results for case #1 of the 3D embedded simulation: a) representation of the initial configuration of drop-to-channel height ratio, b) pressure field along a 6.5 mm (H) x 6.5 mm (W) x 120 mm (L) channel driven by airflow at 6 SLPM, c) external pressure acting on a water drop (Lagrangian domain), d) profile of sliding water drops on PTFE substrate, e) pressure evolution at the inlet of the channel, and f) evolution of the average sliding velocity.	174

5.15	Numerical results for case #2 of the 3D embedded simulation: a) representation of the initial configuration of drop-to-channel height ratio, b) pressure field along a 6.5 mm (H) x 6.5 mm (W) x 120 mm (L) channel driven by airflow at 10 SLPM, c) external pressure acting on a water drop (Lagrangian domain), d) profile of sliding water drops on PTFE substrate, e) pressure evolution at the inlet of the channel, and f) evolution of the average sliding velocity.	175
5.16	Numerical results for transitional flow inside a 6.5 mm (H) x 6.5 mm (W) x 120 mm (L) channel driven by airflow at 19 SLPM, without the drop: a) pressure field along the channel, b) pressure evolution at the inlet of the channel.	177
5.17	Numerical results for transitional flow in the 3D embedded simulation, pressure field along a 6.5 mm (H) x 6.5 mm (W) x 120 mm (L) channel driven by airflow at 19 SLPM: a) at $t = 0.01$ s, b) at $t = 0.055$ s, c) at $t = 0.064$ s, and d) pressure evolution at the inlet of the channel.	178
5.18	Numerical results for transitional flow in the 3D embedded simulation, drop profiles inside a 6.5 mm (H) x 6.5 mm (W) x 120 mm (L) channel driven by airflow at 19 SLPM: a) initial drop profile, b) external pressure at $t = 0.055$ s, c) top view $t = 0.055$ s, and d) side view $t = 0.055$ s. . . .	179
5.19	Profile of sliding water drops on PTFE substrate, driven by an inlet airflow of 19 SLPM: a) experimentally, b) numerically.	180
5.20	Numerical results for case #2 of the 3D embedded simulation: a) pressure field along a 6.5 mm (H) x 6.5 mm (W) x 120 mm (L) horizontal channel in the absence of the drop, b) pressure field along a 6.5 mm (H) x 6.5 mm (W) x 120 mm (L) horizontal channel in the presence of the drop, c) external pressure acting on a water drop (Lagrangian domain), d) profile of sliding water drops on PTFE substrate (top view), e) pressure evolution at the inlet of the channel, and f) evolution of the average sliding velocity.	182
5.21	Numerical results for case #3 of the 3D embedded simulation: a) pressure field along a 6.5 mm (H) x 6.5 mm (W) x 120 mm (L) horizontal channel driven by airflow at 3.95 m s^{-1} (side view of drop-to-channel height ratio of ~ 0.65), b) external pressure acting on a water drop (Lagrangian domain), c) profile of sliding water drops on PTFE substrate (top view), d) pressure evolution at the inlet of the channel, and e) evolution of the average sliding velocity.	183

5.22	Numerical parametric analysis for different values of inlet air velocity (v_{in}): (a) inlet air velocity vs pressure drop along the channel (in the presence of the drop) and (b) inlet air velocity vs average sliding velocity of the drop.	184
5.23	Numerical profiles of water drops on PTFE substrate: (a) initial drop configuration, (b) sliding profile for case #1, (c) sliding profile for case #2, (d) sliding profile for case #3.	185
A.1	Schematic representation of: a) initial mesh nodes configuration, b) mesh connectivity by Delaunay triangulation, and c) mesh nodes after implementing the alpha shape method. Figures are reproduced from [55].	197
A.2	Schematic representation of a) Voronoï diagram, figure is reproduced from [212] and b) Delaunay triangulation, figure is reproduced from [55].	198
E.1	Geometrical parameters of a drop (a) on an omniphilic substrate and (b) on an omniphobic substrate.	208
H.1	Permission to include the published articles in this dissertation.	212

ABSTRACT

Liquid drop dynamics on solid surfaces play an important role both in nature and engineered applications. The prediction of drop spreading and/or sliding motions has far-reaching implications in many fields of application, including microfluidics, phase change applications, or coating technology. Modeling liquid drop spreading, sliding, deformation, and detachment is an active area of research, involving contact line motion, wetting, and interfacial effects.

Many analytical models have been established to predict and analyze thin liquid film and droplet dynamics. However, these models are valid only for predefined geometries and do not accurately account for gravitational and interfacial effects. Numerical models have proven to be more effective tools for predicting single-phase and two-phase flows, as they can take into account complex geometries and many physical effects such as gravity, surface tension, and interfacial forces in the vicinity of moving contact lines. One of the widely used numerical approaches to simulate two-phase flows is the Volume of Fluid (VOF) method, a front-capturing, mass-conserving Eulerian scheme. However, it requires small time-marching steps, as a result of the explicit treatment of the surface tension term. Furthermore, the VOF approach is based on a fixed background computational mesh, which makes it challenging to track the free-surface of a fluid due to its high geometric complexity and time-evolving nature. In addition to the VOF method, level-set Eulerian methods can also be used to enhance tracking of the air-water interface by using larger time steps. Furthermore, these methods are not considered mass conserving for free surface hydrodynamics problems. An alternative approach to computing two-phase flows implicitly is the Lagrangian method. Its advantage stems from its ability to accurately track fluid interfaces, its implicit treatment of surface tension, thus allowing large time steps, and finally its ability to conserve mass. Its main disadvantage is due to the requirement of remeshing the entire

computational domain after each time step to avoid mesh degradation, thereby increasing the computational cost. By combining the advantages of both the Eulerian and the Lagrangian methods, it is possible to develop a powerful scheme, known as the Eulerian-Lagrangian scheme. It is found to be effective for the accurate tracking of the gas-liquid interface and to account for the changes in material properties, such as viscosity, density, and surface tension. It also properly deals with the jump discontinuity of pressure across the interface, and it allows for the use of a large time step when compared to the pure Eulerian approach.

This dissertation presents a multidimensional numerical model based on one of the most recent Lagrangian frameworks, namely the Particle Finite Element Method (PFEM), for the prediction of the spreading and sliding motion of liquid drops (single-phase). The model includes the effect of the physical dissipative force acting at the solid-liquid interface, and of a retention force that acts in the vicinity of the drop's moving contact line. The proposed model is validated by using experimental data, covering a wide range of applications, drop size, and physical properties. Our numerical results are found to be mesh-independent and in very good agreement with experiments.

An embedded two-phase flow is also considered in this work. Examples of two-phase flow can be found in many applications of natural and industrial importance. Of particular interest in this work are two-phase flows which involve drops, and for which surface tension and partial wetting are key factors to predict their spatiotemporal evolution. As a relevant engineering example, we consider the dynamics of drops injected into the channels of Proton Exchange Membrane Fuel Cells (PEMFCs) which act as conduits for the fuel cell reactants (such as air). We developed a two-phase flow model in 2D and 3D configurations, and we devised an Eulerian-PFEM scheme to accurately predict the motion of drops under a variety of conditions. In particular, we studied the effect of substrate wettability and drop-to-channel height ratio on the spatio-temporal evolution of the water drop, thereby providing some insight into possible improvements in fuel cell design.

Chapter 1

MOTIVATION AND BACKGROUND

Drop dynamics modeling is an active area of research in the computational fluid dynamics (CFD) community due to its relevance in natural phenomena and its increasing role in advanced industrial applications. For instance, the spreading, sliding or rolling motion of water drops plays an important role in sustaining the life of certain plants and insects [106]. The hydrophobicity of some plant leaves, such as the lotus leaves, causes water droplets to be repelled from their surfaces. Thus, it facilitates contaminant particle removal and, in turn, endows the leaf its self-cleaning ability [92, 111]. In contrast, the hydrophilicity of *stipagrostis sabulicola* leaves guides water droplets down towards the roots of the plant (Fig. 1.1(a)) [33, 73, 183]. Some species of beetles depend on surface wettability either directly or indirectly [33, 106, 169]. For example, water drops are formed on hydrophilic bumps of a desert beetle, and slides on hydrophobic channels towards its mouth (Fig. 1.1(b)). Scientists have taken advantage of such natural wetting phenomena to manufacture surfaces with custom-made wetting properties [27]. In the field of biomedical engineering, the study of the wetting and sliding properties of blood and plasma drops contributes to improve the design of biomedical devices against blood contaminated surfaces [21, 154]. In the field of energy conversion, liquid drops on hydrophobic substrates is found to be functional and efficient for self-cleaning applications, such as on solar panels [93, 210]. Understanding the detachment and subsequent sliding of water drops formed within the gas diffusion layer plays a major role in improving water management of proton exchange membrane (PEM) fuel cells [15, 115, 187, 189, 197, 249]. In the field of micro- and nano-fabrication, controlling the surface wettability is found to be essential for implementing adhesion and traction in micro electro mechanical systems (MEMS), microfluidic devices, and robotic tactile sensors [79,

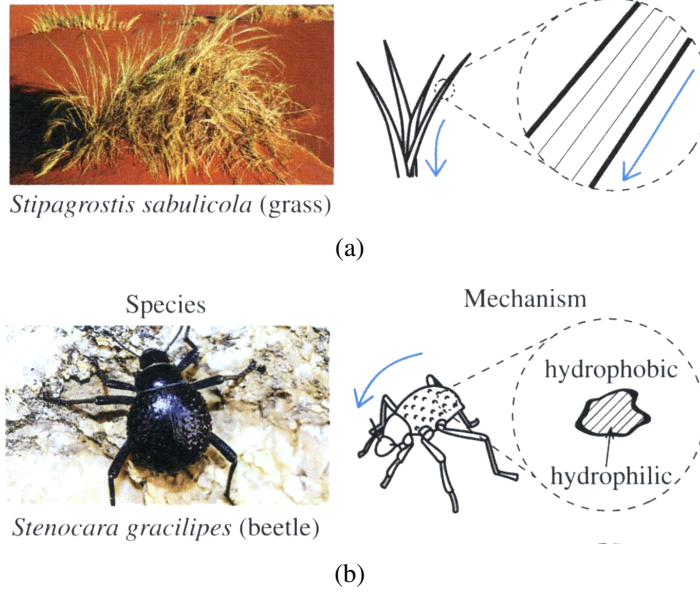


Figure 1.1: Examples of water drops and surfaces with different wettabilities in the natural world (a) water drops travel through hydrophilic leaves downward towards the roots [33, 73, 183] and (b) water drops are formed on hydrophilic bumps and slides down on hydrophobic channels towards the mouth of a desert beetle, reproduced from [33, 169].

105, 128, 191, 209]. Other important applications involve coating formulation and surface texturing [76, 230, 243].

In these applications, characterized by dominant capillary forces, the liquid phase is found in contact with solid substrates which can be omniphobic, omniphilic, or chemically heterogeneous [193]. The dynamic behavior of liquid drops depends on their interaction with solids and the corresponding substrate wettabilities. The goal of this dissertation is to develop numerical models for drop dynamics which can reliably predict drop motion, such as drop detachment, spreading or sliding, in a wide range of conditions. This work takes advantage of the recent progress in numerical modeling based on a Eulerian-Lagrangian framework developed in references [114, 187]. In the case of spreading and sliding, the model will be validated by using experimental data found in the published literature. In the case of drop injection in channels, the model will be validated by using available experimental data obtained by the UC Berkeley and U Alberta Energy Systems Design Laboratory (ESDL) research groups. Our ultimate goal is to obtain accurate, physical, and mesh-independent

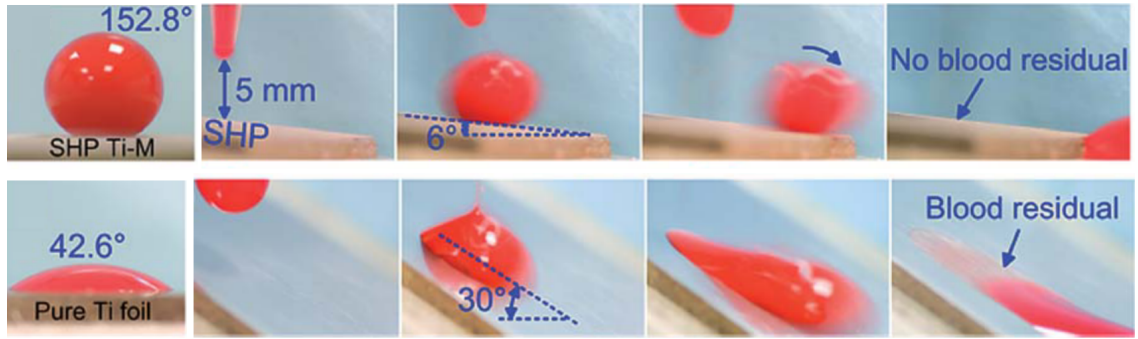


Figure 1.2: Example of surface wettability effects on blood drops, using two different titanium (Ti) base substrates: superhydrophobic (SHP) Ti and pure Ti foil. A blood drop rolls off the superhydrophobic substrate, leaving no stains. A blood drop slides down the pure Ti foil, leaving behind a blood. Figure is reproduced from reference [137].

results applicable to a wide variety of critical engineering applications.

1.1 Physical phenomena and modeling challenges

The action of interfacial forces at the vapor-liquid and liquid-solid interfaces plays a fundamental role in all drop dynamical phenomena. Three crucial phenomena must be studied in detail when considering drop dynamics: i) surface tension and partial wetting, ii) drop spreading, and iii) drop sliding.

1.1.1 Surface tension and partial wetting

Surface tension plays an important role in biology and ecosystems. For instance, it enables water striders to walk on the surface of water. It prevents sea water from evaporating into the atmosphere and, thus, preserves the ecosystem [58, 214]. Furthermore, surface tension is critical to the enhancement of the oil recovery process [130]. It is also critical in pharmaceutical manufacturing and drug delivery, such as tablet polymers coating, drug solubility, and drug stability [38, 177]. Surface tension is found to be of paramount significance to improve pharmaceutical drug manufacturing and processing, whereby drug bioavailability, digestibility, adsorption, and dissolution, depend on the surface tension of the drug formulation [20]. Other important applications can be found in surfactants and coating formulation. To achieve the maximum possible painted surface area, the interfacial tension between the

paint and the coated substrate must dominate the surface tension between the paint and the vapor interface. To do so, surfactants are commonly added to liquid coatings to control their surface tension [58, 190, 230].

The concept of surface tension finds its origin with the work of Young in 1805 who first developed the well-known Young equation. This equation was then studied by Laplace, and now takes the form of Equation (1.1.1), known as Young-Laplace equation: [82, 170].

$$p_{\alpha} - p_{\beta} = \gamma \kappa \quad (1.1.1)$$

where, in the context of the liquid-vapor interface of a static drop, p_{α} is the pressure inside the drop, p_{β} is the pressure outside the drop, γ is the surface tension (N/m), and κ is the mean curvature of the liquid surface.

For a spherical drop, Young–Laplace equation indicates that the internal pressure is greater than the external pressure (see Fig. 1.3.a). Surface tension can be interpreted physically in terms of inter-molecular forces, as it is caused by the attractive van der Waals forces of cohesion between liquid molecules, thereby minimizing the free energy by decreasing the interfacial area [23, 109]. Surface tension is also associated to partial wetting phenomena of a liquid phase on a solid surface. Partial wetting can be interpreted as a solid-liquid-vapor interaction. Wettability of the substrate by the liquid at rest can be characterized by the notion of equilibrium contact angle. To relate this physical quantity to the liquid surface tension, one method consists of balancing the interfacial forces acting on the contact line of the liquid with the substrate (also known as the triple line). When normalized to a unit length, these forces are the interfacial tensions between the three phases (solid/liquid/gas). By projecting the equilibrium forces on the solid plane, one obtains Young’s relation (see Fig. 1.3.b) [88, 245, 246]:

$$\gamma_v \cos \theta_e = \gamma_{sv} - \gamma_{sl} \quad (1.1.2)$$

where γ_{sl} , γ_v , and γ_{sv} are solid liquid, liquid-vapor, and solid-vapor interfacial tensions,

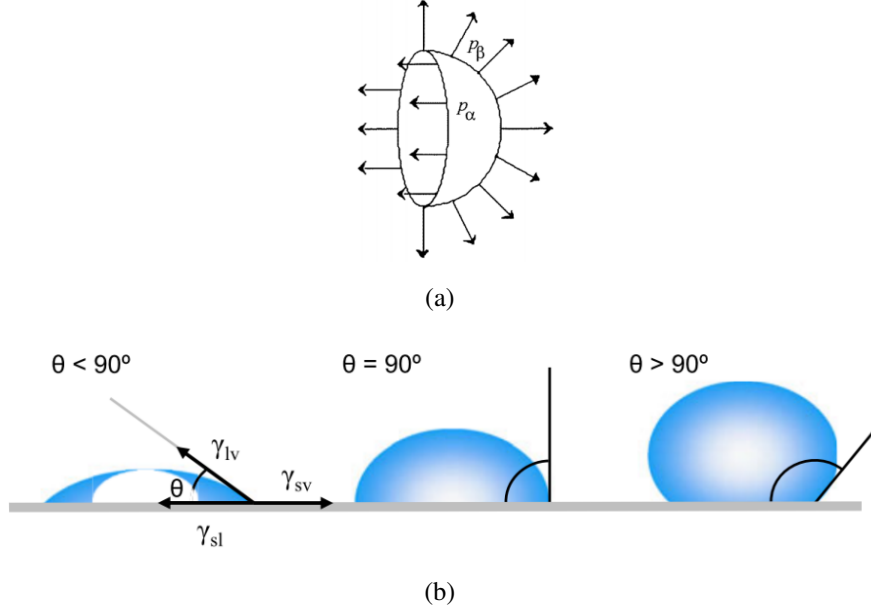


Figure 1.3: Representation of (a) Young-Laplace equation, reproduced from [170] and (b) wetting of surfaces, reproduced from [246].

and where θ_e is the equilibrium contact angle. The contact angle θ_e is a measure of surface wettability, i.e., wettability of the surface by the liquid. Due to the topographical and chemical heterogeneity of the substrate, there is no unique equilibrium contact angle on real surfaces [84, 208]. The term “omniphilic” indicates high wettability conditions, when the equilibrium contact angle is less than 90° . In contrast, the term “omniphobic” indicates low wettability conditions, i.e., when $\theta_e > 90^\circ$ [24, 40]. For water/substrate pairs, the terms “hydrophilic” and “hydrophobic” are commonly used instead of “omniphilic” and “omniphobic”, respectively.

1.1.2 Drop spreading

The first step in understanding drop dynamics is to study and predict its spreading behavior. Drop spreading is fundamentally tied to two dynamic interfacial phenomena, namely, contact line motion and free-surface deformation. It is caused by the capillary action, whereby the adhesive force between the liquid and the substrate dominates the cohesive

force between the liquid molecules [7, 28].

For drops in contact with a solid substrate, Young's stress is induced at the contact line as the drop spreads [37]. Young's stress is a force per unit length, which relates the dynamic contact angle to the tension force acting at the contact line [178]. This leads to a special slip regime where the contact line velocity evolves proportionally to the dynamic contact angle [178]. The Navier-Stokes equations are incompatible with the no-slip condition at the substrate and, therefore, lead to a singularity at the contact line [77]. This leads to nonphysical velocity evolution and energy dissipation known as "Huh and Scriven's paradox" [30, 37, 71, 104, 202]. For drops and thin films on hydrophilic surfaces, lubrication approximation theory can be used as a valid simplified and cost-efficient numerical model to regularize the contact line singularity with the concepts of disjoining pressure and precursor films [77]. However, this theory is not valid for hydrophobic surfaces. Thus, more sophisticated models are needed to analyze drop dynamics (drop deformation, pinning, and spreading) in the case of hydrophobic substrates. For both hydrophobic and hydrophilic substrates, the contact line singularity can be relieved by introducing i) a slip zone at the contact line, that accounts for the normal and tangential stresses, and the capillary action at the contact line, and ii) a slip zone away from the contact line, that accounts for shear and viscous stresses acting within the solid-liquid interfacial region [37, 143, 178, 227].

Previous work has shown that moving-grid models are well-suited to drop modeling [114, 115, 186, 187]. However, these models do not adequately allow contact line motions, which are fundamental to drop dynamics. One of the objectives of this dissertation is to address this deficiency.

1.1.3 Drop sliding

Drop sliding under the effect of gravity or other physical forcing is commonly observed in both the natural and industrial world. Due to its important role in countless applications, its numerical simulation is an active area of research [94, 129, 243, 244]. The prediction of the drop dynamic characteristics is important for various fields of application [138, 220]. For instance, the velocity reached by water drops sliding down the channels

of cooling towers is an important factor to predict the optimal heat exchange between water and ambient air [126, 144]. Understanding the detachment and subsequent sliding of water drops formed within the gas diffusion layer plays a major role in addressing the thermal and water managements of PEMFCs [15, 115, 187, 189, 197, 249].

A liquid drop on an inclined surface can roll, slide, or remain pinned [218, 231, 237]. A pinned drop remains attached to the substrate as long as the plane is tilted below a threshold inclination angle [16, 34, 69, 75, 80, 81, 166, 231, 242]. Upon crossing this threshold, a sudden depinning occurs, and the drop is observed to move according to three possible modes: a sliding mode, rolling mode, or a transition mode between sliding and rolling [60, 75, 218, 237]. The omniphobicity of the surface is an important factor that controls the mode of motion [24, 25, 218, 233]. Sliding motion can be observed either on omniphilic surfaces, commonly found in nature [67, 238], or on omniphobic surfaces. Rolling motion is observed as the shape of the drop approaches that of a sphere on a superomniphobic substrate [60, 133, 218]. For a water drop, pearl-shaped drops can be observed for a superhydrophobic substrate if the advancing contact angle is found to approach 180° [60].

When a liquid drop is deposited on a solid flat substrate, it spreads towards its static, equilibrium, configuration [208]. As the substrate is slowly inclined, the drop starts to deform and lean toward the downward direction, until the advancing edge of the drop moves before its receding edge [80, 151]. To model the effect of surface forces acting on the contact line, an empirical “retention force” can be devised. This force is experimentally known to be a function of i) the surface tension force, ii) the aspect ratio of the drop footprint, and iii) the contact angle hysteresis [80].

In the context of sliding liquid drops, the contact angle hysteresis is an important physical phenomenon. It is a physical property of the liquid in contact with a solid surface and, therefore, independent of the tilting angle. Both advancing and receding edges of a sliding liquid drop demonstrate different levels of interfacial free energies, corresponding to corresponding changes in the interfacial areas [84]. The advancing and receding contact angles are defined as the largest and lowest contact angles, respectively, in the total free energy range [1, 84]. The value of the contact angle hysteresis is defined as the difference

in the advancing and receding contact angles, which represents the total activation energy required to move the contact line of a sliding liquid drop [84].

The retention force balances both the gravitational and capillary forces acting at the contact line and, thus, opposes the motion of the liquid drop [84]. The gravitational force is dominant as the substrate reaches a threshold inclination angle, forcing the drop to move towards its direction. Despite the large body of work in this field, there is a critical need for accurate prediction of drop sliding dynamics in wide range of conditions [142].

1.2 Embedded two-phase flow

A flow in which two physical states of a substance, or different substances such as water and air, are simultaneously present is known as a two-phase flow [109]. Interfacial phenomena play an important role in two-phase flows, especially when the liquid volume becomes smaller in size, as in drops, rivulets, and thin films, for which surface tension effects become dominant [224, 225].

Two-phase flows are critical in various important applications. For example, two-phase flows are present in i) renewable and non-conventional energy sources, such as in fuel cells, ii) heat transfer systems, such as in cooling towers [62], iii) additive manufacturing technologies, such as in inkjet printing [95], iv) the enhancement of the oil recovery process [130]. In the following sections, we describe a few engineering applications and the related technical questions.

1.2.1 Polymer electrolyte membrane fuel cells

Fuel cells are electrochemical devices that transfer the chemical potential energy of a fuel into electrical energy [205]. Electrochemical reaction of an oxidizing agent, commonly oxygen, with hydrogen fuel takes place inside fuel cells to generate electrical current and heat [116]. Fuel cells encompass a wide variety of designs, with operating temperatures from -40°C to 1000°C [112]. Hence, fuel cells are promising energy conversion devices, as alternatives to conventional energy system. Compared to other types of fuel cells, polymer electrolyte membrane fuel cells (PEMFCs) deliver high-power density [205]. The principal

components of PEMFCs are i) electrolyte membrane across which the hydrogen protons travel, ii) catalyst layers, iii) the gas diffusion layers (GDL), iv) bipolar plate with structured gas channels. Figure 1.5 illustrates the main components and processes of the PEMFC [13].

In PEMFC, hydrogen is channeled to the anode, while oxidant is channeled to the cathode. A catalyst, usually platinum, is used to enhance both the hydrogen oxidation reaction occurring at the anode and the oxygen reduction reaction at the cathode. At the anode, hydrogen is split into protons (positive hydrogen ions) and electrons. The protons pass to the cathode through the polymer electrolyte membrane, while the electrons travel to the cathode along an external circuit, thereby creating the electrical current. At the cathode protons, electrons and oxygen react to generate water and heat. The formed water must flow out of the channel to avoid blockage and performance deterioration.

Despite their advantages, key challenges remain for their wide-scale adoption, such as their durability and high cost compared to conventional energy devices [205, 229]. For instance, the cost analysis of 80 kW-net automotive PEMFC-based, projected to a volume of half a million units/year, is shown in Fig. 1.4 [145, 211].

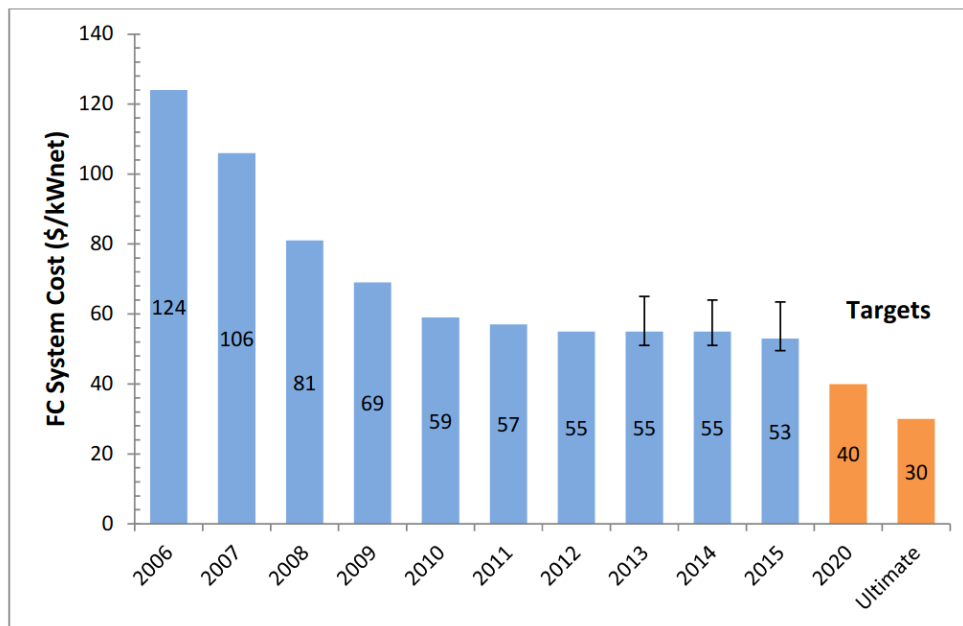


Figure 1.4: Cost analysis for automotive PEMFC systems [145, 211].

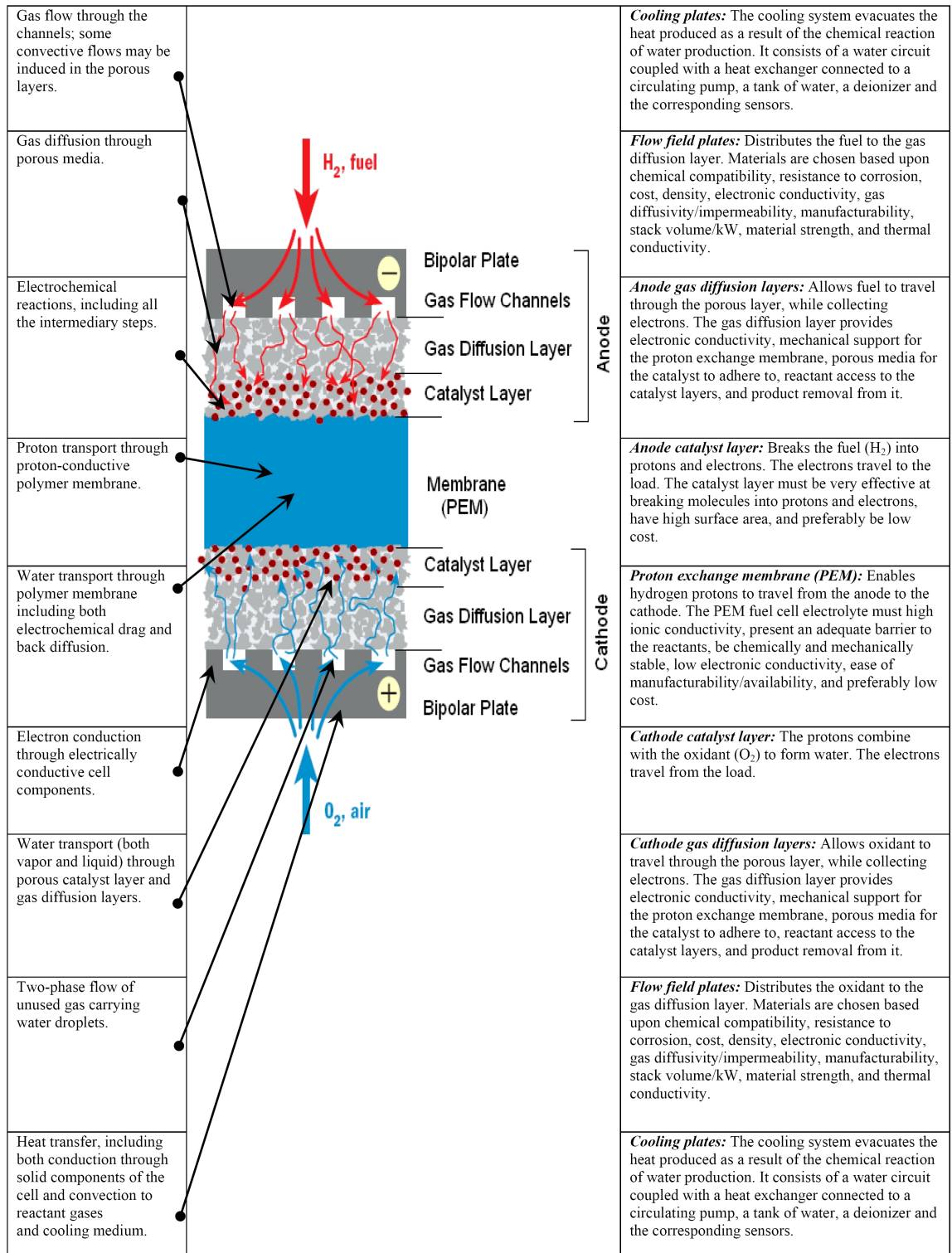
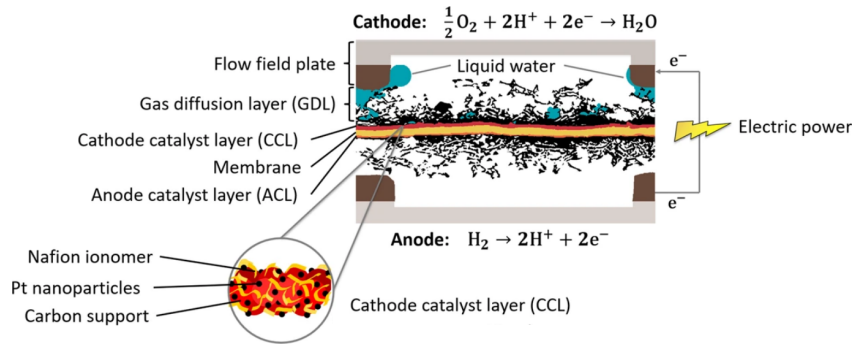
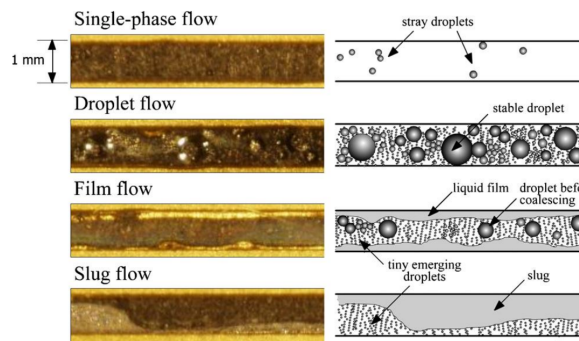


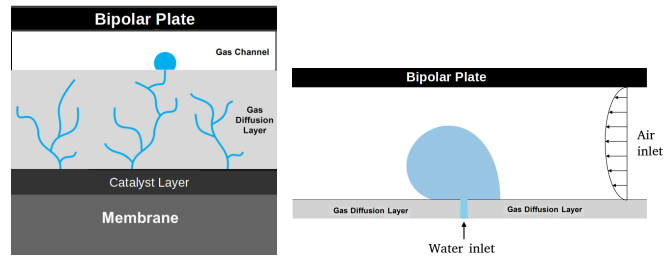
Figure 1.5: Schematic representation of the main components and processes of the PEMFC. Figure is reproduced from [13].



(a) Liquid water generation in PEMFCs [232]



(b) Types of flow encountered in PEMFC cathode channel [41]



(c) Water drop formation in the membrane, diffusion through the gas diffusion layer, and emerging into the gas flow channel [187]

(d) Two-phase flow, embedded, modeling zone [112, 116]

Figure 1.6: Example of two-phase flow applications in PEMFCs.

One of the issues facing PEMFCs is the water management within the gas channels (Fig. 1.6). Under high current density conditions, water vapor condenses in the GDLs. Fuel cell flooding blocks the gas channel causing shortage of reactants at the reaction side and, thus, a decrease of the current density. Therefore, the GDL is commonly treated with hydrophobic agents, such as Polytetrafluoroethylene (PTFE), to facilitate the removal of excessive water condensation. Nevertheless, fuel cell dry-out is not recommended as the membrane requires a hydrated environment to maintain proton conductivity. This problem can be studied by conducting numerical simulations to serve as predicting tools, and to provide design guidelines for optimal operating conditions.

Though we restrict our numerical model to isothermal conditions, it could readily be extended to include additional effects relevant to other two-phase flow applications. This includes, but is not limited to, evaporative cooling in wet cooling towers, piezoelectric inkjet printing, and oil and gas processing.

1.2.2 Evaporative cooling in wet cooling towers

Wet cooling towers (Fig. 1.7) are designed to utilize the ambient air temperature to cool down streams of process water [144]. However, water is lost extensively during this cooling process, mainly due to evaporation. As an example of a typical cooling tower plant in the southern area of Brazil, 1000 m³/h of water is evaporated and lost for cooling of a volume of 50,000 m³/h from 42C° to 27C° [144]. Accordingly, two-phase flow analyses based on reliable numerical models to simulate drop, rivulet, or thin film dynamics under thermal conditions can serve to identify optimal operating conditions of cooling towers, so as to minimize water loss.

Wet cooling towers efficiencies depend on fill efficiencies [127], where the maximum contact between the two phases takes place. Fig. 1.8 is a representation of the fill zone. Proper fill design requires sufficient liquid surface area to maximize the convection process. However, the pressure drop along the channel should be minimized. In addition, the fill material should be selected to have good wettability and durability. Hence, a reliable simulation tool is required to test and recommend an optimal fill design [36].

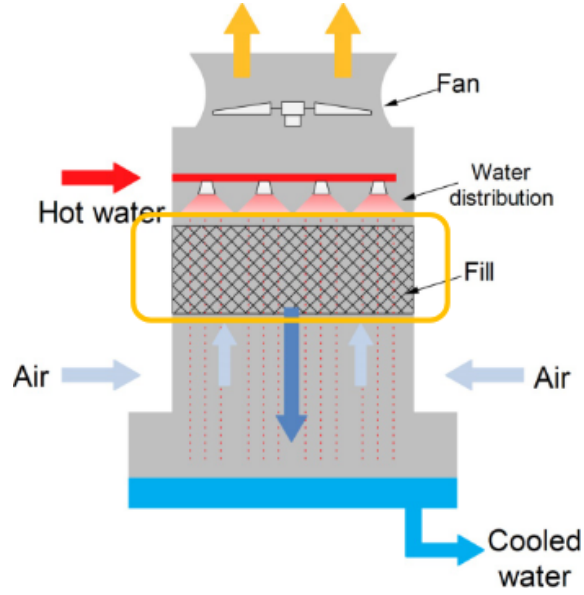


Figure 1.7: Schematic diagram of a cooling tower [35].

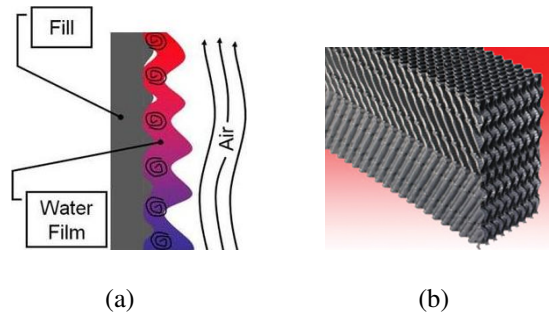


Figure 1.8: Fill zones: (a) two-phase flow inside the fill zone, reproduced from [36] and (b) fill arrangements inside the cooling tower, reproduced from [35].

1.2.3 Piezoelectric inkjet printing

Piezoelectric, drop-on-demand, inkjet printing technology involves both two-phase flow and free-surface evolution phenomena (see Fig. 1.9) [235]. It is one of several advanced additive manufacturing technologies, that belongs to the class of material extrusion/jetting methods. Due to its biocompatibility and geometric design flexibility, printing technology has demonstrated high potential and capabilities in different fields of applications such as MEMS, fuel cells, and biomedical engineering [150, 161]. Furthermore, inkjet printing

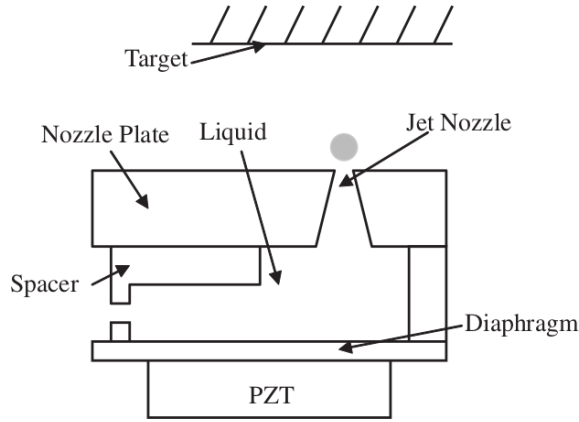


Figure 1.9: Schematic diagram of a piezoelectric inkjet printer, reproduced from [235].

technology can be implemented at elevated temperature and, thus, it can be implemented for viscous polymer dispensing applications [95].

The main issues in piezoelectric inkjet printing are avoiding nozzle clogging [101, 167] and maintaining high printing resolution and stability [122]. Fluid viscosity, inertia, and surface tension are the critical parameters controlling jetting and printing [59]. By controlling these parameters, our proposed model can help in predicting the optimal drop size, orifice size, and ink-substrate compatibility. Therefore, orifice clogging may be avoided while guaranteeing high printing resolution.

1.2.4 Oil and gas processing

Two-phase flow phenomenon is relevant to nearly every step of the oil-gas processing. It starts in gas-oil separation plants, where natural gas and water are separated from crude oil [3]. Crude oil is then dehydrated, de-salted, and sent to refineries for further processing.

In refineries, crude oil is sent to fractional distillation columns and turned into usable products such as gasoline and diesel (see Fig. 1.10). During the fractional distillation process, crude oil is piped through a steam-heated column. Heat boils off hydrocarbons and turned them into vapor. Accordingly, vapor rises the distillation column. Vapor condenses to liquid drops and films as it cools down. Condensed liquids are collected and turned into products. The final products are transported through pipelines for storage, usage, and shipping.

During transportation process, pressure drop across pipelines causes liquid products to evaporate. High pressure drop results in flow instability within the pipe and, therefore, introduces severe mechanical vibrations. Fittings (vent valves) must be connected throughout the piping system to vent excess vapor to minimize the pressure drop [3, 9].

A reliable two-phase flow model may improve both the productivity and efficiency of the oil and gas industry. For instance, variation of both i) the physical properties of both fluids and ii) the two-phase flow parameters (velocity, and pressure) can control both the density and temperature of the liquid/gas mixture [3, 9]. Furthermore, identifying the optimal design of the pipeline network can avoid high pressure drop across the pipelines and, thus, maintain their integrity.

1.3 Numerical modeling

The dynamic simulation of drops, in single or two-phase flow, typically encounters several challenges when faced with surface tension and moving contact line phenomena: i) the accurate detection of the gas-liquid interface [113, 227, 234], ii) the tracking of the changes of material properties (such as viscosity and density), iii) the proper accounting of the pressure jump discontinuity across the free-surface [115, 186], iv) the identification of the interaction forces between liquids and substrates [29, 178, 226, 248], and v) the guarantee of mesh-independent solutions [12, 37, 221, 239].

Modeling approaches can be categorized as either numerical or analytical. Analytical approaches utilize balance equations and predefined boundary conditions [50, 116]. With respect to drop dynamics, for which surface tension is dominant, analytical approaches lack continuity in tracking the interface and in conserving the fluid properties. Relative errors between the analytical prediction and the experimental values can exceed 30% under high deformation [113]. Alternatively, numerical approaches can be developed to overcome these difficulties.

Two commonly used numerical approaches have been developed for drop dynamics to address moving deformable interfaces and moving contact lines: the Eulerian approach and the Lagrangian approach. [113, 115] (see Fig. 1.11).

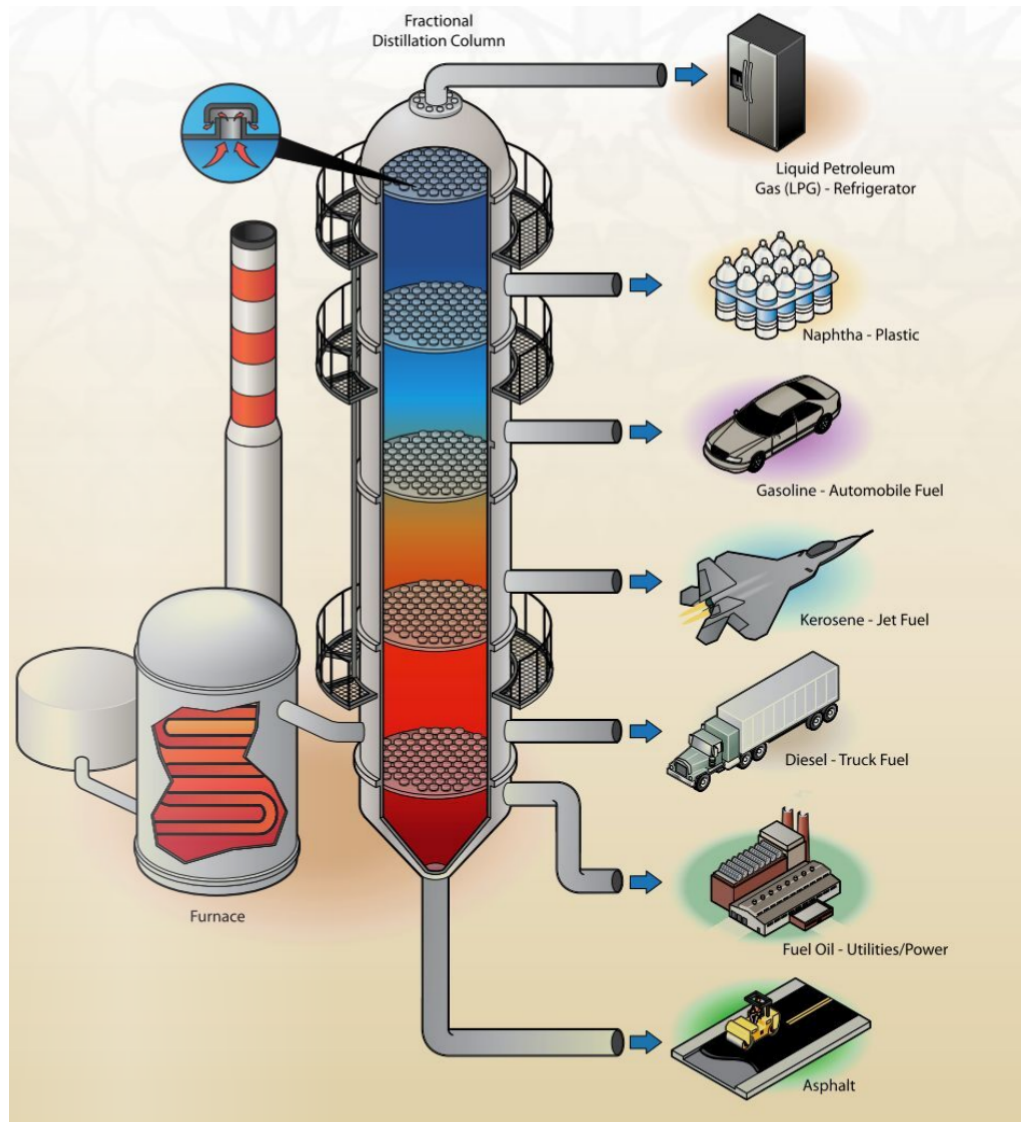


Figure 1.10: Schematic diagram of a fractional distillation, reproduced from [3].

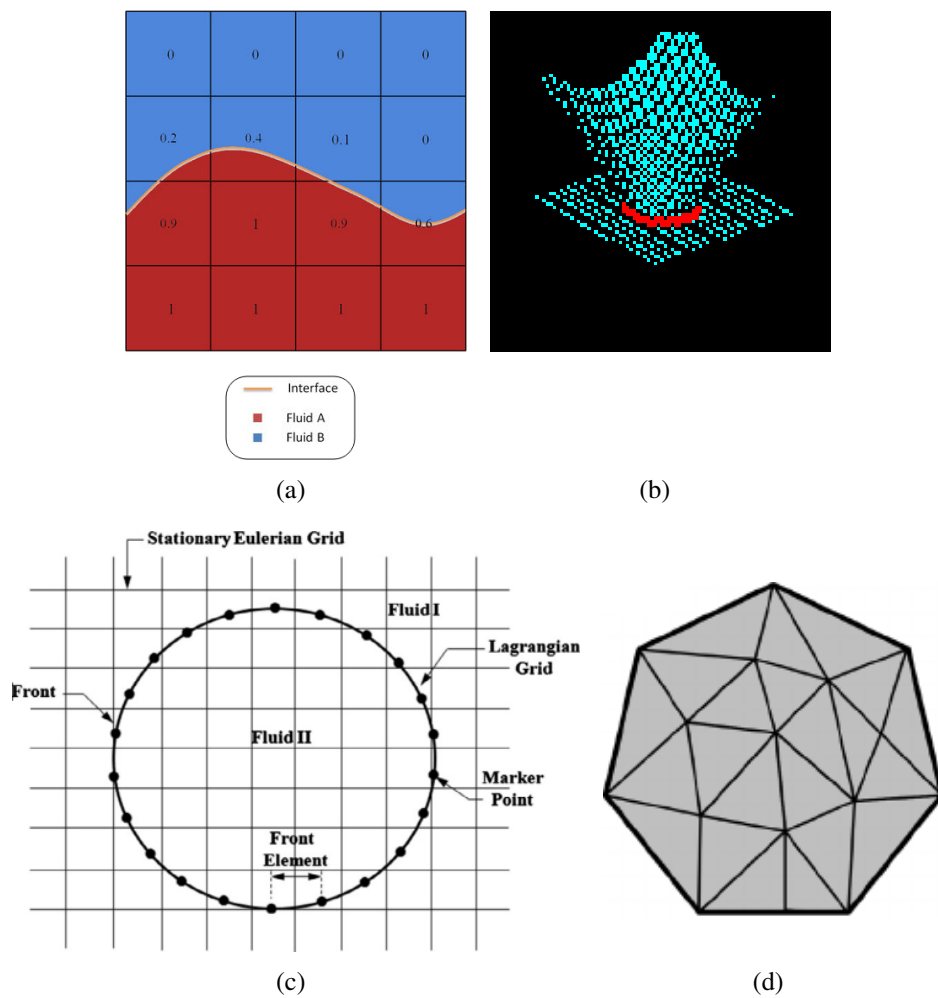


Figure 1.11: Schematic representations of a) an Eulerian, front capturing, volume of fluid approach [90], b) an Eulerian, front capturing, level set approach: red color curve is the zero level set [6], c) an Eulerian, front tracking technique [110], and d) a Lagrangian approach [113].

The Eulerian approach is a fixed mesh numerical method, which is ideal for handling large deformations. However, the discretization of advective terms is a challenge, whenever one is dealing with small deformation and interface tracking. This may lead to interfacial diffusion, smearing of the interface, and the need for larger computational time steps [213]. Two methods are generally utilized for the treatment of the gas-liquid interface: front capturing method and front tracking method [113, 186].

Front capturing techniques use scalar functions to define the interface. Two commonly used techniques are the volume of fluid (VOF) and the level set (LS) methods [113, 175, 181, 203]. The VOF method (Fig. 1.11(a)) is based on adding an additional term to the mass and momentum equations, which is the continuous fraction function C_K . This leads to a convection equation governing the interface volume fraction. The quantity C_K takes values between zero and one: it will take the value of zero for nodes outside the fluid K , the value of one for nodes inside the fluid, and values between zero and one at the interface [112]. Difficulties facing the method of VOF are the existence of a jump discontinuity of the volume fraction function at the interface, and the appearance of artificial diffusion at the interface [115, 186, 187].

An alternative to VOF is the LS method (Fig. 1.11(b)), which represents another front capturing technique. In this method, the interface is represented by the zero level set of a smooth scalar function $\phi(x)$. The position of the interface is defined implicitly by the nodal values of the function $\phi(x)$, such that positive values nodes are inside the fluid domain, and negative values nodes are outside the fluid domain [112]. Difficulties encountered by the LS method are a consequence of the fact that it does not always accurately estimates the interface curvature, and that it does not guarantee mass conservation [89, 187].

The front tracking Eulerian scheme (Fig. 1.11(c)) is an alternative to the front capturing methods. This method uses Lagrangian markers to account for the interface explicitly. The velocity at the interface is evaluated and interpolated using the Eulerian mesh. Accordingly, remeshing is required at the boundary for tracking and updating these interface markers, leading to high computational cost [112, 171].

A second common methodology is based on a Lagrangian scheme (Fig. 1.11(d)). In

this approach, moving meshes are used for computing the domain, and moving boundary meshes for the interfaces are created [153]. There exist two main advantages of the Lagrangian approach: (i) its ability to track the interfaces accurately at smaller time steps, and (ii) the generation of symmetric matrices representing the convective terms within the discretized system of equations [112, 153]. One main disadvantage of the purely Lagrangian method is the necessity of remeshing the computational domain after each time step in order to avoid mesh degradation, thereby increasing the computational cost [17].

The Lattice Boltzmann method (LBM) is another simulation scheme developed in computational fluid dynamics. LBM considers a collection of particles as a single unit, governed by classical kinetic theory at the mesoscopic level. It is based on streaming and collision mechanisms of particles, utilizing square grids in 2D or cubical lattices in 3D. LBM uses the lattice Boltzmann equation to represent the particles in terms of distribution functions, where only a single variable is unknown at any given time. Accordingly, the velocity and pressure fields are represented by the momentum of these distribution functions [48]. LBM is easier to implement than numerical schemes based on Navier-Stokes equations. Yet, accurate tracking of the macroscopic fluid properties, such as viscosity and surface tension coefficient, remains a key challenge for the LBM approach, especially when curved grids and refining are essential [48, 112].

Another method is the Particle Finite Element Method (PFEM). PFEM is a combination of the finite element method and the particle method, where a set of particles represent the Lagrangian domain [153]. These particles follow the Lagrangian fluid movement using the Delaunay triangulation technique, whereby the physical properties of the domain are transported with the particle motion [61, 163]. The work presented in this dissertation is based on the PFEM approach. Our novel and significant contribution to this scheme is to accurately account for dynamic interfacial and wetting phenomena. This had yet to be done properly. Further details regarding the PFEM are introduced in the following section.

1.4 The Particle Finite Element Method (PFEM)

The Particle Finite Element Method (PFEM) is an active field of research in the area of numerical analysis and scientific computation [55]. It was introduced in the last two decades by Oñate et al. [163] and Idelsohn et al. [107]. The motivation behind the development of this advanced scheme was to predict the breaking waves and splashing behavior of fluid flows with free-surfaces, where large deformation of the interface is expected [107].

The PFEM has proven to be an effective and robust numerical technique for simulating complex applications in engineering. It is a powerful numerical tool for handling problems with evolving domains and large topological deformation [55]. For instance, applications involving change of phase, such as melting objects in fires, have been successfully simulated by the PFEM [185]. Furthermore, the PFEM is commonly used to solve fluid–structure interaction problems, such as in dam-break tests [55].

The PFEM merges the FEM with the particle method. It solves the governing equations of the Lagrangian domain by the standard Galerkin formulation of the FEM. Consequently, the convective term in the continuum and/or thermal equations vanishes, and therefore the non-linearity of the system of equations is eliminated or reduced [19]. In the PFEM, the nodes of the finite element mesh are represented by particles. Each particle stores the mathematical information and physical quantities assigned to it. The particle moves in the domain following its force and velocity fields. At each time step, the domain boundaries are reconstructed (re-meshed) using the Delaunay triangulation/tetrahedralization algorithm and the alpha shape method [55, 107, 185]. Thus, no artificial diffusion is added by the PFEM scheme [115]. Typical steps of the PFEM scheme are demonstrated in Fig. 1.12 [55]. Appendix A provides additional information on both the Delaunay triangulation/tetrahedralization and the alpha shape method.

The application of a PFEM model has proven to be particularly advantageous when dealing with drop dynamics and surface tension-dominated problems. It allows to accurately track the evolution of the liquid domain boundary, without introducing enrichment shape functions or smearing the surface tension via continuous force approach [107, 163]. A two-phase incompressible fluid flow model based on the PFEM has also been developed to study

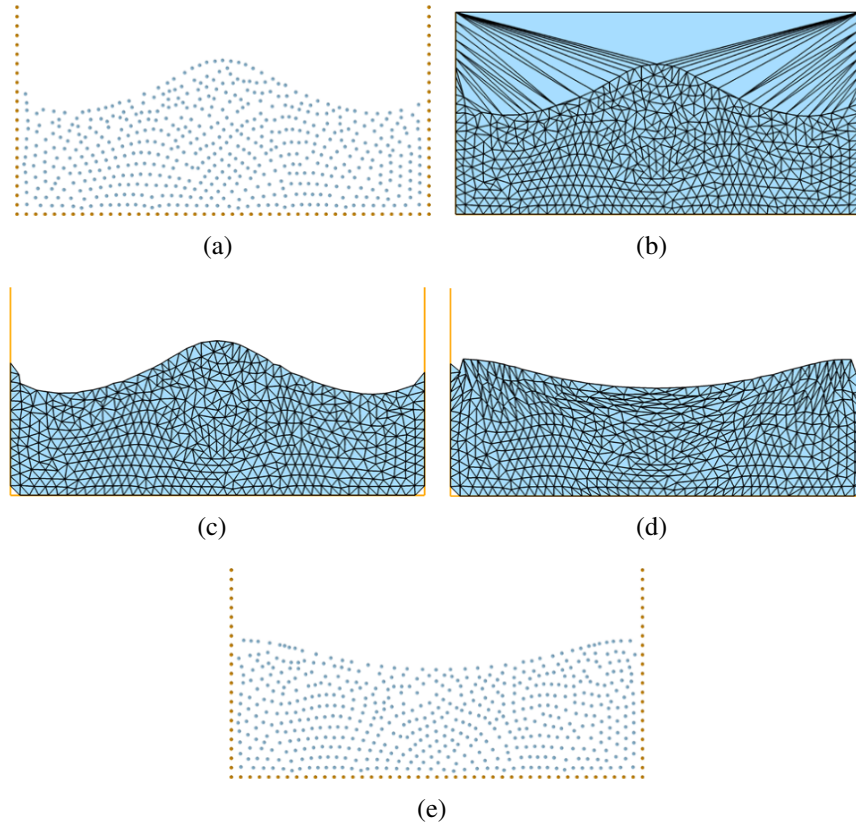


Figure 1.12: Steps of the PFEM scheme: a) starting with an initial configuration of mesh nodes, i.e., particles where mathematical information and physical quantities are stored, b) generating mesh connectivity by Delaunay triangulation, c) recovering domain boundaries by the alpha shape method, d) updating the mesh after computations and, accordingly, e) updating the mesh nodes position. Figures are reproduced from [55].

problems with surface tension-dominated interfacial flows, such as water transport in fuel cell gas channels [186]. The Lagrangian PFEM scheme is used to model the liquid phase, whereas the gas phase is solved using the fixed grid Eulerian approach. However, partial wetting phenomena, including both liquid spreading and sliding dynamics, have never been considered in any of the previous PFEM-based models, which is one of the main objectives of this dissertation.

1.5 Goals and implementation methodology

The primary goal of this dissertation is to develop 2D and 3D PFEM single-phase hydrodynamic drop models, with the ability to accurately predict the spatio-temporal evolution of both spreading and sliding liquid drops on smooth surfaces. Single-phase dynamic models are then extended to embedded two-phase flow, more specifically to simulate the motion of drops injected into and pressure driven out of channels. Throughout these studies, the numerical results obtained by these models are systematically validated by experiments obtained either in the published literature or by collaborating research groups.

Numerical models are implemented using the Updated Lagrangian Fluid (ULF) application within *Kratos Multi-Physics* [182], a C++ object oriented finite element open-source framework [57]. Results are obtained using a Linux operating system with an Intel® Core(TM) i7-8750H CPU @ 2.20GHz, 12 processors, and 32 GB RAM.

1.6 Dissertation outline

The two-dimensional numerical model for drop spreading dynamics is described in chapter 2. This chapter considers the spontaneous spreading of liquid drops driven by capillary forces. We introduce boundary conditions that alleviate the contact line singularity. Our proposed model is equipped with i) an effective slip boundary condition that balances the induced Young's stress at the contact line, and ii) a solid-liquid slip boundary condition that accounts for the viscous dissipation along the solid-liquid interface. Mesh size and time step criteria are derived in accordance with the capillary action at the contact line. The governing equations are discretized using the PFEM scheme. Mesh dependence study is

performed, whereby the spatio-temporal evolution obtained by the proposed boundary conditions is compared with alternate choices of boundary conditions commonly found in the literature. Our drop spreading model is validated using experimental data retrieved from the literature. The model is further validated using sessile-drop injection data provided by the UC Berkeley and U Alberta ESDL research groups.

In chapter 3, we extend the spreading model proposed in chapter 2 to liquid drop sliding down an incline. The model includes the effect of the retention force associated with the aspect ratio of the drop footprint (represented by a shape factor parameter), surface tension force, and contact angle hysteresis. The extended model is validated experimentally using seven different scenarios of sliding drops down on inclined substrates. For these cases, we study the effects of i) both the physical parameters and volume of the liquid drops and ii) both the omniphilicity and angle of inclination of substrates. Parametric studies are performed on each case to demonstrate the effect of the shape factor parameter on the development of a physical sliding drop dynamics model.

The 2D model does not predict out-of-plane geometric variations since it does not account for out-of-plane forces. Thus, our proposed 2D single-phase drop dynamics model is extended to 3D in chapter 4. To properly account for their geometrical effect, we first consider the simulation of the equilibrium of viscous liquid drops. We compare the numerical configuration obtained by both the 2D and 3D models with the experimental data obtained from the literature. Moreover, we validate our proposed 3D model experimentally using different liquid drop spreading and sliding scenarios presented in chapters 2 and 3, respectively.

The single-phase drop dynamics models presented in chapters 2-4 are extended to embedded two-phase flows. Different detachment modes of liquid drops are investigated under the effect of external gas flow. Chapter 5 demonstrates the success of the Eulerian-PFEM two-phase flow formulation. The main advantage of the Eulerian-PFEM scheme is its ability to track the liquid-gas interface while reducing the computational cost. This chapter introduces the governing equations and boundary conditions of the proposed Eulerian-PFEM approach, followed by the discretization techniques and coupling strategies. We first validate

the Eulerian scheme, both in 2D and 3D, by using the approximate analytical solution for estimating the pressure drop inside two different channels. Then, we validate the model using experimental data collected by the UC Berkeley and U Alberta ESDL research groups. This task aims to predict the dynamic behavior of water drops inside fuel cell channels of varying wettability. Drop motions are studied at various airflow rates and drop-to-channel height ratios. The effects of both i) surface hydrophobicity and ii) drop-to-channel height ratio on the spatio-temporal evolution of the water drop are demonstrated.

Chapter 6 concludes this dissertation and highlights its main achievements. It also suggests a number of promising areas for future work.

Chapter 2

A TWO-DIMENSIONAL NUMERICAL MODEL FOR DROP SPREADING DYNAMICS

2.1 Introduction

Liquid drop spreading is the natural phenomenon to occur when a spherical drop comes into contact with a flat wettable surface [28, 68]. It is crucially important in industrial and advanced surface engineering applications such as plant treatment, pesticide deposition, spray cooling, paints, anti-corrosive coating, lubrication, MEMS, microfluidics, and inkjet printing technologies [68, 134, 135].

Physically, two main regimes are observed for a spreading liquid drop: an initial inertial regime, followed by slow viscous regime [68, 141]. The initial rapid spreading regime is caused by the capillary-driven action, i.e., when the adhesion force between the liquid and substrate strongly dominates the cohesive forces between the liquid molecules [28, 141]. The viscous spreading regime, however, is caused by the viscous dissipation of fluid, i.e., when the liquid viscous forces balance the contact line capillary forces [68, 216].

Mathematically, the moving contact line paradox of infinite energy dissipation (see Sec. 1.1.2) must be resolved for both regimes of liquid drop spreading [30, 37, 71, 104, 202, 208]. To do so, the Navier-stokes equation must be equipped with an effective boundary condition at the contact line. Consequently, the main challenges in the numerical modeling of drop spreading on solid substrates are i) regularizing the contact line singularity [12, 37, 143, 178], and ii) tracking the corresponding free-surface deformation. Jarauta *et al.* [114] developed a numerical model based on the PFEM that can accurately track the free-surface evolution. However, resolving the contact line singularity remains a challenge, which we address in this chapter.

The simplest attempt to resolve the singularity at the contact line consists in applying a static contact angle condition where the direction of the vector normal to the liquid-air surface at the contact line is constant and related to the equilibrium contact angle for the substrate at hand [49, 219, 250]. However, this approach cannot account for drop pinning, and therefore, cannot predict the dynamics of spreading drops. A dynamic contact angle condition is actually needed to account for the liquid drop spreading phenomenon [114, 115]. The most basic dynamic contact line condition imposes a slip boundary condition, i.e., a contact line velocity normal to the substrate is zero, when a critical contact angle is reached [226]. This condition implies that no energy is dissipated as the contact line moves on the solid substrate, and that the velocity of the contact line is unbounded, which is in contradiction with experimental observations [200].

Various boundary conditions have been proposed to alleviate the singularity at the contact line. Huh and Scriven [104] introduced a Navier-slip condition to account for a viscous dissipation along the solid-liquid interface as a function of the shear stress. Hocking proposed a surface roughness condition in terms of a shear flow along a corrugated surface [99]. Alternatively, Frumkin [83], Derjaguin [64], Hervet and De Gennes [97], and Eres *et al.* [77] included the concepts of precursor film and disjoining pressure in order to model the effect of both short-range and long-range surface interactions. Blake introduced a molecular-kinetic model that treats the contact line movement in terms of molecular adsorption and desorption densities at the substrate [96]. Furthermore, Van *et al.* [223] devised empirical, power-law, models that relate the dynamic contact angle to the capillary number [32, 117, 199]. Recently, several authors have proposed a combination of the mechanisms described above to alleviate the contact line singularity [178, 200].

Lubrication models, which use the disjoining pressure theory to resolve the contact line singularity, have been developed to predict the evolution of thin films and drops while taking into account the effect of surface forces [77, 196]. However, these models are limited to small contact angles, and face great numerical difficulties to resolve the length scales below which surface forces are effective. In this work, we consider a macroscopic dissipative force model which takes into account the capillary and viscous forces, both acting along

the contact line [75, 81, 84, 141], as well as the viscous dissipation along the solid-liquid interface [104, 173].

Here, we will discuss in further detail the theories behind two commonly used boundary conditions for modeling the hydrodynamic Navier-Stokes equations, which are i) the disjoining pressure theory and ii) the dissipative force and viscous dissipation models.

2.1.1 Disjoining pressure model

A common approach to relieve the moving contact line singularity is by taking into account the disjoining pressure which is a measure of the surface forces [208]. The term “disjoining pressure” is indicative of a repulsion phenomenon between phase boundaries. The term is also used for attraction between boundaries, for which “conjoining pressure” would be more appropriate.

The disjoining pressure appears at the contact line due to the influence of the surface forces on the liquid boundary layers (see Fig. 2.1) [208]. The main components of the disjoining pressure are i) the molecular/dispersion component, which is the van der Waals component, ii) the electrostatic component caused by the electrical double layer formation, and iii) the structural component caused by the liquid and solid interactions. Most disjoining pressure models found in the literature are simplified. They do not take into account the actual values of the disjoining pressure components, which are experimentally found to be in the realm of nano-mechanics [208].

The inadequacy of considering the FEM approach in modeling the disjoining pressure theory is commonly overlooked in the literature. The value of the flat equilibrium liquid film in front of the drop (region 4 in Fig. 2.1) is critical to obtain the exact value of the balancing forces at the contact line. The thickness of this thin film is experimentally found to be less than 10^{-7} m [208]. Thus, the FEM, which is the numerical technique used in this dissertation, is not adequate for modeling such small length-scale effects (see Fig. 2.2) [222].

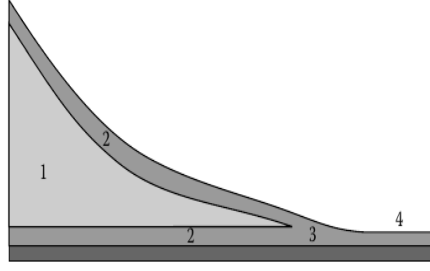
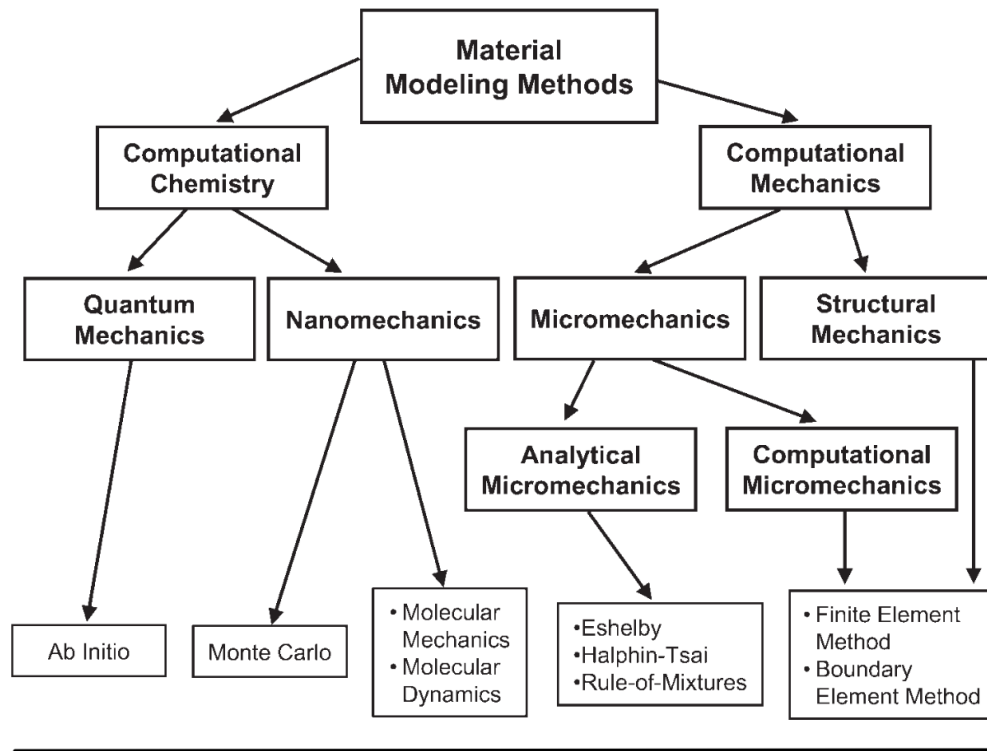


Figure 2.1: Liquid profile in the vicinity of the apparent contact line: (1) bulk liquid, (2) liquid–air and liquid–solid interfaces, (3) region where surface forces boundary layers overlap, and (4) region of thin equilibrium film. The disjoining pressure is the dominating mechanism at regions (3) and (4). Figure is reproduced from [208].

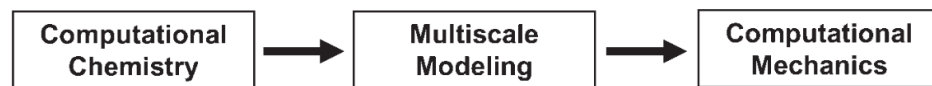
2.1.2 Dissipative and viscous force models

To achieve a physically relevant contact line velocity, several authors alleviate the contact line singularity by devising dissipative force models. Spelt [204] proposed a linearly dependent contact angle condition that is a function of the sign of the contact line velocity. Manservigi and Scardovelli [143] added a dissipative, resistive force applied to the contact line as a function of the capillary number. Buscaglia and Ausas [37] presented a variational formulation of a surface tension model that included a dissipative force acting on the contact line. In their formulation, the value of the dissipative force was inversely proportional to the contact line velocity. However, their model did not account for contact line pinning, which often takes place on rough substrates. In addition to the dissipative force condition, Ren and E [178] observed that the normal stress inside the solid-liquid interface exhibits a large jump across the contact line, which varies linearly with its velocity, and hence should be balanced and considered as an additional boundary condition. Moreover, Venkatesan *et al.* [226] observed that the tangential stress at the contact line is proportional to its tangential velocity, which was included as an additional term in their numerical formulation.

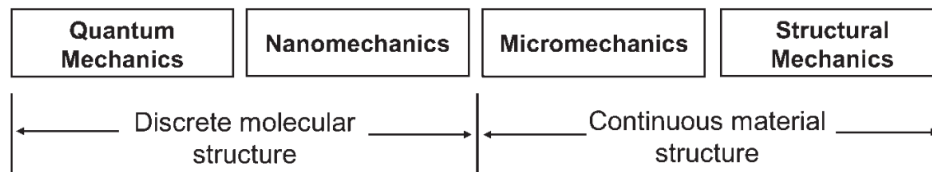
Obtaining a mesh-independent solution is an additional modeling challenge. Several authors have studied the dependence of the numerical solution of wetting phenomena on the mesh size. In reference [143], Manservigi and Scardovelli studied the spreading behavior of



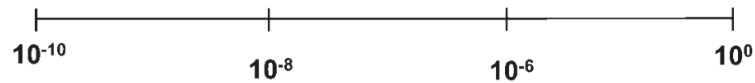
Modeling methods



Modeling tools



Length scale (m)



Time scale (sec)

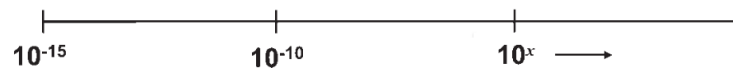


Figure 2.2: Categories of commonly used modeling methods, and their corresponding length and time scales. Figure is reproduced from [222].

drops by utilizing the Lagrangian front tracking approach, and concluded that adding the dissipative energy term reduces the spreading rate until a nearly no-slip condition is achieved. Afkhami *et al.* [12] conducted a numerical study using the volume-of-fluid (VOF) method to analyze the dependence of the dynamic contact angle evolution on the mesh size. They observed that this dependence could be reduced by relating the dynamic contact angle to the capillary number and to the mesh size. More recently, Buscaglia and Ausas [37] introduced a variational formulation and analyzed the effect of adding a dissipative force as a constant value on the mesh dependency of the solution. They concluded that increasing the dissipative force term leads to a mesh-independent solution. In addition, Venkatesan *et al.* [226] used an Arbitrary Lagrangian-Eulerian (ALE) finite element formulation and introduced a slip coefficient in the Navier-slip term that is a function of the mesh size, Weber number, and Reynolds number. They managed to alleviate spurious mesh dependency. However, they observed that the proposed relation did not work properly for hydrophobic surfaces.

In this chapter, we propose a drop spreading model using an updated Lagrangian framework to solve for the governing equations within the liquid domain. The curvature of the liquid surface is tracked accurately using a deforming boundary mesh. Dissipative and viscous forces are included in the formulation to alleviate the singularity at the solid-liquid interface. The chapter is organized as follows. Sections 2.2-2.5 describe the physical model, governing equations, and boundary conditions for the proposed PFEM-based model in the context of drop spreading dynamics. Special attention is given to the boundary conditions applied at the solid-liquid interface including the contact line. The FEM discretization and solving strategies are discussed in Sec. 2.6, followed by the mesh size and time step criteria in Sec. 2.7. Numerical results are shown in Sec. 2.8, including a detailed analysis of the manner in which a dissipative force can produce a mesh-independent solution. In Sec. 2.9, the model is validated by comparing numerical results for drop spreading on hydrophilic and hydrophobic surfaces with experimental data. The model is further validated using available drop injection experimental data provided by the UC Berkeley and U Alberta Energy Systems Design Laboratory groups. The main concepts, figures, and outcomes of this chapters

are reproduced from [Elaf Mahrous, Alex Jarauta, Thomas Chan, Pavel Ryzhakov, Adam Z Weber, R Valéry Roy, and Marc Secanell. A particle finite element-based model for droplet spreading analysis. *Physics of Fluids*, 32(4):042106, 2020.], with the permission of AIP Publishing (See Appendix H for more information about the publisher's permission).

2.2 Physical model and governing equations

In order to predict the spreading rate of the drop on the solid substrate and track the corresponding contact angle evolution, a dissipative force at the contact line is included in the formulation in addition to the Navier-slip boundary conditions at the solid–liquid interface. The inclusion of these boundary conditions makes it possible to account for the induced Young's stress at the contact line and for the viscous dissipation along the solid–liquid interfacial region.

Let us consider a domain Ω which represents a liquid drop in contact with a solid substrate, as shown in Fig. 2.3. The boundary of the domain is split into three regions $\partial\Omega = \Gamma_I \cup \Gamma_S \cup \partial\Gamma$. The part of the domain boundary corresponding to the liquid in contact with a substrate, excluding the contact line, is designated as Γ_S . The contact line is denoted by $\partial\Gamma$. The rest of the boundary of the liquid phase is denoted by Γ_I , which corresponds to the drop's free-surface. For two-dimensional problems, the contact line reduces to two triple points. The drop is assumed to be surrounded by its saturated liquid-vapor phase [58]. It is assumed that the velocity of the vapor is negligible, i.e., it exerts no mechanical action upon the drop and thus the drop can be analyzed as an isolated entity.

The equations expressing momentum and mass conservation for an incompressible Newtonian fluid are as follows:

$$\nabla \cdot \mathbf{v} = 0 \quad \text{on } \Omega \quad (2.2.1)$$

$$\rho \frac{D\mathbf{v}}{Dt} - \nabla \cdot \boldsymbol{\sigma} = \rho \mathbf{g} \quad \text{on } \Omega \quad (2.2.2)$$

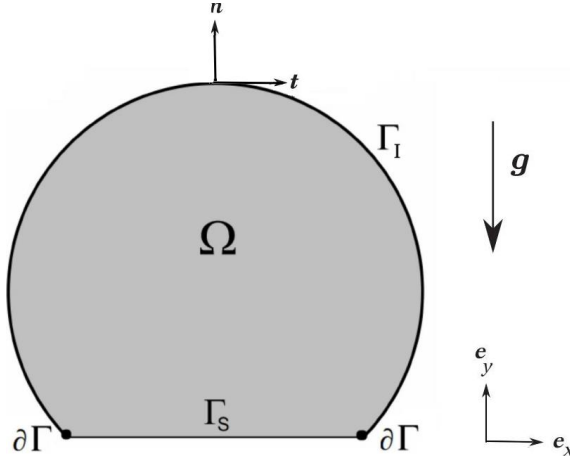


Figure 2.3: Schematic representation of the considered Lagrangian domain at the continuum level.

where \mathbf{v} is the velocity vector, ρ is the fluid density, t is time, $\frac{D}{Dt}$ represents the material derivative, \mathbf{g} is the gravitational acceleration, and $\boldsymbol{\sigma}$ is the Cauchy stress tensor governed by:

$$\boldsymbol{\sigma} = -p\mathbb{I} + \mu(\nabla\mathbf{v} + \nabla^T\mathbf{v}) \quad (2.2.3)$$

where p is the pressure, μ is the dynamic viscosity, and \mathbb{I} is the identity tensor. Substituting eq. 2.2.3 into 2.2.2 yields:

$$\rho \frac{D\mathbf{v}}{Dt} - \nabla \cdot \mu(\nabla\mathbf{v} + \nabla^T\mathbf{v}) + \nabla p = \rho\mathbf{g} \quad \text{on } \Omega \quad (2.2.4)$$

In the Lagrangian approach, we use the material derivative to find the evolution of the velocity field. The dynamic viscosity μ and the volumetric mass density ρ are assumed to be constant parameters.

2.3 Boundary conditions at the liquid-vapor interface Γ_I

At the interface Γ_I , a Cauchy stress boundary condition in the normal direction of the stress is applied corresponding to the surface tension force:

$$\mathbf{f}_{\Gamma_I} = \boldsymbol{\sigma}\mathbf{n} = \gamma\kappa\mathbf{n} \quad \text{at } \Gamma_I \quad (2.3.1)$$

where \mathbf{f}_{Γ_I} is the surface tension force, \mathbf{n} is the unit normal to surface Γ_I , γ is the surface tension coefficient, and κ is the mean curvature. Decomposing eq. 2.3.1 into normal and tangential components yields:

$$\mathbf{n} \cdot (\boldsymbol{\sigma} \mathbf{n}) = \gamma \kappa \quad \text{at } \Gamma_I \quad (2.3.2)$$

and

$$\mathbf{t} \cdot (\boldsymbol{\sigma} \mathbf{n}) = 0 \quad \text{at } \Gamma_I \quad (2.3.3)$$

where \mathbf{t} is the unit tangent to surface Γ_I . Assuming a stationary exterior fluid and substituting eq. 2.2.3 into eq. 2.3.2 yields:

$$p - \mu \mathbf{n} \cdot ([\nabla \mathbf{v} + \nabla^T \mathbf{v}] \cdot \mathbf{n}) = \gamma \kappa \quad \text{at } \Gamma_I \quad (2.3.4)$$

2.4 Curvature in 2D

The curvature equation for 2D analysis is defined as follows [112, 114]:

$$\kappa = \nabla_s \cdot \mathbf{n} = \left\| \frac{d\mathbf{n}}{ds} \right\| \quad (2.4.1)$$

where ∇_s is the surface gradient operator and $\frac{d\mathbf{n}}{ds}$ is the rate of change of the normal direction.

Using Fig. 2.4, we define the following quantities:

\mathbf{r}_1 the vector starting at node $(I - 1)$ and ending at node (I) , \mathbf{r}_2 the vector starting at node (I) and ending at node $(I + 1)$, and the unit vector $\hat{\mathbf{r}}_k$ is defined by:

$$\hat{\mathbf{r}}_k = \frac{\mathbf{r}_k}{\|\mathbf{r}_k\|} \quad (2.4.2)$$

The curvature is approximated using the norm of vector $(\hat{\mathbf{r}}_1 - \hat{\mathbf{r}}_2)$ over the polyline segment connecting these nodes, i.e (node $(I + 1)$ node - $(I - 1)$) as follows:

$$\kappa = \frac{\|\hat{\mathbf{r}}_1 - \hat{\mathbf{r}}_2\|}{\|\mathbf{r}_1\| + \|\mathbf{r}_2\|} \quad (2.4.3)$$

2.5 Forces at the solid-liquid interface

At the solid-liquid interface excluding the contact line, Γ_S , the applied boundary condition corresponds to the shear stresses in order to account for viscous dissipation. It is obtained by projecting the Cauchy stress tensor on the normal direction of Γ_S [37, 178]:

$$\mathbf{f}_{\Gamma_S} = \boldsymbol{\sigma} \cdot \mathbf{e}_y = -\beta_{\Gamma_S} \mathbf{v} \quad \text{at } \Gamma_S \quad (2.5.1)$$

where \mathbf{f}_{Γ_S} and β_{Γ_S} are the dissipative force and the slip coefficient applied at the solid-liquid interface, respectively, and \mathbf{v} is the slip velocity of the fluid on the solid-liquid interface. A variety of models have been proposed in the literature for the slip coefficient, β_{Γ_S} , at the solid-liquid interface such as, Navier-slip condition (β_s) [159, 178, 226, 227], prescribed slip profile condition [178], and a constant slip coefficient that depends on the grid size [37]. The Navier-slip model is considered in this work, as it accounts for the shear rates and viscous dissipation along the solid-liquid interface during drop deformation [12, 178, 226, 227].

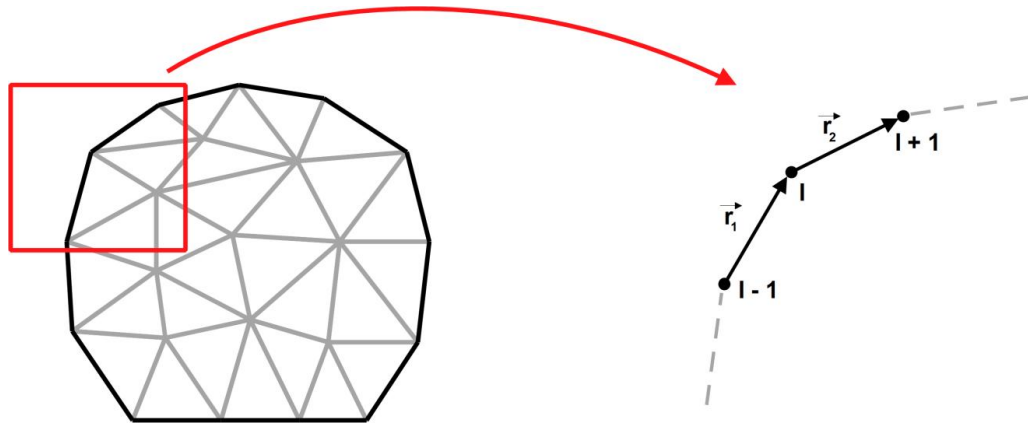


Figure 2.4: Changes in directions in discrete boundary [112, 114].

At the contact line, an effective slip boundary condition is applied corresponding to the total dissipative force, including the contribution of i) the capillary effect (ζ), ii) normal stress coefficient (β_n), and iii) Navier-slip coefficient (β_s), and is proportional to the velocity of the contact line [37, 178, 226, 227]:

$$f_{\partial\Gamma} = -\beta_{\partial\Gamma}v \quad \text{at } \partial\Gamma \quad (2.5.2)$$

where $f_{\partial\Gamma}$ is the dissipative force applied at the contact line, $\beta_{\partial\Gamma}$ is the effective slip coefficient at the contact line, and v is the slip velocity of the fluid at the contact line.

The details on the dissipative force applied at the contact line and the solid-liquid interface are presented next.

2.5.1 Forces acting at the contact line, $\partial\Gamma$

Let us consider a steady drop in contact with a flat surface forming a static contact angle θ_e (Fig. 2.5). Under this condition, the equilibrium is expressed as the balance of the liquid surface tension (γ_{lv} , or simply denoted by γ), solid surface energy (γ_{sv}), and interfacial tension (γ_{sl}). When normalized to a unit length, these forces are the interfacial tensions between the three phases (solid/liquid/vapor). By projecting the equilibrium forces on the solid plane, one obtains the well-known Young's equation [245, 246]:

$$\gamma_v \cos \theta_e = \gamma_{sv} - \gamma_{sl} \quad (2.5.3)$$

The contact line velocity that corresponds to this equilibrium state is $v = 0$. In this case, the boundary condition applied to the contact line is the following: if the contact angle is within a given range of values, i.e., $\theta \in [\theta_{min}, \theta_{max}]$, the contact line is fixed. A fixed contact line is usually referred to as a *pinned* contact line. The values of minimum and maximum contact angle to achieve contact line pinning, which depend on both the liquid and the substrate, are determined experimentally [115, 193].

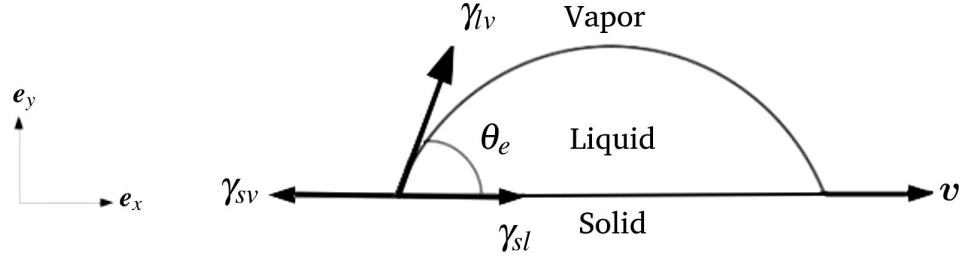


Figure 2.5: Schematic representation of the forces acting on a contact line of a sessile drop.

As the drop starts to spread, eq. (2.5.3) does not hold any longer and therefore a slip boundary condition is applied for the velocity at the contact line $\partial\Gamma$ [115, 116]:

$$\mathbf{v} \cdot \mathbf{e}_y = 0 \quad (2.5.4)$$

This condition, however, results in an unrealistic contact angle evolution because the velocity of the contact line is not restricted by the physical viscous dissipation at the solid-liquid interface, leading to a non-physical spreading of the moving contact line. Instead, according to [37, 178], the velocity of the contact line can be related to the Young's stress acting on it:

$$u \propto \gamma(\cos \theta_e - \cos \theta_d) \quad (2.5.5)$$

where u is the tangential component of the velocity vector at the contact line, i.e., $u = \mathbf{v} \cdot \mathbf{e}_x$, and θ_d is the dynamic contact angle. The proportionality coefficient between the contact line velocity and Young's stress is the effective slip boundary condition defined as follows [178]:

$$\beta_{\partial\Gamma} u = \gamma(\cos \theta_e - \cos \theta_d) \quad (2.5.6)$$

where $\beta_{\partial\Gamma}$ is the effective slip coefficient, and is defined as [12, 22, 30, 37, 143, 178, 226, 227, 245]:

$$\beta_{\partial\Gamma} = \zeta + \beta_S|_{\partial\Gamma} + \beta_n \quad (2.5.7)$$

where ζ is the dynamic capillary effect coefficient, $\beta_S|_{\partial\Gamma}$ is the Navier-slip coefficient, and

β_n is the normal stress coefficient.

The capillary effect coefficient is expressed as follows [37, 143]:

$$\zeta = \frac{\gamma}{u} R(Ca) \quad (2.5.8)$$

where $R(Ca)$ is a function of the capillary number calculated from the contact line velocity [143]. In several experimental studies, expressions for $R(Ca)$ were obtained by fitting empirical data. Among these studies, the models proposed by Jiang [117], Bracke [32], and Seeberg are commonly used [199]. The numerical and dynamic contact angle simulations in reference [223] concluded that Jiang's model was able to predict higher capillary flow velocities among these three empirical models. For capillary-driven spreading drop, the contact line velocity is of the order of an impact velocity of a drop [28, 200]; therefore, Jiang's expression is used in this work, i.e., [117]:

$$R(Ca) = (\cos \theta_e + 1) \tanh \left(4.96 Ca^{0.702} \right) \quad (2.5.9)$$

where θ_e is the static contact angle, and $Ca = u\mu/\gamma$ is the capillary number calculated using the contact line velocity. Thus, the coefficient ζ in eq. (2.5.8) is expressed as follows:

$$\zeta = \frac{\gamma}{u} (\cos \theta_e + 1) \tanh \left(4.96 Ca^{0.702} \right) \quad (2.5.10)$$

The Navier-slip coefficient, $\beta_S|_{\partial\Gamma}$ in eq. (2.5.7), is a function of the shear stress, and it is calculated using [12, 178, 226, 227]:

$$\beta_S|_{\partial\Gamma} = \frac{1}{u} \mu \nabla (\mathbf{v} \cdot \mathbf{e}_x) \cdot \mathbf{e}_y \quad (2.5.11)$$

In addition, larger jump in normal stresses is introduced across the contact line as its velocity increases [178]. The normal stress jump across the contact line is balanced by

including the coefficient β_n , which is expressed as follows [178]:

$$\beta_n = \frac{1}{u} \mu \nabla (\mathbf{v} \cdot \mathbf{e}_x) \cdot \mathbf{e}_x \quad (2.5.12)$$

where u is the tangential component of the velocity vector at the contact line, i.e., $u = \mathbf{v} \cdot \mathbf{e}_x$.

After considering the contributions of the capillary effects, the Navier-slip as well as the normal stresses in eq. (2.5.7), the coefficient $\beta_{\partial\Gamma}$ is used to obtain the total dissipative force and to apply the boundary condition defined by eq. (2.5.2).

2.5.2 Forces acting at the solid-liquid interface away from the contact line, Γ_S

When a viscous fluid is in contact with a solid substrate, the velocity of the fluid at the fluid-solid interface is equal to the velocity of the solid. If the solid is at rest, a no-slip boundary condition is applied in this region. In wetting problems, however, the no-slip condition contradicts the physical dissipation phenomena on the solid-liquid interfacial regime. It has been observed that introducing a Navier-slip boundary condition on drop spreading problem partially resolves this contradiction, and also reduces the mesh-dependency of the numerical solution [12, 37, 178, 226, 227]. Therefore, at the solid-liquid interface, Γ_S , the Navier-slip boundary condition is applied in the present work, according to eq. (2.5.1). Accordingly, the slip coefficient β_{Γ_S} at the solid-liquid interface Γ_S is expressed as follows:

$$\beta_{\Gamma_S} = \beta_s = \frac{1}{u} \mu \nabla (\mathbf{v} \cdot \mathbf{e}_x) \cdot \mathbf{e}_y \quad (2.5.13)$$

where u is the tangential component of the velocity vector at the solid-liquid interface. Eq. (2.5.13) is used in combination with eq. (2.5.1) to apply the boundary condition at the solid-liquid interface.

2.6 Discretization technique

The numerical method adopted in this dissertation is introduced in this section. First, a brief introduction of the Finite Element method (FEM) will be introduced. Then, the discretization technique and solving strategy will be exposed.

2.6.1 Introduction to the finite element method

The finite element method (FEM) can be traced back to the middle of the twentieth century [254]. It is a numerical method to generate approximate solutions of partial differential equations (PDE) [254]. The FEM procedure typically starts with the development of a weak formulation of the PDE by introducing a family of test functions. The solution to the newly generated problem is found by using a local approximation function for the test functions, such as Lagrange linear functions. Hence, a physical domain is discretized into finite elements associated with approximation functions, and solved by one global system of equations. The main advantage of FEM over other computational methods is its ability to handle high complexities of the geometrical domain [185].

The most common FEM method is the Galerkin, weighted residual, FEM where the test function belongs to the solution approximation function space [185, 254]. The Galerkin method has been proven to be a reliable tool in structural dynamics applications, exhibiting optimal convergence rates, since it produces a symmetric, positive-definite system of linear equations. Hence, excellent agreement is obtained between the exact and the approximate solution [185].

The FEM is faced with two main challenges when dealing with fluid dynamic applications: (i) the treatment of the convective terms, and (ii) the pressure instability [66, 185]. The presence of the convective term, which reflects the material deformation concerning a fixed Eulerian domain, will produce a non-symmetric linear system, which can lead to a divergence of the velocity field [66, 185]. The second issue arises due to the incompressibility of the fluid, which can lead to instabilities in the pressure field [66, 185]. To resolve these two issues, stabilization techniques have been established. The concept behind the stabilization techniques is to improve the system behavior by modifying the weak form, ensuring the consistency of the problem to be solved [53, 66, 185].

2.6.2 Discretized governing equations

Let $\Omega \subset \mathbb{R}^n$, where $n \in \{2,3\}$. Also, let $\mathcal{L}^2(\Omega)$ represent the Hilbert space of a square integrable scalar function over Ω equipped with inner product and the norm defined by [112, 114, 116, 186, 187]:

$$(u, v) = \int_{\Omega} uv d\Omega \quad (2.6.1)$$

and,

$$\|u\|_{\mathcal{L}^2} = (u, u)^{\frac{1}{2}} \quad (2.6.2)$$

The function and its derivative are assumed to be square integrable. This will be in the Sobolev space denoted by $\mathcal{H}^k(\Omega)$, which is the space where both the function and its derivative up to k order are square integrable (more information about Sobolev spaces can be found in references [11, 66]). Since $\mathcal{L}^2(\Omega) = \mathcal{H}^0(\Omega)$, the $\mathcal{L}^2(\Omega)$ space is a Sobolev space. Also, $\mathcal{H}^1(\Omega)$ is defined as follows:

$$\mathcal{H}^1(\Omega) = \{u \in \mathcal{L}^2(\Omega) \mid \frac{\partial u}{\partial x_i} \in \mathcal{L}^2(\Omega), i = 1, \dots, n\} \quad (2.6.3)$$

This definition can be extended for vector functions, such as the velocity field, by defining $\mathcal{H}^k(\Omega)$ as the space of vector functions \mathbf{v} such that each of its components belongs to $\mathcal{H}^k(\Omega)$.

To start the discretization of eq. 2.2.4 and eq. 2.2.1, the Galerkin variational formulation is obtained by multiplying these two equations by a test function, and by integrating over the domain. Two sets of test functions will be used. The first set will satisfy the homogeneous boundary condition, that is:

$$\mathcal{V} = \mathcal{H}_0^1(\Omega) = \{\mathbf{v} \in \mathcal{H}^1(\Omega) \mid \mathbf{v} = 0 \text{ on } \Gamma_D\} \quad (2.6.4)$$

where Γ_D is the Dirichlet portion of the boundary Γ [66]. The second set will satisfy the non-homogeneous boundary conditions, as follows:

$$\mathcal{S} = \mathcal{H}_0^1(\Omega) = \{v \in \mathcal{H}^1(\Omega) \mid v = \bar{v} \text{ on } \Gamma_D\} \quad (2.6.5)$$

The weak form of the problem will then be defined as follows: Find $v \in \mathcal{S} \mid \forall w \in \mathcal{V}$, and $\forall q \in \mathcal{L}^2$ such that:

$$\int_{\Omega} \left(\rho \frac{Dv}{Dt} \cdot w - w \cdot (\nabla \cdot \sigma) \right) d\Omega = \int_{\Omega} \rho g \cdot w d\Omega \quad (2.6.6)$$

and:

$$\int_{\Omega} q \nabla \cdot v d\Omega = 0 \quad (2.6.7)$$

Using the divergence theorem, letting $F = w \cdot \sigma$, and noting that $\int_{\Omega} \nabla \cdot F d\Omega = \int_{\Gamma} F \cdot n d\Gamma$

we obtain:

$$\int w \cdot (\nabla \cdot \sigma) d\Omega = \int w \cdot \sigma n d\Gamma - \int \sigma : \nabla w d\Omega$$

Upon integrating by parts and applying the divergence theorem, this leads to

$$\int_{\Omega} \left(\rho \frac{Dv}{Dt} \cdot w + \mu (\nabla v + \nabla^T v) : \nabla w - p \nabla \cdot w \right) d\Omega = \int_{\Omega} \rho g \cdot w d\Omega + \int_{\Gamma} w \cdot \sigma n d\Gamma \quad (2.6.8)$$

Therefore, the variational formulation takes the following expression:

$$\begin{aligned} & \int_{\Omega} \left(\rho \frac{Dv}{Dt} \cdot w + \mu (\nabla v + \nabla^T v) : \nabla w - p \nabla \cdot w \right) d\Omega = \\ & \int_{\Omega} \rho g \cdot w d\Omega + \int_{\Gamma_I} \gamma \kappa n \cdot w d\Gamma_I + \int_{\partial\Gamma} \beta_{\partial\Gamma} u n \cdot w d\partial\Gamma + \int_{\Gamma_S} \beta_{\Gamma_S} u n \cdot w d\Gamma_S \end{aligned} \quad (2.6.9)$$

$$\int_{\Omega} q \nabla \cdot \mathbf{v} d\Omega = 0 \quad (2.6.10)$$

Next, to find the interpolation functions according to the standard FEM procedure, we consider the partition of domain Ω into elements Ω_e such that:

$$\Omega \approx \Omega_h = \bigcup_{e=1}^{n_{element}} \Omega_e \quad (2.6.11)$$

where $n_{element}$ is the total number of elements. Three-nodes triangular elements will be used for two dimensional solutions. Four nodes tetrahedral elements will be used for three dimensional solutions.

The interpolation functions for the velocity and pressure are represented as follows:

$$\mathbf{v}_i(x, t) \approx \mathbf{v}_i^h(x, t) = \sum_{J=1} N_J(x) \mathbf{v}_i^J(t) = \mathbf{N}^T \mathbf{v}_i \quad (2.6.12)$$

$$p(x, t) \approx p^h(x, t) = \sum_{J=1} N_J(x) p^J(t) = \mathbf{N}^T p \quad (2.6.13)$$

where $N_J(x)$ represents the vector of interpolation function,

\mathbf{v}_i^J and p^J represent the nodal values for the i^{th} component of the velocity field and pressure field.

Here, both the velocity and pressure are approximated using linear Lagrange functions to reduce the size of the computational problem, i.e., number of total elements, leading to low computational cost [66, 112, 132]. Note that the pressure field must be of the same interpolation degree as the velocity field.

Combining these equations leads to the following discrete form

$$M\dot{\mathbf{v}} + \mu L\bar{\mathbf{v}} + G\bar{p} = \bar{F} + \bar{F}_{st} + \bar{F}_{\partial\Gamma} + \bar{F}_{\Gamma_s} \quad (2.6.14)$$

and

$$D\bar{v} = 0 \quad (2.6.15)$$

where M is the mass matrix, L is the Laplacian matrix, G is the Gradient matrix, \bar{F} is the body force vector, \bar{F}_{st} is the Surface Tension force vector, D is the divergence matrix, v and \bar{p} are the velocity and pressure, respectively. The matrices are assembled from the elemental contributions as follows:

$$M^{ab} = \rho \int_{\Omega_X} N^a N^b d\Omega_X = \rho \int_{\Omega} N^a N^b J(\mathbf{X}) d\Omega \quad (2.6.16)$$

$$L^{ab} = \int_{\Omega_X} \frac{\partial N^a}{\partial X_i} \frac{\partial N^b}{\partial X_i} \Omega_X = \int_{\Omega} \frac{\partial N^a}{\partial x_i} \frac{\partial N^b}{\partial x_i} J(\mathbf{X}) d\Omega \quad (2.6.17)$$

$$G_i^{ab} = - \int_{\Omega_X} \frac{\partial N^a}{\partial X_i} N^b d\Omega_X = - \int_{\Omega} \frac{\partial N^a}{\partial x_i} N^b J(\mathbf{X}) d\Omega \quad (2.6.18)$$

$$f_i^a = \rho \int_{\Omega_X} N^a g_i d\Omega_X = \rho \int_{\Omega} N^a g_i J(\mathbf{X}) d\Omega \quad (2.6.19)$$

$$D_i^{ab} = \int_{\Omega_X} N^a \frac{\partial N^b}{\partial X_i} d\Omega_X = \int_{\Omega} N^a \frac{\partial N^b}{\partial x_i} J(\mathbf{X}) d\Omega \quad (2.6.20)$$

$$f_{st,i}^a = - \int_{\Gamma_{l,X}} \gamma \kappa N^a n_i d\Gamma_X = - \int_{\Gamma_l} \gamma \kappa N^a n_i J_{\Gamma}(\mathbf{X}) d\Gamma \quad (2.6.21)$$

$$f_{\partial\Gamma,i}^a = - \int_{\partial\Gamma_X} \beta_{\partial\Gamma} u_i N^a d\partial\Gamma_X = - \int_{\partial\Gamma} \beta_{\partial\Gamma} u_i N^a J_{\Gamma}(\mathbf{X}) d\partial\Gamma \quad (2.6.22)$$

$$f_{\Gamma_S,i}^a = - \int_{\Gamma_{S,X}} \beta_{\Gamma_S} u_i N^a d\Gamma_X = - \int_{\Gamma_S} \beta_{\Gamma_S} u_i N^a J_{\Gamma}(\mathbf{X}) d\Gamma \quad (2.6.23)$$

where N^a represents the standard finite element shape function at node a , and the index i is used for the spatial components. The present model is based on the Updated Lagrangian Formulation (ULF), and therefore the integration domains, Ω_X , correspond to the updated configuration. The transformation between the reference configuration, Ω , and the updated one is performed using the Jacobians $J(\mathbf{X})$ and $J_{\Gamma}(\mathbf{X})$.

A standard Backward Eulerian time-marching scheme is used as follows:

$$\frac{\mathbf{v}_{n+1} - \mathbf{v}_n}{\Delta t} = \dot{\mathbf{v}}_{n+1} \quad (2.6.24)$$

However, we will be using a Newmark-Bossak time-marching scheme. This scheme is useful for non-linear problems. It takes the following form:

$$\bar{\mathbf{v}}_{n+1} = \frac{\zeta}{\beta} \left(\frac{\bar{\mathbf{u}}_{n+1} - \bar{\mathbf{u}}_n}{\delta t} \right) - \left(\frac{\zeta}{\beta} - 1 \right) \bar{\mathbf{v}}_n - \frac{\delta t}{2} \left(\frac{\zeta}{\beta} - 2 \right) \bar{\mathbf{a}}_n$$

and

$$\bar{\mathbf{a}}_{n+1} = \frac{\bar{\mathbf{u}}_{n+1} - \bar{\mathbf{u}}_n}{\beta \delta t^2} - \frac{1}{\beta \delta t} \bar{\mathbf{v}}_n - \frac{1-2\beta}{2\beta} \bar{\mathbf{a}}_n$$

where $\zeta = \frac{1}{2} - \alpha^\beta$, and $\beta = \frac{(1-\alpha^\beta)^2}{4}$, and also with $\alpha^\beta > 0$.

Accordingly, the temporal and spatial discretization process of the governing equations yields the following final equations:

$$M \frac{\bar{\mathbf{v}}_{n+1} - \bar{\mathbf{v}}_n}{\Delta t} + \mu L \bar{\mathbf{v}}_{n+1} + G \bar{p}_{n+1} = \bar{\mathbf{F}} + \bar{\mathbf{F}}_{st} + \bar{\mathbf{F}}_{\partial\Gamma} + \bar{\mathbf{F}}_{\Gamma_s} \quad (2.6.25)$$

$$D \bar{\mathbf{v}}_{n+1} = 0 \quad (2.6.26)$$

where $\bar{\mathbf{v}}_n$ and \bar{p}_n are the velocity and pressure at time t_n .

The system of equations eqs. 2.6.25 and 2.6.26 is solved using the monolithic approach.

2.6.3 Monolithic approach

The monolithic strategy [112, 114, 116, 186, 187], also known as the coupled approach, consists of solving both velocity and pressure fields simultaneously. Numerical instabilities will arise whenever the inf-sup condition, also known as the Ladyzhenskaya

Babuska Brezzi (LBB) condition, is not fulfilled. In this dissertation, the Algebraic Sub-Grid Scales (ASGS) method is used to enhance numerical stability. The main advantage of ASGS is to maintain the symmetry of the linear systems of equations.

Stabilization is achieved by adding the following term to the left-hand side of equations 2.6.25 and 2.6.26:

$$\sum_{e=1}^{n_e} \int_{\Omega_e} \tau [F - \mathcal{L}(\mathbf{v}_h)]^T \mathcal{L}^*(\mathbf{w}_h) d\Omega \quad (2.6.27)$$

where $\mathcal{L}(\mathbf{v}_h)$ is the time-dependent residual, which takes the expression

$$\mathcal{L}(\mathbf{v}_h) = \begin{bmatrix} \rho \frac{\partial \mathbf{v}_h}{\partial t} - \mu \nabla \cdot (\nabla \mathbf{v}_h + \nabla^T \mathbf{v}_h) + \nabla p_h \\ \nabla \cdot \mathbf{v}_h \end{bmatrix} = \begin{bmatrix} \rho \frac{\partial \mathbf{v}_h}{\partial t} + \nabla p_h \\ \nabla \cdot \mathbf{v}_h \end{bmatrix} \quad (2.6.28)$$

The Laplacian term, $\nabla \cdot (\nabla \mathbf{v}_h + \nabla^T \mathbf{v}_h)$, in the previous equation above vanishes, since linear interpolation functions are used for the spatial discretization.

Using the Backward Euler time scheme, the time dependent residual will be:

$$\mathcal{L}(\mathbf{v}_h) = \begin{bmatrix} \rho \frac{\mathbf{v}_{n+1} - \mathbf{v}_n}{\Delta t} + \nabla p_{n+1} \\ \nabla \cdot \mathbf{v}_{n+1} \end{bmatrix} \quad (2.6.29)$$

where \mathcal{L}^* is the adjoint of operator \mathcal{L} , given by [112, 185]:

$$\mathcal{L}^*(\mathbf{w}_h) = \begin{bmatrix} -\mu \Delta \mathbf{w}_h - \nabla q_h \\ -\nabla \cdot \mathbf{w}_h \end{bmatrix} = \begin{bmatrix} -\nabla q_h \\ -\nabla \cdot \mathbf{w}_h \end{bmatrix} \quad (2.6.30)$$

where ν is the kinematic viscosity. Hence, we find the resulting stabilizing term as follows:

$$\int_{\Omega_e} \tau_1 \nabla q_h \left(\rho \frac{\mathbf{v}_{n+1} - \mathbf{v}_n}{\Delta t} + \nabla p_{n+1} - \mathbf{f} \right) d\Omega + \int_{\Omega_e} \tau_2 (\nabla \cdot \mathbf{w}_h) (\nabla \cdot \mathbf{v}_{n+1}) d\Omega \quad (2.6.31)$$

The term pre-multiplying q_h will be added to the continuity equation. Likewise, the term pre-multiplying w_h will be added to the momentum equation. Upon expanding the previous equation and using interpolation functions, we find:

$$\int_{\Omega_e} \frac{\rho}{\Delta t} \tau_1 \frac{\partial N^a}{\partial x_i} N^b d\Omega + \int_{\Omega_e} \tau_1 \frac{\partial N^a}{\partial x_i} \frac{\partial N^b}{\partial x_i} d\Omega - \int_{\Omega_e} \rho g_i \frac{\partial N^a}{\partial x_i} \left(\frac{\rho}{\Delta t} N^a + N^a \right) d\Omega + \int_{\Omega_e} \tau_2 \frac{\partial N^a}{\partial x_i} \frac{\partial N^b}{\partial x_i} d\Omega \quad (2.6.32)$$

where τ_1 is the first algorithmic stabilization parameter given by:

$$\tau_1 = \frac{1}{\frac{2\|\bar{v}\|}{h} + \frac{4\nu}{h^2}} \quad (2.6.33)$$

and τ_2 is the second algorithmic stabilization parameter given by:

$$\tau_2 = \frac{h^2}{\tau_1} \quad (2.6.34)$$

where h is the element size. Hence, the stabilized governing equations now become as follows:

$$\left(M \frac{1}{\Delta t} + \mu L + S_K \right) \bar{v}_{n+1} + G \bar{p}_{n+1} = \bar{F} + \bar{F}_{st} + \bar{F}_{\partial\Gamma} + \bar{F}_{\Gamma_s} + M \frac{\bar{v}_n}{\Delta t} \quad (2.6.35)$$

$$(D + S_D) \bar{v}_{n+1} + S_L \bar{p}_{n+1} = \bar{F}_q \quad (2.6.36)$$

where,

$$S_K^{ab} = \int_{\Omega} \tau_2 \frac{\partial N^a}{\partial x_i} \frac{\partial N^b}{\partial x_i} J(\mathbf{X}) d\Omega \quad (2.6.37)$$

$$S_D^{ab} = \int_{\Omega} \frac{\rho}{\Delta t} \tau_1 \frac{\partial N^a}{\partial x_i} N^b J(\mathbf{X}) \, d\Omega \quad (2.6.38)$$

$$S_L^{ab} = \int_{\Omega} \tau_1 \frac{\partial N^a}{\partial x_i} \frac{\partial N^b}{\partial x_i} J(\mathbf{X}) \, d\Omega \quad (2.6.39)$$

$$f_q^a = \int_{\Omega} \rho g_i \frac{\partial N^a}{\partial x_i} \left(\frac{\rho}{\Delta t} N^a + N^a \right) J(\mathbf{X}) \, d\Omega \quad (2.6.40)$$

where S_L is the Laplacian stabilization matrix.

This system of equations is nonlinear and will be solved by the Newton-Raphson method.

First, we rearrange the equation in residual form:

$$\bar{r}_m = \bar{F} + \bar{F}_{st} + \bar{F}_{\partial\Gamma} + \bar{F}_{\Gamma_S} - M \frac{\bar{\mathbf{v}}_{n+1} - \bar{\mathbf{v}}_n}{\Delta t} + (\mu L + S_K) \bar{\mathbf{v}}_{n+1} - G \bar{\mathbf{p}}_{n+1} = 0 \quad (2.6.41)$$

$$\bar{r}_c = \bar{F}_q - (D + S_D) \bar{\mathbf{v}}_{n+1} - S_L \bar{\mathbf{p}}_{n+1} = 0 \quad (2.6.42)$$

Then, the Taylor series of the residual gives:

$$0 = \begin{pmatrix} \bar{r}_m \\ \bar{r}_c \end{pmatrix} + \begin{pmatrix} \frac{d\bar{r}_m}{d\bar{\mathbf{v}}^i} & \frac{d\bar{r}_m}{d\bar{\mathbf{p}}^i} \\ \frac{d\bar{r}_c}{d\bar{\mathbf{v}}^i} & \frac{d\bar{r}_c}{d\bar{\mathbf{p}}^i} \end{pmatrix} \begin{pmatrix} d\bar{\mathbf{v}} \\ d\bar{\mathbf{p}} \end{pmatrix} + \mathcal{O}(d\bar{\mathbf{v}}, d\bar{\mathbf{p}})^2 \quad (2.6.43)$$

where index i represents the level of iteration of the Newton-Raphson scheme, $d\bar{\mathbf{v}} = \bar{\mathbf{v}}_{n+1}^{i+1} - \bar{\mathbf{v}}_{n+1}^i$, and $d\bar{\mathbf{p}} = \bar{\mathbf{p}}_{n+1}^{i+1} - \bar{\mathbf{p}}_{n+1}^i$.

Finally, upon finding the derivative and neglecting the second order and higher terms of

equation, we find

$$\begin{pmatrix} \bar{r}_m(\bar{\mathbf{v}}^i, \bar{p}^i) \\ \bar{r}_c(\bar{\mathbf{v}}^i, \bar{p}^i) \end{pmatrix} = \begin{pmatrix} d\bar{\mathbf{v}} \\ d\bar{p} \end{pmatrix} \begin{pmatrix} M_{\Delta t}^{\frac{1}{2}} + \mu L + S_K + H_{ST} & G \\ D + S_D & S_L \end{pmatrix} \quad (2.6.44)$$

Here, H_{ST} is the matrix representing linearizing the linearized surface tension term, that stabilizes the time step restrictions.

The velocity, pressure, and displacement/position are updated as follows:

$$\bar{\mathbf{v}}_{n+1}^{i+1} = \bar{\mathbf{v}}_{n+1}^i + d\bar{\mathbf{v}}_{n+1}, \text{ and, } \bar{p}_{n+1}^{i+1} = \bar{p}_{n+1}^i + d\bar{p}_{n+1}, \text{ and, } \bar{X}_{n+1}^{i+1} = \bar{X}_n + \Delta t \cdot \bar{\mathbf{v}}_{n+1}^{i+1} \quad (2.6.45)$$

Once the convergence is achieved, the final mesh position is evaluated in terms of the velocity, $\bar{\mathbf{v}}_{n+1}$ as follows:

$$\bar{X}_{n+1} = \bar{X}_n + \Delta t \cdot \bar{\mathbf{v}}_{n+1} \quad (2.6.46)$$

The viscous stress implementations, both in 2D and 3D, are presented in [Appendix B](#).

2.6.4 Solution algorithm

Given a known configuration X_n , velocity $\bar{\mathbf{v}}_n$, and pressure \bar{p}_n , at time t_n , the procedure for obtaining the values of these variables at the next time step t_{n+1} is summarized in [Algorithm 1](#). A complete general algorithm, including a two-phase flow model, can be found in reference [\[186\]](#).

2.7 Mesh size and time step criteria

Even though a substantial effort has been invested in developing robust and efficient numerical models for contact line dynamics of sessile drops, a physically accurate and mesh-independent model does not currently exist to the best of our knowledge.

Algorithm 1: Simulation algorithm of the liquid phase problem using a PFEM formulation.

```

1 for  $t = t_{n+1}$  do
2   Current configuration is the known configuration, such that:  $\mathbf{X}_{n+1}^k = \mathbf{X}_n$ ;
3   for nonlinear iteration  $k$  do
4     Obtain curvature at  $\mathbf{X}_{n+1}^k$ ;
5     Update discrete operators in eqs. (2.6.16)-(2.6.20);
6     Compute  $f_{st,i}^a$ ,  $f_{\partial\Gamma,i}^a$ , and  $f_{\Gamma_S,i}^a$  using eq. (2.6.21), eq. (2.6.22), and
       eq. (2.6.23), respectively;
7     Solve system of equations for liquid phase, eq. (2.6.44);
8     Update both velocity and pressure, such that:  $\bar{\mathbf{v}}_{n+1}^{k+1} = \bar{\mathbf{v}}_{n+1}^k + \delta\bar{\mathbf{v}}$  and
        $\bar{p}_{n+1}^{k+1} = \bar{p}_{n+1}^k + \delta\bar{p}$ , respectively;
9     Update configuration, such that:  $\mathbf{X}_{n+1}^{k+1} = \mathbf{X}_{n+1}^k + \Delta t \cdot d\bar{\mathbf{v}}$ ;
10    Remesh;
11  end
12   $\mathbf{X}_{n+1} = \mathbf{X}_n + \Delta t \cdot \bar{\mathbf{v}}_{n+1}$ ;
13 end

```

As the drop spreads, capillary waves are generated at the contact line and move toward the free-surface, i.e., from $\partial\Gamma$ towards Γ_I [46, 123]. For a spreading drop, the maximum spreading velocity is of the order of the drop impact velocity [200, 228]. At this velocity, Yuriko *et al.* [180] concluded that the capillary wave is observed when $We > 1$, where the Weber number defined as:

$$We = \frac{\rho R u_{max}^2}{\gamma} \quad (2.7.1)$$

where ρ is the liquid density, R is the drop radius, and u_{max} is the maximum value of the tangential component of the velocity vector at the contact line. The latter value, u_{max} , can be estimated experimentally, and it is known to depend on both the fluid and the substrate [136, 180, 200, 228]. In this dissertation, different values of u_{max} are used based on the experimental scenarios illustrated in Section 2.9.

Yuriko *et al.* [180] also observed that the capillary wavelength, λ , corresponding to

the contact line capillary propagation is estimated by:

$$\lambda = \frac{\gamma}{\rho u_{max}^2} \quad (2.7.2)$$

Numerically, the mesh size at the contact line is restricted by the wavelength of the capillary wave propagation, and its maximum value h can be estimated to be [63]:

$$h = \frac{\lambda}{2} \quad (2.7.3)$$

Substituting eq. (2.7.2) into eq. (2.7.3) yields:

$$h = \frac{\gamma}{2\rho u_{max}^2} \quad (2.7.4)$$

Moreover, the wave velocity corresponding to the dominant capillary wavelength is calculated as [70, 136]:

$$c = \sqrt{\frac{2\pi\gamma}{\rho\lambda}} \quad (2.7.5)$$

where c is the wave velocity. The critical time step corresponding to this capillary wave, Δt_{cap} , can also be estimated as [63]:

$$\Delta t_{cap} = \frac{1}{2f} \leq \frac{h}{c} \quad (2.7.6)$$

where f is the maximum frequency in s^{-1} corresponding to the capillary wave propagation at the contact line. Substituting eq. (2.7.5) and eq. (4.2.24) into eq. (2.7.6) yields:

$$\Delta t_{cap} \leq \sqrt{\frac{2}{\pi}} \frac{\gamma}{4\rho |u_{max}^3|} \quad (2.7.7)$$

2.8 Mesh dependence study

This section illustrates the effects of enriching the drop model by including the dissipative forces at both the solid-liquid interface and at the contact line. The impact of this

enrichment upon drop spreading, contact angle evolution, and of the mesh dependency of the solution is analyzed.

Following the experimental settings of Buscaglia and Ausas [37], the geometry considered here is a sessile drop with an initial radius of 0.125 mm, an initial contact angle of 90° , and a static contact angle of $\theta_e = 45^\circ$ (see Fig. 2.6). The driving forces acting on the drop are due to surface tension and gravity. Fluid density, viscosity and surface tension coefficient are set to $\rho = 1000 \text{ kg m}^{-3}$, $\mu = 8.90 \times 10^{-4} \text{ kg m}^{-1} \text{ s}^{-1}$, $\gamma = 0.072 \text{ N m}^{-1}$, respectively, in order to represent a water drop. Initial pressure in the liquid is set to $p_0 = 0 \text{ Pa}$.

For this study, the maximum spreading velocity at the initial stage, i.e., $t < 0.25 \text{ ms}$, is assumed, based on experimental analysis, to be $u_{max} \sim 2.5 \text{ m} \cdot \text{s}^{-1}$. This data corresponds to a water drop of $\sim 2 \times 10^{-4} \text{ m}$ radius spreading on Triethoxysilybutraldehyde with a static contact angle of 43° [28]. Therefore, this gives the estimations $\lambda \sim 1.165 \times 10^{-5} \text{ m}$, $c \sim 6.27 \text{ m} \cdot \text{s}^{-1}$, $h \sim 5.8 \times 10^{-6} \text{ m}$, and $\Delta t = 4.6 \times 10^{-7} \text{ s}$ from eq. (2.7.2), eq. (2.7.5), eq. (4.2.24), and eq. (2.7.7).

Six cases are analyzed to illustrate the effect of the slip coefficient parameters at the contact line and at the solid-liquid interface excluding the contact line, $\beta_{\partial\Gamma}$ and β_{Γ_S} , as shown in table 2.1:

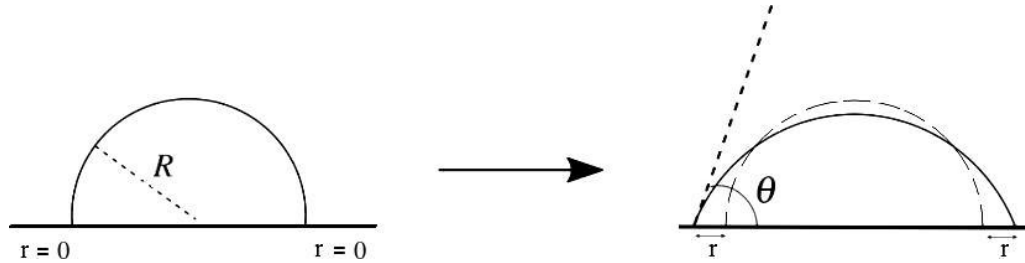


Figure 2.6: Initial and steady-state configuration for a sessile drop starting with an initial contact angle of 90° , and evolving with a spreading displacement of r .

Figure 2.7 shows the predicted spreading displacement defined as r in Fig. 2.6, and contact angle evolution when no dissipative forces are applied. To compare the general spreading behavior with Buscaglia and Ausas results [37], a time step of $\Delta t = 2 \times 10^{-7} \text{ s}$

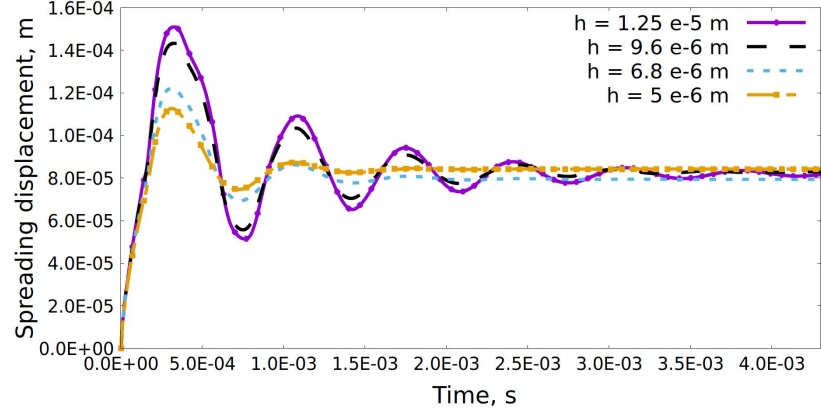
Case number	$\beta_{\partial\Gamma}$	β_{Γ_s}
Case 0	0	0
Case 1	0	$1 \times 10^{-5} \text{ Pa}\cdot\text{s}$
Case 2	0	$1 \times 10^{-3} \text{ Pa}\cdot\text{s}$
Case 3	$1 \times 10^{-3} \text{ Pa}\cdot\text{s}$	$1 \times 10^{-3} \text{ Pa}\cdot\text{s}$
Case 4	0	β_s , using eq. (2.5.13)
Case 5	ζ , using eq. (2.5.10)	0
Case 6	$\zeta + \beta_s + \beta_n$, using eqs. (2.5.10)–(2.5.12)	β_s using eq. (2.5.13)

Table 2.1: Analyzing different slip coefficient parameters at the contact line and at the solid-liquid interface excluding the contact line, $\beta_{\partial\Gamma}$ and β_{Γ_s} .

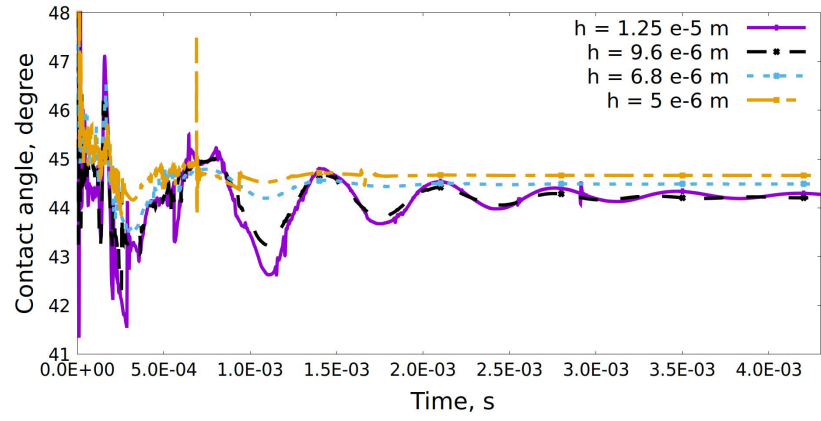
is used. Four different mesh sizes were adopted in order to study the solution sensitivity to mesh size, prior to adding the proposed boundary conditions (i.e., eq. (2.5.1) and eq. (2.5.2)), as follows: i) $h = 1.25 \times 10^{-5} \text{ m}$ with 340 elements, ii) $h = 9.6 \times 10^{-6} \text{ m}$ with 598 elements, iii) $h = 6.8 \times 10^{-6} \text{ m}$ with 1205 elements, and iv) $h = 5 \times 10^{-6} \text{ m}$ with 2206 elements. Parameter h represents the minimum distance between the nodes of a triangular mesh. As observed by Buscaglia and Ausas [37], when no dissipative force boundary conditions are applied, the solution is mesh-dependent, and the contact angle evolution is highly oscillatory.

The coarsest and the finest meshes, i.e., $h = 1.25 \times 10^{-5} \text{ m}$ and $h = 5 \times 10^{-6} \text{ m}$, are considered for further study. These are displayed in Fig. 2.8. For each mesh size, the six above-mentioned sets of dissipative forces and slip conditions were included.

Figure 2.9 shows spreading displacement and contact angle evolution for coarse mesh simulations. The absence of the dissipative term (ζ), normal stress coefficient (β_n), or the



(a)



(b)

Figure 2.7: Evolution of (a) spreading displacement and (b) contact angle, for $\beta_{\partial\Gamma} = 0$ and $\beta_{\Gamma_S} = 0$; case 0 in table 2.1, using different mesh sizes.

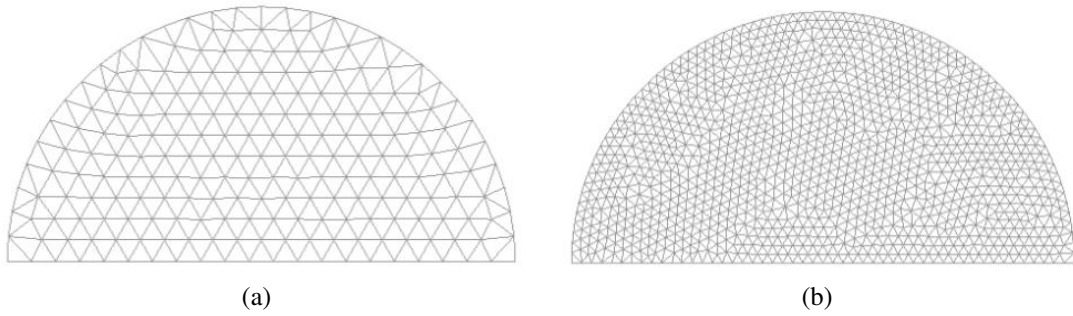
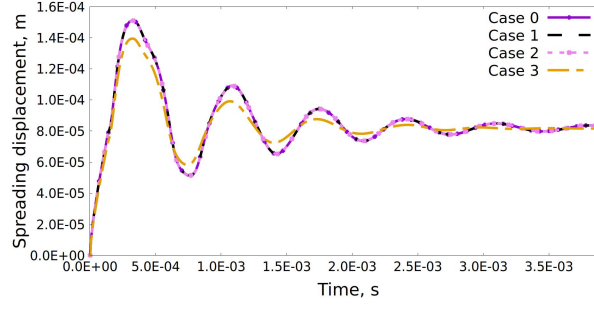
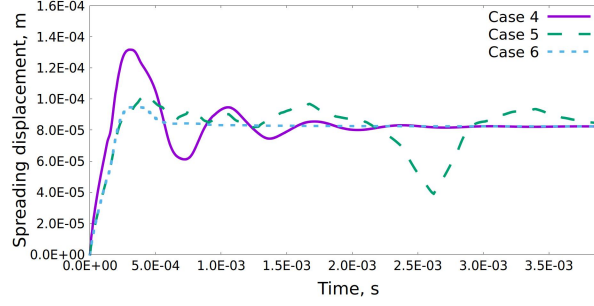


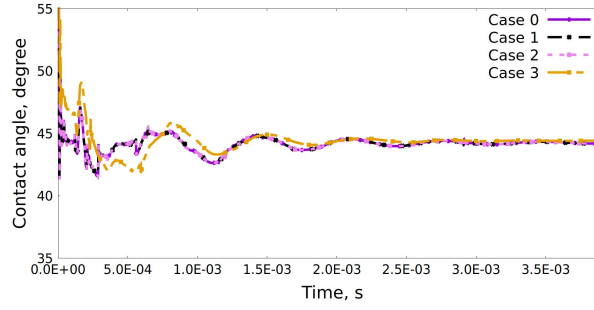
Figure 2.8: Initial configuration of a sessile drop with a starting contact angle of 90° : a) coarse mesh of 1.25×10^{-5} m and b) fine mesh of 5×10^{-6} m.



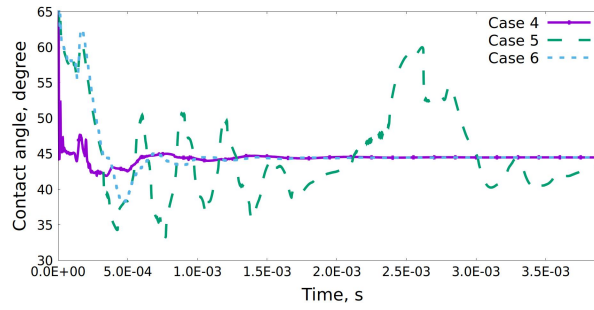
(a)



(b)



(c)



(d)

Figure 2.9: Evolution of spreading displacement for constant $\beta_{\partial\Gamma}$ and β_{Γ_S} (a) and using eq. (2.5.7) and (2.5.13) (b). Contact angle evolution for constant $\beta_{\partial\Gamma}$ and β_{Γ_S} (c), and using eq. (2.5.7) and (2.5.13) (d), see table 2.1. Mesh size of $h = 1.25 \times 10^{-5}$ m (coarse mesh).

Navier-slip coefficient (β_s) causes an oscillatory spreading behavior and contact angle evolution (Fig. 2.9(a), Fig. 2.9(c)). Experimental results [28, 200, 228] do not show this oscillatory behavior for a fluid on hydrophilic substrates. Therefore, these spurious oscillations are hypothesized to be due to the numerical scheme [37, 143]. The initial non-physical spreading evolution causes the contact line to exceed its equilibrium contact angle, i.e., $\theta_d < 45^\circ$. Hence, the contact line retracts toward its equilibrium state again. The contact line spreads back and forward in a manner proportional to the induced Young's stress (eq. (2.5.5)) until its effect vanishes and the drop reaches its equilibrium condition.

The first two cases show that increasing the constant value of the Navier-slip coefficient at the solid-liquid interface, β_{Γ_S} , does not guarantee a physical spreading evolution. Adding a constant slip coefficient at the contact line, i.e., case 3, reduces the contact angle and spreading rate oscillatory behavior, and increases the convergence rate. Yet, these constant values do not produce physical contact angle and spreading evolution rates.

Adding the Navier-slip condition on Γ_S (eq. (2.5.13), case 4) reduces the contact line singularity and enhances the convergence rate towards the equilibrium condition (Fig. 2.9(b) and Fig. 2.9(d)). However, the contact angle continues to behave in a non-physical manner due to the absence of the dynamic capillary term (ζ).

Adding the dynamic capillary term alone, case 5, at the contact line (eq. (2.5.10)) results in unstable contact angle evolution and spreading rate (Fig. 2.9(b) and Fig. 2.9(d)). This is interpreted by the absence of the physical viscous dissipation and stress balance terms acting on the solid-liquid interface, including the contact line.

Adding the dissipative force terms at the contact line and at the solid-liquid interface ($\beta_{\partial\Gamma}$ and β_{Γ_S} , respectively) using eq. (2.5.7), and (2.5.13) enhances the overall behavior of both contact angle and contact line evolution (Fig. 2.9(b) and Fig. 2.9(d)). The contact line reaches its equilibrium state after 0.0006 s, i.e. $\approx 85\%$ faster than without resorting to the proposed boundary conditions; the non-physical oscillatory spreading behavior vanishes. Furthermore, case 6 in Fig. 2.9(b) shows two physical regimes. The first regime is the inertial regime, $0 < t < 4 \times 10^{-4}$ s, where the drop spreads at a rate proportional to the induced Young's stress. The second regime is the viscous regime, $t > 4 \times 10^{-4}$ s, where the viscous

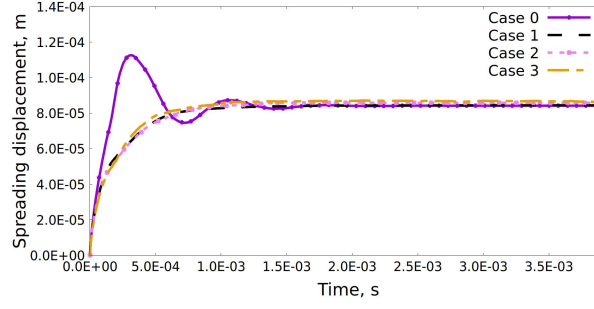
dissipation is dominating as the drop reaches its equilibrium contact angle [28, 47, 200, 228].

The proposed boundary conditions at the solid-liquid interface are critical to achieving physically acceptable drop spreading solutions with the use of coarse meshes. Results for the refined mesh, i.e., $h = 5 \times 10^{-6}$ m, are displayed in Fig. 2.10. In the absence of the dissipative term, normal stress coefficient, and Navier-slip coefficient, a smoother spreading displacement evolution is achieved, compared to the coarser mesh (Fig. 2.10(a) and Fig. 2.9(a)). Furthermore, the equilibrium state is reached after 0.0012 s. However, a non-physical oscillatory contact angle temporal evolution with low amplitudes is observed in Fig. 2.10(c). A more refined mesh leads to a lower nodal velocity and slip length coefficient, l_β , at the vicinity of the contact line compared to a coarse mesh [179, 226]. Accordingly, a higher slip coefficient, β_s , is imposed in the Navier-slip formulation, such that [12, 37]:

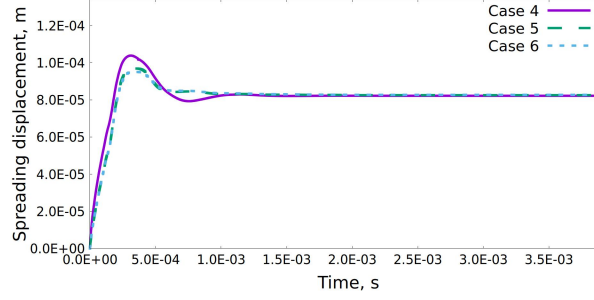
$$\beta_s = \frac{\mu}{l_\beta} \quad (2.8.1)$$

where μ is the fluid dynamic viscosity. On the one hand, the use of more refined mesh results in a smoother contact angle evolution and spreading behavior. On the other hand, the oscillatory behavior of the contact angle evolution is due to the missing dissipative force term that controls the contact angle evolution as a function of the dynamic capillary effect. Adding the capillary effect, ζ , at contact line, case 5 and case 6, results in smooth physical transition between the inertial and viscous regimes for both spreading displacement and contact angle evolution.

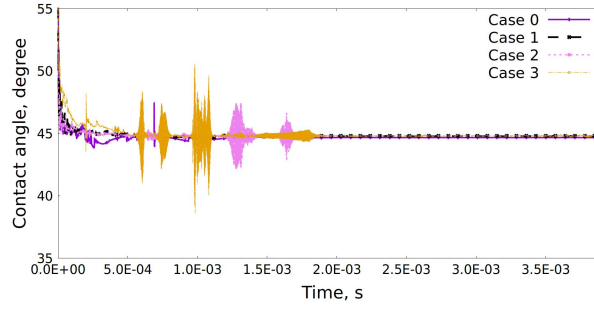
The contact angle evolution and spreading rate for both mesh sizes are compared before and after applying the complete set of proposed boundary conditions at the solid-liquid interface and contact line are shown in Fig. 2.11. Results obtained without imposing the dissipative force boundary conditions are grid dependent and display large, non-physical oscillations. In contrast, the results obtained with the numerical solver with the proposed



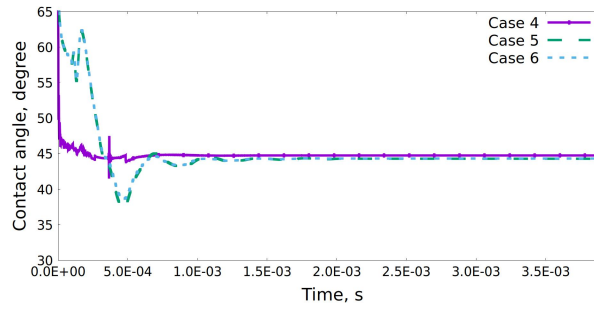
(a)



(b)



(c)



(d)

Figure 2.10: Evolution of spreading displacement for constant $\beta_{\partial\Gamma}$ and β_{Γ_S} (a) and using eq. (2.5.7) and (2.5.13) (b). Contact angle evolution for constant $\beta_{\partial\Gamma}$ and β_{Γ_S} (c), and using eq. (2.5.7) and (2.5.13) (d), see table 2.1. Mesh size of $h = 5 \times 10^{-6}$ m (fine mesh).

boundary conditions are grid independent and nearly free of oscillations with a smooth physical transition between both the inertial regime, $0 < t < 2 \times 10^{-4}$ s, and the viscous regime, $t > 5 \times 10^{-4}$ s. A small contraction of the contact line is observed in Fig. 2.11(a). The accompanied dewetting may be due to a spurious numerical artifact, although this particular phenomenon has been identified in drop spreading and drop impact experiments [28, 228]. These results demonstrate that the proposed boundary conditions enhance the stability of the contact line motion and achieve a mesh-independent solution with larger element sizes.

2.9 Experimental validation

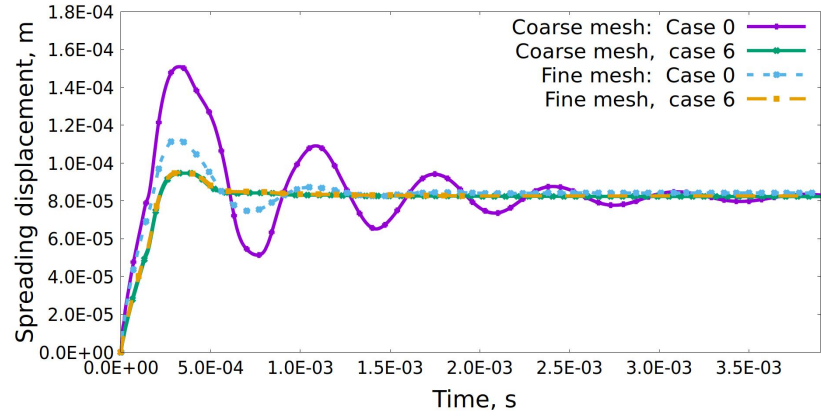
In order to assess the validity of the proposed numerical model, we compare in this section experimental and numerical results of several studies available in the literature involving spreading of fluids on flat smooth surfaces with a variety of equilibrium contact angles. Specifically, the following cases are studied:

- Case #1: spreading of a water drop on a hydrophobic substrate, i.e., Triethoxysilane, (with equilibrium contact angle of 117.0°) [28].
- Case #2: spreading of a squalane ($C_{30}H_{62}$) drop on a silica substrate (with equilibrium contact angle of 38.8°) [200].
- Cases #3 and #4: spreading of water on teflon (hydrophobic) and kapton (hydrophilic) substrates (with equilibrium contact angles of 108° [165] and 75° [74], respectively).

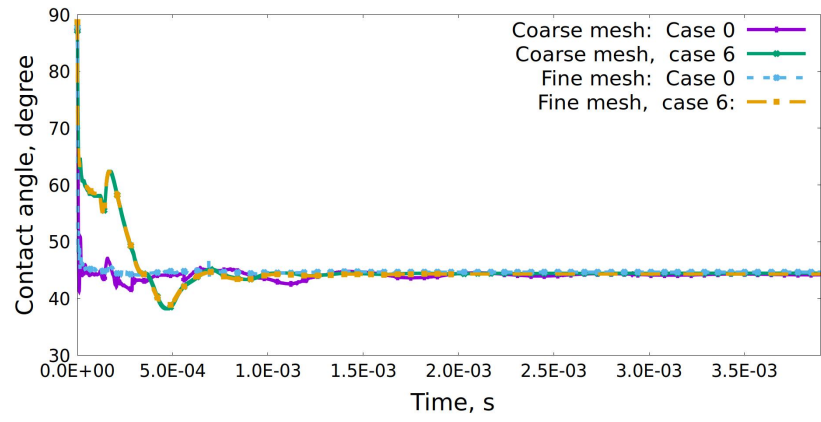
2.9.1 Case #1: spreading of a water drop on a hydrophobic triethoxysilane substrate

The proposed model is used to simulate the sessile water drop deposition experiments performed by Bird *et al.* [28]. In this study, a drop was placed on the Triethoxysilane substrate through a needle. The drop contacts the substrate at a diameter of 1 mm, and allowed to spread spontaneously over the substrate until equilibrium was reached, i.e., $\theta = \theta_e = 117^\circ$. Spreading displacement (r) was measured over time during the initial time of wetting.

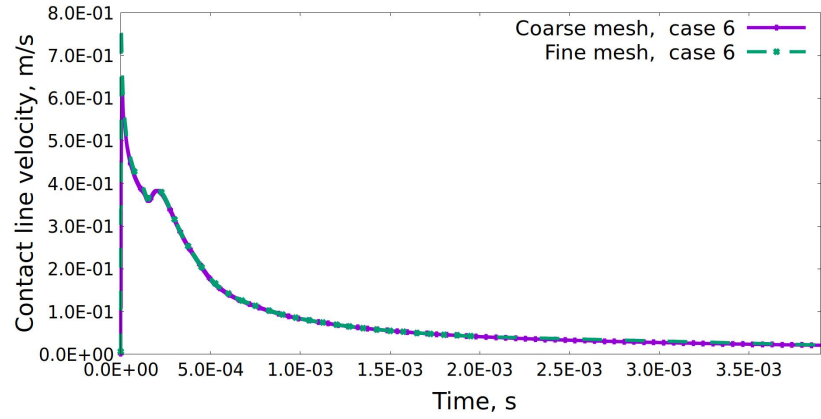
In order to reproduce this experiment numerically, a drop is placed on the substrate with an initial radius $R = 5 \times 10^{-4}$ m, contact angle of 180° , and liquid pressure of $p_0 = 0$ Pa



(a)



(b)



(c)

Figure 2.11: Mesh-independent results for (a) spreading displacement evolution, (b) contact angle temporal evolution, and (c) contact line velocity evolution, using our proposed boundary conditions and for two different triangular mesh sizes of $h = 1.25 \times 10^{-5}$ m (coarse mesh) and $h = 5 \times 10^{-6}$ m (fine mesh).

(Fig. 2.12). Then, the drop is allowed to deform until equilibrium is achieved, i.e., $\theta_e = 117^\circ$. Fluid density, viscosity and surface tension coefficient are set to $\rho = 1000 \text{ kg m}^{-3}$, $\mu = 8.90 \times 10^{-4} \text{ kg m}^{-1} \text{ s}^{-1}$, $\gamma = 0.072 \text{ N m}^{-1}$, respectively. Assuming that the capillary waves at the contact line are dominant and u_{max} of the order $\sim 1 \text{ m s}^{-1}$ [28], two simulations were performed using the boundary conditions of eq. (2.5.7) and (2.5.13), two element sizes, i.e., $h = 4 \times 10^{-5} \text{ m}$ with 1085 elements, and $h = 8 \times 10^{-5} \text{ m}$ with 282 elements, as displayed in Fig. 2.13, and a time-step size of 10^{-7} s .

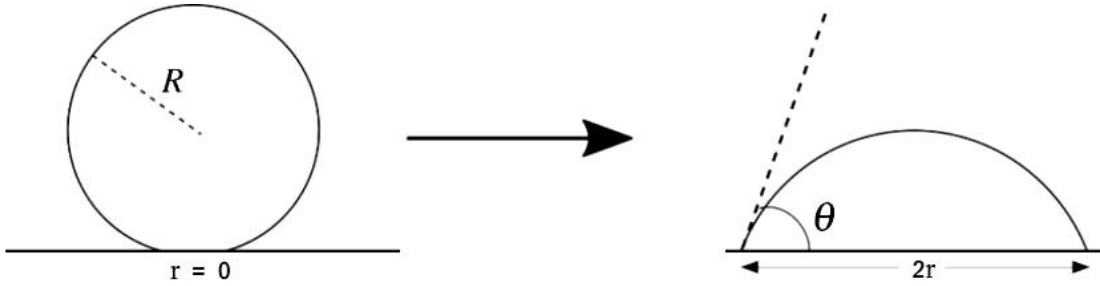


Figure 2.12: Initial and steady-state configuration for the sessile drop starting with an initial contact angle $\approx 180^\circ$, and evolving with a spreading displacement of r .

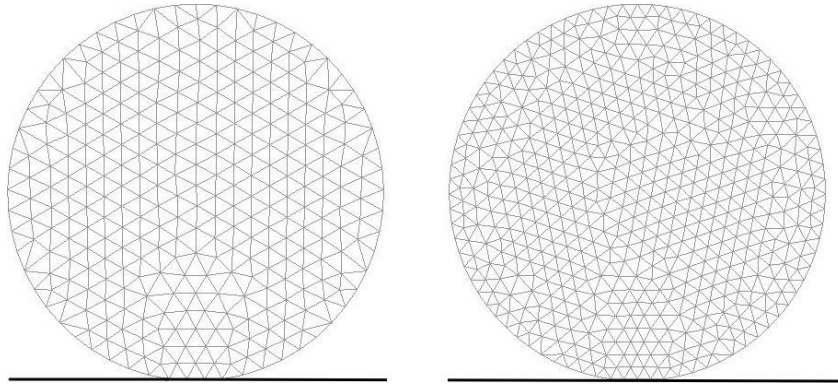
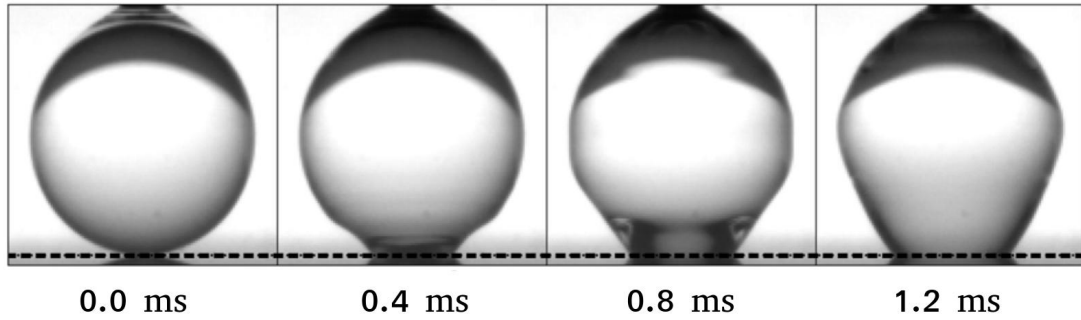
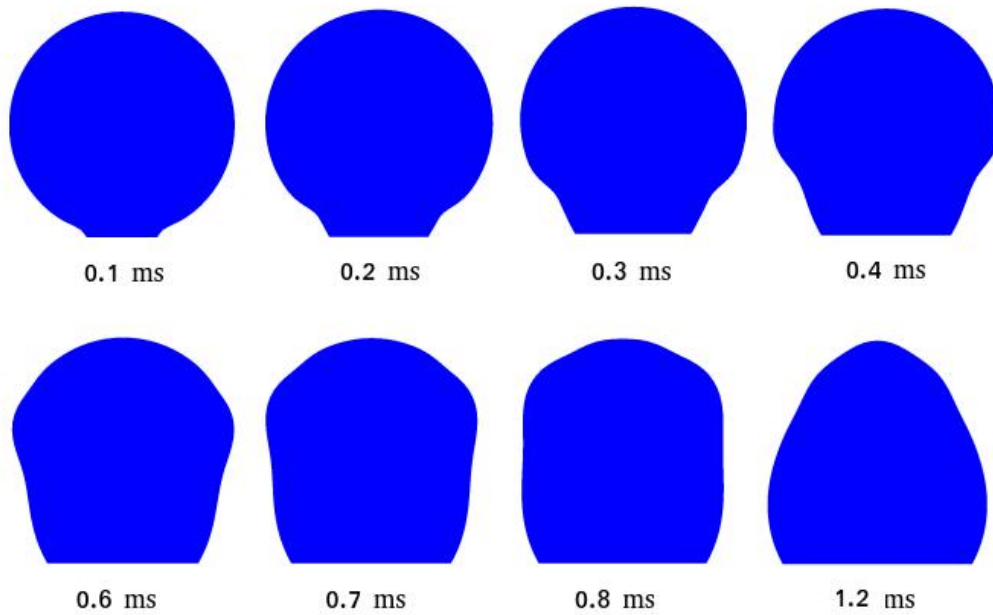


Figure 2.13: Two different mesh sizes, $h = 8 \times 10^{-5} \text{ m}$ and $h = 4 \times 10^{-5} \text{ m}$, representing the initial-stage of 0.001 m diameter drop.

Fig. 2.14 shows the spreading profile within the first millisecond when the initial capillary wave propagation is dominating at the contact line and moving toward the free-surface. The profile obtained numerically is in good agreement with the experimental profile [28].



(a) Water drop of a radius 0.82 ± 0.01 mm [28].



(b) Water drop of a radius 0.5 mm.

Figure 2.14: Case #1: water drop spreading on Triethoxysilane, for $0 < t \leq 1.2$ ms, with a dominant capillary wave propagation at the contact line (a) experimentally, (reproduced with permission from J. Phys. Rev. Lett. 100, 234501 (2008). Copyright 2008 American Physical Society), and (b) numerically.

Fig. 2.15 shows the spreading displacement, and spreading rate evolution observed experimentally and predicted numerically using the two meshes. Experimental and numerical results are in very good agreement, and the two meshes provide very similar results, i.e., the numerical results are mesh-independent. The initial contact line velocity reaches 1 m s^{-1} , which corresponds to the predicted velocity regime for an impact or spreading drop starting from rest [200, 228]. Fig. 2.14 and Fig. 2.15 show that the numerical model is able to capture the early spreading regime, $t < 0.1 \text{ ms}$ where the spreading rate is independent of the wettability of the substrate [28, 45, 54]. Furthermore, the inertial regime characterized by the capillary waves [47, 65] is captured numerically. This can be verified based on the transition time interval, T_t , formula between the inertial dominated regime, T_i , and the viscous dominated regime, T_v , i.e., $T_i < T_t < T_v$, such that [26, 47, 54]:

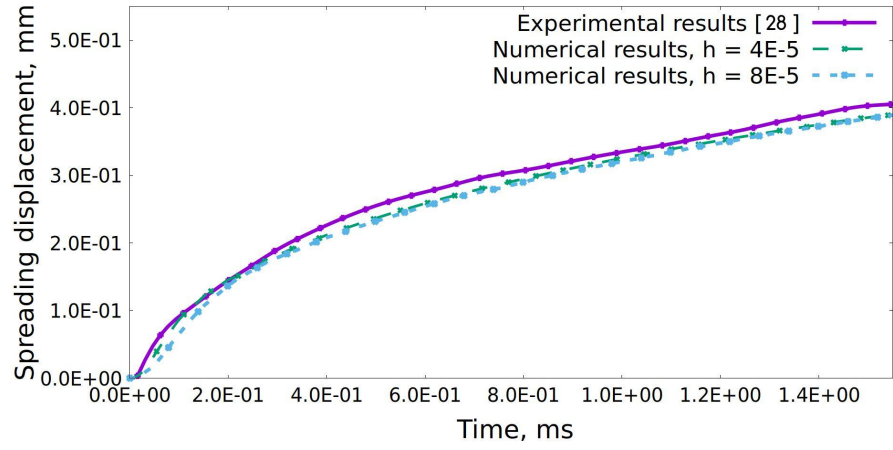
$$\left(\frac{\rho R^3}{\gamma}\right)^{0.5} < T_t < \left(\frac{\rho R^3}{\gamma}\right)^{0.5} \left(\frac{\rho \gamma R}{\mu^2}\right)^{0.125} \quad (2.9.1)$$

where T_t is the transition time interval between the inertial and the viscous regimes, ρ is the fluid density, R is the initial drop radius, γ is the surface tension coefficient, and μ is the dynamic viscosity. Eq. (2.9.1) implies that the inertial regime for a water drop of radius 0.5 mm is in the range of $T_i < 1.3 \text{ ms}$, after which the transition regime takes place. Finally, Fig. 2.14 shows that the spreading regime depends on the initial drop radius, i.e., the smaller the drop initial radius the faster the transition from inertial to viscous regimes, in agreement with eq. (2.9.1).

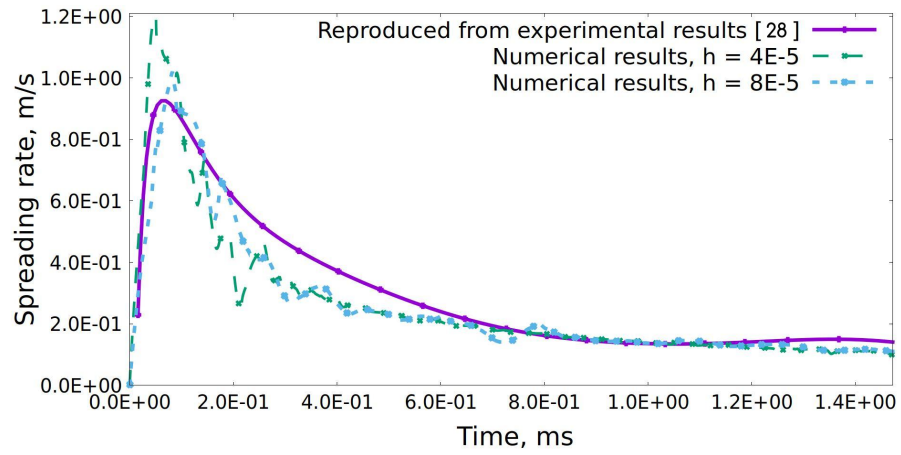
2.9.2 Case #2: spreading of a squalane (C30 H62) drop on a silica substrate

In this section, the numerical model is used to reproduce the experimental results obtained by Seveno *et al.* [200] where squalane is allowed to spread over a silica substrate. The static contact angle of squalane on silica is 38.8° .

To reproduce this experiment numerically, the same initial and boundary conditions are used as in the previous case, as shown in Fig. 2.12. The initial drop diameter is 0.0018 m and the physical properties of the fluid are $\rho = 810 \text{ kg m}^{-3}$, $\mu = 0.0314 \text{ kg m}^{-1} \text{ s}^{-1}$, and $\gamma = 0.0311 \text{ N m}^{-1}$. The expected spreading rate is of the order 10^{-1} m s^{-1} [200]. Assuming



(a)



(b)

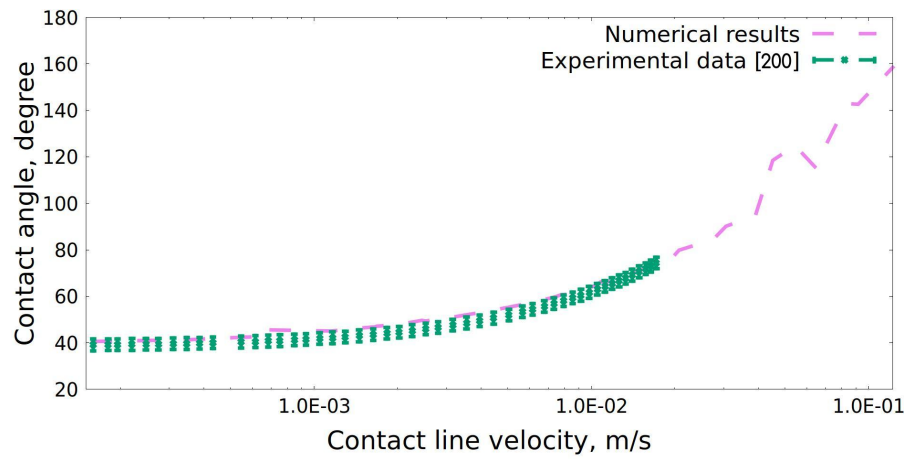
Figure 2.15: Case #1: water drop spreading rate on Triethoxysilane: (a) spreading displacement evolution (numerically vs. experimentally) and (b) contact line velocity evolution (numerically vs. experimentally).

$u_{max} = 0.5 \text{ m s}^{-1}$, the capillary wavelength and corresponding mesh sizes are obtained by eq. (2.7.2) and eq. (4.2.24) as $\lambda = 1.5 \times 10^{-4} \text{ m}$ and $h = 7.510^{-5} \text{ m}$ with 1014 elements, respectively. Also, since $We > 1$ as per eq. (3.4.2), the capillary wave propagation should be expected from numerical model. The time step is chosen as $\Delta t = 10^{-7} \text{ s}$, according to eq. (2.7.7) covering the range of contact line velocities of the order 10^{-1} m s^{-1} .

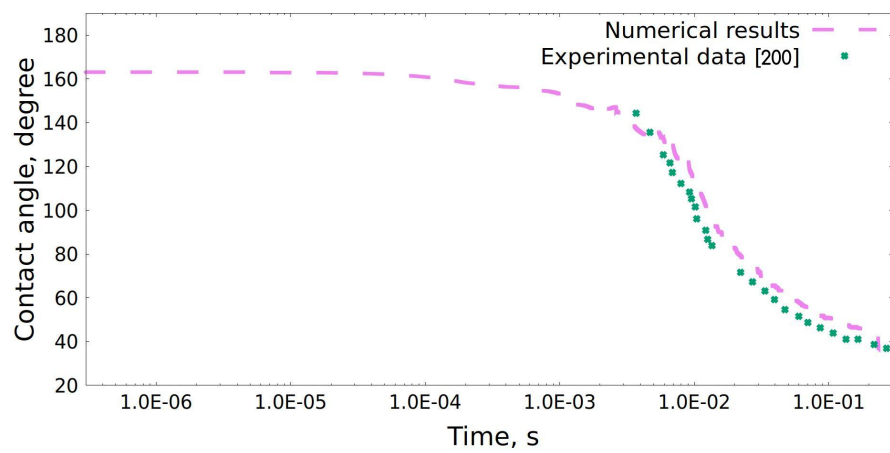
Fig. 2.16 shows the contact angle evolution versus the contact line velocity, followed by the contact angle evolution versus time. The numerically predicted contact line velocity evolution is in agreement with measured experimental data (see Fig. 2.16(a)) and is proportional to the temporal evolution of the contact angle (Fig. 2.16(b)). Furthermore, the initial squalane drop velocity on silica is of the order of $\sim 0.1 \text{ m s}^{-1}$ (Fig. 2.16(a)) as indicated by Seveno *et al.* [200]. Both numerical and experimental results show that the contact line spreading is initially dominated by inertial effects, followed by a reduction of the contact line velocity, where viscous effects dominate. This observation is in agreement with eq. (2.9.1), where the transition time interval between the inertial and the viscous regimes is predicted as, $4.3 \times 10^{-3} \text{ s} < T_t < 6.4 \times 10^{-3} \text{ s}$. In this time interval, the contact angle value varies between approximately 150° and 125° (Fig. 2.16(b)). Therefore, the numerical oscillatory behavior in this region, as shown in Fig. 2.16(a), is hypothesized to be due to the transition between the inertial and the viscous regimes.

2.9.3 Cases #3 and #4: injection of water drops on teflon (hydrophobic) and kapton (hydrophillic) substrates

To further validate the proposed model, water injection experiments on hydrophillic (kapton, static contact angle of 75° [74]) and hydrophobic (PTFE, static contact angle of 108° [165]) substrates were performed by the UC Berkeley and U Alberta Energy Systems Design Laboratory groups. In the experiment, water was injected from a small conduit of $6 \times 10^{-4} \text{ m}$ diameter in the substrate using a peristaltic pump at two constant flow rates, i.e., $5 \text{ }\mu\text{L/s}$ and $10 \text{ }\mu\text{L/s}$. Three experiments were performed: i) water injection at a rate of $Q = 5 \text{ }\mu\text{L/s}$ on kapton surface, ii) water injection at a rate of $Q = 5 \text{ }\mu\text{L/s}$ on PTFE, and iii) water injection at a rate of $Q = 10 \text{ }\mu\text{L/s}$ on PTFE. The injection profile is displayed in



(a)



(b)

Figure 2.16: Case #2: Squalane drop on silica: (a) contact angle evolution vs. contact line velocity (numerical vs. experimental), and (b) contact angle evolution vs. time (numerical vs. experimental).

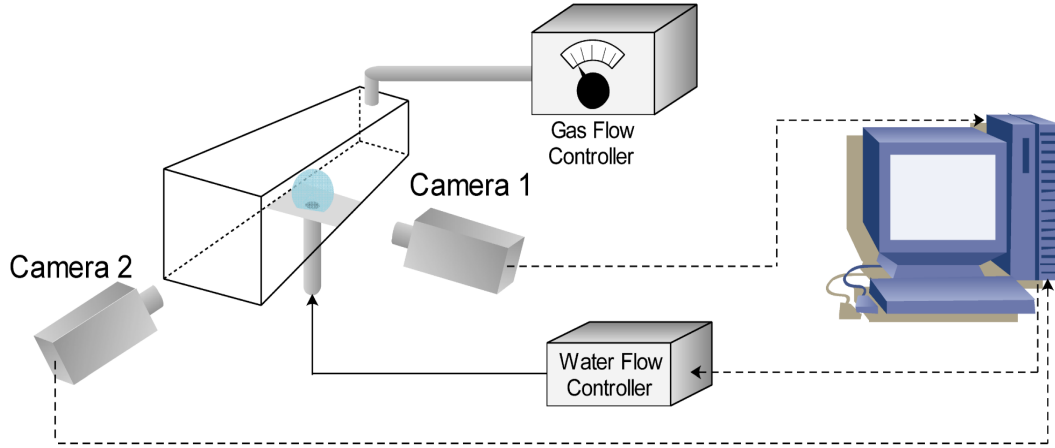


Figure 2.17: Fuel cell channel and injection simulation: Illustration of the experimental setup. Reference: T. Chan. Validation of a Semi-Analytical Model for drop Dynamics in a PEMFC. Berkeley Lab.

Fig. 2.20. Two cameras, positioned perpendicular to each other, were used to capture the injection process as shown in Fig. 2.17. The spreading displacement were extracted from the recorded videos using built-in tracking feature of ImageJ [195], where the spreading regimes were identified by tracking the contact line every 0.2 second. The contact angle measurements were extracted using the “B-Spline Snake” feature of the drop-analysis plugin of ImageJ [206]. “B-Spline Snake” feature measures the contact angle locally following a concept of polynomial fit. Therefore, an error of $\pm 2.5^\circ$ was taken into account when measuring the contact angle, as shown in Fig. 2.18(b) and Fig. 2.19(b).

In order to perform the numerical simulations, initial drop configurations of volume ≈ 0.04 and $\approx 0.2 \mu\text{L}$ and initial contact angle of 75° and 108° for kapton and PTFE, respectively, are selected. Fluid density, viscosity and surface tension coefficient are set to $\rho = 1000 \text{ kg m}^{-3}$, $\mu = 8.90 \times 10^{-4} \text{ kg m}^{-1} \text{ s}^{-1}$, $\gamma = 0.072 \text{ N m}^{-1}$. Initial pressure in the liquid is set to $p_0 = 0 \text{ Pa}$. Considering 2D simulations, the injection rates are normalized from 3D to 2D. Our numerical results show that using a scale shape factor of π provides reliable results. The injection rates were of the order of micro seconds; hence, the average spreading rate for this experiment was of the order 10^{-3} m s^{-1} , as shown in Fig. 2.18(a)

and Fig. 2.19(a), which yields $We < 1$. Accordingly, the capillary effect at the moving contact line is neglected compared to the dominant surface tension force. The time step and mesh size used for these simulations are chosen as $\Delta t = 3 \times 10^{-3}$ s and $h = 1.5 \times 10^{-4}$ m, respectively.

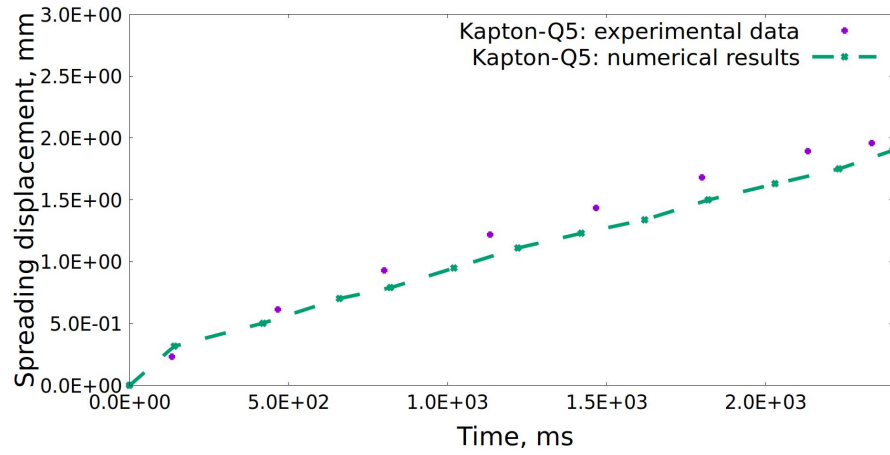
2.9.3.1 Kapton

Fig. 2.18 shows the experimental and numerical results. Experimentally, the data was collected using videos instead of high speed capturing cameras, therefore, the spreading rate and contact angle evolution could not be tracked accurately at the initial stage, i.e., for $t < 0.1$ s. Accordingly, a jump in the spreading radius and contact angle evolution was observed experimentally at the initial stage. Similarly, the initial injection rate causes an initial jump as well for the spreading radius for $t < 0.1$ s.

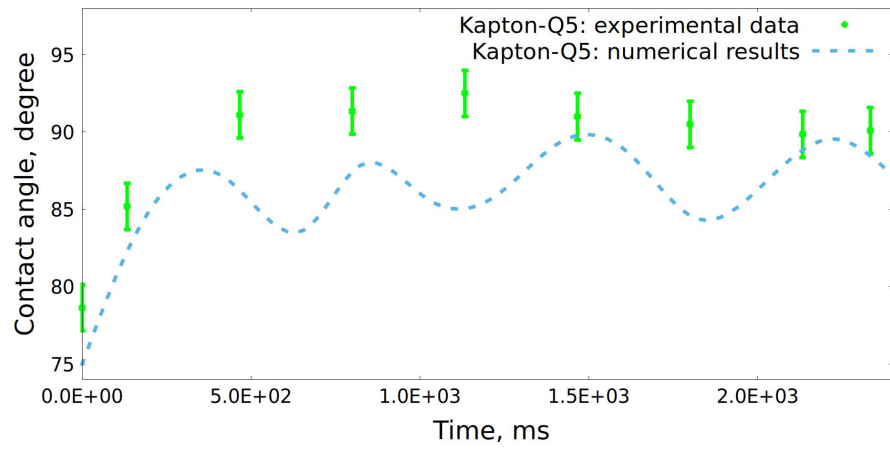
It was observed experimentally and numerically that the spreading rate decreased as the drop volume increased. Furthermore, the contact angle evolution displayed oscillations, both experimentally and numerically, and an average increase of $\sim 15^\circ$. This behavior of the contact angle evolution is interpreted in term of the work of adhesion. In general, the work of adhesion increases as the hydrophobicity of the surface decreases [192]. Accordingly, higher energy is required to detach or separate a liquid from hydrophilic surfaces due to the strong bonding between the liquid and the substrate [192]. During the initial stage of the injection process, this work of adhesion partially withstands the effect of the induced Young's stress as the drop spreads towards its equilibrium contact angle. Hence, the contact angle increases as the injection process starts, i.e., from 75° to $\sim 90^\circ$, as shown in Fig. 2.18(b). The maximum errors between the experimental data and the numerical results for both spreading rate and contact angle temporal evolution are estimated to be about 10%, as shown in Fig. 2.18(a).

2.9.3.2 PTFE

Figure 2.19 shows the spreading radius and contact angle evolution as a function of time obtained experimentally and numerically. Experimental and numerical drop radius are in excellent agreement at high injection flow rate, while at the lower flow rate the numerical



(a)



(b)

Figure 2.18: Case #3: water-kapton injection analysis and comparison: (a), spreading displacement evolution, and (b) contact angle evolution.

results underpredict the spreading radius. The contact angle is nearly constant throughout both the experiment and simulation, as opposed to the case of kapton where there was a gradual increase in the contact angle. The average maximum errors of both injection rates was about 10%. The contact angle evolution for both injection rates were in good agreement as well, with a maximum variation of 3° , i.e., about 2.5% (Fig. 2.19(b)).

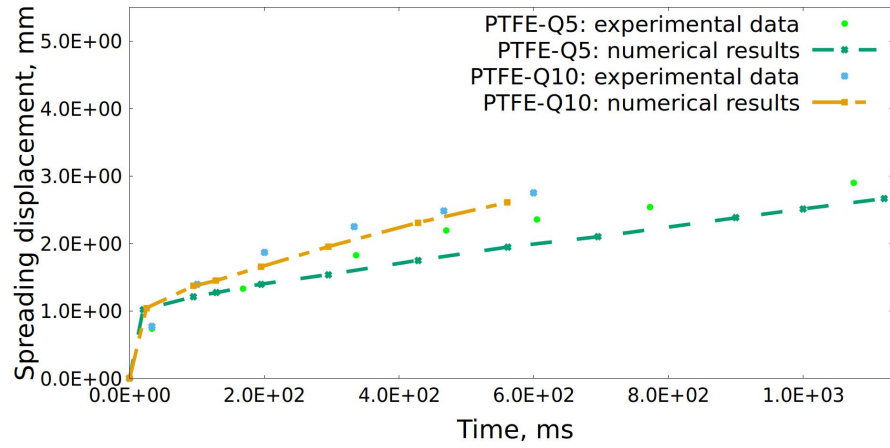
As in the case of kapton, an initial jump was observed experimentally and numerically for the spreading radius for $t < 20$ ms. Moreover, it is observed that the spreading rate decreased as the drop volume increased. However, in the case of PTFE, the sessile drop showed higher spreading rate at the initial stage due to the reduced work of adhesion between the liquid and substrate (hydrophobic substrate).

Fig. 2.20 shows a comparison between the experimental and simulated drop profiles during injection. The model is capable of capturing the drop profiles during the early stages of the process. After the drop has grown substantially, predicted profiles show some disagreement with the experimental observations. It is hypothesized that the reason for the discrepancy is the lack of three dimensional information. The current 2D model neglects out-of-plane forces, which may play a significant role in determining the drop shape and spreading rate [187].

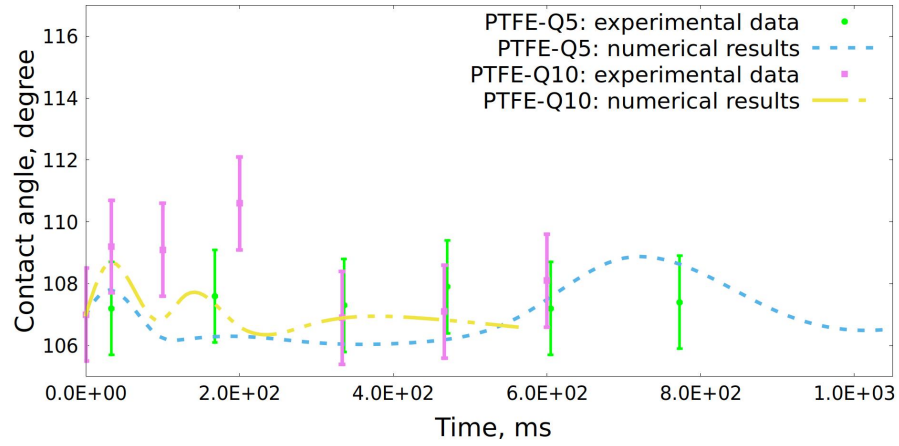
2.10 Conclusion

A PFEM-based model for the simulation of drop spreading on solid substrates was presented for a wide range of wettability conditions. The advantage of the PFEM scheme for modeling drop spreading dynamics is depicted in Figs. 2.14 and 2.20, as it i) precisely tracks the evolution of the boundaries in accordance with the force and velocity fields and ii) reconnects the domain during deformation and/or expansion.

Appropriate dynamic boundary conditions at the solid-liquid interface and the contact line were identified to provide physically meaningful results in drop spreading simulations. A Navier-slip boundary condition is applied at the liquid-solid interface excluding the contact line. At the contact line, an effective slip coefficient was introduced as a function of capillary effects, and the balance of stresses acting on the vicinity of the contact line.



(a)

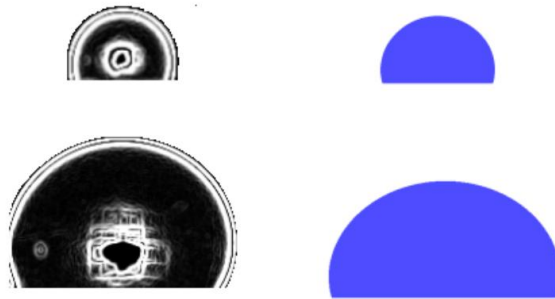


(b)

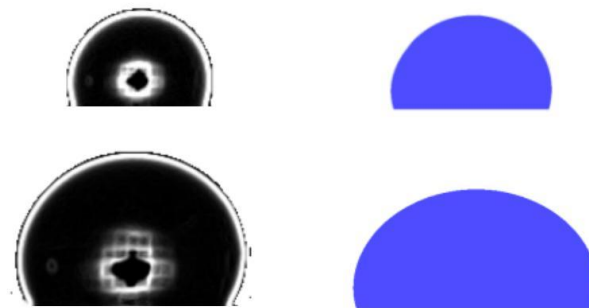
Figure 2.19: Case #4: water-PTFE injection analysis and comparison: (a), spreading displacement evolution, and (b) contact angle evolution.



(a)



(b)



(c)

Figure 2.20: Initial and final sessile drop profiles, experimentally (in black color) vs numerically (in blue color), for: (a) water injected at flow rate of $5 \mu\text{L/s}$ on kapton substrate, (b) water injected at flow rate of $5 \mu\text{L/s}$ on PTFE substrate, and (c) water injected at flow rate of $10 \mu\text{L/s}$ on PTFE substrate.

The mesh size dependency of the solution was studied. First, the importance of the capillary wave propagation phenomena, and its numerical consequences in choosing the mesh size and time step were pointed out. Then, mesh-dependency studies were performed to show that the proposed dynamic boundary conditions alleviate the mesh-dependency of the solution.

The proposed drop spreading model was validated by comparison with experimental results for a variety of liquids on hydrophobic and hydrophilic substrates. Spreading rates and contact angle temporal evolution obtained numerically were in good agreement with the experimental data. The model was able to capture the early spreading regime and the inertial to viscous transition regimes.

The model was compared with micro sessile-drop injection experiments for water on hydrophilic and hydrophobic substrates. The experimental and numerical results were again in good agreement. A three-dimensional model must be developed to properly account the geometrical effects of the spreading drop. This 3D model will be particularly important to account for out-of-plane effect and non-planar geometries during spreading, injection and other interfacial dynamic phenomena. This will be addressed Chapter 4.

Chapter 3

A TWO-DIMENSIONAL NUMERICAL MODEL FOR SLIDING MOTION OF LIQUID DROPS

3.1 Introduction

In this chapter, we consider the dynamics of a sliding liquid drop under the effect of gravity. The sliding of liquid drops on a tilted substrate is of relevance in both natural and human-made applications. This includes, and is not limited to, biological and agricultural systems [106], self-cleaning surfaces [240, 245] as in lotus leaves [100, 149], the field of biomedical engineering [21, 154], advanced surface engineering as in coating formulation and surface texturing [76, 230, 243], and non-conventional energy conversion devices as in PEMFCs [113, 186] (see chapter 1 for more details).

The sliding motion of liquid drops shares some common features to their spreading motion. Both phenomena involve: i) contact line movement, ii) the effect of the capillary action on the contact line, and iii) the effect of gravitational forces normal to the substrate. Thus, the main challenges in the mathematical and numerical modeling for sliding liquid drops are similar to those of spreading liquid drops, i.e., regularizing the contact line singularity, predicting the contact line temporal evolution, and tracking the free-surface deformation. However, additional effects must be accounted for during sliding, specifically, the effect of the retention force acting in the vicinity of the contact line (see Sec. 1.1.3). This chapter is an extension to chapter 2. It presents a numerical model based on the PFEM for the prediction of the sliding motion of liquid drops by including the effect of a retention force. The proposed model, limited to two-dimensional geometries, is validated by using experimental data found in the published literature, covering a wide range of drop size and physical properties.

It has been experimentally demonstrated that this retention force can be expressed in terms of the surface tension force, the aspect ratio of the drop footprint, and the contact angle hysteresis [80]. The contact angle hysteresis is defined as the difference between the advancing and the receding contact angles [80, 81, 84]. Initially, the retention force balances the gravitational force [16, 34, 69, 75, 80, 81, 166, 242]. When this force reaches a critical value, the drop begins to slide [80, 84].

Several authors have studied the drop depinning mechanism and detachment modes under the effect of gravity and/or external gas flow. An overview of recent experimental work can be found in [151, 231, 237]. Consequently, various analytical models have been proposed to predict the modes of drop motion. For example, ElSherbini and Jacobi [75] developed an analytical model that expresses the threshold angle as a function of the contact angle hysteresis. Xie *et al.* [237] studied the motion of a sliding drop under the effect of gravity and an impinging gas flow. The authors derived an analytical criterion for the onset of drop motion in terms of the equilibrium contact angle. Recently, White and Schmucker [231] proposed a depinning model for a liquid drop under the effect of both gravitational and wind forces. Their model was validated using water drops on an aluminum substrate. They found that the depinning phenomenon can be predicted in terms of the aspect ratio of the drop, the threshold angle, and both the Weber and Bond numbers.

Numerical models have also been presented in the literature to predict the pinning phenomenon and the different modes of drop motion. For instance, Park and Kang [168] developed a numerical feedback deceleration model, based on a conservative level set approach, to predict the pinning mechanism in terms of the contact angle hysteresis. In their model, the contact line is decelerated by controlling the contact angle, using an estimated control coefficient as a function of time. The model successfully predicts different pinning and contact angle evolution for hanging drops and drops impacting a dry solid substrate. Thampi *et al.* [218] performed two-dimensional (2D) numerical simulations, using a hybrid lattice Boltzmann algorithm and diffuse interface model, to predict the motion of a liquid drop under the effect of gravity. They observed that the rolling angular speed is directly

proportional to both the contact line velocity and the viscosity of the drop, and inversely proportional to the wetting diameter. Annapragada *et al.* [16] developed a pseudo-Lagrangian based model, using the volume of fluid-continuous surface force (VOF-CSF) approach, for drop sliding analysis. They examined sliding water drops on hydrophobic polytetrafluoroethylene (PTFE) substrates by correlating the static contact angle with the contact angle hysteresis and Bond number, and their 2D numerical results were found to be in good agreement with experimental measurements. Yilbas *et al.* [242] proposed a 2D numerical model, based on an Arbitrary Lagrangian–Eulerian (ALE) formulation, for predicting the rolling dynamics of water drops on a hydrophobic substrate. Their model was validated using water drops on hydrophobic solution-crystallized surface. They observed that the adhesion force between the drop and the substrate increased as the wetting diameter increased. Thus, the rotational speed increased as the drop size decreased. To the best of our knowledge, a numerical, mesh-independent model for sliding drops has yet to be subjected to a rigorous experimental validation process for a variety of experimental conditions.

To this end, we develop in this chapter a 2D Lagrangian PFEM scheme for the prediction of the temporal evolution of sliding liquid drops under the effect of gravity. We extend the dissipative force model first proposed in the previous chapter by including a retention force acting on the drop contact line, and we then validate the extended model with experimental data. This chapter is organized as follows: The governing equations and boundary conditions for sliding liquid drops are described in Sec. 3.2, followed by a description of the discretization strategy of the governing equations in Sec. 3.3. The mesh size and time step criteria are discussed in Sec. 3.4. Finally, in Sec. 3.5, the model is validated by examining six different experimental scenarios of sliding liquid drops for a variety of drop size, physical properties, and substrate wettabilities. The main concepts, figures, and outcomes of this chapter are reproduced from [Elaf Mahrous, R Valéry Roy, Alex Jarauta, and Marc Secanell. A two-dimensional numerical model for the sliding motion of liquid drops by the particle finite element method. *Physics of Fluids*, 33(3):032117, 2021.], with the permission of AIP Publishing (See Appendix H for more information about the publisher’s permission).

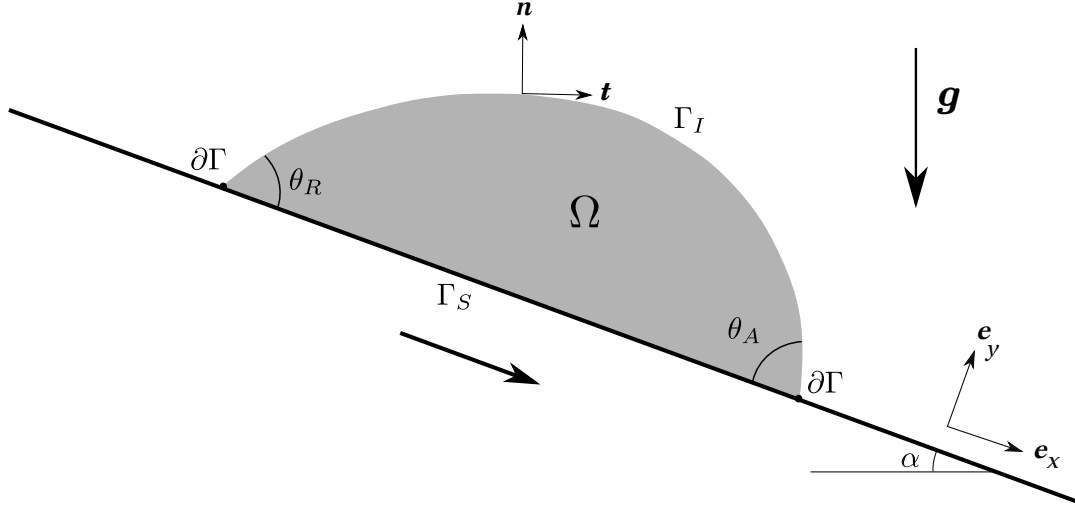


Figure 3.1: Sketch of a drop sliding down an inclined plane.

3.2 Physical model

3.2.1 Governing equations

Let Ω , Γ_I , Γ_S and $\partial\Gamma$ denote the domain occupied by the drop, its liquid-vapor interface, its solid-liquid interface, and its contact line, respectively. In 2D, the contact line is represented by two triple points (see Fig. 3.1). The equations expressing momentum and mass conservation for an incompressible Newtonian fluid are as indicated in Sec. 2.2.

3.2.2 Boundary conditions

As a drop starts to move, Young's stress is induced at the contact line $\partial\Gamma$. The contact line velocity is assumed to be proportional to the induced Young's stress [37, 141, 178]:

$$u \propto \gamma(\cos \theta_e - \cos \theta_d) \quad (3.2.1)$$

where $u = \mathbf{v} \cdot \mathbf{e}_x$ is the tangential component of the velocity vector at the contact line, θ_e is the equilibrium contact angle, and θ_d is the dynamic contact angle.

In the case of drop spreading on a flat substrate, the corresponding factor of proportionality is modeled in terms of viscous and capillary forces acting at the contact line [37,

[141]. It was shown in the previous chapter that the inclusion of these forces as boundary conditions is essential to alleviate the contact line singularity and to obtain mesh-independent spatiotemporal evolution of spreading drops (see [141] for details). As the inclination of the substrate is slowly increased, experiments show that the drop is acted upon by a force, referred to as retention force, which impedes the motion. When this force reaches a critical value, the drop begins to slide [80, 84].

3.2.2.1 Retention force

It has been shown experimentally that the retention force acting along the contact line is a function of the drop size, the aspect ratio of the wetting perimeter, the surface tension coefficient, and the contact angle hysteresis, as demonstrated by the following empirical expression [34, 75, 80, 125, 241, 242]:

$$F_{retention} = ka\gamma(\cos \theta_R - \cos \theta_A) \quad (3.2.2)$$

where k is a function of the aspect ratio of the drop footprint, a is the wetting radius of the liquid drop before deformation, θ_R is the receding contact angle, and θ_A is the advancing contact angle. In this chapter, the angles θ_A and θ_R are treated as dynamic angles which evolve with time and reach steady state values. If we had the advancing and receding contact angles, we would have been able to predict the onset of sliding.

The parameter k is a macroscopic material property. It is a reflection of surface forces acting in the vicinity of the contact line [80, 84]. The constant k is commonly assumed to take the value of $(48/\pi^3)$ [172, 241, 242] as devised by ElSherbini and Jacobi [75]. In reality, the actual value of k differs from one liquid/substrate pair to another. It has been reported that the value of k ranges from $4/\pi$ to π [34, 72, 75, 80, 81, 166], which can lead to a large variation of the retention force. Accordingly, the accuracy of this force depends on the experimental value of parameter k .

For 2D simulations, eq. 3.2.2 is found in the literature to take the following expression [16, 69]:

$$F_{retention(2D)} = \gamma(\cos \theta_R - \cos \theta_A) \quad (3.2.3)$$

The absence of the parameter k in eq. 3.2.3 is too restrictive [80, 81]. Our goal is to replicate the 2D profile of a sliding drop by consideration of parameter k . The scale shape factor k/π is adopted in this work, whereby the value $k = 4/\pi$ corresponds to a drop of a circular contact line [34, 80, 81]. Moreover, the value $k = \pi$ [75] recovers eq. 3.2.3. Consequently, the retention force acting at the contact line is expressed as follows:

$$F_{retention(2D)} = \frac{k}{\pi} \gamma(\cos \theta_R - \cos \theta_A) \quad (4/\pi < k \leq \pi) \quad (3.2.4)$$

Our numerical results appear to support this scaling, by choosing k according to experimental conditions, as will be shown in Sec. 3.5.

3.2.2.2 Total dissipative force acting at the contact line $\partial\Gamma$

The total dissipative force acting at the contact line is expressed in terms of the induced Young's stress as follows [37, 141]:

$$f_{\partial\Gamma} = -\gamma(\cos \theta_e - \cos \theta_d) = -\beta_{\partial\Gamma} u \quad \text{at } \partial\Gamma \quad (3.2.5)$$

where $f_{\partial\Gamma}$ and $\beta_{\partial\Gamma}$ are the total dissipative force per unit length and the effective slip coefficient, both acting at the contact line.

This boundary condition includes the contribution of i) the capillary force coefficient (ζ), ii) the normal viscous stress coefficient (β_n), iii) the Navier-slip coefficient (β_S), and iv) and the retention force coefficient ($\beta_{retention}$). Accordingly, the coefficient $\beta_{\partial\Gamma}$ is defined as follows:

$$\beta_{\partial\Gamma} = \zeta + \beta_n + \beta_S + \beta_{retention} \quad (3.2.6)$$

Coefficients ζ , β_n and β are discussed in Sec 2.5.1. Coefficient $\beta_{retention}$ which accounts for the effect of the retention force is given by:

$$\beta_{retention} = \frac{\gamma k}{u\pi} (\cos \theta_R - \cos \theta_A) \quad (3.2.7)$$

3.2.2.3 Forces acting at the solid-liquid interface away from the contact line, Γ_S

Boundary conditions along the solid-liquid interface excluding the contact line are imposed in terms of the Navier-slip coefficient. It is expressed as a function of the normal projection of Cauchy stress tensor as discussed in Sec 2.5.2.

3.3 Discretized governing equations

This section summarizes the detailed discretization technique in Sec. 2.6, including the retention force in the formulation. The continuity and momentum equations, eq. 2.2.1 and 2.2.4, are discretized in space using the PFEM scheme. The domain is represented by a set of particles, and is evolved in a Lagrangian manner. The physical information is stored at each node, and the domain is deformed according to the force and velocity fields. At each time step, the domain is re-meshed to ensure that its boundaries are reconstructed in accordance with the calculated velocity field. Both velocity and pressure are approximated using first-order Lagrange elements on 2D triangular meshes. The Newark-Bossak scheme is used for the temporal discretization. However, a Backward-Euler scheme is used here to simplify the expressions. The complete algorithm for the discretization and time marching schemes can be found in [114, 184, 186].

The velocity and pressure, $\bar{\mathbf{v}}_n$ and \bar{p}_n , are assumed to be known at the current time, t_n . The updated values of velocity and pressure, $\bar{\mathbf{v}}_{n+1}$ and \bar{p}_{n+1} , are found at the next time step, t_{n+1} , by solving:

$$\mathbf{M} \frac{\bar{\mathbf{v}}_{n+1} - \bar{\mathbf{v}}_n}{\Delta t} + \mu \mathbf{L} \bar{\mathbf{v}}_{n+1} + \mathbf{G} \bar{p}_{n+1} = \bar{\mathbf{F}} + \bar{\mathbf{F}}_{st} + \bar{\mathbf{F}}_{\partial\Gamma} + \bar{\mathbf{F}}_{\Gamma_S} \quad (3.3.1)$$

$$\mathbf{D} \bar{\mathbf{v}}_{n+1} = 0 \quad (3.3.2)$$

where \mathbf{M} is the mass matrix, \mathbf{L} is the Laplacian matrix, Δt is the time step, \mathbf{G} is the gradient matrix, $\bar{\mathbf{F}}$ is the vector of external forces, $\bar{\mathbf{F}}_{st}$ is the surface tension force vector acting at the fluid-fluid interface, $\bar{\mathbf{F}}_{\partial\Gamma}$ is the dissipative force vector acting along the contact line, $\bar{\mathbf{F}}_{\Gamma_s}$ is the dissipative force vector acting along the solid-liquid interface away from the contact line, and \mathbf{D} is the divergence matrix. The expressions of the local matrices and vectors are given in Appendix C. Eqs. 3.3.1 and 3.3.2 are linearized using a Newton method. Moreover, the pressure is stabilized using the algebraic sub-grid scales (ASGS) [52, 53, 157] stabilization technique as the linear velocity-pressure elements do not fulfill the compatibility condition [66]. The solution algorithm and implementation methodology are described in more detail in Appendix D.

3.4 Mesh size and time step criteria

Our previous numerical work on drop spreading (chapter 2.8) demonstrated that the implementation of the proposed boundary conditions into a PFEM numerical scheme results in physically acceptable behavior and produces mesh-independent solutions. The adopted mesh size, h , is estimated as a function of the wetting radius, a , as follows:

$$h \sim \frac{a}{10} \quad (3.4.1)$$

Adaptive mesh refinement can also be implemented at the boundaries in order to reduce the computational cost. Mesh dependency analysis is presented in Sec. 3.5.2.

The main constraint for choosing the time step is the maximum velocity at the contact line which must satisfy the range of applicability of Jiang's model, that is $0 < Ca \leq 0.03$. In the present work, the time step criteria is calculated based on the Weber number (We) defined as [180]:

$$We = \frac{\rho R u_{max}^2}{\gamma} \quad (3.4.2)$$

where R is the radius of the drop (see Appendix E), and u_{max} is the maximum value of the tangential component of the velocity vector at the contact line. On one hand, if the capillary

wave propagation at the contact line is dominant, i.e, $We > 1$ [180], the time step is governed by the following equation [141]:

$$\Delta t \leq \sqrt{\frac{2}{\pi}} \frac{\gamma}{4\rho|u_{max}^3|} \quad (3.4.3)$$

On the other hand, if $We < 1$, the time step limit is governed by the Courant-Friedrichs-Lewy condition as follows [185]:

$$\Delta t \leq \frac{CFL}{\frac{|u_{max}|}{h} + \frac{2\mu}{h^2}} \quad (3.4.4)$$

where CFL is the Courant-Friedrichs-Lewy number and h is the mesh size. In practice, the range of CFL is between 0.5 and 0.9.

In summary, in this work eq. 3.4.2 is used to estimate the Weber number, the step size is then chosen to satisfy either eq. 3.4.3 or eq. 3.4.4.

3.5 Experimental validation

Six different experimental scenarios obtained from the published literature are examined to validate the proposed sliding drop model for a variety of liquid and substrate properties. Only steady-state profiles are examined, due to the lack of data during the unsteady, initial drop motion which typically lasts a few milliseconds. The physical properties of the liquids, the inclination angles of the substrates, and the corresponding simulation parameters are summarized in Tables 3.1 and 3.2.

3.5.1 Cases #1 and #2: ethylene glycol drop on an omniphilic polycarbonate substrate

We first examine the sliding experiments performed by Kim *et al.* [125] for ethylene glycol drop sliding down an inclined polycarbonate substrate. The drop of volume 29.2 μL wets a circular surface of the substrate of diameter 5.66 mm (see Appendix E). The drop is allowed to slide over the substrate until it reaches its steady-state velocity. Two inclination angles are considered, $\alpha = 11^\circ$ and $\alpha = 20^\circ$. The steady-state velocities for

Case #	Liquid	Substrate	ρ	μ	γ	θ_e	Volume	α
			(kg.m ⁻¹)	(Pa.s)	(N.m ⁻¹)	(°)	(μ L)	(°)
1 [125]	ethylene glycol	polycarbonate	1114	0.0209	0.0484	70.2	29.2	11
2 [125]							29.2	20
3 [16]	water	PTFE	997	0.00089	0.0728	120	7.5	60
4 [16]							10	60
5 [151]	water	PMMA	997	0.00089	0.0728	74.4	30	0-70 at 20° s ⁻¹
6 [238]	PEG	smooth glass	1080	0.285	0.0533	34.0 [194, 215, 238]	100	27

Table 3.1: Physical properties of the liquids and substrate inclination angles.

$\alpha = 11^\circ$ and $\alpha = 20^\circ$ were found experimentally to be $3.75 \times 10^{-4} \text{ m s}^{-1}$ and $1.557 \times 10^{-3} \text{ m s}^{-1}$, respectively [125].

The simulations are performed using the physical properties for cases #1 and #2 in Table 3.1. The wetting radius is $a = 0.00283 \text{ m}$ (see Table 3.2). Thus, the mesh size used here is $h = 3 \times 10^{-4} \text{ m}$ (eq. 3.4.1). Assuming the steady-state velocity is unknown for both cases, the following steps are followed to estimate the time step. The maximum contact line velocity, u_{max} , is estimated first based on the range of applicability of Jiang's model, i.e., $0 < Ca \leq 0.03$. For the case of ethylene glycol, the critical velocity is then estimated to be $u_{max} = 0.07 \text{ m s}^{-1}$. The next step is to calculate the Weber number as a function of u_{max} using eq. 3.4.2. For this case, $We = 0.34$. Accordingly, eq. 3.4.4 is used to obtain the limiting time step, and is found to be $\Delta t \approx 1 \times 10^{-6} \text{ s}$.

The value of k in eq. 3.2.4 is imposed using experimental results for a sliding ethylene glycol sliding drop. Different sliding experiments have been performed with drop volumes varying between $26 \mu\text{L}$ to $46 \mu\text{L}$ [80]. For a contact angle hysteresis varying between 7.4° to 45.3° , the average value of k was found experimentally to be 1.41, i.e., $\frac{k}{\pi} \approx 0.45$. The values

Case #	Volume, (μL)	Radius, R , (m)	Wetting radius, a , (m)	Mesh size, (m)	Δt , (s)	Computational time (minutes)
1 & 2	29.2	0.00301	0.00283	3E-4	1E-6	~ 60
3	7.5	0.001285	0.0011	1E-4	1E-6	~ 40
4	10	0.001414	0.0012	1.2E-4	1E-6	~ 40
5	30	0.002869	0.002763	3E-4	5E-6	~ 330
6	100	0.010492	0.00586	5E-4	2E-7	~ 150

Table 3.2: Simulation parameters.

of angles θ_A and θ_R can be estimated experimentally [80] as 76.2° and 58.4° , respectively.

The steady-state profiles of the sliding drop are shown in Fig. 3.2. The contact angle evolution and both the advancing and receding velocities for the values of $\frac{k}{\pi} = 0.4, 0.45$, and 0.49 are presented in Figs. 3.3 and 3.4.

Fig. 3.2 shows that the difference in the advancing and receding sliding angles increases as the angle of inclination is increased from $\alpha = 11^\circ$ to $\alpha = 20^\circ$. The advantage of the PFEM-based model for the applications of drop dynamics is depicted in Figs. 3.2(b) and 3.2(c), as it allows to accurately treat the evolution of the domain boundaries in accordance with the calculated velocity field (Fig. 3.2(d) and 3.2(e)).

In Fig. 3.3(a) and 3.3(b), the difference in the sliding advancing and receding angles for $\alpha = 11^\circ$ and $\alpha = 20^\circ$ are found to be 20° and 33° , respectively. At these two inclination angles, different values of parameter $\frac{k}{\pi}$ do not affect the steady-state sliding angles

due to the high liquid viscosity, about 23 times greater than that of water. However, higher oscillatory behavior is observed for higher $\frac{k}{\pi}$ values due to the higher resulting retention force along the contact line, in agreement with eq. 3.2.2.

Anti-correlated oscillations are observed between the advancing and the receding contact angles (Fig. 3.3). This oscillatory behavior is found to be, qualitatively, in agreement with a number of experiments of drops sliding on inclined surfaces [80, 81, 151]. Specific phases of sliding motion are typically observed: i) an initial advancing phase, (ii) a receding phase, and finally (iii) a detachment phase [80, 81, 151]. Specifically, the drop initially leans towards the gravitational field, until its advancing edge moves before its receding edge. Thus, the advancing contact angle increases while the receding contact angle decreases. At the same time, the retention force opposes the contact line motion and, consequently, the advancing edge holds while the receding edge starts to slide. Finally, both the advancing and the receding edges slide simultaneously, i.e., the drop completely detaches. Larger drops were observed to slide with the absence of the second receding phase. In contrast, smaller drops were found to move back and forth between the first and the second sliding phases before they completely detach.

In Fig. 3.4(a) and 3.4(b), both the advancing and receding velocities increase as spreading and sliding start simultaneously. Both velocities approach the steady-state velocity as sliding becomes dominant. For $\frac{k}{\pi} = 0.45$, the steady-state velocities are $5.51 \times 10^{-4} \text{ m s}^{-1}$ and $1.26 \times 10^{-3} \text{ m s}^{-1}$ for $\alpha = 11^\circ$ and $\alpha = 20^\circ$, respectively. Numerical vs. experimental steady-state velocities are presented in Table 3.3. The difference between the experimental and numerical results are 46.9% and 19.1% for $\alpha = 11^\circ$ and $\alpha = 20^\circ$, respectively. The relative error increases as $\frac{k}{\pi}$ deviates from 0.45. A parametric study for three values of $\frac{k}{\pi}$ is presented in Table 3.4. The data indicates that the steady-state velocity is inversely proportional to the parameter $\frac{k}{\pi}$, i.e., the velocity is inversely proportional to the retention force acting along the contact line, in agreement with eqs. 3.2.4 and 3.2.7.

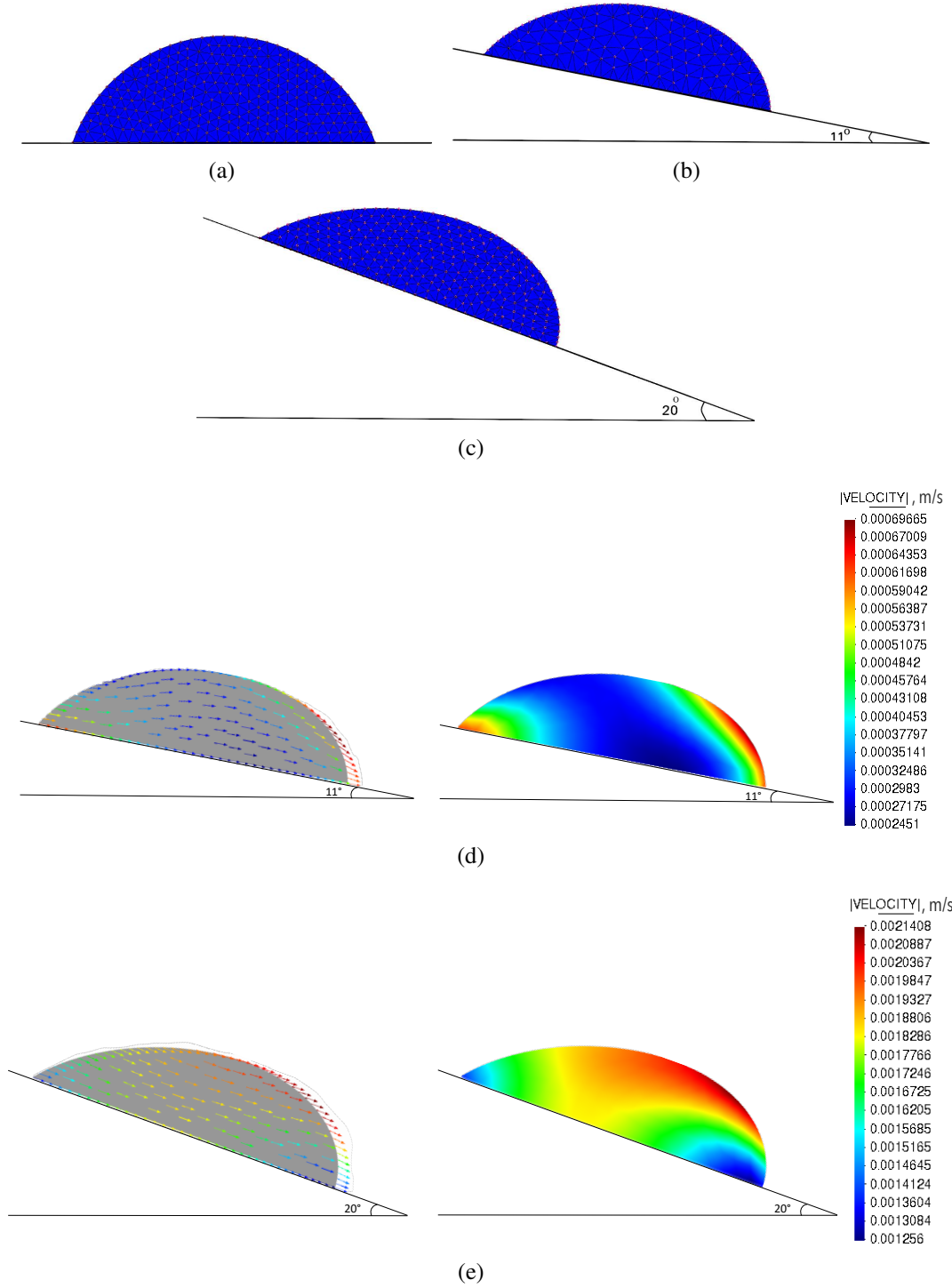
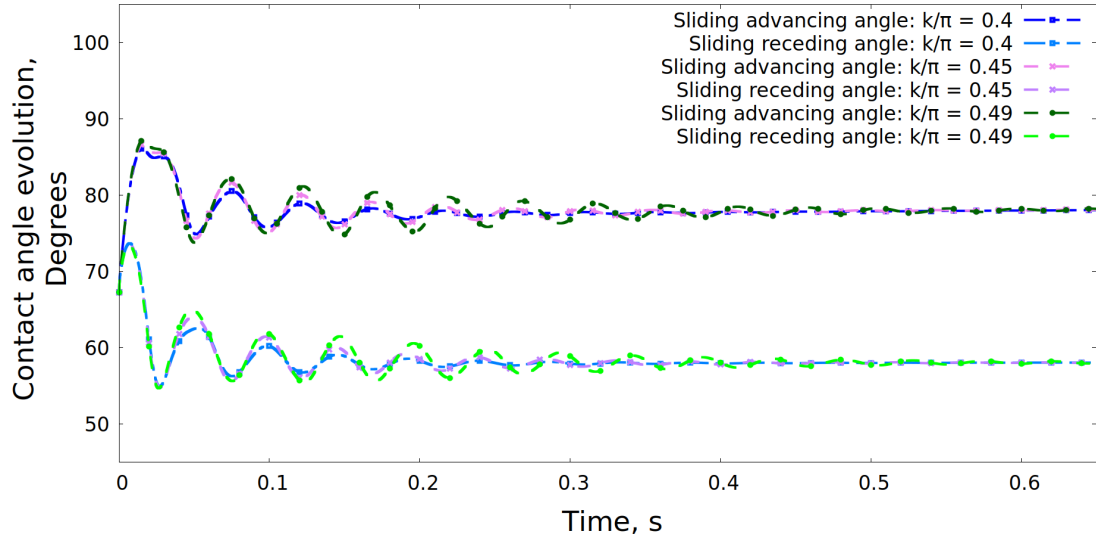
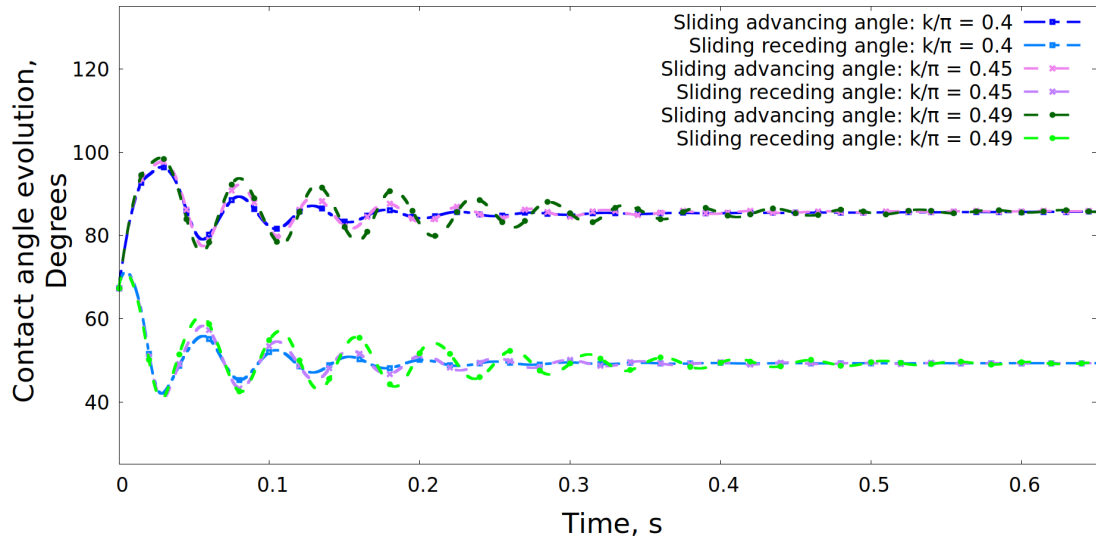


Figure 3.2: Cases #1 and #2: a 29.2 μL ethylene glycol drop sliding on an inclined plane of inclination angle α : (a) initial drop profile at $\alpha = 0^\circ$ and $t = 0$ s, (b,c) steady-state profiles at $\alpha = 11^\circ$ and 20° , respectively, and (d,e) drop velocity fields at $\alpha = 11^\circ$ and 20° , respectively.

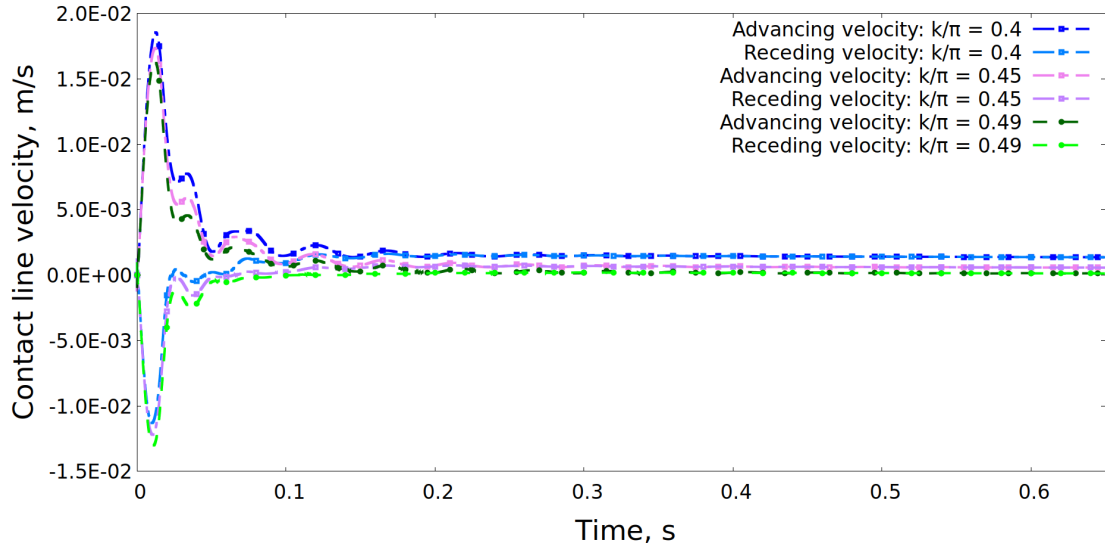


(a)

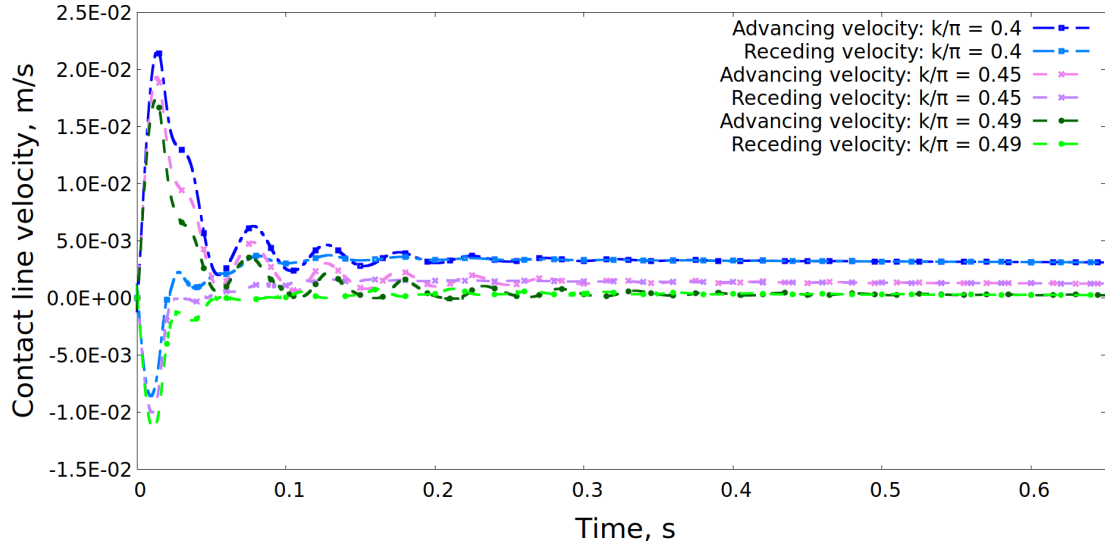


(b)

Figure 3.3: Cases #1 and #2: a $29.2 \mu\text{L}$ ethylene glycol drop sliding on an inclined plane, with angle of inclination α : (a) contact angle evolution for $\alpha = 11^\circ$, (b) contact angle evolution for $\alpha = 20^\circ$.



(a)



(b)

Figure 3.4: Cases #1 and #2: a $29.2 \mu\text{L}$ ethylene glycol drop sliding on an inclined plane, with angle of inclination α : (a) advancing and receding velocities for $\alpha = 11^\circ$, (b) advancing and receding velocities for $\alpha = 20^\circ$.

Case #	Volume (μL)	α ($^\circ$)	k (3D)	$\frac{k}{\pi}$ (2D)	Experimental u_{ss} (m s^{-1})	Numerical u_{ss} (m s^{-1})	Error in u_{ss} (%)
1	29.2	11	1.41 [80]	0.45	3.75E-4 [125]	5.51E-4	46.9%
2	29.2	20	1.41 [80]	0.45	1.557E-3 [125]	1.26E-3	19.1%
3	7.5	60	1.35 [80]	0.43	0.12 [16]	0.11	8.3%
4	10	60	1.35 [80]	0.43	0.23 [16]	0.2	13.0%
5	30	0-70 (20° per seconds)	Eq. 3.5.1 [80, 81]	0.43–0.5 [80, 81]	————	————	————
6	100	27	2 [238]	0.64	7.75E-4 [238]	8.7E-4	12.3%

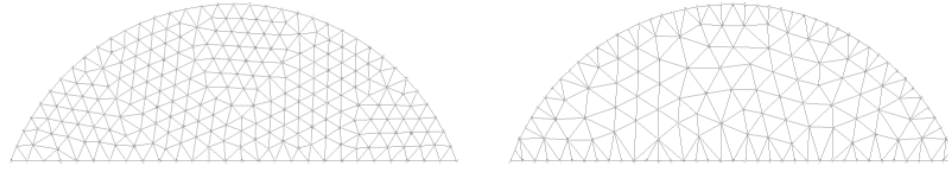
Table 3.3: Numerical vs. experimental steady-state velocities (u_{ss}).

3.5.2 Mesh dependency analysis

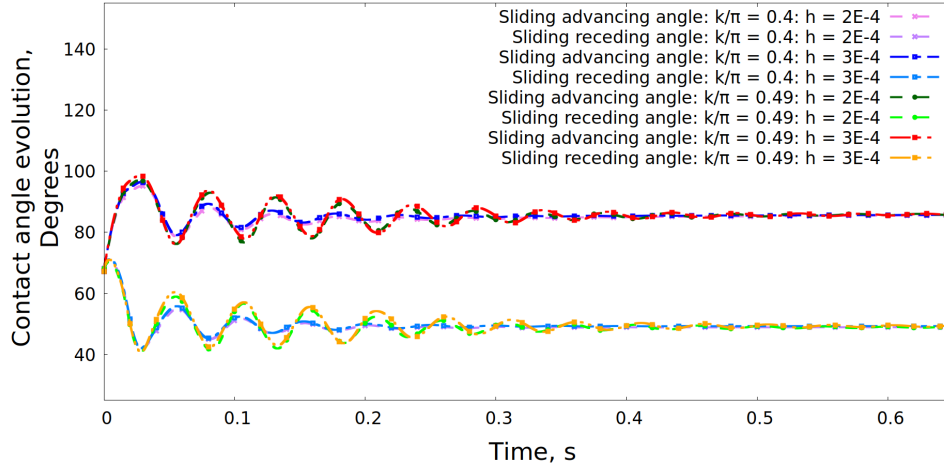
For the drop spreading numerical model, the inclusion of the dissipative force as boundary conditions results in a mesh-independent solution (see Sec. 2.8). For further validation, the numerical results for the ethylene glycol drop sliding on an inclined plane with $\alpha = 20^\circ$, in Sec. 3.5.1, is compared for the two extreme values of the parameter $\frac{k}{\pi}$, i.e. 0.4 and 0.49, using two mesh sizes. The first mesh size is set to $h = 2 \times 10^{-4}$ m, with 431 triangular elements. The second mesh size is obtained based on an adaptive mesh refinement approach, such that $h = 3 \times 10^{-4}$ m in the bulk part of the drop, and refined to 2×10^{-4} m near the boundaries. The total triangular elements of 226, about 50% fewer triangular elements than in the first case (see Fig. 3.5(a)). The contact angle evolution and both the advancing and receding velocities for both meshes are compared in Figs. 3.5(b) and 3.5(c). These results illustrate that the dynamic behavior obtained numerically is stable and mesh-independent.

3.5.3 Cases #3 and #4: water drop on a hydrophobic PTFE substrate

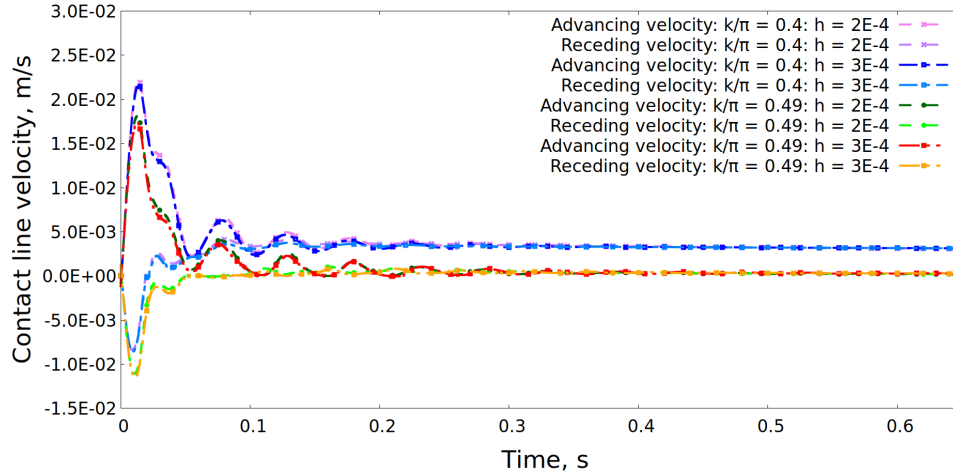
The third and fourth validations consider the experiments performed by Annapragada *et al.* [16]. In these experiments, two water drops of volume 7.5 μL and 10 μL slide on an inclined PTFE substrate. Under equilibrium condition, the contact angle θ_e is 120° . Both drops are sliding on a tilted plate at an inclination angle of 60° . The steady-state sliding velocities were experimentally found to be 0.12 m s^{-1} and 0.23 m s^{-1} for the 7.5 μL and



(a)



(b)



(c)

Figure 3.5: Demonstration of mesh-independence for a $29.2 \mu\text{L}$ ethylene glycol drop sliding on an inclined plane of inclination angle $\alpha = 20^\circ$: (a) two different mesh sizes of $h = 2 \times 10^{-4}$ m and $h = 3 \times 10^{-4}$ m representing the initial configuration, (b) contact angle evolution, (c) advancing and receding velocities.

Case #	Volume (μL)	α ($^\circ$)	Experimental u_{ss} (m s^{-1})	k (3D)	$\frac{k}{\pi}$ (2D)	Numerical u_{ss} (m s^{-1})	Error in u_{ss} (%)
1	29.2	11	3.75E-4	1.26	0.4	1.37E-3	265.3%
				1.41	0.45	5.51E-4	46.9%
				1.54	0.49	1.41E-4	62.4%
2	29.2	20	1.557E-3	1.26	0.4	3.08E-3	97.8%
				1.41	0.45	1.26E-3	19.1%
				1.54	0.49	3.2E-4	79.4%
3	7.5	60	0.12	1.13	0.36	0.18	50%
				1.35	0.43	0.11	8.3%
4	10	60	0.23	1.35	0.43	0.2	13.0%
				1.54	0.49	0.03	86.9%
6	100	27	7.75E-4	1.5	0.48	1.79E-3	97.6%
				2	0.64	8.71E-4	12.3%
				2.5	0.8	2.03E-4	73.8%

Table 3.4: Parametric analysis for different k values.

10.0 μL drops, respectively.

Using the physical properties and drop geometries for cases #3 and #4 in Table 3.1 and 3.2, the simulations are performed with corresponding mesh sizes of $h = 1 \times 10^{-4}$ m and $h = 1.2 \times 10^{-4}$ m, respectively. For a sliding water drop on PTFE substrate, the corresponding value of k was found experimentally to be 1.35 [80]. The values of angles θ_A and θ_R are found experimentally to be 122.4° and 100.0° , respectively [80].

The quantity u_{max} is found to be 2.45 m s^{-1} in order to satisfy the range of applicability of Jiang's model and, thus, $We > 1$. From eq. 3.4.3, the limiting time step is $\Delta t \approx 1 \times 10^{-6}$. Alternatively, the limiting time step can be predicted by assuming the steady-state sliding velocities, u_{ss} , based on the experimental results found in [16] to be 0.12 m s^{-1} and 0.23 m s^{-1} for the 7.5 μL and 10.0 μL drops, respectively. From eq. 3.4.2, We is found to be ≤ 1

for both cases. Therefore, according to eq. 3.4.4, we find $\Delta t = 3 \times 10^{-6}$ s and $= 4 \times 10^{-6}$ s for the 7.5 μ L and 10.0 μ L drops, respectively. Both eq. 3.4.3 and 3.4.4 give the same order of magnitude of the limiting time steps, which is indicative of stability during the transition between inertial to viscous regimes [141].

The experimental and numerical steady-state profiles are displayed in Fig. 3.6. Numerically, the difference in the sliding advancing and receding angles are found to be 23° and 31° for the 7.5 μ L and 10 μ L drops, respectively. Experimentally, these quantities are measured using the drop analysis plugin of the ImageJ software [206], and found to be 21° and 27° for the 7.5 μ L and 10 μ L drops. The drop profiles obtained numerically are in good agreement with the experimental profiles. Moreover, the numerical profiles shown in Fig. 3.6(d) and Fig. 3.6(c) show that large drop deformation leads to increasing triangular remeshing over the domain at each time step. The velocity fields are shown in Figs. 3.6(e) and 3.6(f) for the 7.5 μ L and 10 μ L drops, respectively. As in the case of EG drops (Figs. 3.2(d) and 3.2(e)), the velocity field is constrained by the imposed boundary conditions. However, the velocity field is found to be more uniform along the solid-liquid interface for water drop on PTFE substrate. This indicates that the work of adhesion forces along the solid-liquid interface decreases as the hydrophobicity of the surface increases [192].

The contact angle evolution, and both the advancing and receding velocities are illustrated in Fig. 3.7. The steady-state velocities for the 7.5 μ L and 10 μ L drops are numerically found to be 0.11 m s^{-1} and 0.12 m s^{-1} , respectively. The difference between the experimental and numerical results are 8.3% and 13.0% for the 7.5 μ L and 10 μ L drops, respectively (Table 3.3). The error increases as the parameter $\frac{k}{\pi}$ deviates from 0.43 (see Table 3.4). Similar to the EG drop on polycarbonate substrate, Sec. 3.5.1, the steady-state velocity of the water drop on PTFE decreases as the parameter $\frac{k}{\pi}$ increases. For the value of $\frac{k}{\pi} = 0.49$ corresponding to an over-predicted value of the retention force acting in the vicinity of the contact line, both advancing and receding edges slide and overlap leading to nonphysical oscillations, as shown in Fig. 3.7(b). Using the adequate/experimental value of the parameter k of 1.35 [80], minor fluctuations are observed for the water drop at higher velocities, in agreement with [16], which is hypothesized to be due to higher dissipation along the contact.

Furthermore, due to the low water viscosity compared to ethylene glycol of Sec. 3.5.1, the difference in the sliding advancing and receding angles increases as the value of $\frac{k}{\pi}$ increases, as shown in Fig. 3.7(a).

3.5.4 Case #5: water drop on a hydrophilic PMMA substrate with time-varying inclination

Here, we examine the deformed profiles of a water drop sliding on a rotating PMMA substrate. Maurer *et al.* [151] studied the sliding profiles for a water drop of 30 μL volume. The drop was initially at rest on a flat PMMA substrate, with contact angle $\theta_e = 74.4^\circ$. The substrate was then rotated at a constant angular velocity of $\dot{\alpha} = 20^\circ$ per second (Fig. 3.8).

The dynamic receding and advancing angles are measured at the inclination angles $\alpha = 10^\circ, 40^\circ, 55^\circ$, and 70° . High drop deformation is expected, especially at high inclination angles. Therefore, the value of the parameter k is chosen based on the retention force and contact angle hysteresis relation obtained experimentally by Extrand and Kumagai [80]. Accordingly, our numerical simulations are performed by using the following piecewise representation of parameter k :

$$k = \begin{cases} 1.34 & \text{for } 0 < (\cos \theta_R - \cos \theta_A) \leq 0.7 \\ 2.8 - \frac{1}{(\cos \theta_R - \cos \theta_A)} & \text{for } 0.7 < (\cos \theta_R - \cos \theta_A) < 1.0 \end{cases} \quad (3.5.1)$$

The values of angles θ_A and θ_R are found experimentally to be 77.0° and 47.4° [80], respectively. The relevant physical properties can be found in Table 3.1, case #5. The mesh size and time steps are chosen to be 3×10^{-4} m and 5×10^{-6} s, respectively. The gravitational field is modeled proportional to the time-varying inclination of the substrate, and rotational inertia forces are neglected.

The drop profiles and corresponding sliding angles evolution, both experimentally and numerically, are shown in Fig. 3.8. The experimental values of contact angle were measured using the drop analysis plugin of the ImageJ software. The numerical profiles are found to be in good agreement with the experiments. The maximum error between the experimental and numerical results is found to be $\approx 10\%$, localized near the advancing

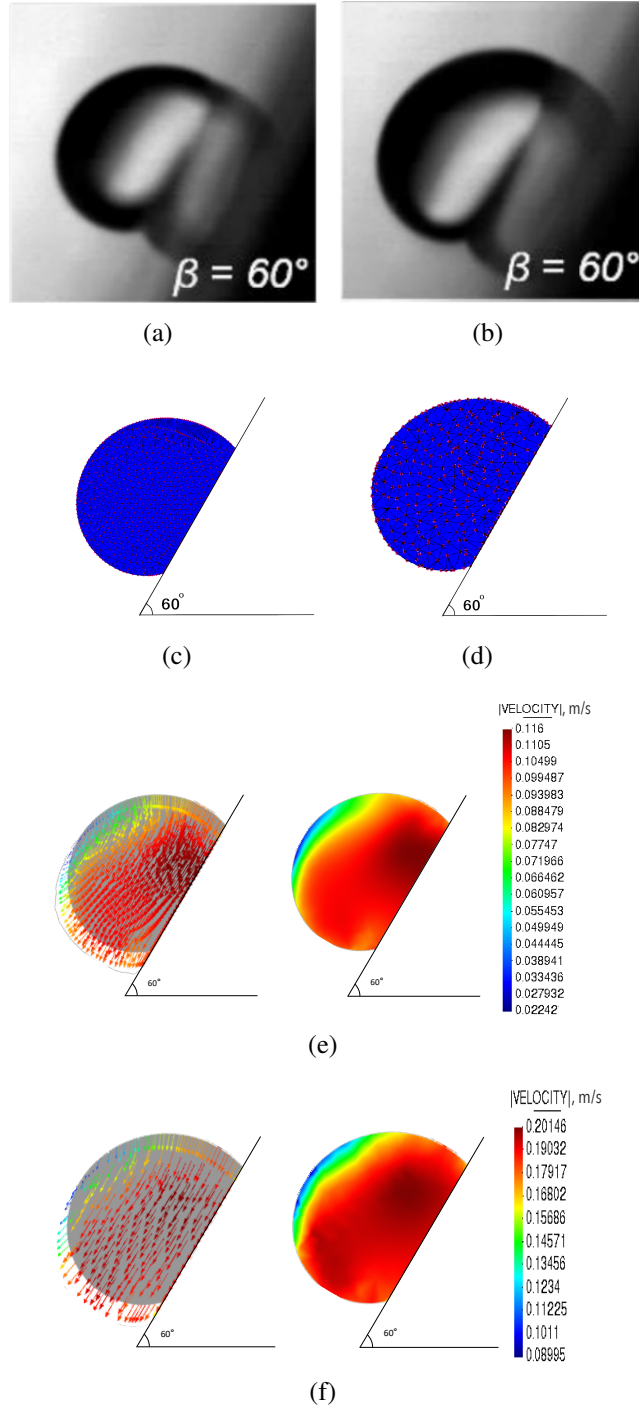
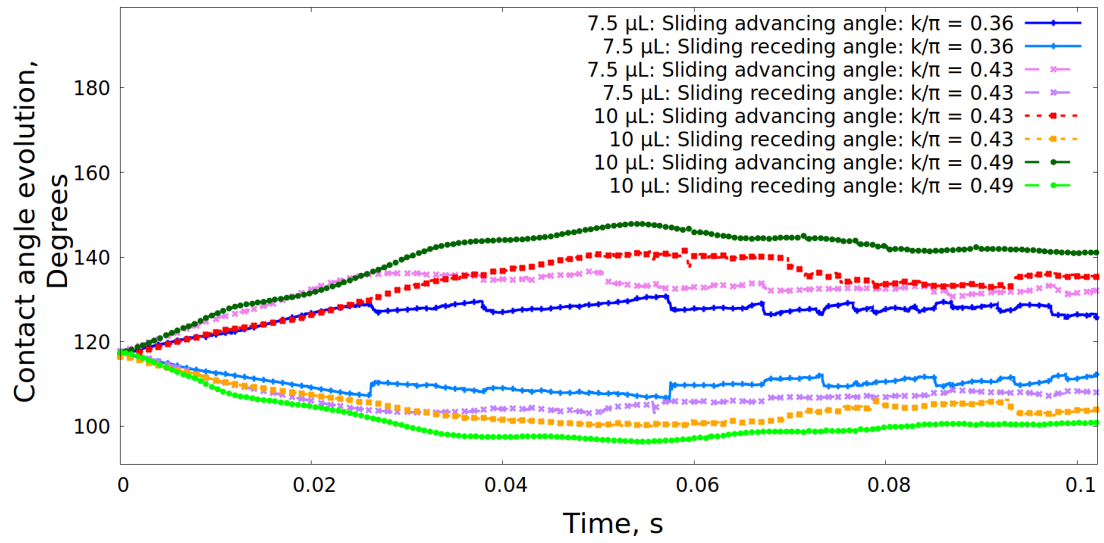
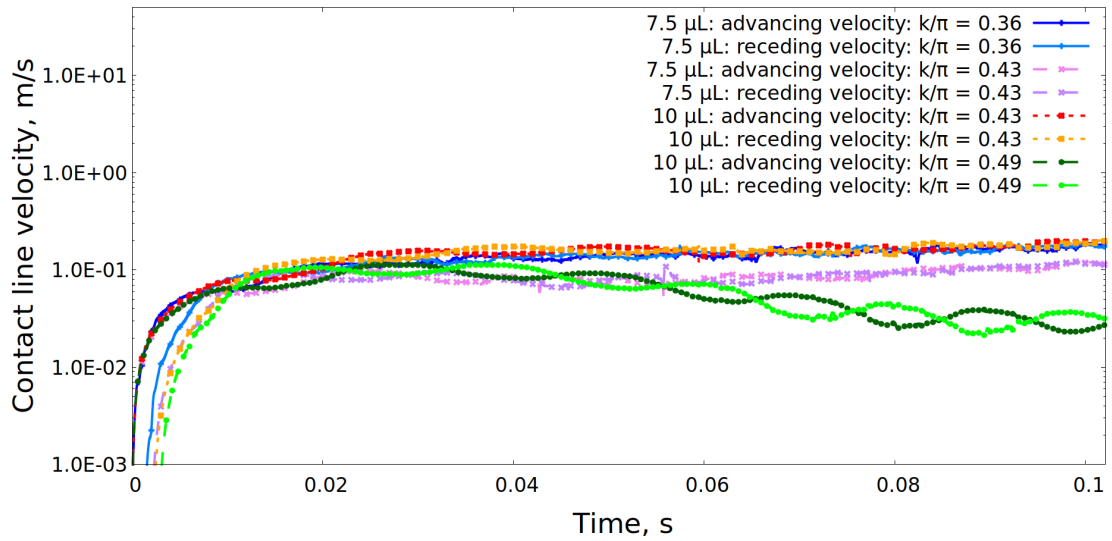


Figure 3.6: Cases #3 and #4: water drops sliding on PTFE substrate, inclined at angle $\alpha = 60^\circ$: (a,b) steady-state profile obtained experimentally for drop volumes of $7.5 \mu\text{L}$ and $10 \mu\text{L}$, respectively [reproduced with permission from Annapragada *et al.* Int. J. Heat Mass Transf. **55**, 5-6 1466-1474 (2012). Copyright 2011 Elsevier Ltd.], (c,d) numerically obtained steady-state profiles for drop volumes of $7.5 \mu\text{L}$ and $10 \mu\text{L}$, respectively, and (e,f) velocity fields for drop volumes of $7.5 \mu\text{L}$ and $10 \mu\text{L}$, respectively.



(a)



(b)

Figure 3.7: Cases #3 and #4: water drops sliding on a PTFE substrate, inclined at angle $\alpha = 60^\circ$: (a) contact angle evolution, (b) advancing and receding velocities.

contact line at $\alpha = 70^\circ$. It is hypothesized to be due to the limitation of the 2D simulations in replicating the exact profile of the sliding drop.

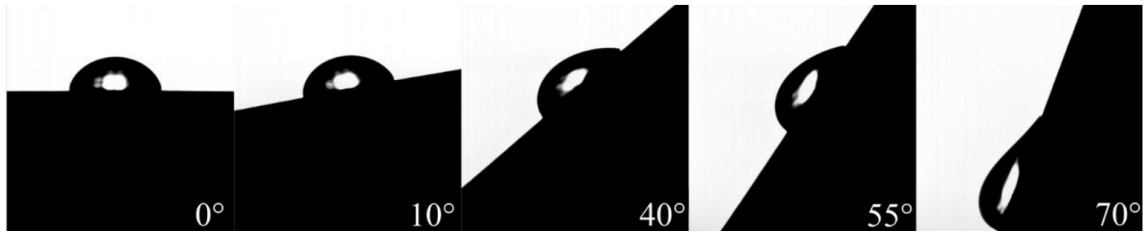
3.5.5 Case #6: viscous Newtonian drop on an omniphilic smooth glass

The sixth validation aims to reproduce the experimental steady-state velocity obtained by Xu *et al.* [238], where a polyethylene glycol (PEG) drop slides on an omniphilic smooth glass, with contact angle $\theta_e = 34^\circ$. The volume of the drop is $100 \mu\text{L}$, yielding an initial wetting radius of $a = 5.5 \text{ mm}$. The drop slides at an inclination angle of $\alpha = 27^\circ$. The steady-state velocity was experimentally found to be $7.75 \times 10^{-4} \text{ m s}^{-1}$. Due to the high viscosity of the liquid, as shown in Table 3.1, high deformation is expected in this case. Hence, the value of k is set to 2.0 [238].

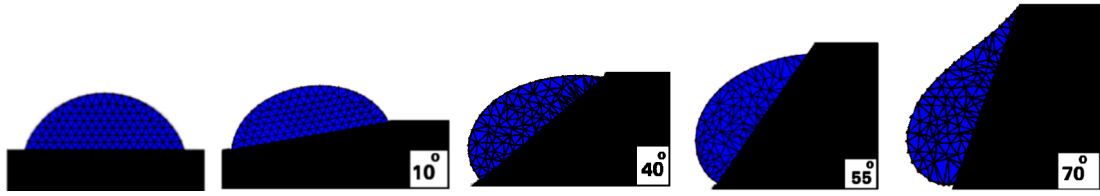
The simulation is performed using the physical properties for case #6 in Table 3.1. Adaptive mesh size is used with an initial grid size $h = 5 \times 10^{-4} \text{ m}$, and refined to $h = 2.5 \times 10^{-4} \text{ m}$ near the boundaries. The time step is set to $\Delta t = 2 \times 10^{-7} \text{ s}$.

The sliding angle evolution is shown in Figs. 3.9 and 3.10. The values of angles θ_A and θ_R are found experimentally to be 58° and 12° [238], respectively. Large wetting radius and contact angle hysteresis lead to high adhesion and retention forces along the contact line [238, 243]. Fig. 3.9(c) shows the drop's velocity field. The work done by the retention and dissipative force at solid-liquid interface opposes gravitational forces and, thus, reduces the velocity field near the contact line. Thanks to the high liquid viscosity and the omniphilicity of the substrate, the drop elongates and leaves a thin film on the substrate as it slides, as shown in Fig. 3.9(b) and 3.10(a). This qualitative behavior is in agreement with experimental observations of sliding viscous drops on omniphilic surfaces [238]. Figure 3.10(a) shows a jump in the sliding receding angle at $t = 0.04 \text{ s}$. It is caused by the addition of mesh nodes, which is a feature of the PFEM [55], to account for the large elongation at the receding edge.

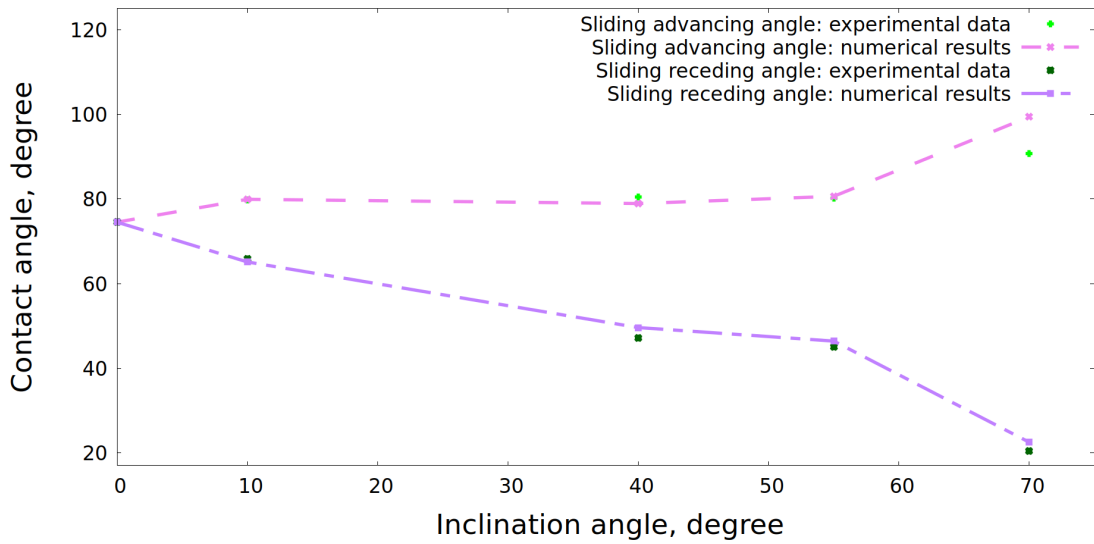
The numerical value of the steady-state velocity, which corresponds to the velocity of the sliding advancing edge, is found to be $8.7 \times 10^{-4} \text{ m s}^{-1}$. As shown in Table 3.3, the difference between the experimental and numerical results is 12.3%. The initial numerical



(a)



(b)



(c)

Figure 3.8: Case #5: a 30 μL water drop sliding on a rotating PMMA substrate: (a) sliding profile (experimentally)[reproduced with permission from Maurer *et al.* Proceedings of the 3rd Int. Conf. on FFHMT'16, 134 (2016). Copyright 2020, International ASET Inc.], (b) numerically obtained drop profile, and (c) comparison of the advancing and receding contact angle evolutions.

instability observed in the time interval $0 < t < 0.005$ s is thought to be due to high viscous dissipation during the simultaneous spreading and sliding of the drop.

A parametric study for two additional values of the shape factor $k = 1.5$ and $k = 2.5$ is presented in Table 3.4. Similar to cases # 1 and #2, Fig. 3.10(a) shows that the difference in the sliding advancing and receding angles obtained numerically are similar for the three chosen values of k , which is likely due to the high fluid viscosity. Moreover, the steady-state velocity decreases as the parameter k increases. However, larger k value leads to a non-physical negative velocity in the time interval $0.005 < t < 0.02$, as shown in Fig. 3.10(b). The velocity then increases as the drop stretches, until it reaches the steady-state velocity.

3.6 Rolling viscous drops

The lower the work of adhesion between the liquid-solid interface the higher the tendency for a drop to roll [10, 192]. It has been demonstrated that the mode of motion of a viscous drop on a superomniphobic inclined surface is pure rolling [10, 218]. The value of the descent rolling velocity of a small viscous rolling drop is expected to be of the order of 0.01 m s^{-1} [10]. Accordingly, the capillary number is expected to exceed 0.003 and, thus, Jiang's model is no longer applicable. Moreover, no-slip along the solid-liquid interface has been observed for rolling viscous drop [10]. Hence, the Navier-slip condition, which assumes constant slip length at the solid-liquid interface, is also not applicable for the case of pure rolling. Furthermore, the retention force plays no major role [10, 140]. Instead, only the no-slip boundary condition, i.e., $\mathbf{v} \cdot \mathbf{t} = 0$, along the solid-liquid interface is adopted in this case.

In conclusion, the governing equations used for modeling rolling viscous drops are the classical continuity and momentum equations for an incompressible, viscous, Newtonian fluid expressed in eqs. 2.2.1 and 2.2.2. At the liquid-vapor interface, the Cauchy stress boundary condition corresponding to the surface tension force is applied in the normal direction of the stress (see Sec. 2.3). The no-slip boundary condition is applied along the solid-liquid interface.

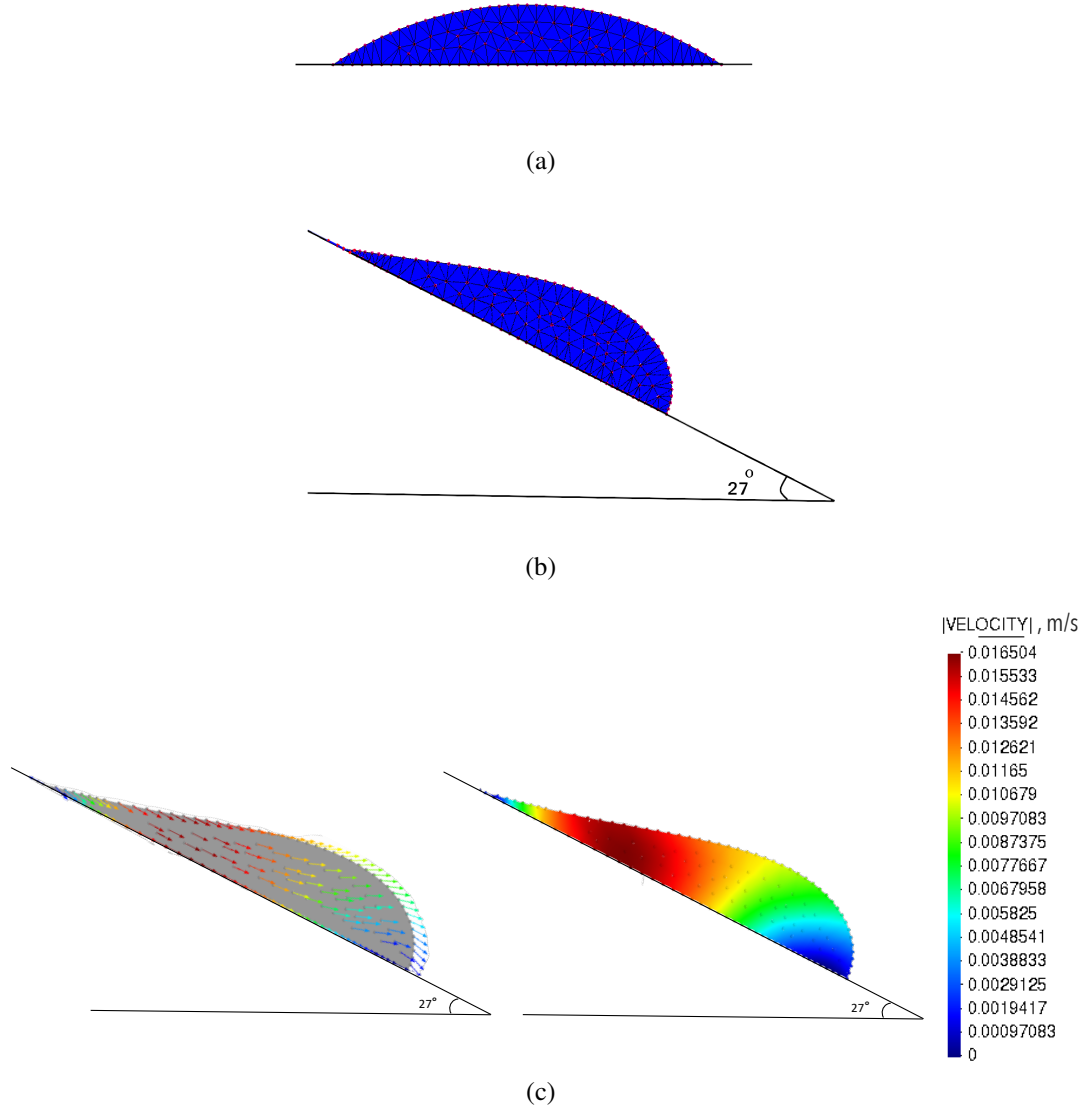
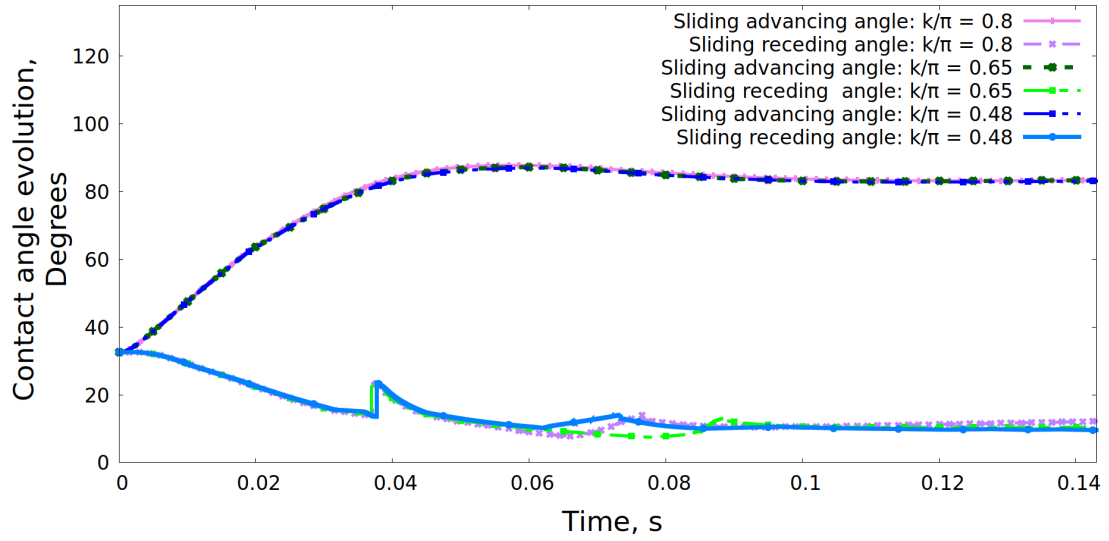
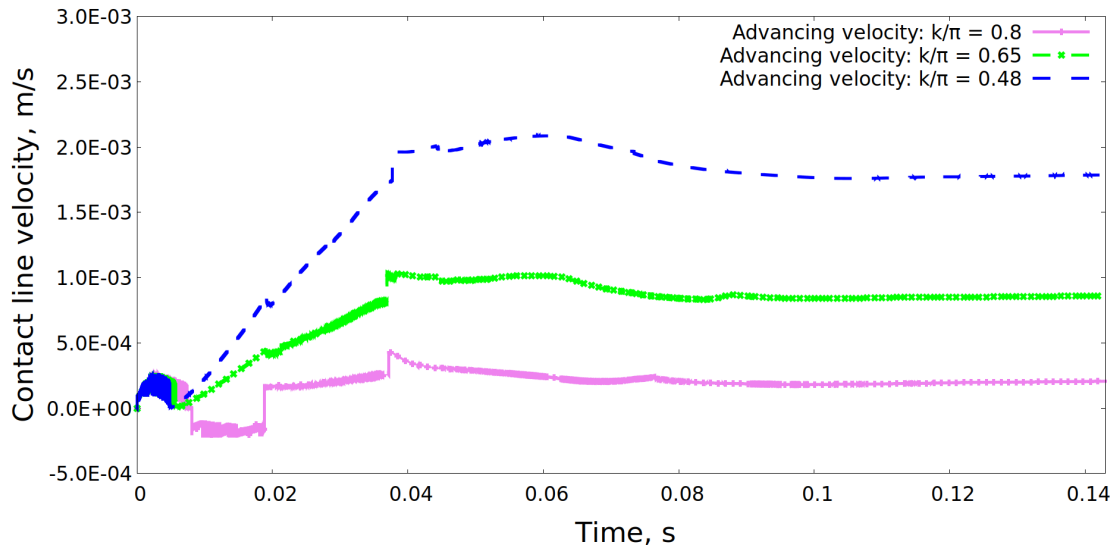


Figure 3.9: Case #6: a $100\ \mu\text{L}$ PEG sessile drop sliding on smooth glass, inclined at $\alpha = 27^\circ$: (a) initial drop profile at $\alpha = 0^\circ$ and $t = 0\ \text{s}$, (b) steady-state profile at $\alpha = 27^\circ$, (c) velocity fields.



(a)



(b)

Figure 3.10: Case #6: a 100 μL PEG sessile drop sliding on smooth glass, inclined at $\alpha = 27^\circ$: (a) contact angle evolution and (b) sliding advancing velocity evolution.

Rolling viscous glycerol drop on smooth PETG surface

In this example we validate the proposed drop rolling model using the rolling experiment performed by Abolghasemibizaki *et al.* [10]. Glycerol drop of volume $5\mu\text{L}$ is allowed to roll on smooth PETG surface until it reaches its descent steady-state velocity. Two inclination angles are considered, $\alpha = 15^\circ$ and $\alpha = 20^\circ$. The steady-state velocities for $\alpha = 15^\circ$ and $\alpha = 20^\circ$ are found experimentally to be 0.033 m s^{-1} and 0.044 m s^{-1} , respectively.

Two simulations are performed using the physical properties of glycerol on PETG substrate: $\rho = 1261 \text{ kg m}^{-3}$, $\mu = 1.076 \text{ kg m}^{-1} \text{ s}^{-1}$, $\gamma = 0.0646 \text{ N m}^{-1}$, and $\theta_e = 169.1^\circ$. The mesh size used for these simulations is chosen as $h = 1.1 \times 10^{-4} \text{ m}$. This problem is a surface tension dominant problem, i.e., both the capillary and the Bond numbers ($Bo = \frac{\rho g H^2}{\gamma}$, where H is the height of the drop [253]) are smaller than unity [112].

Thus, the time step criteria presented by Sussman and Ohta [213] is adopted as follows:

$$\Delta t_{crit} \leq \sqrt{\frac{(\rho_L + \rho_g)h^3}{\gamma(2\pi)^3}} \quad (3.6.1)$$

From eq. 3.6.1, we choose $\Delta t = 1 \times 10^{-6} \text{ s}$. The average computational time for the drop to reach its steady-state velocity was 30 minutes.

The numerical results of the rolling drops are shown in Fig. 3.11. The descent steady-state velocities are found to be 0.0278 m s^{-1} and 0.0354 m s^{-1} for the $\alpha = 15^\circ$ and $\alpha = 20^\circ$, respectively. The difference between the experimental and numerical results are 15% and 19.5% for $\alpha = 15^\circ$ and $\alpha = 20^\circ$, respectively. Fig. 3.12 shows the velocity vectors for a rolling viscous drop at $\alpha = 15^\circ$, which is different than the those for sliding liquid drops previously shown in Figs. 3.2(d), 3.2(e), 3.6(e), 3.6(f), and 3.9(c).

3.7 Conclusion

We extended our PFEM-based model for liquid drop spreading, presented in chapter 2, to drop sliding under the effect of gravity, by including a retention force associated with the aspect ratio of the drop footprint, surface tension force, and contact angle hysteresis.

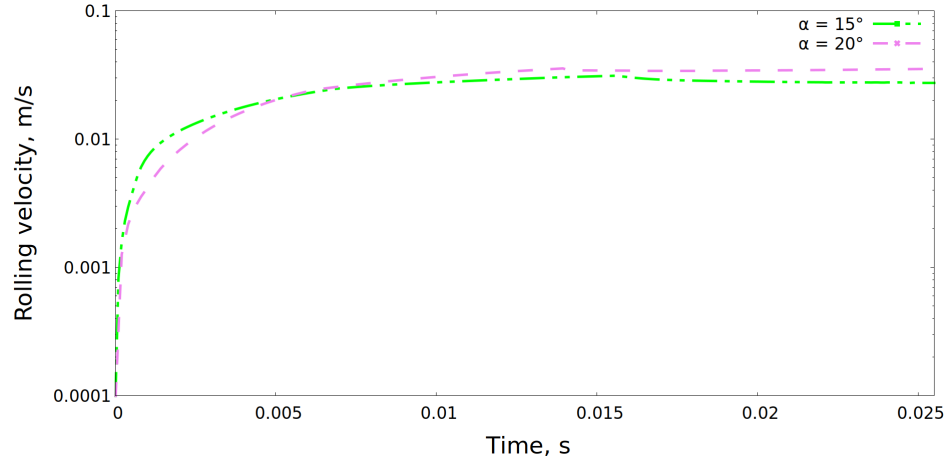


Figure 3.11: Descent rolling velocities for a $5 \mu\text{L}$ glycerol drop rolling on smooth PETG surface at $\alpha = 15^\circ$ and 20° .

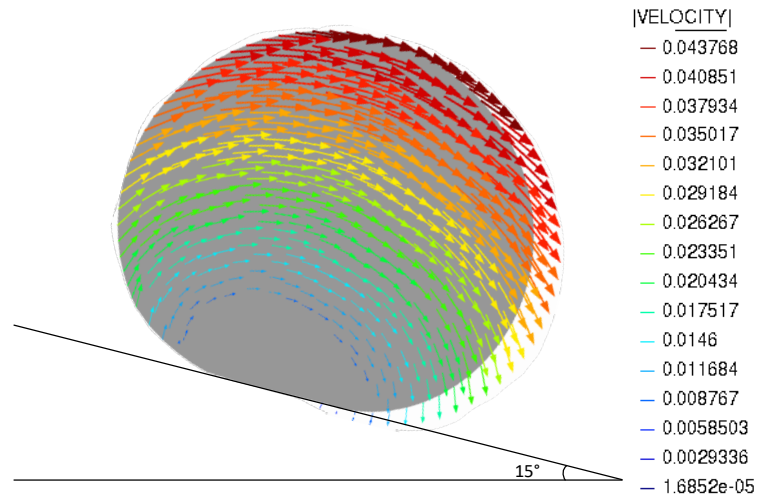


Figure 3.12: Velocity vector for a $5 \mu\text{L}$ rolling glycerol drop on smooth PETG surface at $\alpha = 15^\circ$.

For 2D sliding simulations and with an adequate choice of the shape factor k , the model has been validated by using published experimental results, under a variety of physicochemical conditions. These simulations demonstrate that the value of the shape factor k is one of the key factors to obtain predictive and realistic results. For the most common liquids and on a variety of substrates, such as water and ethylene glycol drops on polymer substrates, the value of k is well documented and can be obtained using published experimental data.

The steady-state velocity was found to be inversely proportional to k , and the closeness between the experimental and numerical results was directly related to the chosen value of this parameter. The temporal evolution of the contact line was found to be in good agreement with the experiments, and the model produced mesh-independent results. The drop profiles were validated as well. Moreover, interesting phenomenon associated with drop sliding can be captured qualitatively using 2D simulation, such as was obtained in the temporal free-surface evolution of a highly viscous drop.

By altering the boundary conditions at the solid-liquid interface, i.e. ignoring the effect of retention and dissipative forces at the contact area, we proposed a simplified two-dimensional numerical model for rolling viscous drops. The results of the model were found to be in very good agreement with the experiments. However, the proposed scheme cannot be used to study the transition from sliding to rolling motion. It is hypothesized that rolling motion could be analyzed by modifying the boundary conditions at the liquid-solid interface.

The proposed 2D drop model produces numerical results comparable to experimental observations with significantly less computational cost than would be required in a 3D model. The proposed model is also applicable to embedded two-phase flow simulations [186], had the driving gravitational force been replaced by an external flow field. However, 2D simulations are inherently flawed as they cannot replicate the full shape of a sliding drop nor its exact footprint profile. Nonetheless, our results are encouraging for further development toward full 3D simulation, which we will present in chapter 4.

Chapter 4

DROP DYNAMICS IN 3D

4.1 Introduction

Most drop dynamics models found in the published literature are simplified. They are based on either quasi-static or axisymmetric conditions. In reality, however, drops experience large asymmetric deformations under the effect of gravity and/or external shear flow [113, 162, 207]. These simplifications are not acceptable for modeling situations of i) liquid drop injection, ii) liquid drop sliding, and iii) two-phase embedded flow, which are of interest in this work. Accordingly, simulation in a 3D Cartesian coordinate system can provide a more realistic spatio-temporal evolution than other coordinate systems.

Concerning the spatio-temporal evolution of a spreading drop, our proposed 2D Cartesian-based Lagrangian formulation does not adequately produce axisymmetric drop profiles [141, 142]. Likewise, the 2D model could not replicate the full shape of a sliding drop nor its exact profile, as shown in chapter 3. The temporal evolution was successfully predicted by these 2D models by normalizing geometric parameters, such the mean curvature, the contact line perimeter, and the solid-liquid interfacial area. Moreover, the retention force acting along the contact line was scaled by a factor of π (Sec. 3.2.2.1). This chapter is an extension of our 2D drop dynamics model presented in chapters 2 and 3 to 3D. In addition to the geometric characteristic of the drop, we are interested in predicting the evolution of both its spreading rate and its dynamic contact angle. Similarly, we wish to predict the steady-state sliding velocity of a sliding drop.

This chapter is organized as follows: Sec 4.2 describes the mathematical model governing drop spreading, focusing on numerical treatment of geometric quantities, such as the mean curvature of the free liquid-vapor interface, the perimeter of the solid-liquid-vapor interface, and the wetting area of the solid-liquid interface. Similarly, Sec. 4.3 introduces the

3D sliding model under the effect of gravity. Our 3D model is validated using published experimental results under a wide variety of fluid properties, drop sizes, and physicochemical conditions.

4.2 3D model for drop spreading dynamics

The 2D numerical drop spreading model presented in chapter 2 is re-introduced and extended to 3D, for which the essential differences come from treating the geometry. The following section introduces the governing equations and boundary conditions of the 3D spreading model.

4.2.1 Physical model

4.2.1.1 Governing equations

Adopting the same notations of Sec. 2.2, let Ω represent a liquid drop in contact with a solid substrate, as shown in Fig. 4.1. The boundary of the domain is divided into three regions $\partial\Omega = \Gamma_I \cup \Gamma_S \cup \partial\Gamma$. Γ_S represents the domain boundary corresponding to the liquid in contact with the substrate, excluding the contact line. $\partial\Gamma$ represents the contact line. Finally, Γ_I corresponds to the drop's free-surface.

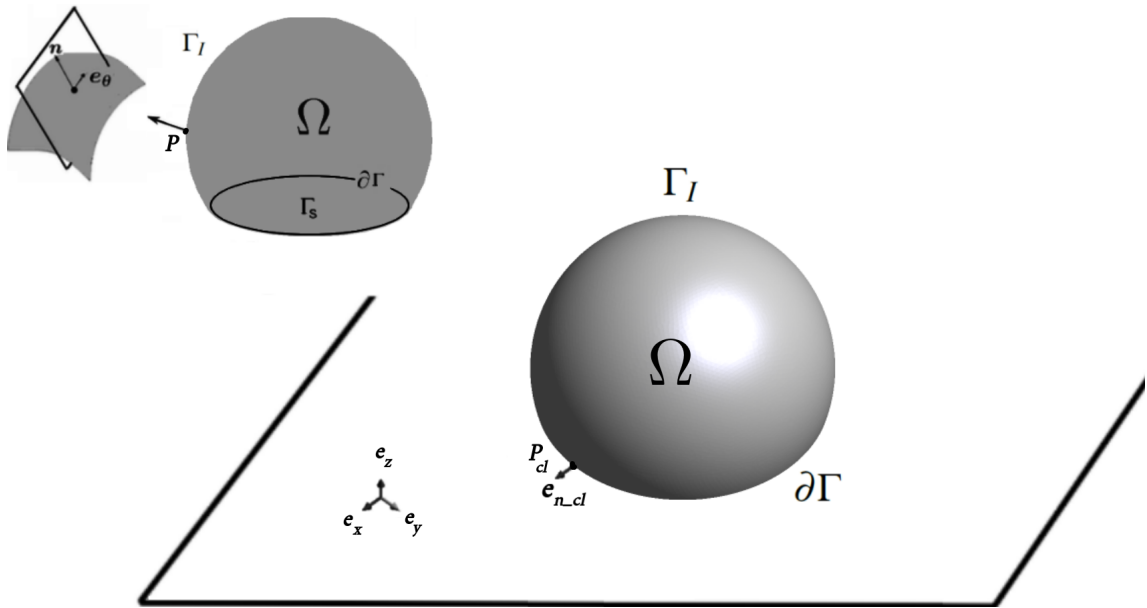


Figure 4.1: Schematic representation of the 3D Lagrangian domain.

The governing equations for the liquid phase are the momentum and mass conservation equations. The fluid is assumed to be incompressible Newtonian. Accordingly, the governing equations are expressed as follows [113, 114]:

$$\rho \frac{D\mathbf{v}}{Dt} - \mu \nabla \cdot (\nabla \mathbf{v} + \nabla^T(\mathbf{v})) + \nabla p = \rho \mathbf{g} \quad \text{on } \Omega \quad (4.2.1)$$

$$\nabla \cdot \mathbf{v} = 0 \quad \text{on } \Omega \quad (4.2.2)$$

where ρ is the fluid density, $\frac{D\mathbf{v}}{Dt} = \frac{\partial \mathbf{v}}{\partial t} + \mathbf{v} \cdot \nabla \mathbf{v}$ is the total material derivative, \mathbf{v} is velocity, t is time, μ is the fluid dynamic viscosity, p is pressure, and \mathbf{g} is the gravitational acceleration. The Lagrangian reference frame is adopted and, thus, the nonlinear convective term is absent in the numerical treatment of eq. 4.2.1 [184].

4.2.1.2 Boundary conditions at the free-surface Γ_I

At the free-surface, Γ_I , a Cauchy stress boundary condition in the normal direction of the stress is applied corresponding to the surface tension force:

$$\mathbf{f}_{\Gamma_I} = \boldsymbol{\sigma} \cdot \mathbf{n} = \gamma \kappa_H \mathbf{n} \quad \text{at } \Gamma_I \quad (4.2.3)$$

where \mathbf{f}_{Γ_I} is the surface tension force, $\boldsymbol{\sigma}$ is the Cauchy stress tensor, \mathbf{n} is the outer unit normal to Γ_I (see Fig. 4.1), γ is the surface tension coefficient, and κ_H is the mean curvature of the free-surface (see Sec. 4.2.1.3). The Cauchy stress tensor $\boldsymbol{\sigma}$ is expressed as:

$$\boldsymbol{\sigma} = -p\mathbb{I} + \mu(\nabla \mathbf{v} + \nabla^T \mathbf{v}) \quad (4.2.4)$$

According to eq. (4.2.3), the normal stress is balanced by the surface tension force [113, 186, 187]. Decomposing eq. 4.2.3 into normal and tangential components yields:

$$\mathbf{n} \cdot (\boldsymbol{\sigma} \mathbf{n}) = \gamma \kappa_H \quad \text{at } \Gamma_I \quad (4.2.5)$$

and

$$\mathbf{e}_\theta \cdot (\boldsymbol{\sigma} \mathbf{n}) = 0 \quad \text{at } \Gamma_I \quad (4.2.6)$$

where \mathbf{e}_θ represents any unit vector tangent to surface Γ_I (Fig. 4.2). Assuming a stationary exterior fluid and substituting eq. 4.2.4 into eq. 4.2.5 yields:

$$p - \mu \mathbf{n} \cdot ([\nabla \mathbf{v} + \nabla^T \mathbf{v}] \cdot \mathbf{n}) = \gamma \kappa_H \quad \text{at } \Gamma_I \quad (4.2.7)$$

4.2.1.3 Curvature in 3D

For surface tension-dominated problems, the driving force depends on the mean curvature of the liquid-vapor interface. Thus, an accurate interface representation is required at each time step. Indeed, drop dynamics models are successful insofar as they accurately track the drop boundaries [14].

In this work, we utilize the 3D PFEM curvature model developed by Jarauta *et al.* [112, 114] for a liquid drop, and extend it to account for both spreading and sliding. The curvature in 3D [112, 114] is approximated using Meyer's method [152] since it is found to be the most accurate approach, based on Tasso et al. analyses [217].

Let S denote a surface in \mathbb{R}^3 . The surface is approximated locally at any point P of S by its tangent plane. The tangent plane is defined by the knowledge of point P and its normal vector \mathbf{n} . Let $\kappa^N(\theta)$ be the normal curvature for any unit tangent vector \mathbf{e}_θ , defined as the curvature of a particular curve (passing through P) that is inscribed in S and is contained into the plane spanned by both \mathbf{e}_θ and \mathbf{n} [152], as shown in Fig. (4.2.a). The mean curvature can then be defined as the average of normal curvatures as follows:

$$\kappa_H = \frac{1}{2\pi} \int_0^{2\pi} \kappa^N(\theta) d\theta \quad (4.2.8)$$

The mean curvature is related to the face area minimization according to:

$$2\kappa_H \mathbf{n} = \mathbf{K} = \lim_{D(dA) \rightarrow 0} \frac{\nabla dA}{dA} \quad (4.2.9)$$

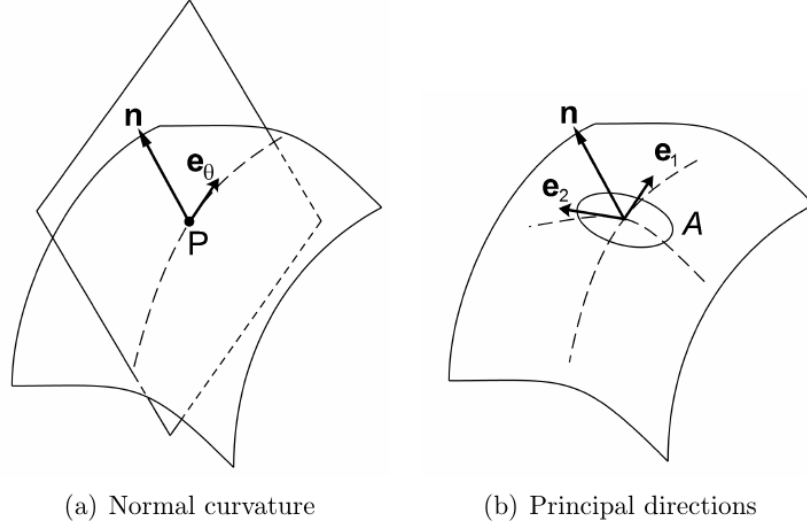


Figure 4.2: (a) Normal curvature, and (b) principal directions in 3D [112].

where, dA is the infinitesimal area at point P , $D(dA)$ is the diameter of the infinitesimal area dA , ∇dA is the gradient of dA , and \mathbf{K} is the mean curvature normal operator at point P [114].

According to the “one-ring neighborhood”, shown in Figure (4.3), let us define x_i as a vertex node of the surface mesh shown in Figure (4.3). Let us find the area around each x_i by defining the local area of each triangle, and then connect its circumcenter to the midpoints of

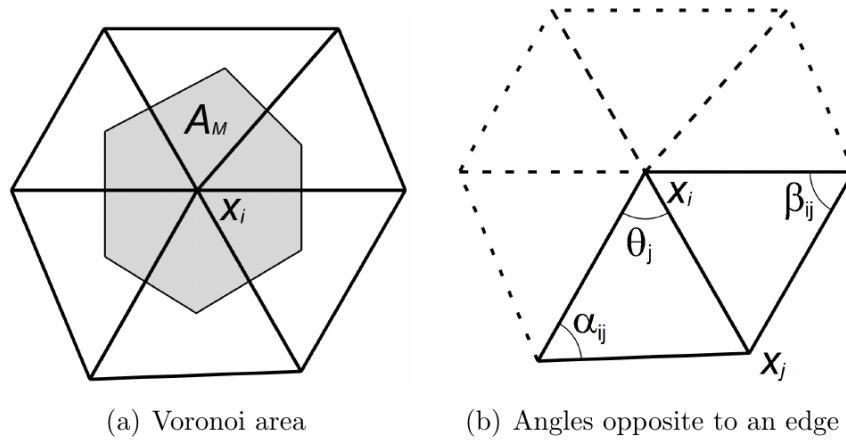


Figure 4.3: (a) The shaded area representing the “one-ring neighborhood” of x_i node, (b) angles located opposite to an edge. Figures are reproduced from [112].

each edge of its adjacent triangles, as shown in Figure (4.3.a). The generated area is known as “local Voronoi area”, A_{Voronoi} . The triangle could be either non-obtuse or obtuse. If the angle at node x_i is obtuse, A_{Voronoi} is computed as $\frac{A_T}{2}$. If one of the other two angles (for the same triangle, and which opposite to the angle at x_i) is obtuse, A_{Voronoi} is computed as $\frac{A_T}{4}$. For each of these cases, the area will be denoted by A_M . After finding A_M for each of the vertex node x_i , the normal operator of the mean curvature, $\mathbf{K}(x_i)$, is computed as follows:

$$\mathbf{K}(x_i) = \frac{1}{2A_M} \sum_{j \in N_1(i)} (\cot \alpha_{ij} + \cot \beta_{ij})(x_i - x_j) \quad (4.2.10)$$

In case of a non-obtuse triangle, the local Voronoi area, A_{Voronoi} will be given by:

$$A_{\text{Voronoi}} = \frac{1}{8} \sum_{j \in N_1(i)} (\cot \alpha_{ij} + \cot \beta_{ij}) \|x_i - x_j\|^2 \quad (4.2.11)$$

where, A_T is the total area of the triangle, α_{ij} and β_{ij} are the angles opposites to the edge $\overline{x_i x_j}$ as shown in Figure (4.3.b), and $N_1(i)$ is the one-ring neighborhood of x_i . It follows that:

$$\mathbf{n} = \frac{\mathbf{K}(x_i)}{\|\mathbf{K}(x_i)\|} \quad (4.2.12)$$

and

$$\kappa_H = \frac{1}{2} \|\mathbf{K}(x_i)\| \quad (4.2.13)$$

Finally, the surface tension term in eq. 4.2.3 can be approximated numerically by combining eqs. 4.2.10, 4.2.12, and 4.2.13 above as follows:

$$\mathbf{f}_{\Gamma_I} = \gamma \kappa_H \mathbf{n} = \frac{\gamma}{2} \left(\frac{1}{2A_M} \sum_{j \in N_1(i)} (\cot \alpha_{ij} + \cot \beta_{ij})(x_i - x_j) \right) \quad (4.2.14)$$

4.2.1.4 Forces acting on the contact line, $\partial\Gamma$

At the contact line, an effective slip boundary condition is applied to account for i) the capillary effect (ζ), ii) normal stress coefficient (β_n), and iii) Navier-slip coefficient (β_s). This effective slip boundary condition is proportional to the velocity of the contact line [37, 178, 226, 227] as follows:

$$\mathbf{f}_{\partial\Gamma} = -\beta_{\partial\Gamma}\mathbf{v} \quad \text{at } \partial\Gamma \quad (4.2.15)$$

where $\mathbf{f}_{\partial\Gamma}$ is the dissipative force applied at the contact line, $\beta_{\partial\Gamma}$ is the effective slip coefficient at the contact line, and \mathbf{v} is the slip velocity of the fluid at the contact line.

At the solid-liquid interface, including the contact line, the direction normal to the solid-liquid interface is represented by \mathbf{e}_z , whereas the tangential directions are represented by \mathbf{e}_x and \mathbf{e}_y (see Fig. 4.1). As the drop starts to spread, the velocity of the contact line can be related to the Young's stress acting on it as follows:

$$\mathbf{v} \cdot \mathbf{e}_{n_{cl}} \propto \gamma(\cos \theta_e - \cos \theta_d) \quad (4.2.16)$$

where \mathbf{v} is the velocity vector at the contact line, θ_d is the dynamic contact angle, and $\mathbf{e}_{n_{cl}}$ is the unit normal vector at the point P at the contact line (P_{cl}), see Fig. 4.1. The proportionality coefficient between the contact line velocity and Young's stress is the effective slip boundary condition defined as follows [178]:

$$\beta_{\partial\Gamma}(\mathbf{v} \cdot \mathbf{e}_{n_{cl}}) = \gamma(\cos \theta_e - \cos \theta_d) \quad (4.2.17)$$

where $\beta_{\partial\Gamma}$ is the effective slip coefficient, and is defined as [12, 22, 30, 37, 143, 178, 226, 227, 245]:

$$\beta_{\partial\Gamma} = \zeta + \beta_s|_{\partial\Gamma} + \beta_n \quad (4.2.18)$$

where ζ is the capillary effect coefficient, $\beta_s|_{\partial\Gamma}$ is the Navier-slip coefficient, and β_n is the normal stress coefficient. They are expressed as follows (see chapter 2 for details):

$$\zeta = \frac{\gamma}{\mathbf{v} \cdot \mathbf{e}_{n_{cl}}} (\cos \theta_e + 1) \tanh \left(4.96 Ca^{0.702} \right) \quad (4.2.19)$$

$$\beta_S|_{\partial\Gamma} = \frac{1}{\mathbf{v} \cdot \mathbf{e}_{n_{cl}}} \mu \nabla (\mathbf{v} \cdot \mathbf{e}_{n_{cl}}) \cdot \mathbf{e}_z \quad (4.2.20)$$

$$\beta_n = \frac{1}{\mathbf{v} \cdot \mathbf{e}_{n_{cl}}} \mu \nabla (\mathbf{v} \cdot \mathbf{e}_{n_{cl}}) \cdot \mathbf{e}_{n_{cl}} \quad (4.2.21)$$

After considering the contributions of the capillary effects, the Navier-slip as well as the normal stresses in eq. (4.3.2), the coefficient $\beta_{\partial\Gamma}$ is used to obtain the total dissipative force and to apply the boundary condition defined by eq. (4.2.15).

4.2.1.5 Forces acting on the solid-liquid interface away from the contact line, Γ_S

At the solid-liquid interface excluding the contact line, Γ_S , the applied boundary condition is obtained by projecting the Cauchy stress tensor on the normal direction of Γ_S [37, 178]:

$$\mathbf{f}_{\Gamma_S} = \boldsymbol{\sigma} \cdot \mathbf{e}_z = -\beta_{\Gamma_S} \mathbf{v} \quad \text{at } \Gamma_S \quad (4.2.22)$$

where \mathbf{f}_{Γ_S} and β_{Γ_S} are the dissipative force and the slip coefficient applied at the solid-liquid interface, respectively, and \mathbf{v} is the slip velocity of the fluid on the solid-liquid interface. The Navier-slip model is considered in this work, as it corresponds to the viscous dissipation along the solid-liquid interface as the drop deforms [12, 178, 226, 227]. Therefore, the slip coefficient β_{Γ_S} at the solid-liquid interface Γ_S is obtained as follows:

$$\beta_{\Gamma_s} = \beta_s = \frac{1}{\mathbf{v} \cdot \mathbf{e}_{n_{cl}}} \mu \nabla (\mathbf{v} \cdot \mathbf{e}_{n_{cl}}) \cdot \mathbf{e}_z \quad (4.2.23)$$

Eq. (4.2.23) is used in combination with eq. (4.2.22) to apply the boundary condition at the solid-liquid interface.

4.2.2 Mesh size and time step criteria

As the drop spreads, capillary waves are generated at the contact line and move from $\partial\Gamma$ towards Γ_I [46, 123]. Numerically, the mesh size at the contact line is restricted by the wavelength of the capillary wave propagation. The values of the mesh size (h) and the time step Δt are estimated as illustrated in Sec. 2.7. For the sake of clarity, we re-introduce those criteria as follows:

$$h = \frac{\gamma}{2\rho v_{max}^2} \quad (4.2.24)$$

and,

$$\Delta t_{cap} \leq \sqrt{\frac{2}{\pi}} \frac{\gamma}{4\rho |v_{max}^3|} \quad (4.2.25)$$

where v is the magnitude of the slip velocity of the fluid on the solid-liquid interface, i.e. $v = \|\mathbf{v}\|$.

4.2.3 Discretized governing equations

The Particle Finite Element Method (PFEM) [108, 147, 148, 163, 164, 184] is used in the present work to discretize eqs. (4.2.1) and (4.2.2) in space. The PFEM adopts the updated Lagrangian description of the governing equations. The fluid domain is discretized by a standard finite element mesh. The nodes can be interpreted as immaterial particles that move according to their velocity. At each solution step, the domain deforms. Thus, in order to avoid excessive mesh degradation, re-meshing is performed at each time step using Delaunay triangulation. For droplet dynamics problems, the re-meshing procedure ensures

that the domain boundaries are reconstructed in accordance with the velocity field. Linear interpolation functions for both velocity and pressure are used over tetrahedral elements. In the present implementation, the discretization in time is performed using the Newmark-Bossak scheme. However, for the sake of clarity, it is expressed here using the Backward-Euler scheme [184]. Given a known $\bar{\mathbf{v}}_n$ and \bar{p}_n at time t_n , the values of these variables at time t_{n+1} are obtained by solving the following system of equations:

$$\mathbf{M} \frac{\bar{\mathbf{v}}_{n+1} - \bar{\mathbf{v}}_n}{\Delta t} + \mu \mathbf{L} \bar{\mathbf{v}}_{n+1} + \mathbf{G} \bar{p}_{n+1} = \bar{\mathbf{F}} + \bar{\mathbf{F}}_{st} + \bar{\mathbf{F}}_{\partial\Gamma} + \bar{\mathbf{F}}_{\Gamma_S} \quad (4.2.26)$$

$$\mathbf{D} \bar{\mathbf{v}}_{n+1} = 0 \quad (4.2.27)$$

where Δt is the time step; \mathbf{M} , \mathbf{L} , \mathbf{G} , and \mathbf{D} are the mass, Laplacian, gradient, and divergence matrices, respectively; and $\bar{\mathbf{F}}$, $\bar{\mathbf{F}}_{st}$, $\bar{\mathbf{F}}_{\partial\Gamma}$, and $\bar{\mathbf{F}}_{\Gamma_S}$ are the vectors of the external forces, the surface tension force, the dissipative force acting on the contact line, and the dissipative force acting on the solid-liquid interface away from the contact line, respectively. Local cell matrices and vectors are defined in Appendix F.

The nonlinear dependence on the unknown configuration, \mathbf{X}_{n+1} , is dealt with by using a Newton method. The governing equations are first written in their residual form:

$$\bar{\mathbf{r}}_m = \bar{\mathbf{F}} + \bar{\mathbf{F}}_{st} + \bar{\mathbf{F}}_{\partial\Gamma} + \bar{\mathbf{F}}_{\Gamma_S} - \left(\mathbf{M} \frac{\bar{\mathbf{v}}_{n+1} - \bar{\mathbf{v}}_n}{\Delta t} + \mu \mathbf{L} \bar{\mathbf{v}}_{n+1} + \mathbf{G} \bar{p}_{n+1} \right) \quad (4.2.28)$$

$$\bar{\mathbf{r}}_c = \mathbf{D} \bar{\mathbf{v}}_{n+1} \quad (4.2.29)$$

Eqs. (4.2.28) and (4.2.29) are then linearized, and the system is solved iteratively. The resulting linearized system of governing equations reads:

$$\begin{pmatrix} \mathbf{M} \frac{1}{\Delta t} + \mu \mathbf{L} + \mathbf{H}_{st} & \mathbf{G} \\ \mathbf{D} & 0 \end{pmatrix} \begin{pmatrix} \delta \bar{\mathbf{v}} \\ \delta \bar{p} \end{pmatrix} = \begin{pmatrix} \bar{\mathbf{r}}_m \\ \bar{\mathbf{r}}_c \end{pmatrix} \quad (4.2.30)$$

where \mathbf{H}_{st} originates from the linearization of the surface tension force term, $\bar{\mathbf{F}}_{st}$. This term

is responsible for the implicit treatment of the surface tension, and it allows for using large time steps. The derivation of this term, as well as the stabilization terms, can be found in reference [114]. The linear velocity-pressure elements used in our model do not fulfill the compatibility condition [66] and therefore pressure must be stabilized. In this work, the algebraic sub-grid scales (ASGS) [52, 53, 157] stabilization technique is implemented (see reference [114] for details). Once the system in eq. (4.2.30) has been solved for $\delta \bar{v}$ and $\delta \bar{p}$, the primary variables are updated according to $\bar{v}_{n+1}^{k+1} = \bar{v}_{n+1}^k + \delta \bar{v}$ and $\bar{p}_{n+1}^{k+1} = \bar{p}_{n+1}^k + \delta \bar{p}$, where k is the nonlinear iteration index, until convergence is achieved. As a final step, the nodal position in the moving mesh is updated according to the employed time integration scheme. In case of Backward Euler integration, this yields $X_{n+1}^{k+1} = X_n + \Delta t \bar{v}_{n+1}^{k+1}$. The solution algorithm is further illustrated in Appendix G.

4.2.4 Numerical examples

The effects of adding a dissipative force on a moving contact line are assessed in this example. The spreading motion is simulated for different initial arbitrarily shaped drops. This example demonstrates the success of our 3D drop dynamics model in i) regularizing the contact line singularity, ii) tracking the deformed boundaries, and iii) achieving the equilibrium configuration. The domain initial configuration is set to be a prismatic (nominal) drop with height $H = 0.02$ cm and two different cross-sections: (a) a square of 0.05 cm per side, and b) a triangle of 0.05 cm per side. The considered substrates are (i) kapton-coated surface with static contact angle value of 75 degrees [74] (hydrophilic), and (ii) polytetrafluoroethylene (PTFE)-coated surface with static contact angle of 108 degrees [165] (hydrophobic).

The driving forces acting on the drop are the surface tension force and gravity directed normal to the substrate. Fluid density, viscosity and surface tension coefficient are set to $\rho = 1000$ kg m⁻³, $\mu = 8.90 \times 10^{-4}$ kg m⁻¹ s⁻¹, $\gamma = 0.072$ N m⁻¹, respectively, representative of a water drop. Initial pressure in the liquid is set to $p_0 = 0$ Pa. The domain is meshed using tetrahedral elements of size 0.005 cm and a time step size of $\approx 1 \times 10^{-6}$ seconds is used. The predicted drop geometry at various times during the simulation is shown in Figure (4.5).

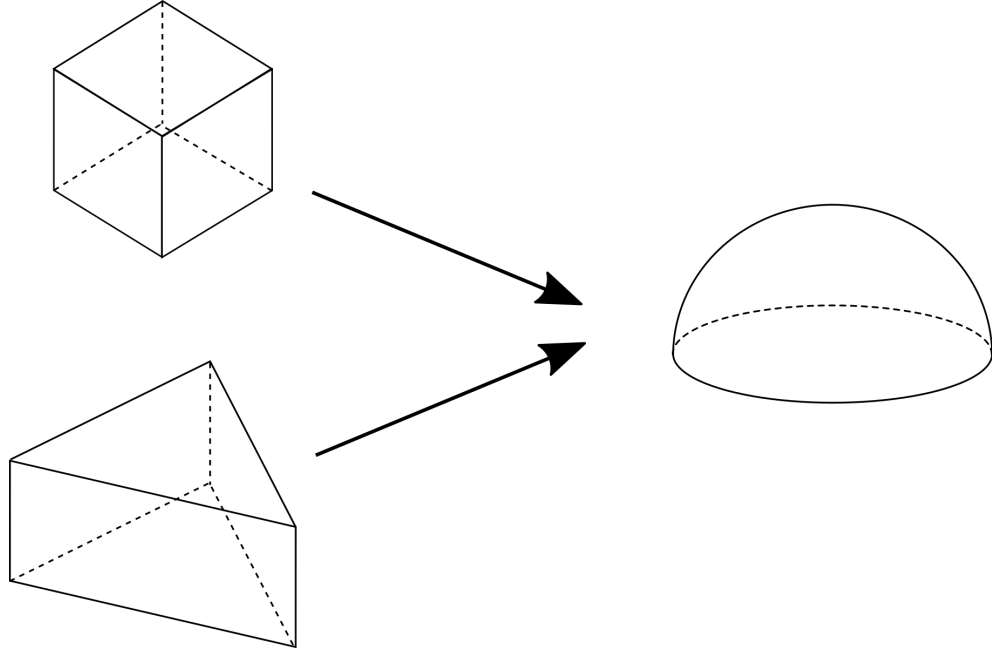


Figure 4.4: Initial and steady-state configurations for sessile drops starting with two different prismatic initial configurations.

In both configurations, the steady-state solution is achieved in less than 4 ms. Table 4.1 shows the obtained value of the contact angle for each configuration and substrate, where θ_{ave} is the node-averaged contact angle. It can be observed that in all cases, the computed relative error was less than 7% for kapton, and 3% for PTFE.

The simulated drops evolved in accordance to the proposed mathematical model and boundary conditions presented in Sec. 4.2.1, until they successfully reached their equilibrium configurations. Our numerical results ensured that the equilibrium configuration of each prism is a drop with the prescribed contact angle, regardless of the initial shape.

4.2.5 Experimental validation

This section emphasizes the limitation of the 2D model in replicating the shape of a drop by examining the equilibrium configuration of two viscous glycerol drops on a smooth polyethylene terephthalate glycol surface. We then validate the 3D drop spreading model using two experimental studies of spreading on smooth flat surfaces with differing contact

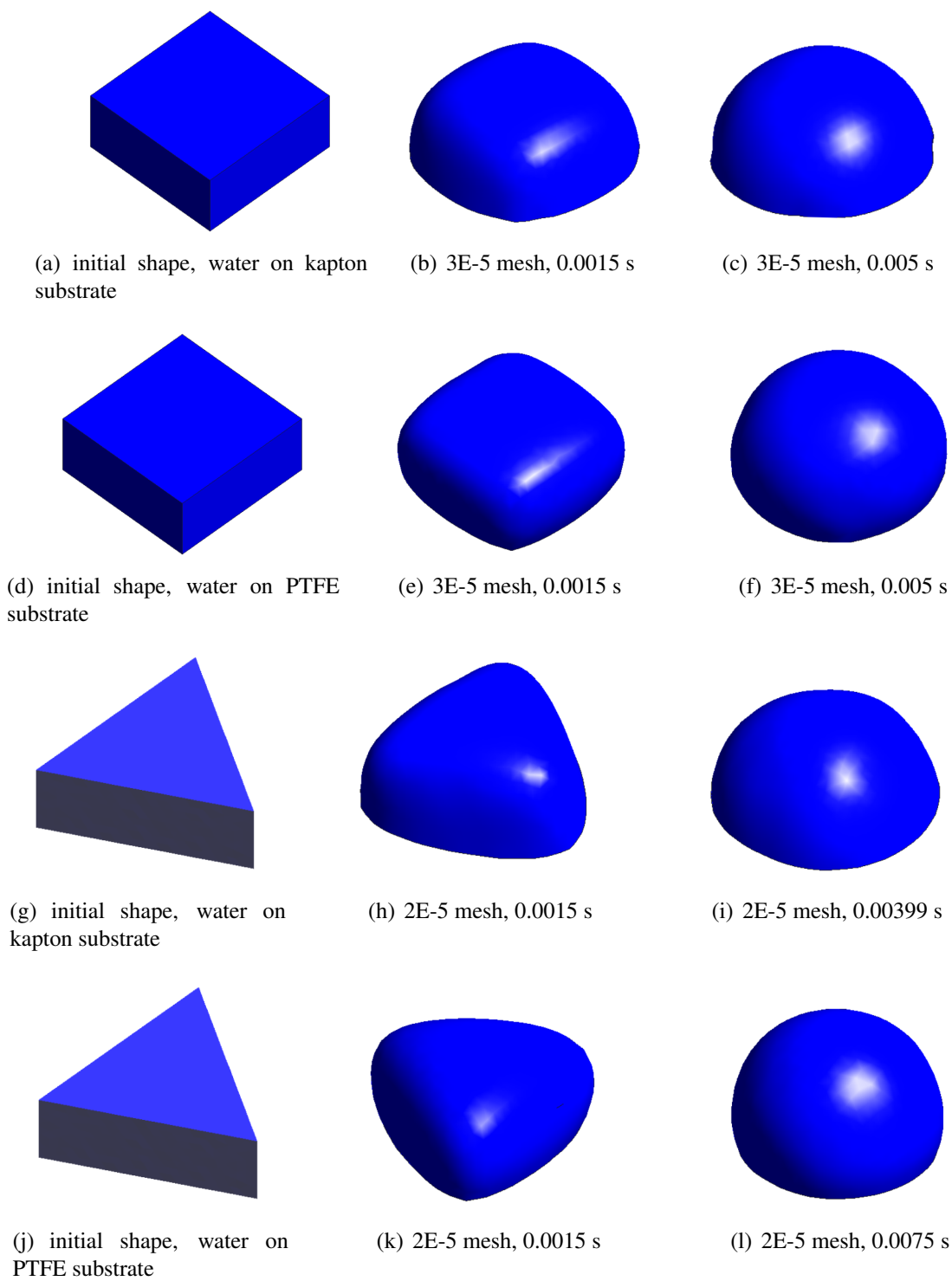


Figure 4.5: Spreading evolution for two different initial geometries.

Configuration	Substrate	θ_{ave} , (deg)	Error ($ \theta_{ave} - \theta_e $) / θ_e , (%)
Square	kapton	79.9	6.5
	PTFE	105.0	2.8
Triangle	kapton	79.3	5.7
	PTFE	104.5	3.2

Table 4.1: Contact angles values obtained numerically (θ_{ave}) for water drops on kapton and PTFE substrates, and the corresponding error with respect to the prescribed equilibrium angle θ_e .

angles. The following cases are studied:

- Cases #1 and #2: equilibrium configurations of 2.2 mm and 4.3 mm diameters viscous glycerol drops on a smooth polyethylene terephthalate glycol surface. At equilibrium, the viscous glycerol drop rests on the polyethylene terephthalate glycol substrate with equilibrium contact angle of 169.1° [10].
- Case #3: spreading of a 1.64 mm diameter water drop on a hydrophobic triethoxysilane substrate, with equilibrium contact angle of 117° [28].
- Case #4: spreading of a 1 mm diameter water drop on a hydrophilic kapton substrate, with equilibrium contact angle of 75° [74].

4.2.5.1 Cases #1 and #2: equilibrium configuration for viscous glycerol drops on smooth polyethylene terephthalate glycol surface

For each case, replicating the exact shape of the drop is the ultimate goal of the spreading simulation. In this section, the equilibrium configuration of a viscous drop is examined both in 2D and 3D. We will take advantage of the experimental work by Abolghasemibizaki *et al.* [10] for viscous glycerol drops on smooth polyethylene terephthalate glycol (PETG) surface.

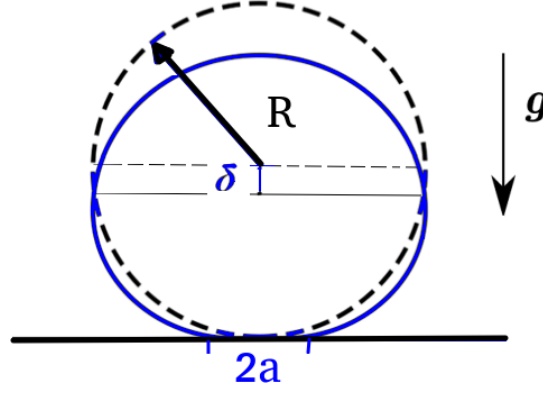


Figure 4.6: schematic representation of the initial configuration (dashed line) and the equilibrium configuration (solid line) of a viscous liquid drop [10].

Two drop sizes of 1.1 mm and 2.15 mm radii are considered. The gravitational field acts normal to the flat substrate. The drop is lowered from its center by a value of δ , forming a wetting radius of a (shown in Fig. 4.6) due to its own weight. At equilibrium, the center of mass displacement, δ , is estimated as [10]:

$$\delta \approx \rho g R^3 / \gamma \quad (4.2.31)$$

The simulations are performed using the physical properties of glycerol on PETG substrate, $\theta_e = 169.1^\circ$. Fluid density, viscosity and surface tension coefficient are set to $\rho = 1261 \text{ kg m}^{-3}$, $\mu = 1.076 \text{ kg m}^{-1} \text{ s}^{-1}$, $\gamma = 0.0646 \text{ N m}^{-1}$, respectively. The mesh sizes are chosen to be 0.00015 and 0.0003 m for the $5.6 \mu\text{L}$ and $41.6 \mu\text{L}$ drops, respectively. The capillary waves at the moving contact line are neglected compared to the dominant surface tension force. Hence, the time step is chosen based on the implicit criteria devised by Jarauta *et al.* [114] as $\Delta t \approx 5 \times 10^{-3} \text{ s}$.

Figs. 4.7 and 4.8 show the equilibrium configuration of each drop. Figure 4.8(c) shows a transparent view, indicating both the distribution and the total number of particles (~ 2808 mesh nodes) for the 2.15 mm radius drop. The mesh is refined at the contact line and, thus, crude meshing is avoided. For both cases, i.e., 1.1 mm and 2.15 mm radii drops, the drop profiles in 3D are found to be in better agreement with the experimental profiles than in

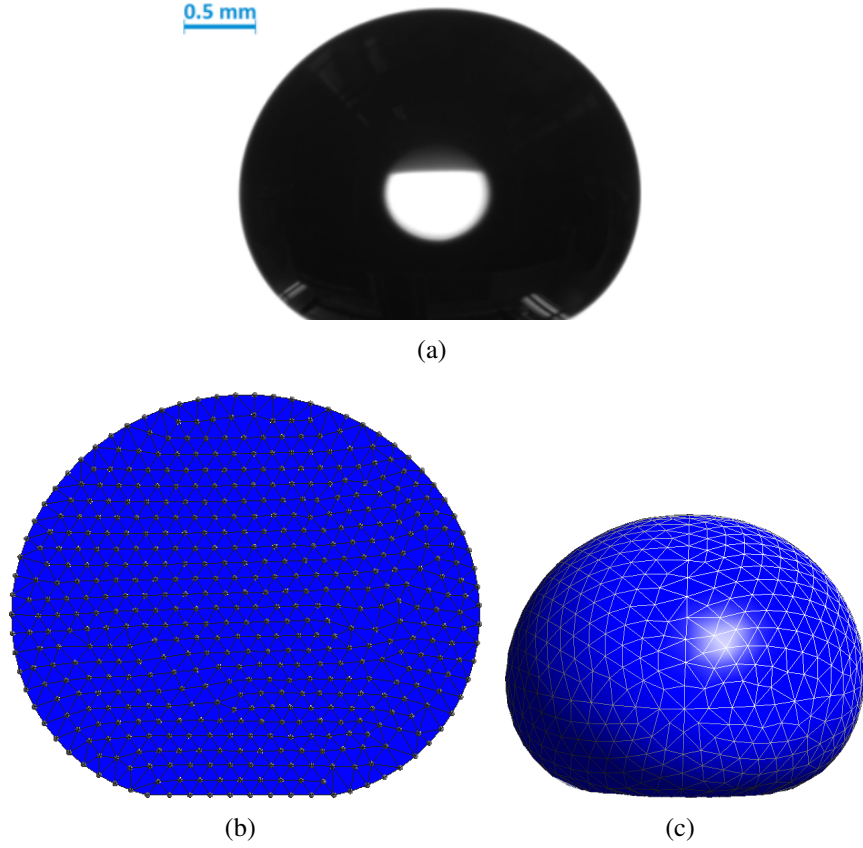


Figure 4.7: Case #1: equilibrium configuration for a glycerol drop on smooth PETG surfaces of: (a) 1.35 mm radius, experimentally [10], (b) 1.1 mm radius, numerically in 2D and (c) 1.1 mm radius, numerically in 3D.

2D. The corresponding change in δ is shown in Table 4.2 for each drop size. As indicated by eq. 4.2.31, the value of δ increases as the drop size increases. The error between numerical and experimental values of δ increases as the weight of the drop increases. The 3D model, however, provides more reliable results than the 2D model, especially for larger drops. This is hypothesized to be due to the limitation of 2D simulations in Cartesian coordinates to properly replicate the full shape of the drop.

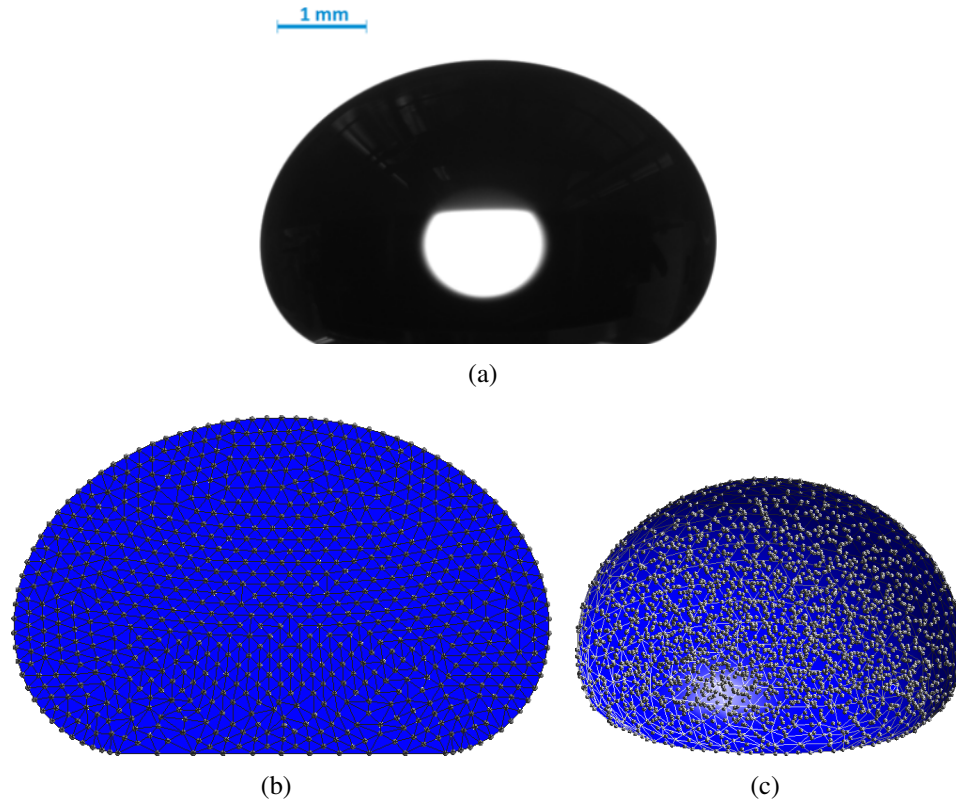


Figure 4.8: Case #2: equilibrium configuration for a glycerol drop on smooth PETG surfaces of: (a) 2.3 mm radius, experimentally [10], (b) 2.15 radius, numerically in 2D and (c) 2.15 radius, numerically in 3D.

Case #	Initial radius R , (mm)	δ , eq. (4.2.31) (mm)	δ , numerically (2D) (mm)	Difference in δ (2D), %	δ , numerically (3D) (mm)	Difference in δ (3D), %
1	1.1	0.25	0.2	20.0%	0.23	8.0%
2	2.15	1.9	1.1	42.1%	1.5	21.1%

Table 4.2: Dimensions of glycerine drops at equilibrium configuration.

Spreading case:	Time, (s)	Experimental spreading diameter ($2a$), (mm)	Numerical spreading diameter ($2a$), (mm)	Error in $2a$, (%)
Water on triethoxysilane	0.4	0.705	0.77	9.2 %
	0.8	0.82	0.9	9.75 %
	1.2	0.9	0.93	3.3 %

Table 4.3: Comparison between numerical and experimental spreading evolution for a water drop of 0.82 radius spreading on a triethoxysilane substrate (based on Fig. 4.9).

4.2.5.2 Case #3: water drop spreading on a hydrophobic triethoxysilane substrate

In this second numerical study, we simulate the sessile water drop deposition experiments performed by Bird *et al.* [28]. In their study, a drop was placed on the triethoxysilane substrate through a needle. The drop contacts the substrate at a diameter of 1.64 mm, and was allowed to spread spontaneously over the substrate until equilibrium was reached, i.e., until the value $\theta = \theta_e = 117^\circ$ is reached. Spreading displacement (a) was measured over the time of spreading.

In order to reproduce this experiment, a drop is placed on the substrate with an initial radius $R = 0.82$ mm, contact angle nearly equal to 180° , and liquid pressure of $p_0 = 0$ Pa. The drop is allowed to deform until equilibrium is achieved, i.e., $\theta_e = 117^\circ$. Fluid density, viscosity and surface tension coefficient are set to $\rho = 1000$ kg m⁻³, $\mu = 8.90 \times 10^{-4}$ kg m⁻¹ s⁻¹, $\gamma = 0.072$ N m⁻¹, respectively. The time step and mesh size are chosen to be $h = 8 \times 10^{-5}$ m and 10^{-7} s, respectively.

Fig. 4.9 and Table 4.3 show that the experimental and numerical profiles are in very good agreement. In addition, the time evolution of the spreading radius is found to be in a

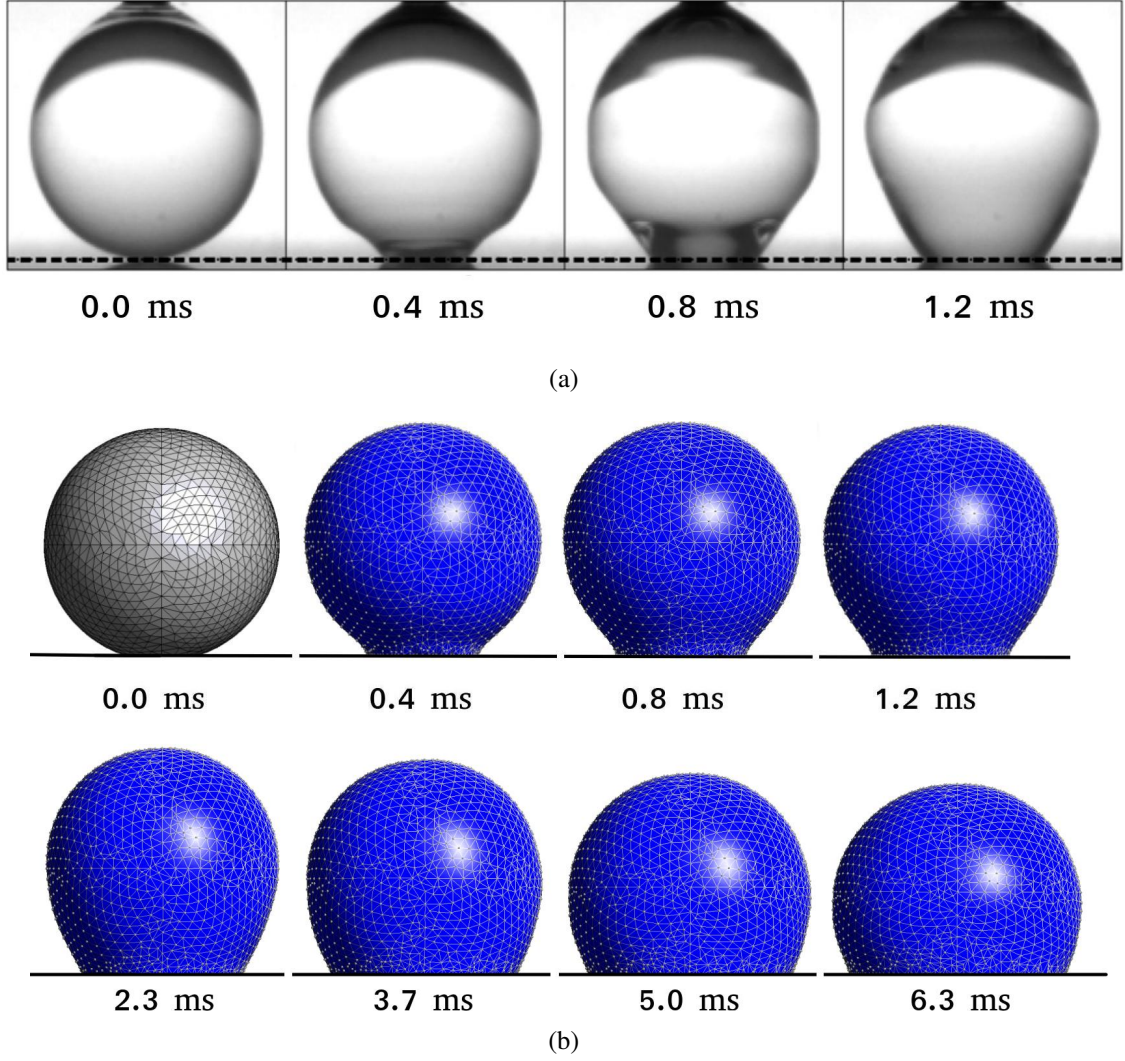


Figure 4.9: Case #3: water drop of a radius 0.82 spreading on triethoxysilane, for $0 < t \leq 1.2$ ms, with a dominant capillary wave propagation at the contact line (a) experimentally [28], (reproduced with permission from J. Phys. Rev. Lett. 100, 234501 (2008). Copyright 2008 American Physical Society), and (b) numerically.

good match with the experimental data. Initial deviation between the numerical and experimental data is observed due to the difference in the initial drop configuration and spreading conditions, i.e., a drop with a spherical configuration was relaxed experimentally while it was attached to a needle.

4.2.5.3 Case #4: water drop spreading on a hydrophilic kapton substrate

The spreading rate for a water drop deposited on a hydrophilic kapton substrate is compared to the average spreading rate obtained experimentally by Bird *et al.* [28]. In that study, water drops of 1 mm diameter were placed on substrates with various levels of hydrophobicity through a needle. Each drop was allowed to spread spontaneously over the substrate until equilibrium was reached. Spreading rates were measured until the drop reaches its steady configuration. The average value of the spreading rate was found to be of the order of 1 m s^{-1} .

The numerical model is used to predict the spreading rate of a water drop of an initial radius $R = 0.495 \text{ mm}$. The equilibrium contact angle of water on kapton is 75° [74]. Fluid density, viscosity and surface tension coefficient are set to $\rho = 1000 \text{ kg m}^{-3}$, $\mu = 8.90 \times 10^{-4} \text{ kg m}^{-1} \text{ s}^{-1}$, $\gamma = 0.072 \text{ N m}^{-1}$, respectively. The contact line velocity is found experimentally to be in the range of 0.8 m s^{-1} . Accordingly, the time step and mesh size for this simulation are chosen to be $\Delta t \approx 2.5 \times 10^{-5} \text{ s}$ and $h \approx 5 \times 10^{-5} \text{ m}$, respectively. The spreading profiles are shown in Fig. 4.10. Furthermore, the spreading rate is shown in Fig. 4.11. The numerical results obtained numerically is in good agreement with the experimental observation.

Our 3D model succeeded in tracking the spatio-temporal evolution of a spreading liquid drop on flat solid substrate. In the next section, we further extend the 3D single-phase drop spreading model to account for sliding motion.

4.3 3D model for sliding liquid drops

As is the case of spreading, this section introduces the numerical treatment for the 3D geometry of a sliding liquid drop. As the drop starts to slide, the effect of the retention force

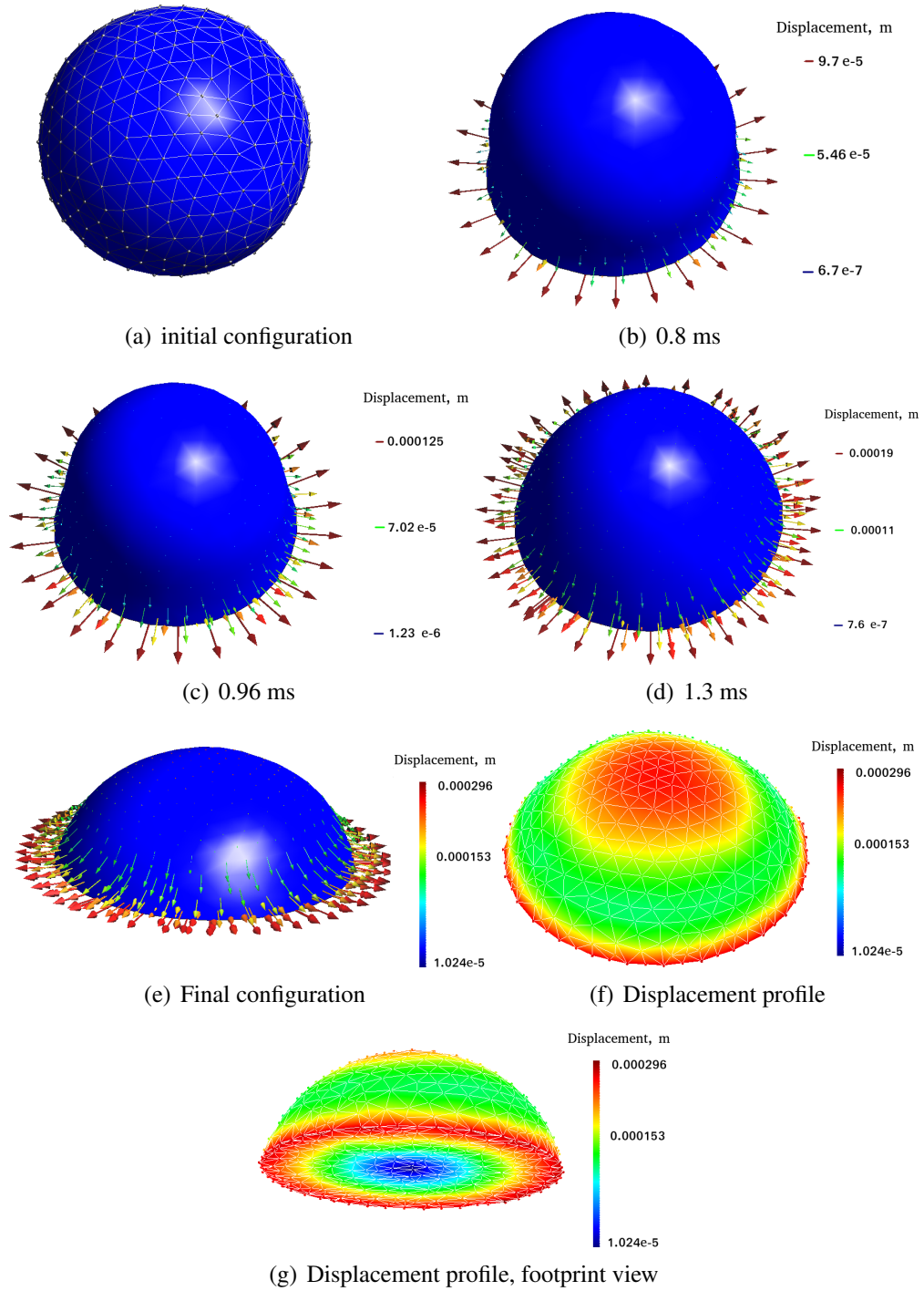


Figure 4.10: Case #4: spreading evolution for water drop on kapton substrate.

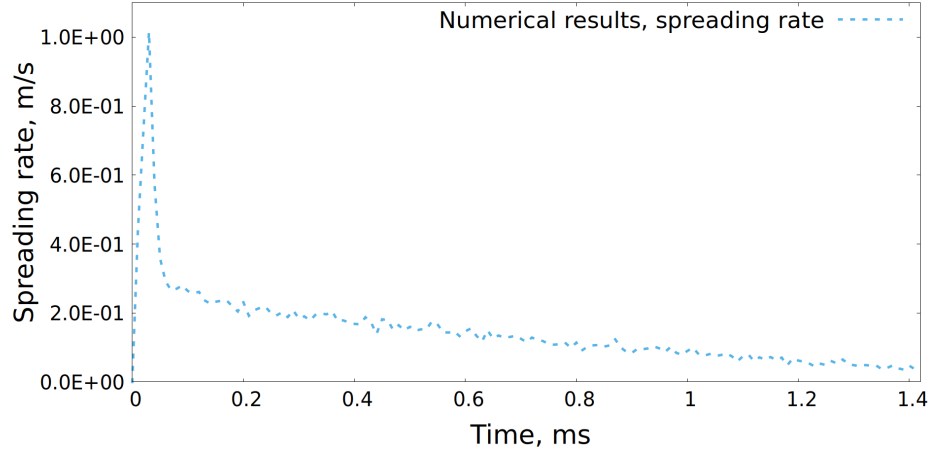


Figure 4.11: Spreading rate evolution for water drop on kapton substrate.

acting on the contact line has to be included. This retention force is known to be a function of i) the drop size, ii) the aspect ratio of the wetting perimeter, iii) the surface tension coefficient, and iv) the contact angle hysteresis, as follows [34, 75, 80, 125, 241, 242] (see Sec. 3.2.2.1 for details):

$$F_{retention} = ka\gamma(\cos \theta_R - \cos \theta_A) \quad (4.3.1)$$

where k is a function of the aspect ratio of the drop footprint, a is the wetting radius of the liquid drop, θ_R is the receding contact angle, and θ_A is the advancing contact angle. The parameters θ_A and θ_R are the maximum and minimum contact angles along the contact line, respectively (see Sec. 1.1.3 for more details). For a liquid drop sliding under the effect of gravity, the retention force will oppose the effect of the gravitational force.

The effect of the retention force is added to eqs. 4.2.15-4.2.21. Accordingly, for the case of sliding liquid drop the coefficient $\beta_{\partial\Gamma}$ is defined as follows:

$$\beta_{\partial\Gamma} = \zeta + \beta_n + \beta_S + \beta_{retention} \quad (4.3.2)$$

The coefficient $\beta_{retention}$ accounts for the effect of the retention force. It is given by:

$$\beta_{retention} = \frac{\gamma ka}{\mathbf{v} \cdot \mathbf{e}_{n_{cl}}} (\cos \theta_R - \cos \theta_A) \quad (4.3.3)$$

Boundary conditions along the solid-liquid interface, excluding the contact line, are expressed in terms of the Navier-slip coefficient as discussed in Sec 4.2.1.5.

4.3.1 Mesh size and time step criteria

Our previous numerical work on drop spreading demonstrated that the implementation of the proposed model results in physically and quantitatively acceptable behavior. The adopted mesh size, h , is estimated as a function of the wetting radius, a , as follows:

$$h \sim \frac{a}{10} \quad (4.3.4)$$

The constraint for choosing the time step is derived by guaranteeing the range of applicability of Jiang's model, that is $0 < Ca \leq 0.03$. The time step criterion is calculated based on the Weber number (We) defined as [180]:

$$We = \frac{\rho R v_{max}^2}{\gamma} \quad (4.3.5)$$

where R is the radius of the drop, and v_{max} is the magnitude of the maximum slip velocity of the liquid at the contact line. The time step can be calculated as follows (see Sec. 3.4 for details):

$$\Delta t \leq \begin{cases} \sqrt{\frac{2}{\pi}} \frac{\gamma}{4\rho |v_{max}^3|} & \text{for } We \geq 1 \\ \frac{CFL}{\frac{|v_{max}|}{h} + \frac{2\mu}{h^2}} & \text{for } We < 1 \end{cases} \quad (4.3.6)$$

where CFL is the Courant-Friedrichs-Lewy number and h is the mesh size. The range of CFL is practically found to be between 0.5 and 0.9. In 3D, the computational cost is very high for smaller mesh sizes and time steps. Thus, for free-surface problems, i.e., $We < 1$, we

will take advantage of the following time step criteria presented by Sussman and Ohta [213]:

$$\Delta t_{crit} \leq \sqrt{\frac{(\rho_L + \rho_g)h^3}{\gamma(2\pi)^3}} \quad (4.3.7)$$

4.3.2 Experimental validation

Three different experimental scenarios obtained from the published literature are examined to validate the proposed sliding drop model for a variety of liquid and substrate properties. The physical properties of the liquids are presented in Tables 4.4.

- Case #1: the first validation examines the steady-state velocity for an ethylene glycol (EG) drop of volume $29.9\mu\text{L}$, sliding on an omniphilic polycarbonate substrate. The corresponding equilibrium contact angle is $\theta_e = 70^\circ$. The inclination angle of the substrate is considered to be $\alpha = 20^\circ$ [125].
- Case #2: the second validation examines the steady-state velocities for water drop of volume $7.5\mu\text{L}$, sliding on an omniphobic PTFE substrate. The corresponding equilibrium contact angle is $\theta_e = 120^\circ$. The drop slides at an inclination angle of $\alpha = 60^\circ$ [16].
- Case #3: the last validation examines the steady-state velocity for a viscous Newtonian omniphilic polyethylene glycol (PEG) drop of volume $100\mu\text{L}$, sliding on a smooth glass substrate. The corresponding equilibrium contact angle is $\theta_e = 34^\circ$. The drop slides at an inclination angle of 27° [238].

4.3.2.1 Case #1: ethylene glycol drop on an omniphilic polycarbonate substrate

We examine the sliding experiment performed by Kim *et al.* [125] for an ethylene glycol drop sliding on an inclined polycarbonate substrate. The drop of volume $29.2\mu\text{L}$ slides over the substrate until it reaches its steady-state velocity. An inclination angle of $\alpha = 20^\circ$ is considered. The steady-state velocities was found experimentally to be $1.557 \times 10^{-3} \text{ m s}^{-1}$ [125].

Case #	Liquid	Substrate	ρ (kg.m ⁻¹)	μ (Pa.s)	γ (N.m ⁻¹)	θ_e (°)	Volume (μL)	α (°)	k
1 [125]	ethylene glycol	polycarbonate	1114	0.0209	0.0484	70.2	29.2	20	1.41
2 [16]	water	PTFE	997	0.00089	0.0728	120	7.5	60	1.35
3 [238]	PEG	smooth glass	1080	0.285	0.0533	34.0	100	27	2.0

Table 4.4: Physical properties of the sliding liquid drops for different liquid/solid pairs.

The simulation is performed using the physical properties for cases #1 of Table 4.4. The wetting radius is $a = 0.00283$ m (see Appendix E). Thus, the mesh size and time step are calculated to be $h = 4 \times 10^{-4}$ m and $\Delta t \approx 1 \times 10^{-6}$ s. The Weber number is found to be < 1 for the given steady-state velocity, i.e., 1.557×10^{-3} m s⁻¹ [125]. Hence, we are able to utilize the advantage of eq. 4.3.7. Therefore, the time step used here is $\Delta t \approx 8 \times 10^{-5}$ s.

The value of k is chosen by using experimental results for a sliding ethylene glycol sliding drop. It is found to be 1.41 [80]. The numerical results are shown in Fig. 4.12 and 4.13. The numerical value of the steady-state velocity is found to be 1.65×10^{-3} m s⁻¹. The error between the experimental and numerical results is found to be $\approx 6\%$, as shown in the first case of Table 4.5.

4.3.2.2 Case #2: water drop on a hydrophobic PTFE substrate

The second validation considers the experiments performed by Annapragada *et al.* [16]. In this experiment, a water drop of volume 7.5 μL slides on an inclined PTFE substrate. Under equilibrium condition, the contact angle θ_e is 120°. The drop is sliding on a tilted plate at an inclination angle of 60°. The steady-state sliding velocity was experimentally found to be 0.12 m s⁻¹.

Using the physical properties for cases #2 of Table 4.4, the simulation is performed with corresponding mesh sizes of $h = 1.1 \times 10^{-4}$ m. The value of the parameter k was found

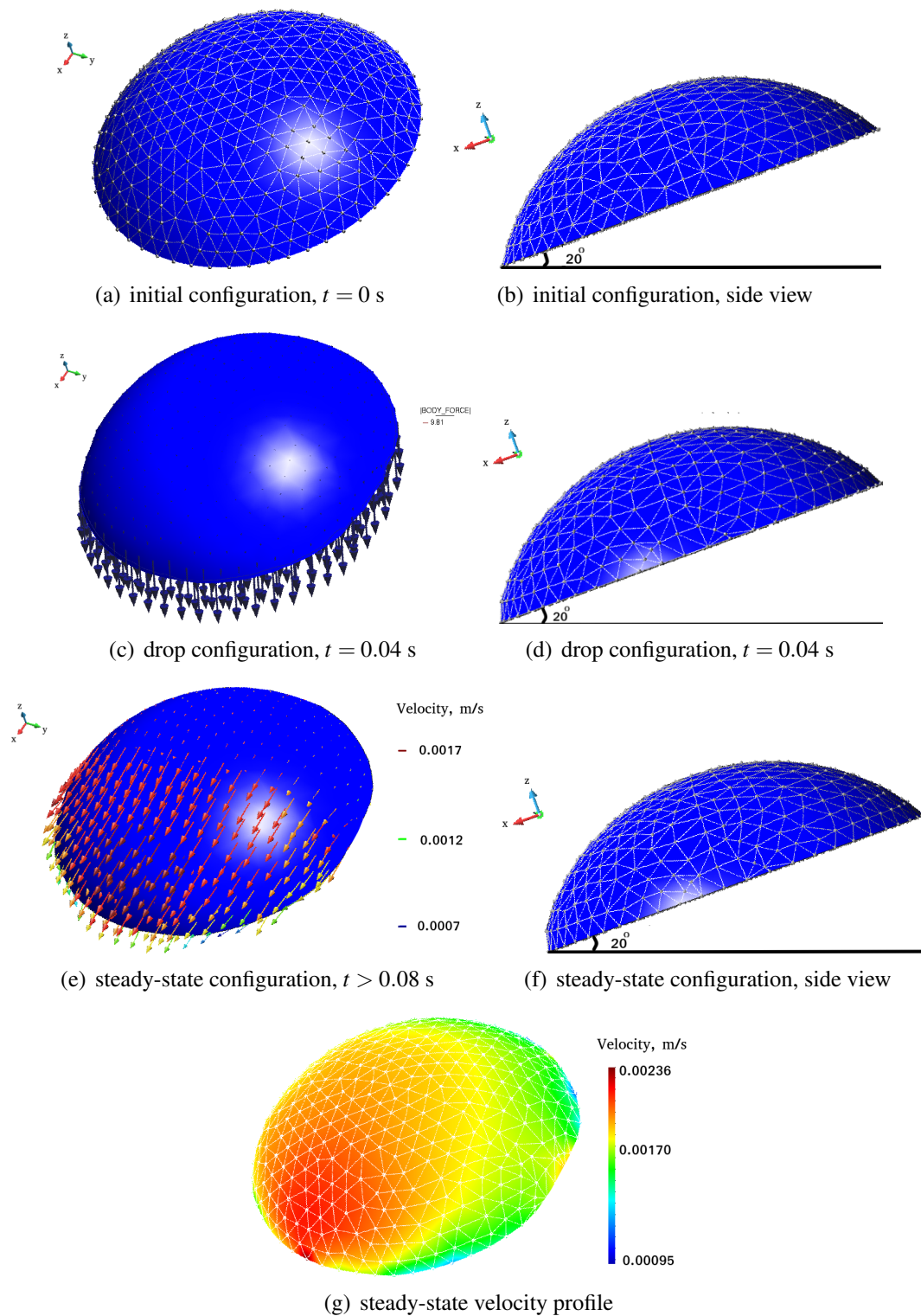
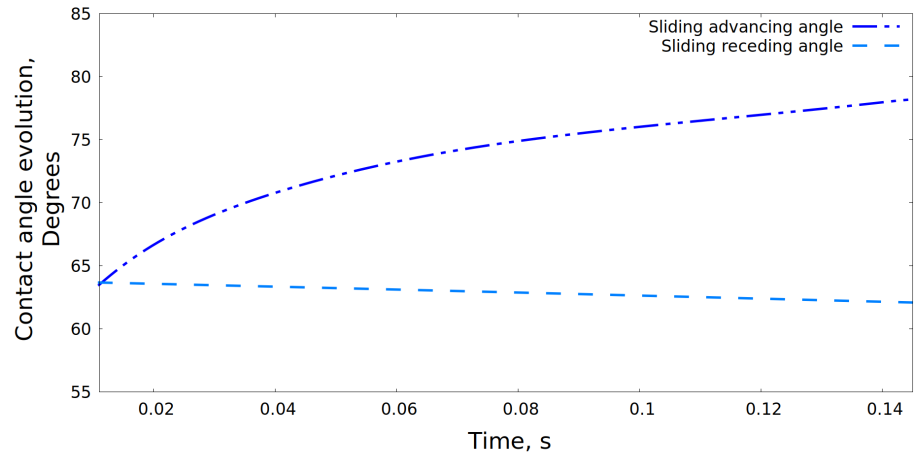
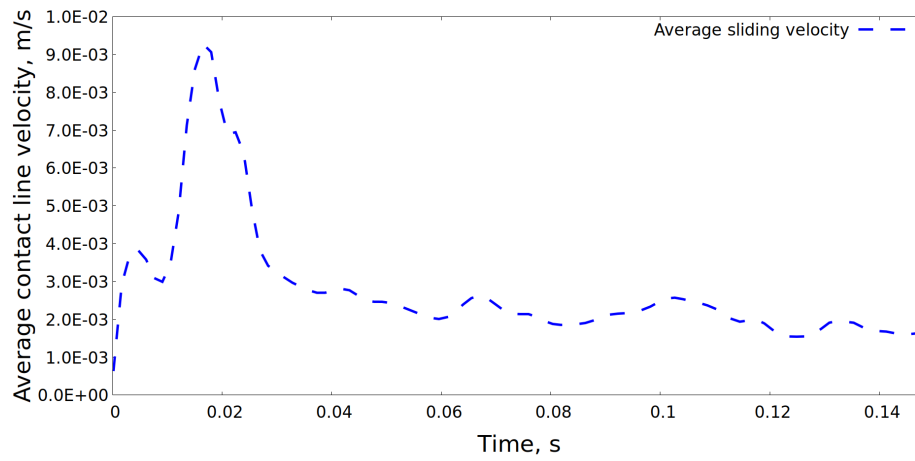


Figure 4.12: Case #1: sliding profiles for EG drop on an omniphilic polycarbonate substrate.



(a) Contact angle evolution



(b) Sliding velocity

Figure 4.13: Case #1: contact angle and spreading rate evolution for EG drop sliding on polycarbonate substrate.

experimentally to be 1.35 [80]. The limiting time step can be predicted by assuming the steady-state sliding velocities, u_{ss} , based on the experimental results found in [16] to be 0.12 m s^{-1} . We is found to be ≤ 1 and, therefore, the time step used here is $\Delta t \approx 1 \times 10^{-5} \text{ s}$ (eq. 4.3.7).

The numerical results are shown in Fig. 4.14 and 4.15. The error between the experimental and numerical results is found to be $\approx 12.5\%$, as shown in the second case of Table 4.5. Figure 4.15 shows fluctuations during sliding, which is hypothesized to be due to both physical and numerical effects. Physically, it has been observed that high contact line velocity leads to higher capillary action [180] and viscous dissipation along the contact line. Due to the nature of the PFEM, minor numerical fluctuations are expected when the mesh nodes are added or deleted as the domain undergoes large deformation. Mesh addition/deletion is performed at each time step as needed to avoid crude meshing and mesh deterioration.

4.3.2.3 Case #3: viscous Newtonian drop on an omniphilic smooth glass

The last scenario aims to simulate the experimental steady-state velocity obtained by Xu *et al.* [238]. In this experiment, a polyethylene glycol (PEG) drop slides on an omniphilic smooth glass, with contact angle $\theta_e = 34^\circ$. The volume of the drop is $100 \mu\text{L}$. The drop slides at an inclination angle of $\alpha = 27^\circ$. The steady-state velocity was experimentally found to be $7.75 \times 10^{-4} \text{ m s}^{-1}$. The value of k is chosen to be 2.0 [238].

The simulation is performed using the physical properties for case #3 of Table 4.4. Adaptive mesh size is used with an initial grid size $h = 9 \times 10^{-4} \text{ m}$, and refined to $h = 6 \times 10^{-4} \text{ m}$ near the boundaries. The time step is set to $\Delta t = 1 \times 10^{-4} \text{ s}$.

The numerical results are shown in Fig. 4.16 and 4.17. The numerical value of the steady-state velocity is found to be $8.1 \times 10^{-4} \text{ m s}^{-1}$. As shown in Table 4.5, the difference between the experimental and numerical results is 4.52%.

The steady-state sliding velocity obtained numerically is found to be in very good

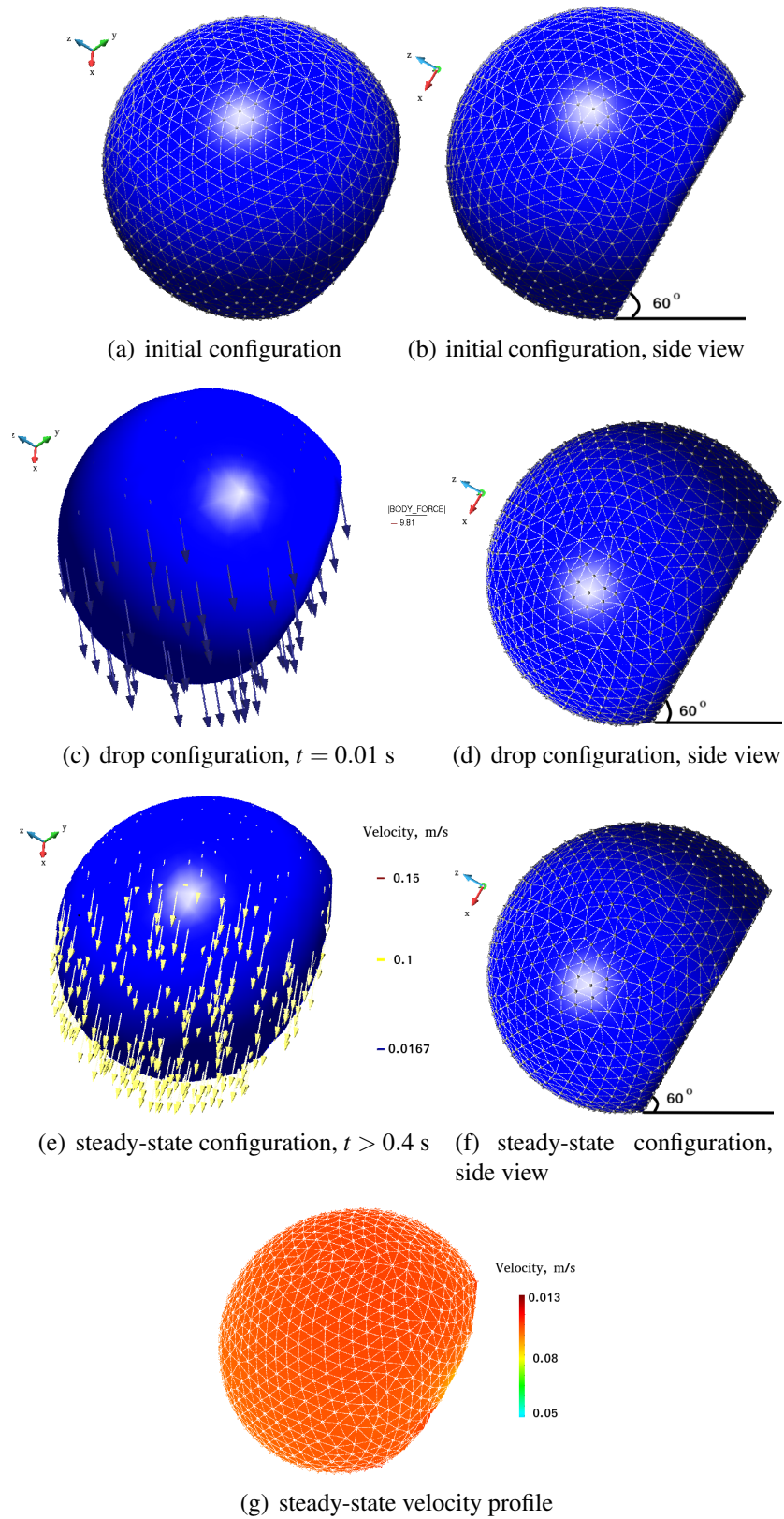
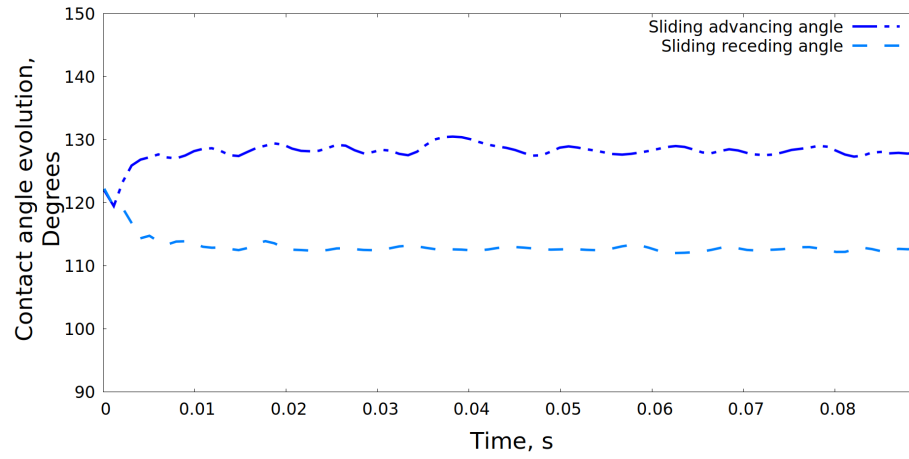
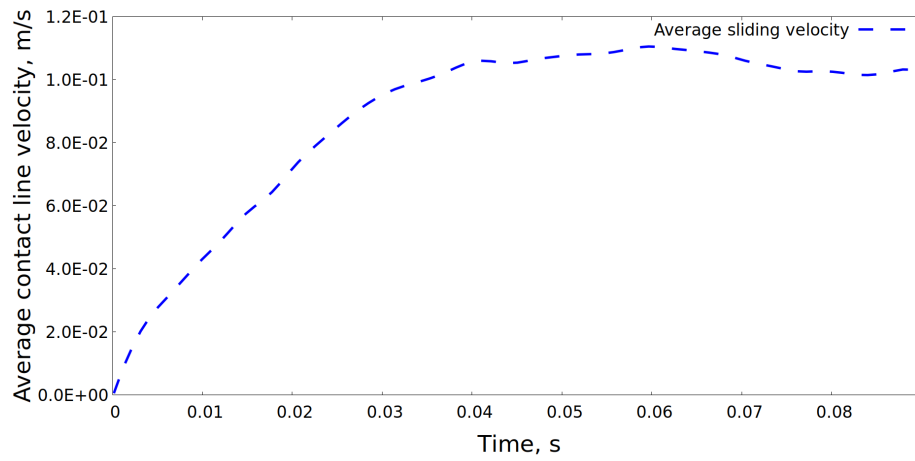


Figure 4.14: Case #2: sliding profiles for water drop sliding on PTFE substrate.



(a) Contact angle evolution



(b) Sliding velocity

Figure 4.15: Case #2: contact angle and spreading rate evolution for water drop sliding on a hydrophobic PTFE substrate.

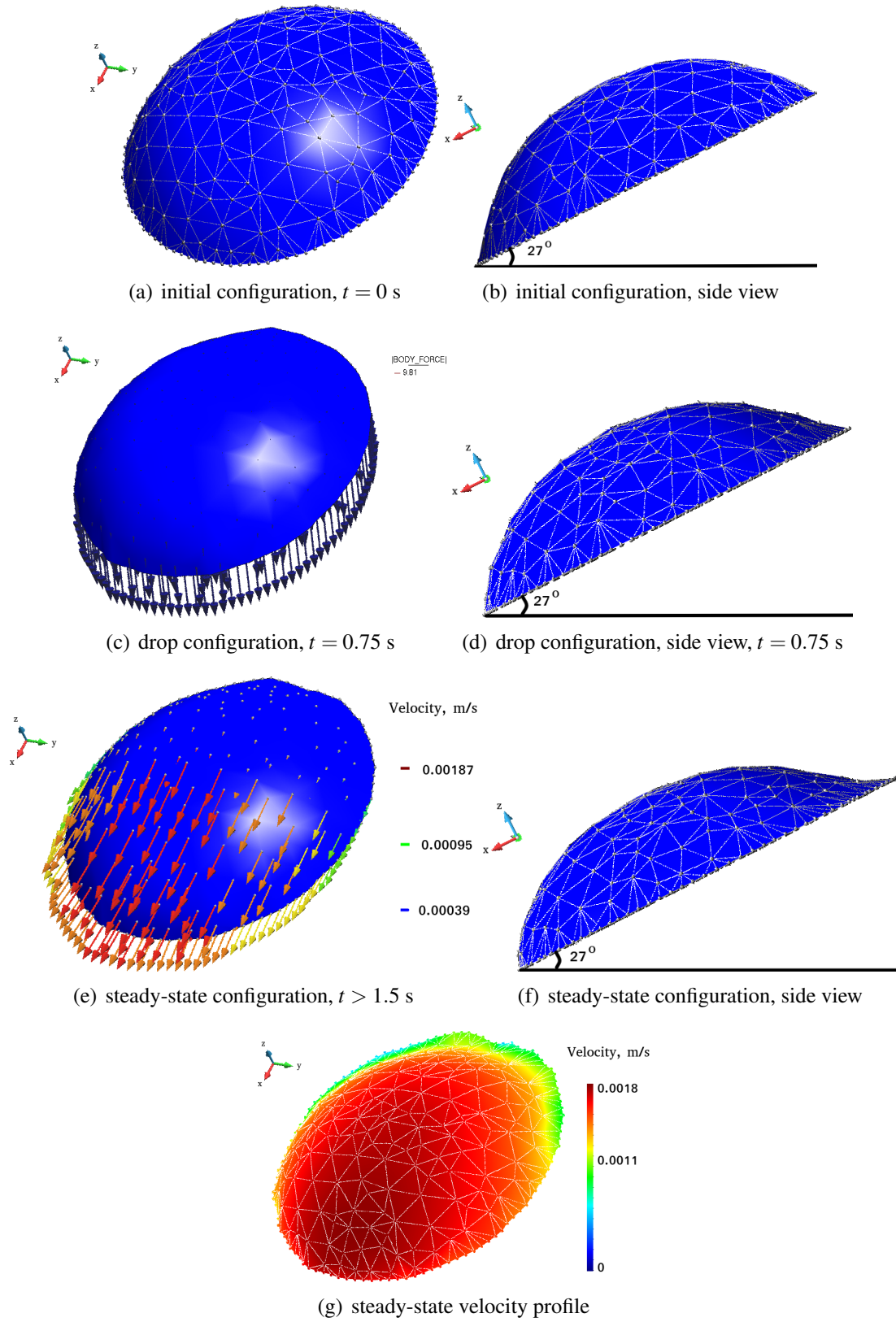
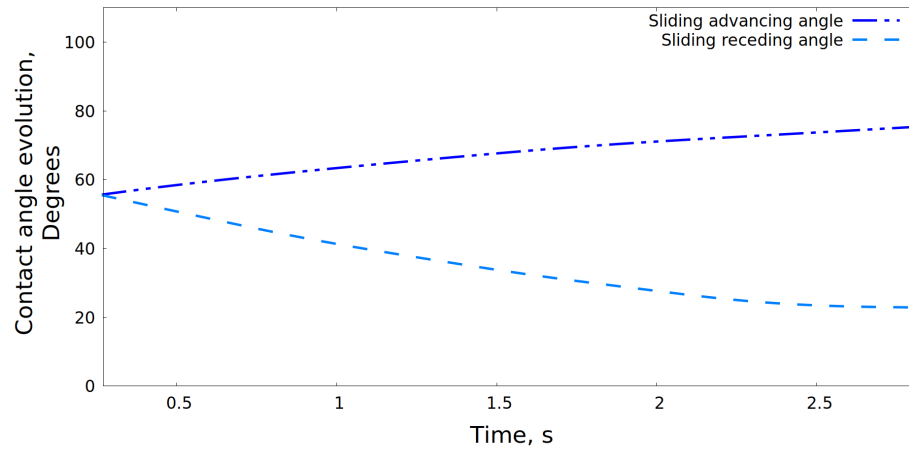
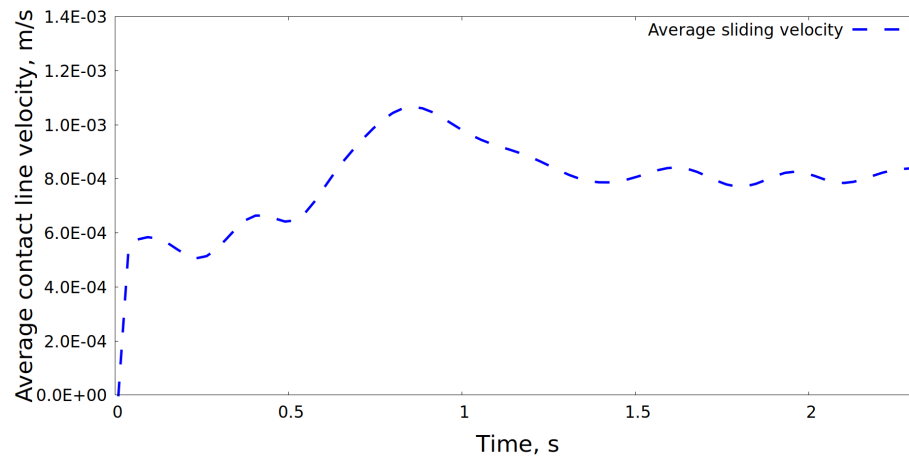


Figure 4.16: Case #3: sliding profiles for viscous Newtonian fluid on an omniphilic smooth glass.



(a) Contact angle evolution



(b) Sliding velocity

Figure 4.17: Case #3: contact angle and spreading rate evolution for viscous Newtonian fluid.

Case #	Volume (μL)	α ($^\circ$)	k (3D)	Experimental u_{ss} (m s^{-1})	Numerical u_{ss} (m s^{-1})	Error in u_{ss} (%)
1	29.2	20	1.41 [80]	1.557E-3	1.65E-3	5.97 %
2	7.5	60	1.35 [80]	0.12	0.105	12.5 %
3	100	27	2 [238]	7.75E-4	8.1E-4	4.52 %

Table 4.5: Numerical vs. experimental steady-state velocities (u_{ss}) in 3D.

Case #	Volume (μL)	α ($^\circ$)	k (3D)	$\frac{k}{\pi}$ (2D)	Experimental u_{ss} (m s^{-1})	Numerical u_{ss} (m s^{-1})	Error in u_{ss} (%)
1	29.2	20	1.41 [80]	0.45	1.557E-3 [125]	1.26E-3	19.1%
2	7.5	60	1.35 [80]	0.43	0.12 [16]	0.11	8.3%
3	100	27	2 [238]	0.64	7.75E-4 [238]	8.7E-4	12.3%

Table 4.6: Numerical vs. experimental steady-state velocities (u_{ss}) in 2D.

agreement with the experiment (Table 4.5). In 3D, compared to 2D, the accuracy of steady-state sliding velocity increased for the case of viscous Newtonian fluid (Table 4.5 vs. Table 4.6). The 3D model demonstrates its ability to replicate the full geometry of a sliding liquid drop and to account for the out-of-plane forces.

4.4 Conclusion

In this chapter, we extended the two-dimensional model for spreading and sliding liquid drops, presented in chapters 2 and 3 to account for full 3D geometries. Our 3D model takes into account the out-of-plane forces and it replicates the full shape of a sliding drop. Seven experiments have been considered for validations, and the numerical results were

found to be in very good agreement. The results of the steady-state velocities in 3D were found to be more accurate than those in 2D.

Our PFEM model was demonstrated to have the ability to predict the drop dynamics in a single phase, i.e., assuming the surrounding gas phase does not affect the liquid drop. The next chapter extends the single-phase PFEM drop dynamics model to an embedded two-phase flow model, where the gas phase exerts an external shear force on the liquid drop.

Chapter 5

AN EMBEDDED TWO-PHASE FLOW

5.1 Introduction

Modeling two-phase flow phenomena is an active and challenging area of research, especially when considering interfacial and wetting phenomena. This includes non-conventional sources of energy, power and heat transfer systems, and additive manufacturing technologies [109]. In this chapter, we develop a numerical model for an embedded two-phase flow, using the Eulerian-PFEM approach, that is capable of predicting the behavior of surface tension dominant problems. The proposed modeling approach is examined in the context of water drop motion in the gas channels of Proton Exchange Membrane Fuel Cells (PEMFCs).

PEMFCs, also known as polymer electrolyte membrane (PEM) fuel cells, are promising, scalable, reliable, and efficient energy conversion devices. They provide high power density and, thus, are suitable for a wide range of applications such as in the transportation domain.

From an engineering point of view, designing an optimal PEMFC remains a challenge. Its mechanical performance and chemical stability are highly dependent on the water management inside the PEMFC channel. Table 5.1 [8, 43, 211] shows the targeted operating conditions of a PEMFC, proposed by the U.S. Department of Energy (DOE).

Water is produced during the fuel cell operation. Under normal operating conditions, water leaves the fuel cell in vapor form. Under high current density, however, the vapor can condense within the GDL. The condensed water blocks the GDL pores and, thus, reduces the GDL permeability. This leads to reactant starvation at the reaction site, causing a drop in current density [112, 252]. If the condensed water is not effectively removed, it can lead to flooding inside the channel. As shown in Fig. 1.5, liquid water can flow inside the PEMFC

Characteristics/Specifications	Target
Maximum Oxygen/Hydrogen crossover	2 mA/cm ²
Membrane conductivity at ambient temperature	0.07 S/cm
	20,000 cycles,
Mechanical & chemical durability	500 hrs
	< 10 sccm crossover

Table 5.1: U.S. DOE technical specifications and targets for automotive PEMFC [8, 43, 211].

channel in the form of drops, films, or slugs. Water drops are formed when the current density is below 0.4 A cm^{-2} . A water film is produced when the current density value is between 0.4 and 1.5 A cm^{-2} . Slugs are observed when the current density exceeds 2 A cm^{-2} [139]. Any type of flooding exacerbates pressure losses along the gas channel [198].

To resolve the water management issue, the GDL is treated with PTFE to mitigate excessive water condensation. At the same time, the membrane needs to be adequately hydrated to maintain proton conductivity [229]. For example, at 30°C , a typical FC membrane has a conductivity of 0.11 S cm^{-1} at 45% of water volume fraction [229]. Hence, a technical challenge is to obtain an optimal PTFE treated GDL that are not saturated with liquid water, while also ensuring proper hydration inside the membrane.

Investigation of drop dynamics in channels of specific geometry and wettability could improve water management and enhance fuel cell performance. Such analyses depend on the spatiotemporal evolution of two-phase flows which are governed by surface tension and partial wetting effects.

Two-phase flow modeling in fuel cell channels has been studied in many publications [44, 115, 193, 219, 229, 236, 251]. Some studies are based on analytical models [44, 116, 131]. These models, however, are found to be valid for small drops of predefined geometries [113]. Alternatively, numerical models have been considered for predicting drop dynamics, as they can better take into consideration the effect of gravity and both interfacial and wetting phenomena [113, 114, 141, 142].

Regarding embedded two-phase flows, early numerical models have been developed to simulate drops deformation in gas channels [86, 87, 203]. For instance, Cai et al. [39] performed numerical simulations, using the VOF method, to predict water film evolution in PEMFC micro-channels. Their results showed that water evacuation is promoted inside a channel when its sidewalls are hydrophilic and its bottom wall is hydrophobic. A similar observation was reported by other studies that modeled drop detachment in straight channels [14, 156, 176].

Identifying the optimal drop-to-channel height ratios of PEMFC channels is an additional challenge for the water management issue. Studies of effects of channel designs on water transport phenomena have also been published in the literature [18, 41, 103, 118, 119, 120, 121, 124, 174, 247]. Cho et al. [49] reported that smaller droplets are detached at higher airflow rates. Jarauta *et al.* [116] reported that the PEMFC channel height has no effect on water drops for a drop-to-channel height ratio of less than 10%. Under this condition, the embedded two-phase flow system can be simplified as a single-phase flow, i.e., ignoring the effect of the external shear flow. For drop-to-channel height ratios greater than 10%, an embedded two-phase flow formulation should be considered.

Experimental validation of numerical models has seldom been performed in the published literature. To the best of our knowledge, the validation of a numerical model analyzing contact angle evolution is still missing [156, 160, 219]. Moreover, the effect of substrate wettability is a critical factor to predict drop detachment, and should be taken into account. In addition, most of the above-mentioned numerical studies use the volume of fluid (VOF) [98] method due to its availability in commercial computational fluid dynamics (CFD) codes (e.g., ANSYS Fluent [2], STAR-CCM [5]) and open-source codes (e.g., GERRIS Flow solver (GFS) [4]). Surface tension is usually modeled with the continuum surface force (CSF) model [31], which is explicit in time and therefore has time step limitations [114, 213]. An alternative to the VOF model is the embedded Eulerian-Lagrangian formulation [115, 146, 186, 187]. Since the drop is discretized with a moving mesh, its interface is tracked precisely, whereas the gas domain is described using a fixed mesh. At every time step, the mesh has to be regenerated. However, the size of the liquid domain is limited

and, therefore, the cost of re-meshing is small.

In this chapter, a novel numerical model for water transport in fuel cell channels is presented both in 2D and 3D. The governing equations for water and air are briefly introduced, as well as the coupling mechanism between both liquid and gas domains. The experimental set-up used to validate the model is described. Experimental observations for drop deformation and contact angle evolution are compared with numerical predictions to validate the model. Furthermore, the proposed model can provide helpful insight in the selection of optimal drop-to-channel height, by examining the spatio-temporal evolution of a wide variety of drop sizes as a function of inlet air velocities.

5.2 Physical model

The working principle of the embedded model hinges on the following ideas [112, 115, 185, 186, 187]. First, the Lagrangian domain, based on the PFEM technique, represents the water liquid phase. Second, the fixed mesh Eulerian domain represents the gas or vapor phase. The advantages of this approach are its ability:

- to accurately track the gas-liquid interface,
- to accurately compute the changes of the material properties such as viscosity and density across the interface, and
- to properly address the jump discontinuity of pressure across the interface, with the possibility of using a time-marching scheme with large time step.

5.2.1 Governing equations for the proposed embedded numerical model

As displayed in Fig. 5.1, let Ω_L and Ω_E represent the Lagrangian domain (for the liquid phase) and the Eulerian domain (for the gas phase), respectively. Let Γ_E be the external boundary of the domain Ω_E where Ω_L is embedded into Ω_E , and Γ_I represents the gas-liquid interface defined by the position of the Lagrangian boundary Γ_L . Boundary Γ_I splits the Eulerian domain into two domains: the gas domain represented by Ω_E^f , and a fictitious Eulerian domain Ω_E^f (which does not have any physical meaning and is used mainly for the coupling

approach). The fictitious Eulerian domain coincides with the Lagrangian domain ($\Gamma_I = \Gamma_L$).

The governing system of equations is based on Navier-Stokes equations accounting for the incompressibility condition:

$$\rho \frac{D\mathbf{v}}{Dt} - \mu \nabla \cdot (\nabla \mathbf{v} + \nabla^T(\mathbf{v})) + \nabla p = \rho \mathbf{g} \quad \text{in } \Omega_E^r \text{ and } \Omega_L \quad (5.2.1)$$

$$\nabla \cdot \mathbf{v} = 0 \quad \text{in } \Omega_E^r \text{ and } \Omega_L \quad (5.2.2)$$

where $\frac{D}{Dt} = \frac{\partial}{\partial t} + \mathbf{v} \cdot \nabla$ is the total material derivative, p is the pressure, t is time, \mathbf{g} is the gravitational body force. ρ and μ are the fluid density and viscosity, respectively, with $\rho = \rho_E$ and $\mu = \mu_E$ in Ω_E , and $\rho = \rho_L$ and $\mu = \mu_L$ in Ω_L .

5.2.2 Boundary and interface conditions

The external and internal boundaries are defined as follows [112, 115, 185, 186, 187]:

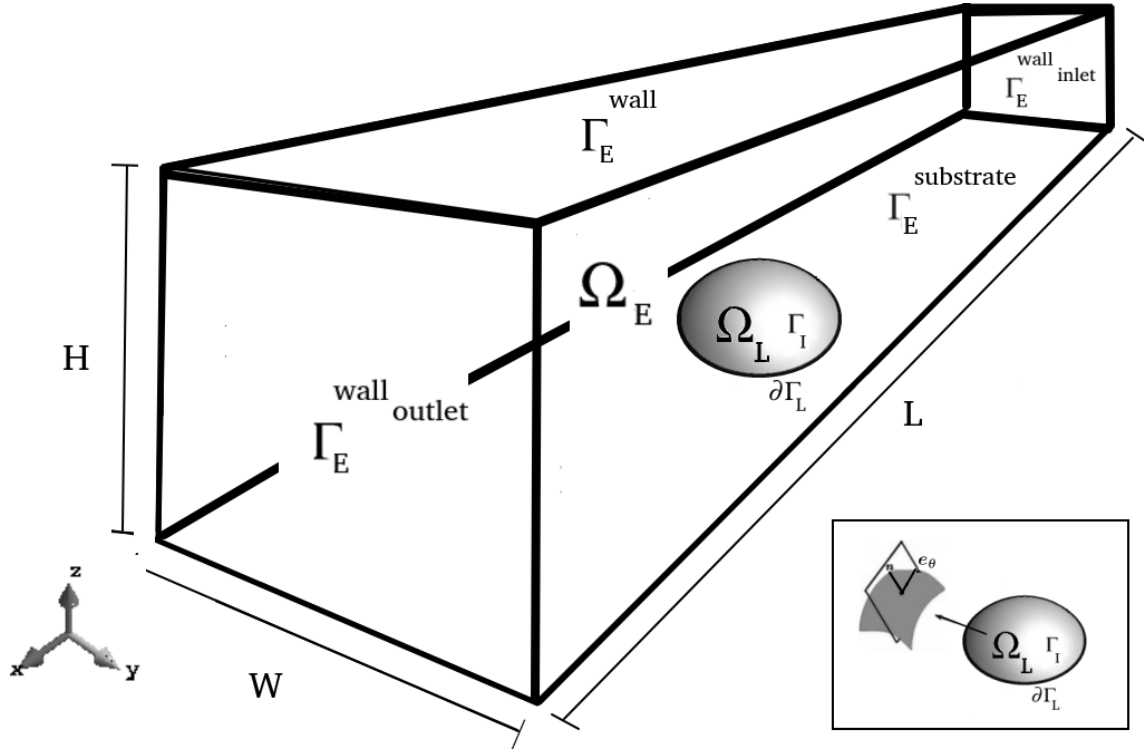
- On the external boundary Γ_E , the following conditions are prescribed:

$$\mathbf{v} = \mathbf{v}_{pr} \quad \text{at } \Gamma_E \quad (5.2.3)$$

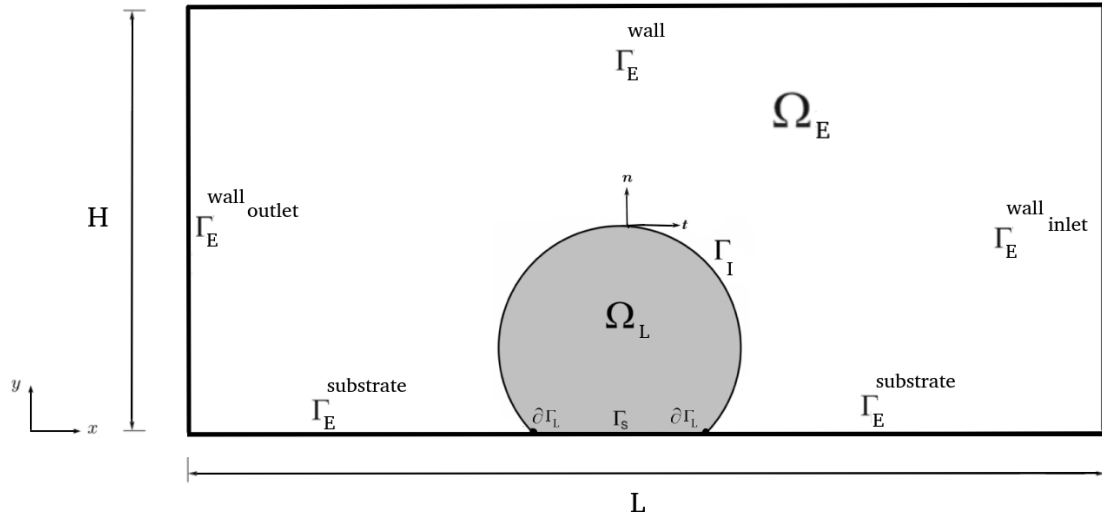
$$\boldsymbol{\sigma} \mathbf{n} = \boldsymbol{\sigma}_n^{pr} \quad \text{at } \Gamma_E \quad (5.2.4)$$

where \mathbf{v}_{pr} is the prescribed inlet velocity, \mathbf{n} is the outer unit normal to Γ_E , and $\boldsymbol{\sigma}_n^{pr}$ is the prescribed traction; in tensor notation this can be written as $\sigma_{n_i}^{pr} = \sigma_{ij} n_j$.

For the Eulerian domain, we impose: i) no-slip boundary conditions on the channel walls and substrate, excluding its inlet and outlet, ii) a prescribed inlet velocity at the inlet, and iii) a prescribed pressure (atmospheric pressure) at the outlet.



(a) Schematic representation of the embedded two-phase flow formulation



(b) side cross-sectional view

Figure 5.1: Schematic graph for the embedded approach [115, 187].

- On the internal interface, Γ_I , the following coupling conditions are imposed:

$$[[\mathbf{v}]] = 0 \quad \text{at } \Gamma_I \quad (5.2.5)$$

$$[[\boldsymbol{\sigma}]]\mathbf{n} = \gamma\kappa_H\mathbf{n} \quad \text{at } \Gamma_I \quad (5.2.6)$$

where \mathbf{n} here is the unit normal to Γ_I interface, γ is the surface tension coefficient, κ_H is the interface mean curvature, and $[[x]]$ symbol is representing the jump of quantity x across the interface. For instance, $[[\mathbf{v}]] = \mathbf{v}_E - \mathbf{v}_L$, where \mathbf{v}_E and \mathbf{v}_L are the velocities corresponding to the Eulerian and Lagrangian domains, respectively.

Eq. 5.2.5 imposes the continuity of the velocity components. The equality of the normal components $\mathbf{v}_{E_n} = \mathbf{v}_{L_n}$ ensures no mass flux across the interface. Equality of the tangential components is equivalent to a no-slip condition. Finally, eq. 5.2.6 indicates that the normal stress across the interface Γ_I is balanced by the surface tension force.

Eq. 5.2.6 can be projected into normal and tangential directions (in 2D) as follows:

$$\mathbf{n} \cdot ([[\boldsymbol{\sigma}]]\mathbf{n}) = \gamma\kappa_H \quad \text{at } \Gamma_I \quad (5.2.7)$$

$$\mathbf{t} \cdot ([[\boldsymbol{\sigma}]]\mathbf{n}) = 0 \quad \text{at } \Gamma_I \quad (5.2.8)$$

where \mathbf{t} is the unit tangent to surface Γ_I . Since $[[\boldsymbol{\sigma}]] = \boldsymbol{\sigma}_E - \boldsymbol{\sigma}_L$, this yields:

$$(p_L - p_E) + [\mu_E \cdot \mathbf{n} \cdot ([\nabla \mathbf{v} + \nabla^T \mathbf{v}]_E \mathbf{n}) - \mu_L \mathbf{n} \cdot ([\nabla \mathbf{v} + \nabla^T \mathbf{v}]_L \mathbf{n})] = \gamma\kappa_H \quad (5.2.9)$$

$$\mu_E \cdot \mathbf{t} \cdot ([\nabla \mathbf{v} + \nabla^T \mathbf{v}]_E \mathbf{n}) - \mu_L \mathbf{t} \cdot ([\nabla \mathbf{v} + \nabla^T \mathbf{v}]_L \mathbf{n}) = 0 \quad (5.2.10)$$

In 3D, the vector \mathbf{t} in eqs. 5.2.8 and 5.2.10 is replaced by \mathbf{e}_θ , Fig. 5.1, and represents any unit vector tangent to surface Γ_I (see Sec. 4.2.1.3 for more details).

5.3 Finite element formulation for the gas phase

The governing equations of the gas phase can be discretized as follows: given $\bar{\mathbf{v}}_n$ and \bar{p}_n at a particular time t_n , the discretization for $\bar{\mathbf{v}}_{n+1}$ and \bar{p}_{n+1} at t_{n+1} yields:

$$M \frac{\bar{\mathbf{v}}_{n+1} - \bar{\mathbf{v}}_n}{\Delta t} + [\bar{K}(\bar{\mathbf{v}}_{n+1}) + \mu L] \bar{\mathbf{v}}_{n+1} + G \bar{p}_{n+1} = \bar{\mathbf{F}} \quad (5.3.1)$$

$$D \bar{\mathbf{v}}_{n+1} = 0 \quad (5.3.2)$$

where M , L , and G are the mass, Laplacian, and Gradient matrices (defined in Sec. 2.6.2). $\bar{K}(\bar{\mathbf{v}}_{n+1})$ represents the non-linear convective term. It is expressed as follows:

$$\bar{K} = k_{IJ} = \rho \int_{\Omega_e} N_I \bar{v}_k \frac{\partial N_J}{\partial x_k} d\Omega \quad (5.3.3)$$

and $\bar{\mathbf{F}}$ is the body force vector, given by:

$$\bar{\mathbf{F}} = \mathbf{f}_I = \int_{\Omega_e} \rho g_k N_I d\Omega \quad (5.3.4)$$

The system of equations, eqs. 5.3.1 and 5.3.2, can be solved using either a monolithic approach or using a fractional step method.

5.3.1 Monolithic approach

Using Algebraic Sub-Grid Scale (ASGS) and following the same procedure described in section 2.6.3, the following term will be added to left-hand side of eqs. 5.3.1 and 5.3.2 [112, 115, 185, 186, 187]:

$$\sum_{e=1}^{n_e} \int_{\Omega_e} \tau [F - \mathcal{L}(\mathbf{v}_h)]^T \mathcal{L}^*(\mathbf{w}_h) d\Omega \quad (5.3.5)$$

Upon applying the Backward Euler scheme, the time dependent residual will be given by:

$$\mathcal{L}(\mathbf{v}_h) = \left[\begin{array}{c} \rho \frac{\partial \mathbf{v}_h}{\partial t} + \rho \mathbf{v}_h \cdot \nabla \mathbf{v}_h - \mu \nabla \cdot (\nabla \mathbf{v}_h + \nabla^T \mathbf{v}_h) + \nabla p_h \\ \nabla \cdot \mathbf{v}_h \end{array} \right] = \left[\begin{array}{c} \rho \frac{\mathbf{v}_{n+1} - \mathbf{v}_n}{\Delta t} + \rho \mathbf{v}_{n+1} \cdot \nabla \mathbf{v}_{n+1} + \nabla p_{n+1} \\ \nabla \cdot \mathbf{v}_{n+1} \end{array} \right] \quad (5.3.6)$$

where the convective term is linearized, assuming a constant convective velocity of \mathbf{v}_{n+1} .

Hence, \mathcal{L}^* , the adjoint of \mathcal{L} , for ASGS is given by [112]:

$$\mathcal{L}^*(\mathbf{w}_h) = \left[\begin{array}{c} -\mathbf{v}_{n+1} \cdot \nabla \mathbf{w}_h - \nabla q_h \\ -\nabla \cdot \mathbf{w}_h \end{array} \right] \quad (5.3.7)$$

Substitution of eqs. 5.3.6 and eq. 5.3.7 into eq. 5.3.5 gives the following resulting stabilizing term:

$$\int_{\Omega_e} \tau_1 (\mathbf{v}_{n+1} \cdot \nabla \mathbf{w}_h + \nabla q_h) \left(\rho \frac{\mathbf{v}_{n+1} - \mathbf{v}_n}{\Delta t} + \rho \mathbf{v}_{n+1} \cdot \nabla \mathbf{v}_{n+1} + \nabla p_{n+1} - \mathbf{f} \right) d\Omega + \int_{\Omega_e} \tau_2 (\nabla \cdot \mathbf{w}_h) (\nabla \cdot \mathbf{v}_{n+1}) d\Omega \quad (5.3.8)$$

Addition of the term obtained by multiplying the momentum equation by \mathbf{w}_h to the term

obtained by multiplying the continuity equation by q_h yields:

$$\begin{aligned}
& \int_{\Omega_e} \tau_1(\mathbf{v}_{n+1} \cdot \nabla \mathbf{w}_h) \left(\rho \frac{\mathbf{v}_{n+1}}{\Delta t} + \rho \mathbf{v}_{n+1} \cdot \nabla \mathbf{v}_{n+1} \right) d\Omega \\
& + \int_{\Omega_e} \tau_2(\nabla \cdot \mathbf{w}_h)(\nabla \cdot \mathbf{v}_{n+1}) d\Omega \\
& + \int_{\Omega_e} \tau_1(\mathbf{v}_{n+1} \cdot \nabla \mathbf{w}_h) \nabla p_{n+1} d\Omega \\
& - \int_{\Omega_e} \tau_1(\mathbf{v}_{n+1} \cdot \nabla \mathbf{w}_h) \left(\rho \frac{\mathbf{v}_n}{\Delta t} + \mathbf{f} \right) d\Omega
\end{aligned} \tag{5.3.9}$$

and:

$$\begin{aligned}
& \int_{\Omega_e} \tau_1 \nabla q_h \left(\rho \frac{\mathbf{v}_{n+1}}{\Delta t} + \rho \mathbf{v}_{n+1} \cdot \nabla \mathbf{v}_{n+1} \right) d\Omega \\
& + \int_{\Omega_e} \tau_1 \nabla p_{n+1} \nabla q_h d\Omega \\
& - \int_{\Omega_e} \tau_1 \nabla q_h \cdot \left(\rho \frac{\mathbf{v}_n}{\Delta t} + \mathbf{f} \right) d\Omega
\end{aligned} \tag{5.3.10}$$

Hence, the stabilized equations are governed by:

$$M \frac{\bar{\mathbf{v}}_{n+1} - \bar{\mathbf{v}}_n}{\Delta t} + [\bar{K}(\bar{\mathbf{v}}_{n+1}) + \mu L + S_K] \bar{\mathbf{v}}_{n+1} + [G + S_G] \bar{p}_{n+1} = \bar{F} + \bar{F}_m \tag{5.3.11}$$

$$[D + S_D] \bar{\mathbf{v}}_{n+1} + S_L \bar{p}_{n+1} = \bar{F}_q \tag{5.3.12}$$

where,

$$S_K = s_{K,IJ} = \int_{\Omega_e} \left[\tau_1 \left(\bar{v}_k \frac{\partial N_I}{\partial x_k} \right) \left(\rho \frac{N_J}{\Delta t} + \rho \bar{v}_k \frac{\partial N_J}{\partial x_k} \right) + \tau_2 \frac{\partial N_I}{\partial x_k} \frac{\partial N_J}{\partial x_k} \right] d\Omega \tag{5.3.13}$$

$$S_G = s_{G,IJ} = \int_{\Omega_e} \tau_1 \left(\bar{v}_k \frac{\partial N_I}{\partial x_k} \right) \frac{\partial N_J}{\partial x_k} d\Omega \tag{5.3.14}$$

$$S_D = s_{D,IJ} = \int_{\Omega_e} \tau_1 \frac{\partial N_I}{\partial x_k} \left(\frac{\rho}{\Delta t} N_J + \bar{v}_k \frac{\partial N_J}{\partial x_k} \right) d\Omega \quad (5.3.15)$$

$$S_L = s_{L,IJ} = \int_{\Omega_e} \tau_1 \frac{\partial N_I}{\partial x_k} \frac{\partial N_J}{\partial x_k} d\Omega \quad (5.3.16)$$

$$\bar{F}_m = f_{m_I} = \int_{\Omega_e} \rho g_k \left(\bar{v}_k \frac{\partial N_I}{\partial x_k} \right) \left(\frac{\rho}{\Delta t} N_I + N_I \right) d\Omega \quad (5.3.17)$$

$$\bar{F}_q = f_{q_I} = \int_{\Omega_e} \rho g_k \frac{\partial N_I}{\partial x_k} \left(\frac{\rho}{\Delta t} N_I + N_I \right) d\Omega \quad (5.3.18)$$

where N_I is the FEM shape function for node I , Ω_e is the element integration domain, and k represents the spatial variables x, y , and z . τ_1 is the first algorithmic stabilization parameter given by:

$$\tau_1 = \frac{1}{\frac{2\|\bar{v}\|}{h} + \frac{4\nu}{h^2}} \quad (5.3.19)$$

and τ_2 is the second algorithmic stabilization parameter given by:

$$\tau_2 = \frac{h^2}{\tau_1} \quad (5.3.20)$$

where h is the element size, ν is the kinematic viscosity. τ_1 has a dimension of time, and corresponds to the momentum equation, coupled through the pressure, whereas τ_2 has the dimension of a numerical kinematic viscosity which controls the volumetric strain rate and the velocity divergence.

5.3.2 Fractional step approach

The fractional step method is more efficient in terms of the computational cost (approximately ten times faster in our case), as compared to the monolithic approach [112, 115, 185, 186, 187]. However, it does not accurately preserve mass conservation. Jarauta et al. [112] shows that the fractional step approach can be used when considering the Eulerian

domain, but not for the Lagrangian domain where excessive remeshing takes place. To reduce the computational cost, this work considers the fractional step approach when solving for the Eulerian domain.

Let \check{v} be an intermediate velocity, defined as follows:

$$M \frac{(\bar{v}_{n+1} - \check{v}) + (\check{v} - \bar{v}_n)}{\Delta t} + [\bar{K}(\bar{v}_{n+1}) + \mu L] \bar{v}_{n+1} + G(\bar{p}_{n+1} - \bar{p}_n + \bar{p}_n) = \bar{F} \quad (5.3.21)$$

Multiplied the Laplacian matrix by the intermediate velocity \check{v} instead of \bar{v}_{n+1} ¹ yields the following:

$$M \frac{(\check{v} - \bar{v}_n)}{\Delta t} + [\bar{K}(\check{v}) + \mu L] \check{v} + G \bar{p}_n = \bar{F} \quad (5.3.22)$$

$$M \frac{(\bar{v}_{n+1} - \check{v})}{\Delta t} + G(\bar{p}_{n+1} - \bar{p}_n) = 0 \quad (5.3.23)$$

We then rearrange the term above in the following form:

$$\check{v} = \bar{v}_{n+1} + \Delta t M^{-1} G(\bar{p}_{n+1} - \bar{p}_n)$$

and multiply each side by D matrix:

$$D\check{v} = D\bar{v}_{n+1} + D\Delta t M^{-1} G(\bar{p}_{n+1} - \bar{p}_n) \quad (5.3.24)$$

From eq. 5.3.2 and eq. 5.3.24, the term $D\bar{v}_{n+1}$ will vanish. Furthermore, $D = -G^T$ and, thus $DM^{-1}G$ can be approximated as L [184, 112]. Using L instead of $DM^{-1}G$ leads to smaller

¹ The fractional step approach has proven to be more efficient in computational cost than the monolithic approach [51, 112]. However, it is not a mass conservative method. Ryzhakov *et al.* [188] devised a numerical technique to enhance the mass-conservation properties of the fractional step formulation by introducing an intermediate velocity field (more details about the fractional step approach can be found in references [51, 185, 188]).

computational cost. Consequently, we find

$$D\check{v} = \Delta t L(\bar{p}_{n+1} - \bar{p}_n) \quad (5.3.25)$$

The three equations of the fractional step approach will take the following form:

$$M \frac{(\check{v} - \bar{v}_n)}{\Delta t} + [\bar{K}(\check{v}) + \mu L] \check{v} + G \bar{p}_n = \bar{F} \quad (5.3.26)$$

$$D\check{v} = \Delta t D M^{-1} G(\bar{p}_{n+1} - \bar{p}_n) \quad (5.3.27)$$

$$M \frac{(\bar{v}_{n+1} - \check{v})}{\Delta t} + G(\bar{p}_{n+1} - \bar{p}_n) = 0 \quad (5.3.28)$$

Eq. 5.3.26 is the fractional momentum equation solving for the intermediate velocity \check{v} , eq. 5.3.27 is the pressure Poisson equation solving for the pressure \bar{p}_{n+1} , and eq. 5.3.28 is the end-of-step momentum equation solving for \bar{v}_{n+1} . Finally, the stabilized system of equations of the fractional approach formulation are given by [112, 115, 185, 186, 187]:

$$M \frac{\check{v} - \bar{v}_n}{\Delta t} + [\bar{K}(\check{v}) + \mu L + S_k] \check{v} + [G + S_G] \bar{p}_n = \bar{F} \quad (5.3.29)$$

$$D\check{v} = [\Delta t L - S_D](\bar{p}_{n+1} - \bar{p}_n) \quad (5.3.30)$$

$$M \frac{\bar{v}_{n+1} - \check{v}}{\Delta t} + [G + S_G](\bar{p}_{n+1} - \bar{p}_n) = 0 \quad (5.3.31)$$

We solve for \check{v} from eq. 5.3.29. Then, \bar{p}_{n+1} is solved by eq. 5.3.30. Finally, \bar{v}_{n+1} is obtained by eq. 5.3.31.

5.4 Finite element formulation for the liquid phase

The finite element formulation for the liquid phase is explained in details in Sec. 2.6.3. For the sake of clarity, the equations governing the liquid phase are re-introduced as follows

[112, 115, 185, 186, 187]:

$$\left(M\frac{1}{\Delta t} + \mu L + S_k\right)\bar{v}_{n+1} + G\bar{p}_{n+1} = \bar{F} + \bar{F}_{int} + \bar{F}_{\partial\Gamma} + \bar{F}_{\Gamma_S} + M\frac{\bar{v}_n}{\Delta t} \quad (5.4.1)$$

$$(D + S_D)\bar{v}_{n+1} + S_L\bar{p}_{n+1} = \bar{F}_q \quad (5.4.2)$$

where \bar{F}_{int} represents the Neumann term including the normal stress, shear stress, and surface tension.

5.5 Coupling strategy

Figure 5.2 defines the following quantities [112, 115, 185, 186, 187]:

- The boundary of the Lagrangian domain is represented by Γ_L . The representation of the Lagrangian boundary on the Eulerian mesh is denoted by Γ_I (note that $\Gamma_L \approx \Gamma_I$ as the element size h goes to zero),
- The embedded interface Γ_I domain (including the interface elements) splits the Eulerian domain into two domains: the real domain (including the real nodes) Ω_E^r and the fictitious domain Ω_E^f (including the fictitious nodes).

In order to model the interacting domains, a coupling approach must be implemented. Dirichlet-Neumann coupling technique is devised as follows [115, 186]:

- The effect of the Lagrangian domain (liquid) on the Eulerian domain (gas) will be represented by the Dirichlet boundary condition at Γ_I (eq. 5.2.5),
- The effect of the Eulerian domain on the Lagrangian domain is represented by the Neumann boundary condition applied at Γ_L . This boundary condition is expressed by eq. 5.2.9 and 5.2.10,

5.5.1 Dirichlet boundary condition

The Dirichlet boundary condition, $v_E = v_L$ imposed on Γ_I , can be implemented by using one of two methods [112, 115, 185, 186, 187]:

- In the first method, the Eulerian elements are split into two elements. Accordingly, Γ_L and Eulerian mesh intersection will coincide with the Lagrangian nodes. This is known as “strong coupling”. One disadvantage of this approach is that when introducing (adding) new nodes in the Eulerian mesh, the system matrices will have additional degrees of freedom, which will increase the computational cost.
- The second method consists of minimizing the difference between velocities of the Lagrangian domain and the Eulerian domain at Γ_L . This implies that the Dirichlet boundary condition will be applied at the fictitious nodes (black nodes shown in Fig. 5.2.c. This coupling approach is known as “weak coupling”. The main advantage of this approach is that no degree of freedom will be added and the matrix system will not be affected.

Following the second approach, the difference in velocity is minimized as follows:

$$\int_{\Gamma_I} (v_k^{n+1} - v_k^L) N_I d\Gamma_I = 0 \quad (5.5.1)$$

where v_k^{n+1} is the velocity of the k^{th} nodes of the Eulerian domain, and v_k^L is the velocity of the Lagrangian domain at Γ_I . Discretization of eq. 5.5.1 yields:

$$M_{\Gamma_I} \bar{v}_{n+1} = f_{\Gamma_I} \quad (5.5.2)$$

where \bar{v}_{n+1} is the velocity at the nodes of the interface, and M_{Γ_I} and f_{Γ_I} are given by:

$$M_{\Gamma_I} = m_{\Gamma_I}^{ab} = \int_{\Gamma_{I,X}} N^a N^b d\Gamma \mathbf{X} = - \int_{\Gamma_I} N^a N^b J_{\Gamma}(\mathbf{X}) d\Gamma \quad (5.5.3)$$

$$f_{\Gamma_I} = f_{\Gamma_I}^a = \int_{\Gamma_{I,X}} N_f^a v_k^L d\Gamma \mathbf{X} = - \int_{\Gamma_I} N_f^a v_k^L J_{\Gamma}(\mathbf{X}) d\Gamma \quad (5.5.4)$$

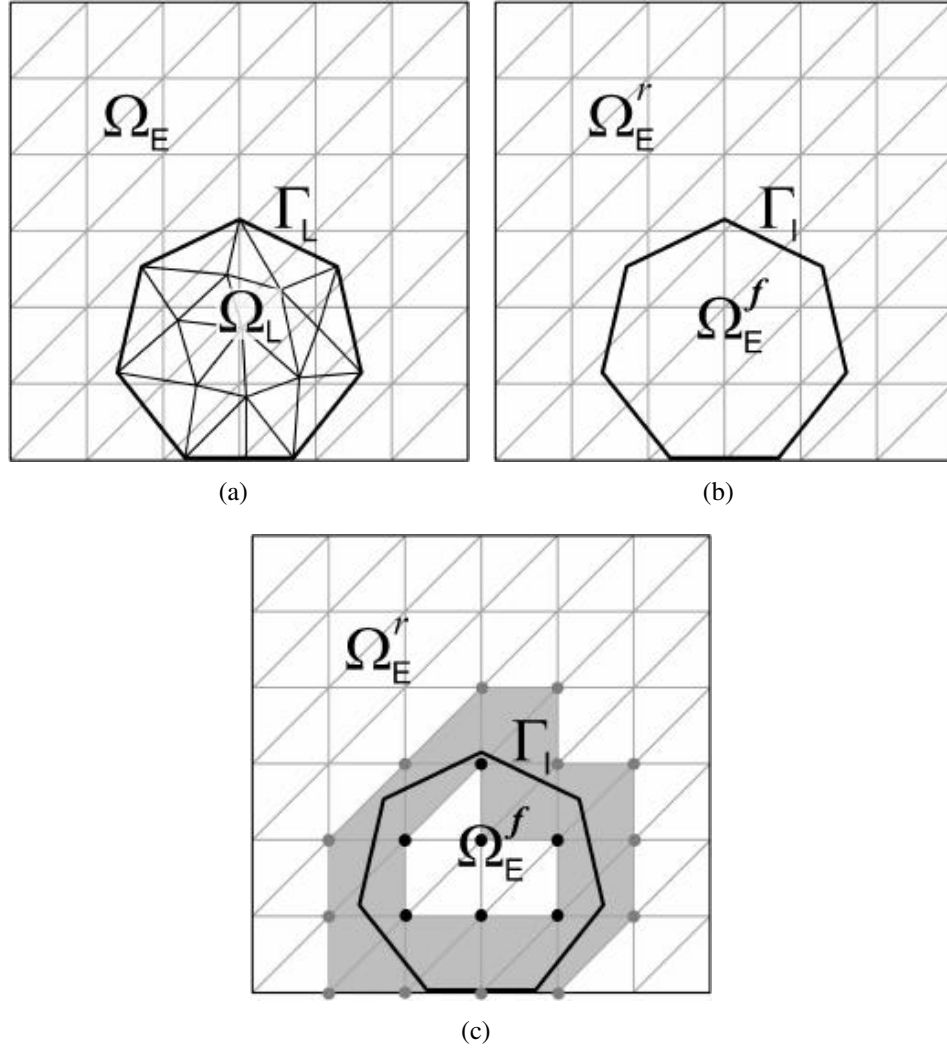


Figure 5.2: Embedded schematic of a) real superimposed discretized Eulerian-PFEM domains, b) fictitious interface on the Eulerian mesh, and c) elements of the interface [112].

where N_f^a is the shape function of the fictitious nodes, and $\bar{\mathbf{v}}_{n+1} = \bar{\mathbf{v}}_{n+1}^r + \bar{\mathbf{v}}_{n+1}^f$ (since the interface domain elements contain both real and fictitious nodes).

Assuming the velocity vectors entries of the real node correspond to zero velocity vectors at fictitious nodes, and vice versa, this yields:

$$M_{\Gamma_I} \bar{\mathbf{v}}_{n+1}^r + M_{\Gamma_I} \bar{\mathbf{v}}_{n+1}^f = \mathbf{f}_{\Gamma_I} \quad (5.5.5)$$

Eq. 5.5.5 can be solved by assuming the real nodes velocities at the interface, in gray colored dots of Fig. 5.2, are equal to the velocities at their previous time step as follows:

$$M_{\Gamma_I} \bar{\mathbf{v}}_{n+1}^f = \mathbf{f}_{\Gamma_I} - M_{\Gamma_I} \bar{\mathbf{v}}_{n+1}^r \quad (5.5.6)$$

$$\bar{\mathbf{v}}_{n+1}^r \approx \bar{\mathbf{v}}_n^r \quad (5.5.7)$$

5.5.2 Neumann boundary condition

Neumann boundary condition will be expressed in terms of the normal and shear stresses exerted by the Eulerian domain (gas) on the Lagrangian domain (liquid), and including the surface tension forces. These forces are represented by $\bar{\mathbf{F}}_{int}$ as follows [112, 115, 185, 186, 187]:

$$\bar{\mathbf{F}}_{int} = \bar{\mathbf{F}}_N + \bar{\mathbf{F}}_{st} + \bar{\mathbf{F}}_{sh} \quad \text{on } \Gamma_L \quad (5.5.8)$$

where,

$$\bar{\mathbf{F}}_N = \mathbf{f}_{N,ij}^a = - \int_{\Gamma_L} N^a \mathbf{n}_i \, d\Gamma + \mu_E \int_{\Gamma_L} \left(\frac{\partial N^a}{\partial x_j} \right)_E \mathbf{n}_i \, d\Gamma_L \quad (5.5.9)$$

$$\bar{\mathbf{F}}_{st} = \mathbf{f}_{st,i}^a = - \int_{\Gamma_L} \gamma \kappa_H N^a \mathbf{n}_i \, d\Gamma_L \quad (5.5.10)$$

$$\bar{F}_{sh} = f_{sh,ij}^a = \mu_E \int_{\Gamma_L} \left(\frac{\partial N^a}{\partial x_j} \right)_E \mathbf{m}_i d\Gamma_L \quad (5.5.11)$$

where, \mathbf{m} represents a vector tangent to Γ_L , and \mathbf{n} represents the vector normal to Γ_L .

5.6 Solution algorithm

The following solution algorithm is followed (see Fig. 5.3 for further clarification):

- Assume both the velocity $\bar{\mathbf{v}}_n$ and the pressure \bar{p}_n at time t_n are known for both the Eulerian and Lagrangian domains Ω_E and Ω_L .
- Start with solving the Lagrangian problem (liquid phase). The output from this step are the Lagrangian mesh new position, $\bar{\mathbf{v}}_{n+1}$, and \bar{p}_{n+1} in Lagrangian domain Ω_L^{n+1} .
- Identify the interface position between Ω_L and Ω_E , including both real and fictitious nodes. The output from this step is the position of Γ_I .
- In the Eulerian domain Ω_E , assign the velocity at the interface real nodes with the known gas velocity. The output from this step is $\bar{\mathbf{v}}_{r,n+1} = \bar{\mathbf{v}}_n$
- Solve eq. 5.5.5 for the fictitious velocity nodes $\bar{\mathbf{v}}_{f,n+1}$. Fix the velocity of the fictitious node (interface Dirichlet boundary condition).
- Solve for the gas problem, using the real part of the Eulerian domain and utilizing the Dirichlet boundary condition at the fictitious nodes on the interface. The output from this step is $\bar{\mathbf{v}}_{n+1}$ and \bar{p}_{n+1} in Ω_E^{n+1}
- Project the gas stress onto the liquid boundary Γ_L surface, using eq. 5.5.8 and eq. 5.5.9 to compute \bar{F}_{int} for the momentum equation of the Liquid.

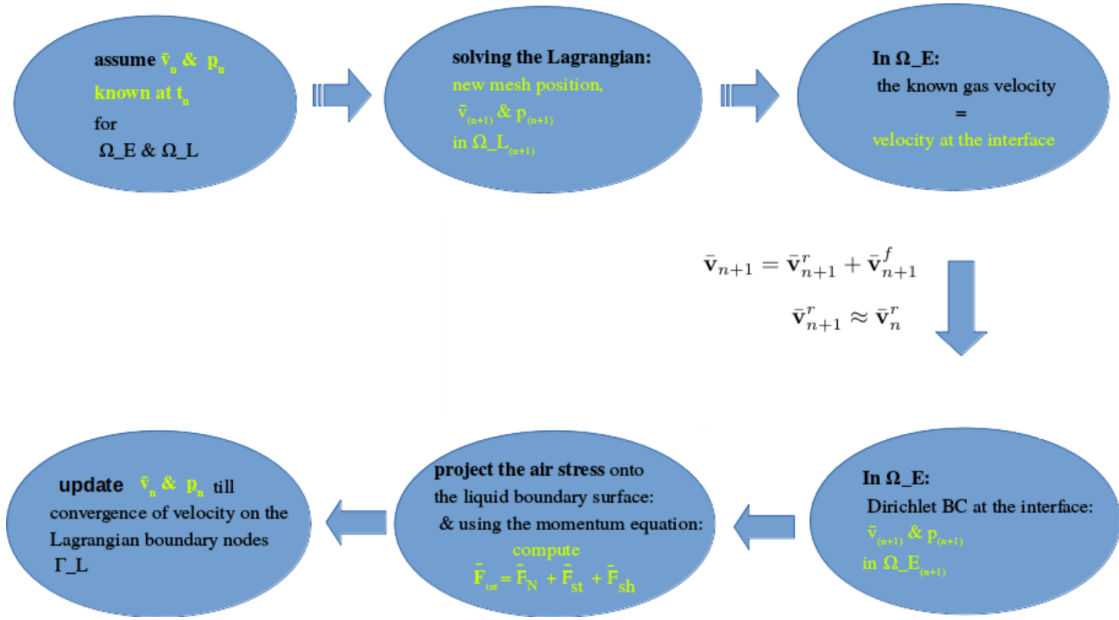


Figure 5.3: Coupling algorithm flowchart.

- Update the velocity and pressure fields until convergence of velocity on the Lagrangian boundary nodes $\Gamma_L = \varepsilon$ as follows:

$$\frac{\|\delta \bar{v}\|}{\|\bar{v}_{n+1}\|} < \varepsilon \quad (5.6.1)$$

5.7 Validating the Eulerian domain

The Lagrangian model for liquid drops has been experimentally validated in chapters 2-4. In this section, we aim to validate the gas flow simulation in the Eulerian domain by comparison with approximate analytical expression of the pressure drop inside a channel of size 6.5 mm x 6.5 mm x 12 mm. The dimension of this channel is chosen based on the experimental work performed by the UC Berkeley Group (see Sec. 5.8). The analytical results are then used to validate the Eulerian model, both in 2D and 3D.

The length of the channel is characterized as short or long, according to the type of the flow profile inside that channel. For a laminar flow inside a horizontal channel, i.e., when the Reynolds number ($Re = \frac{\rho v D_{hy}}{\mu}$, where D_{hy} is the channel hydraulic diameter and v is the

average flow velocity) is below 2300, two types of flow profiles can be observed. The first type is a hydrodynamically developing flow, for which the velocity profile develops in the direction of the flow. The second type is a hydrodynamically fully developed flow, where the velocity profile is invariant in the direction of the flow. The type of velocity profile can be predicted by using the non-dimensional hydrodynamic entrance length of the channel (L_{hy}). The parameter L_{hy} represents the required channel length to achieve a fully developed profile. It is expressed in terms of both Reynolds number and the hydraulic diameter of the channel cross-section as follows:

$$L_{hy} = \frac{L_e}{D_{hy}Re} \quad (5.7.1)$$

where L_e is the dimensional hydrodynamic entrance length, D_{hy} is the hydraulic diameters, and Re is the Reynolds number. The hydraulic diameter is calculated as follows [42]:

$$D_{hy} = 4A_{cs}/\ell_{cs} \quad (5.7.2)$$

where A_{cs} and ℓ_{cs} are the area and perimeter of the channel cross-section (cs), respectively.

Considering various channel geometries, various authors studied the threshold entrance length (L_{hy}^*) as a function of the length-to-diameter ratio of the channel [201]. A hydrodynamically fully developed flow exists when $L_{hy} \geq L_{hy}^*$, whereas a hydrodynamically developing flow exists when $L_{hy} < L_{hy}^*$. Most of the fuel channels are designed with rectangular cross-sections. Different authors proposed different L_{hy}^* criteria for a rectangular channel [199]. In this work, Han's criteria [91], shown in Table 5.2 [201], is considered as it accounts for the rapid flow development inside the channel, i.e., for larger inertial forces relative to the viscous forces [201, 42].

Aspect ratio, $\alpha^* = \text{height} / \text{width}$	L_{hy}^* , Han [91]
1	0.0752
0.750	0.0735
0.5	0.066
0.25	0.0427
0.125	0.0227
0	0.0099

Table 5.2: L_{hy}^* criteria for a fully developed laminar flow inside a rectangular channel [91, 201].

The pressure drop along the channel is estimated as follows [42]:

$$\Delta P = f_D \frac{L}{D_{hy}} \frac{\rho v_{in}^2}{2} \quad (5.7.3)$$

where f_D is the Darcy-Weisbach friction factor along the channel and v_{in} is the prescribed inlet velocity of the gas phase. The value of f_D is given in Table 5.3 for a hydrodynamically developing flow inside a rectangular channel. For a hydrodynamically fully developed flow in a long cylindrical channel of constant cross-section, eq. 5.7.3 becomes the well-known Hagen–Poiseuille equation [42]:

$$\Delta P = \frac{128\mu L v_{in} A_{cs}}{\pi D^4} \quad (5.7.4)$$

where D is the channel diameter. Considering a fully developed flow of the same flow area, the pressure gradient inside a rectangular channel is found to be greater than that of a circular channel. Natarajan and Lakshmanan [158] proposed the following equation that relates the pressure drop gradient along a rectangular channel to that in a circular channel of the same flow area [158, 201]:

$$(\Delta P / \Delta L)_r / (\Delta P / \Delta L)_c = 0.861 (\ell_r / \ell_c)^{2.75} \quad (5.7.5)$$

where ℓ is the perimeter and r & c stand for a rectangular channel and a circular channel, respectively.

Our proposed Eulerian model for gas channel flow is validated using the 6.5 mm x 6.5 mm x 120 mm rectangular channel. Two different inlet flow rates of 6 standard liter per minute (SLPM) and 10 SLPM are considered, (case #1 and case #2, respectively). The physical properties of the gas are $\rho = 1.2 \text{ kg m}^{-3}$, $\mu = 1.81 \times 10^{-5} \text{ kg m}^{-1} \text{ s}^{-1}$. The non-dimensional hydrodynamic entrance length of the channel L_{hy} is found to be 0.018 (eq. 5.7.1). The value of its aspect ratio $\alpha^* = 1$ and, thus, $L_{hy}^* = 0.0752$ (Table 5.2). Accordingly, the value of the parameter L_{hy} is found to be less than L_{hy}^* . Therefore, the flow inside the channel is a hydrodynamically developing flow according to analytical predictions [201].

For each case, the value of ΔP along the channel is found using the approximate analytical solution. For the first case, i.e., inlet flow rate of 6 SLPM, the inlet velocity of the gas and the corresponding Reynolds number are $v_{in} = 2.37 \text{ m s}^{-1}$ and $Re \sim 1000$, respectively. Considering a short channel of $L_{hy} = 0.018$ and $\alpha^* = 1$, the parameter f_D in eq. 5.7.3 can be estimated by $\sim 124/Re$ [102, 201] (see Table 5.3). Thus, f_D takes the value of 0.124. From eq. 5.7.3, the value of ΔP is found to be $\sim 8 \text{ Pa}$. Similarly for the second case, i.e., inlet flow rate of 10 SLPM, the inlet velocity of the gas and the corresponding Reynolds number are $v_{in} = 3.95 \text{ m s}^{-1}$ and $Re \sim 1700$, respectively. Thus, L_{hy} and f_D are found to be 0.01 and 0.09, respectively. Accordingly, the approximate analytical solution of ΔP is found to be $\sim 16 \text{ Pa}$.

Numerical simulations are performed to validate the Eulerian model for both cases, both in 2D and 3D. In 2D, the channel is no longer a real channel. Figure 5.4(a) represents a parallel plate channel. The pressure gradient in parallel plate channels can be estimated analytically using Goldstein's [85] and Mohanty and Das [155] criteria. Accordingly, the pressure drop along a parallel plate channel of 6.5 mm (H) x 120 mm (L) is found analytically to be 3.3 Pa and 6.4 Pa for the first and the second cases, i.e., v_{in} of 2.37 m s^{-1} and 3.95 m s^{-1} , respectively. We aim to demonstrate the limitation of 2D simulations in replicating the actual geometry of the channel, which has a direct effect on the spatio-temporal evolution of

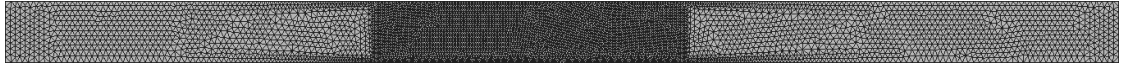
$\frac{L}{ReD_{hy}}$	$\sim (f_D/4) Re$		
	$\alpha^* = 1$	$\alpha^* = 0.5$	$\alpha^* = 0.2$
0.005	51.5	51.8	52.5
0.010	38.0	38.2	38.9
0.015	32.1	23.5	33.3
0.05	21.0	21.8	23.7
0.1	17.8	18.8	21.4

Table 5.3: Approximated value of f_D for developing laminar flow in a rectangular channel [56, 201].

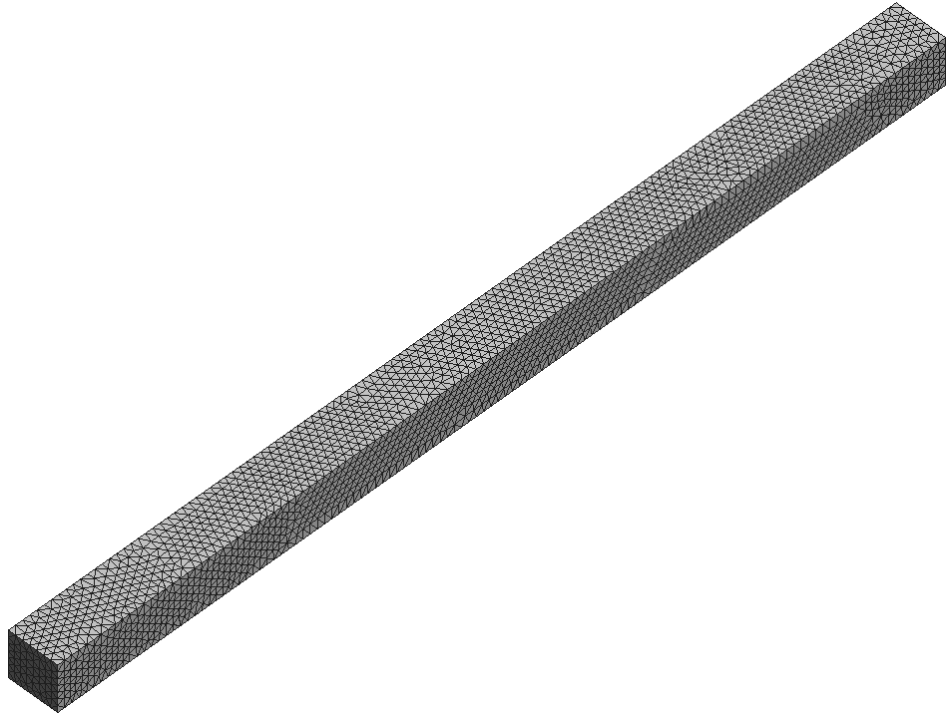
the embedded drop. We shall restrict our injection numerical simulations in 2D only. Full 3D simulations will be conducted in the absence of injection. The mesh sizes are set as 6×10^{-4} and $\sim 1 \times 10^{-3}$ m for the 2D and 3D simulations, respectively (see Fig. 5.4). In 2D, the mesh size is refined to $\sim 2.5 \times 10^{-4}$ m at the center of the channel where the injection takes place. The time step is chosen based on Courant–Friedrichs–Lewy condition to be $\leq 1 \times 10^{-5}$ s and $\leq 1 \times 10^{-4}$ s for the 2D and 3D simulations, respectively.

The values ΔP of case #1 are found to be 3.1 Pa and 7.3 Pa in 2D and 3D, respectively (see Fig. 5.5). For case #2, the values of ΔP are found to be 6.41 Pa and 16.7 Pa in 2D and 3D, respectively (see Fig. 5.6).

The numerical solution of the 3D model is found to be in good agreement with the approximate analytical solution. The 2D results appear to be scaled by a factor of about 3 in both cases. Regarding the pressure drop evolution obtained by the 3D simulations, numerical oscillations are observed at initial time steps, i.e., $0 < t < 0.05$ s, see Figs. 5.5(c) and 5.6(c). This oscillatory behavior is hypothesized to be due to the high value of the prescribed inlet velocity while fixing the exit pressure at atmospheric, i.e., higher oscillations are observed for higher inlet velocity (see Figs 5.5 and 5.6). In 2D, however, no oscillations are observed because the domain is oversimplified and the pressure drop value is under-predicted.

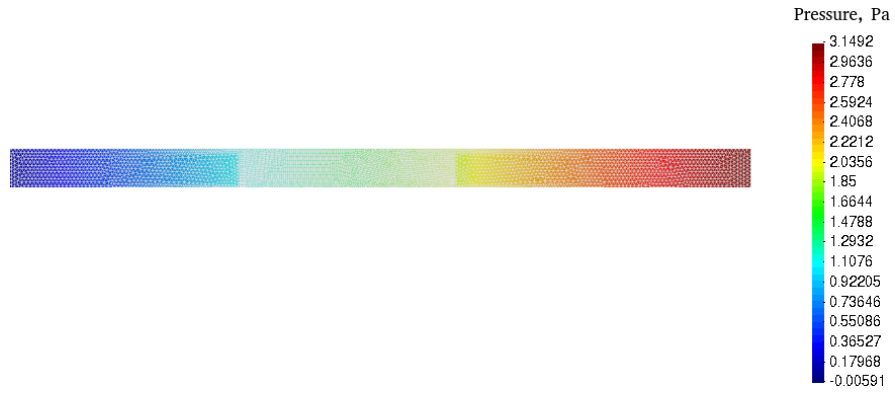


(a)

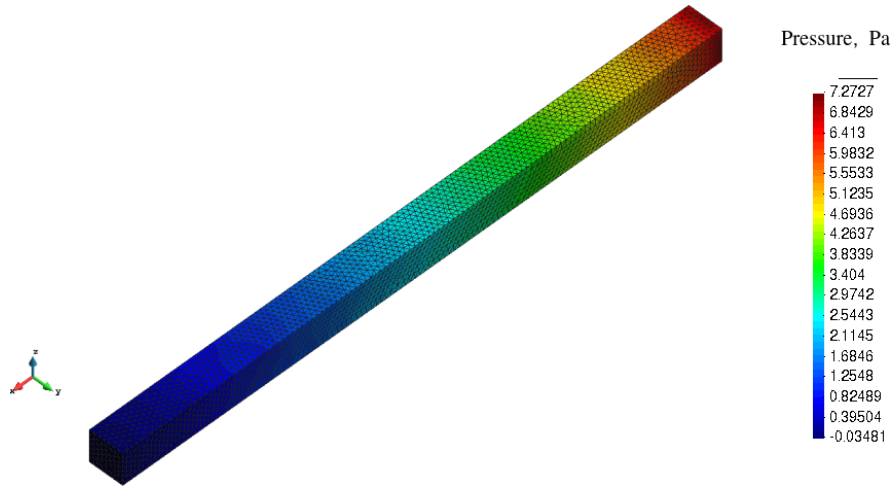


(b)

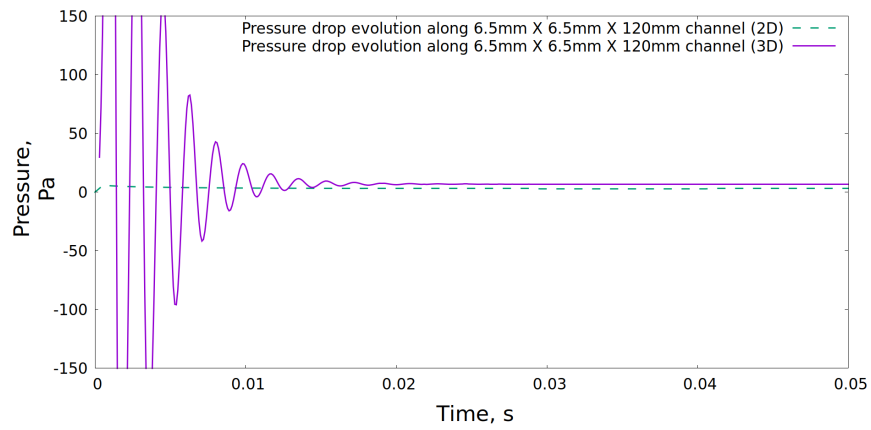
Figure 5.4: Mesh sizes for a 6.5 mm (H) x 6.5 mm (W) x 120 mm (L) channel: (a) a mesh size of 6×10^{-4} m, refined to 2.5×10^{-4} m at the center of the channel where the injection takes place, (b) a mesh size of 1×10^{-3} m.



(a)

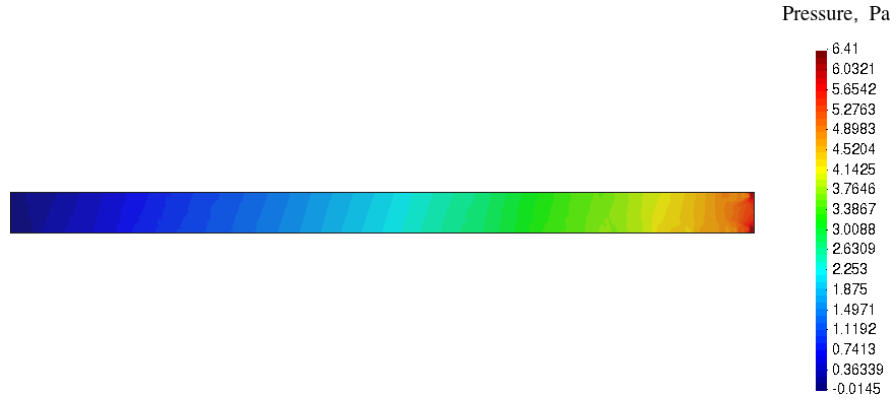


(b)

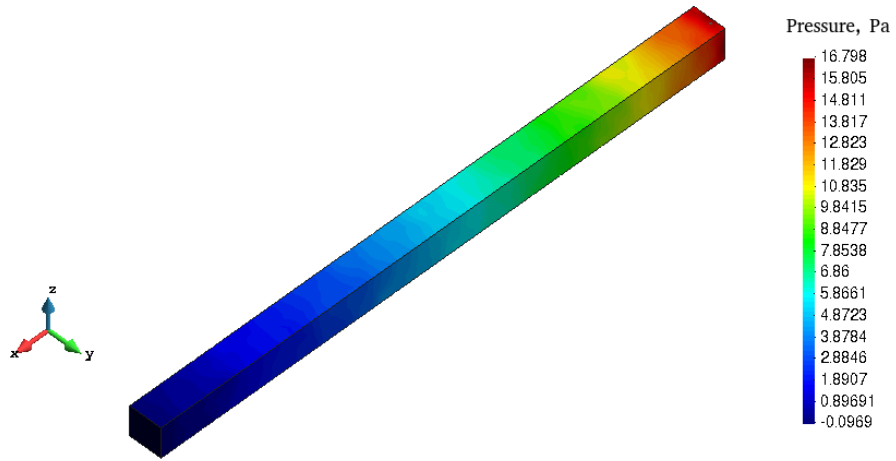


(c)

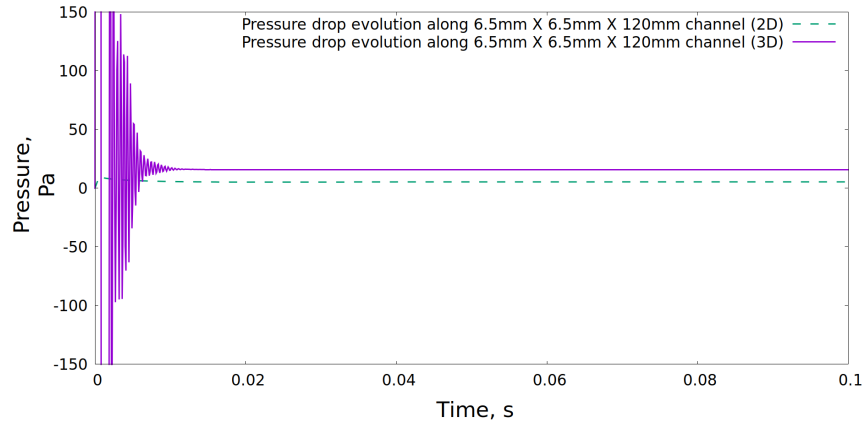
Figure 5.5: Pressure drop along a 6.5 mm (H) x 6.5 mm (W) x 120 mm (L) channel, air inlet flow rate of 6 SLPM : (a) solution of the Eulerian domain in 2D, (b) solution of the Eulerian domain in 3D, and (c) pressure drop evolution both in 2D and 3D.



(a)



(b)



(c)

Figure 5.6: Pressure drop along a 6.5 mm (H) x 6.5 mm (W) x 120 mm (L) channel, air inlet flow rate of 10 SLPM : (a) solution of the Eulerian domain in 2D, (b) solution of the Eulerian domain in 3D, and (c) pressure drop evolution both in 2D and 3D.

5.8 Experimental validation for the embedded, two-phase flow, model

Four drop detachment simulations are considered in this section to reproduce the experimental work performed by the UC Berkeley and ESDLab Groups. The experimental data was obtained by T. Chan at UC Berkeley, under the supervision of A. Weber and M. Secanell. The first two simulations are performed in 2D for water drops injected inside a PFEM channel. Air flows inside the channel during the injection process. Each experiment/simulation is performed using a hydrophilic kapton-coated or a hydrophobic PTFE-coated channel. The third and fourth simulations are performed in 3D to predict the detachment sliding velocity for water drops in a PEMFC channel. Both experiments consider a hydrophobic PTFE channel. Details and results for each validation are introduced in the next subsections.

5.8.1 2D embedded simulation: water drop injection on kapton and PTFE substrates

Our first objective is to assess the 2D numerical model by varying i) the physico-chemical nature of the substrate (PTFE and Kapton) and ii) airflow rate (F) in SLPM and water injection rate (Q) in μL on the dynamic contact angle evolution.

The task consists of simulating the behavior of a water drop inside a channel of 6.5 mm x 6.5 mm x 12 mm (6.5 mm x 12 mm in 2D) driven by airflow. In the experiments, water was injected from the bottom of the channel from a small conduit of 6×10^{-4} m diameter in the substrate using a peristaltic pump, as shown in Fig. 2.17, and driven at an inlet airflow rate of 6 SLPM. The experimental results were analyzed for two cases of i) kapton F6-Q15 and ii) PTFE F6-Q25. Accordingly, two numerical simulations are performed. Each simulation is validated by i) tracking the spatio-temporal evolution of the injected drop using a sequence of dynamic contact angles (measured graphically with ImageJ software) and ii) examining both the formation and flow of the injected water with respect to the channel substrate, specifically, whether a drop would detach or generate a thin film.

While air flows into the channel, water is continuously injected in the substrate at constant flow rates of 15 $\mu\text{L/s}$ and 25 $\mu\text{L/s}$ on kapton and PTFE substrates, respectively. Two simulations are performed to reproduce these two experiments. To reproduce the experiments, we match the initial drop profile with the experimental profile to define our initial

condition, shown in Fig. 5.7(a), 5.8(a), 5.9(a) and 5.10(a). The physical properties of the gas phase are $\rho = 1.2 \text{ kg m}^{-3}$ and $\mu = 1.81 \times 10^{-5} \text{ kg m}^{-1} \text{ s}^{-1}$. The physical properties of the liquid phase are $\rho = 1000 \text{ kg m}^{-3}$ and $\mu = 8.9 \times 10^{-4} \text{ kg m}^{-1} \text{ s}^{-1}$. The mesh size is chosen to be 6×10^{-4} , refined to $\sim 2.5 \times 10^{-4} \text{ m}$ at the center of the channel where the injection takes place.

Drop evolution obtained experimentally and numerically are shown in Figs. 5.7 and 5.8, and Figs. 5.9 and 5.10, for water on kapton and PTFE substrates, respectively. Moreover, profiles of sliding water drops on PTFE substrate, after detachment, is shown in Fig. 5.11.

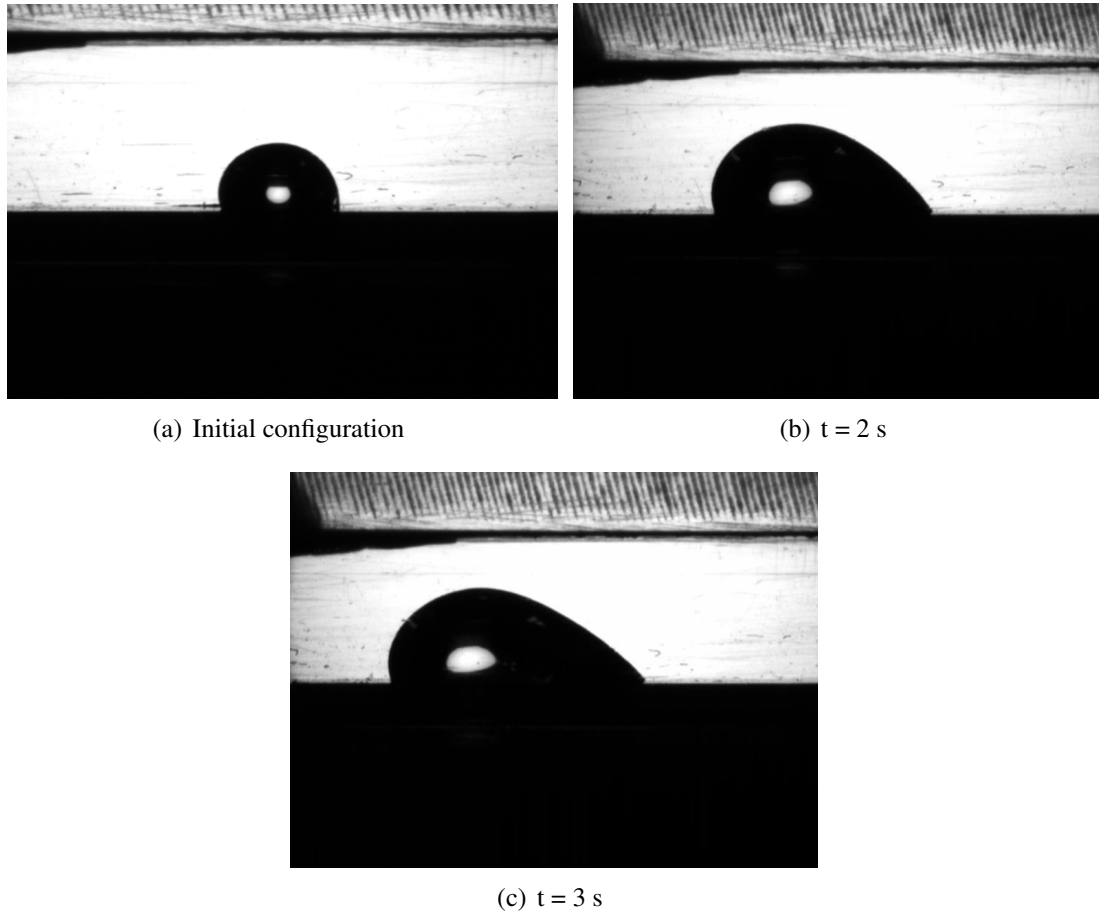


Figure 5.7: Injection experiment: evolution of water drop injected on kapton substrate at flow rates of F6-Q15.

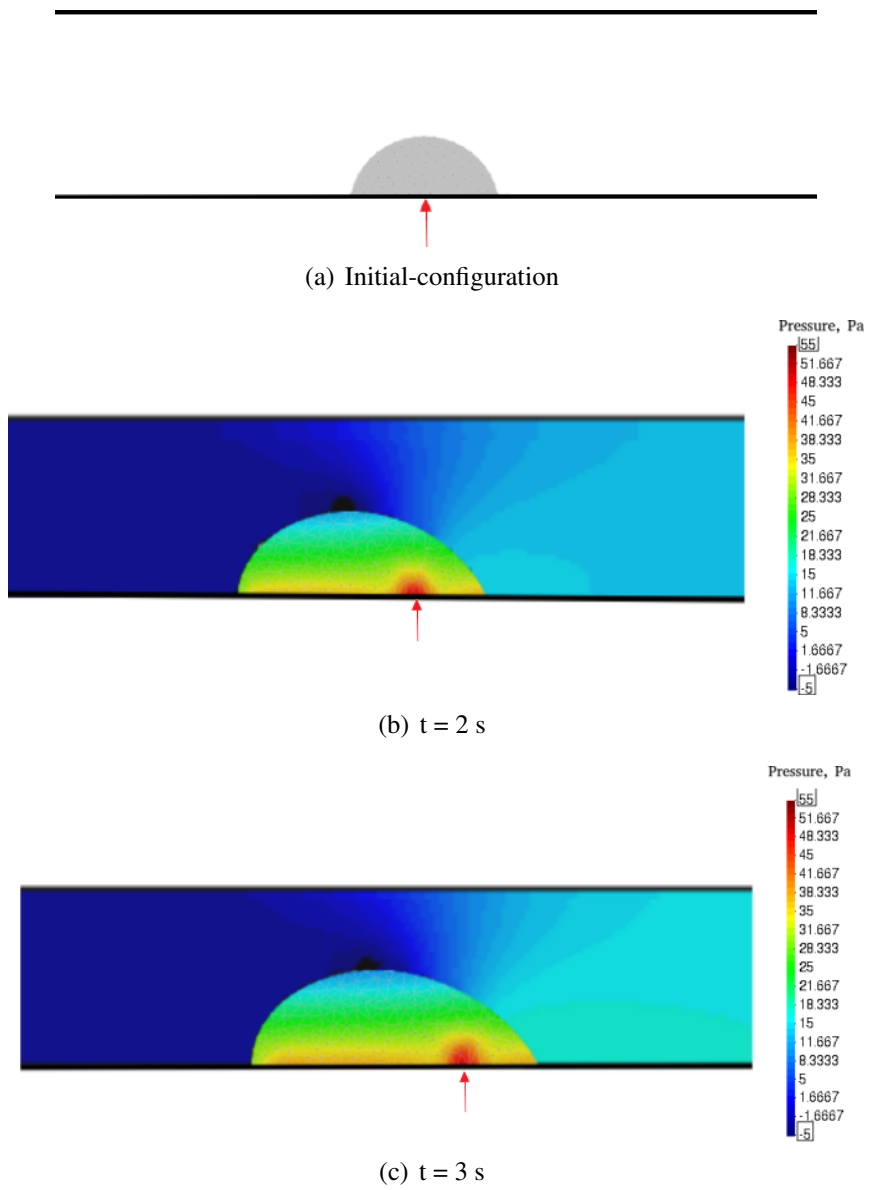
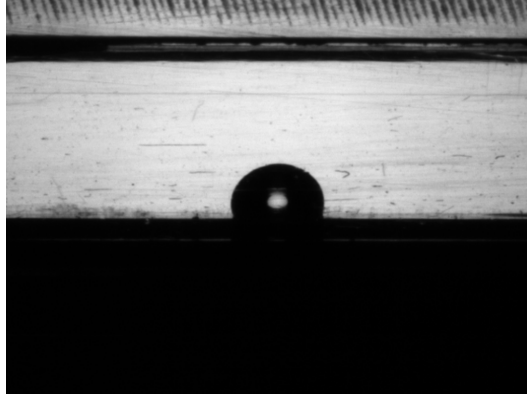


Figure 5.8: Injection simulation: evolution of water drop injected on kapton substrate at flow rates of F6-Q15.



(a) Initial configuration



(b) $t = 0.65 \text{ s}$



(c) $t = 1.3 \text{ s}$

Figure 5.9: Injection experiment: evolution of water drop injected on PTFE substrate at flow rates of F6-Q25.

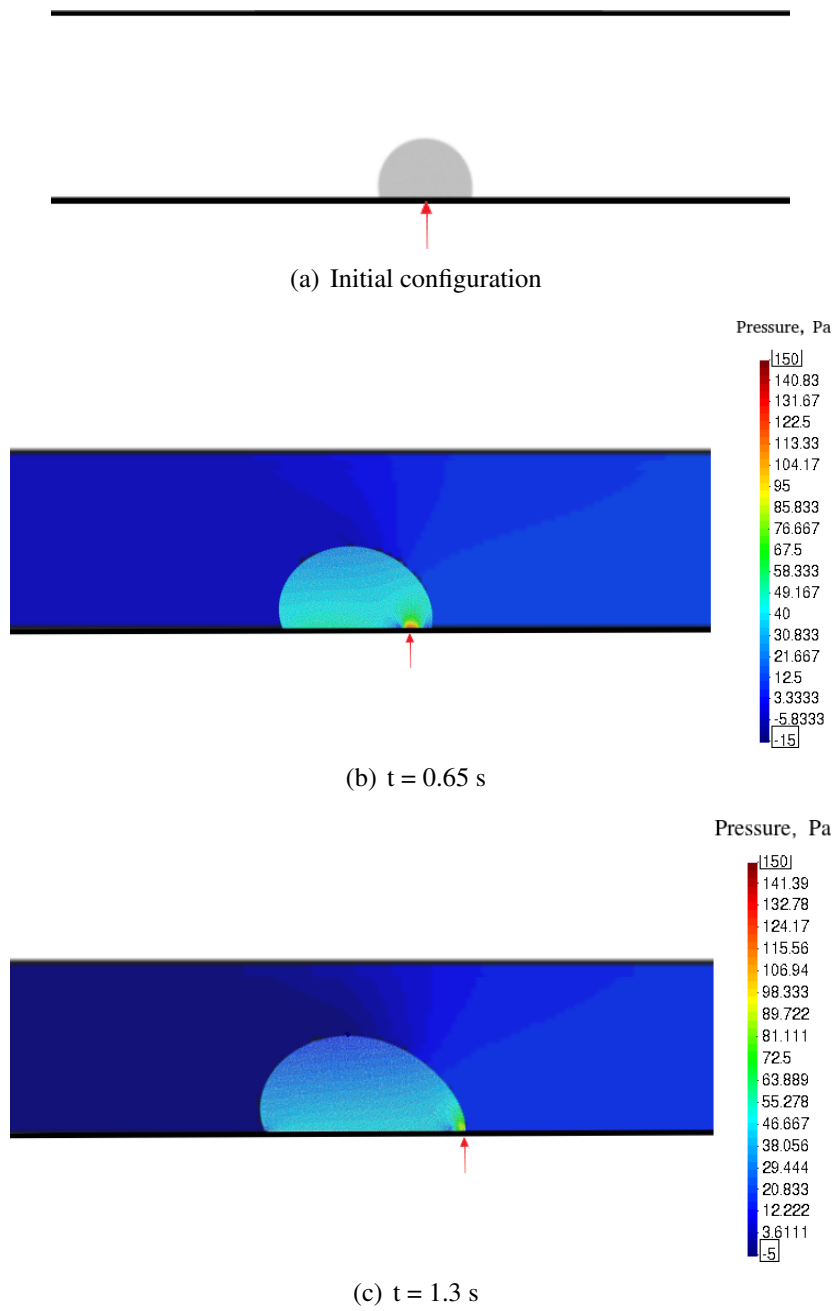
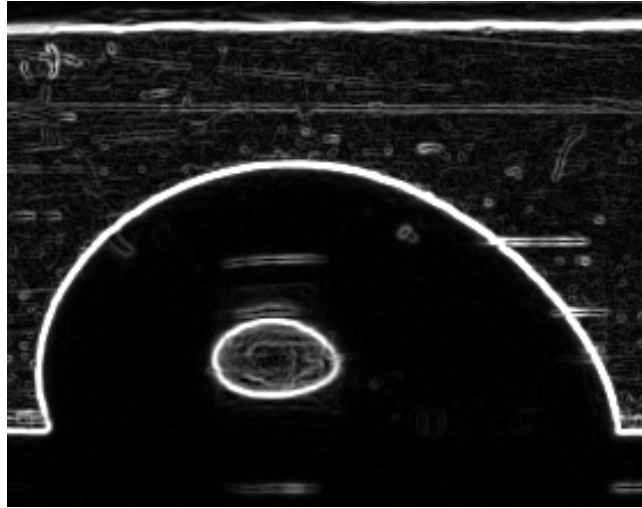
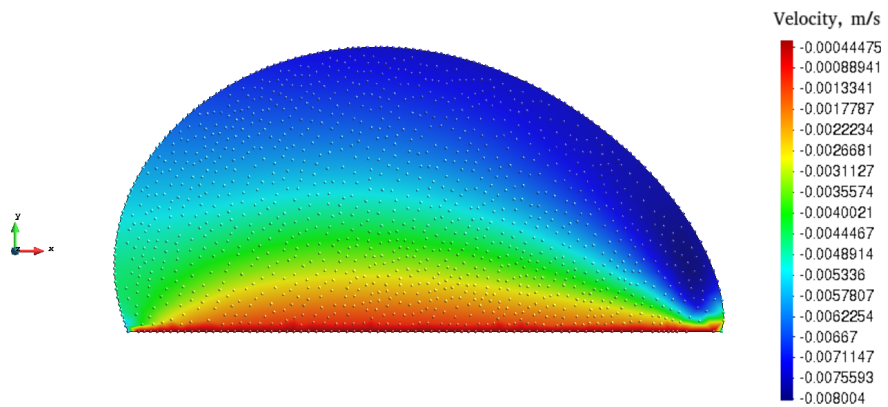


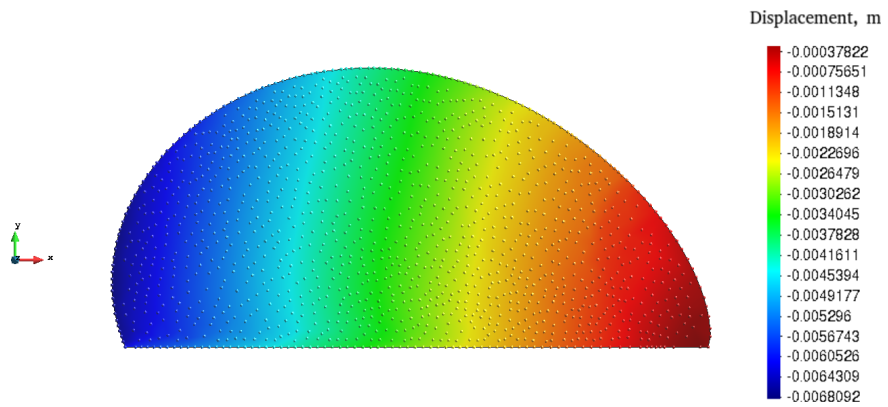
Figure 5.10: Injection simulation: drop evolution of water drop injected on PTFE substrate at flow rate of F6-Q25.



(a)



(b)

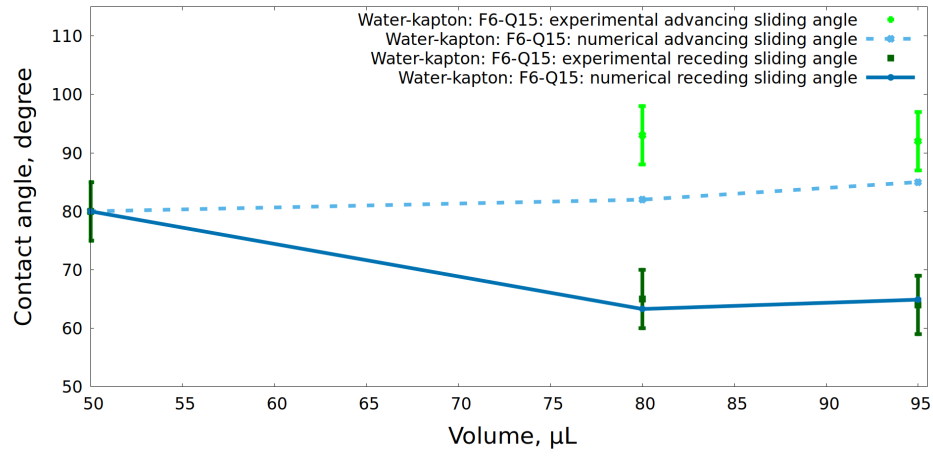


(c)

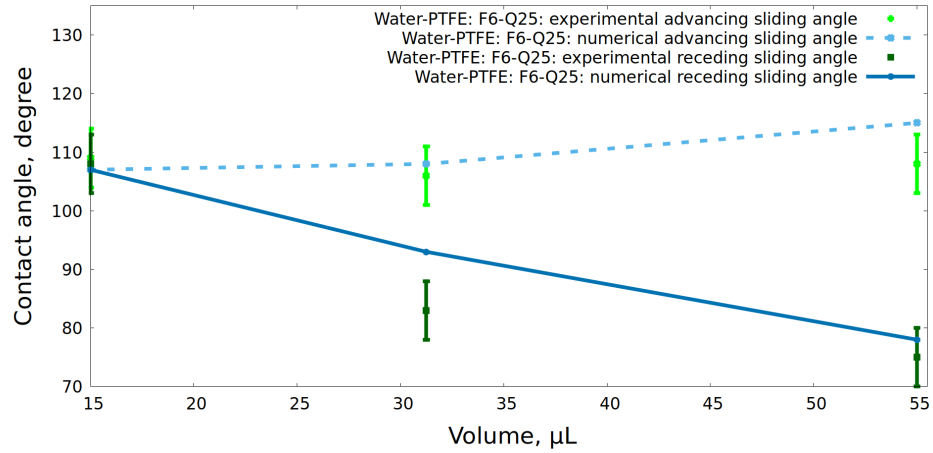
Figure 5.11: Profiles of sliding water drops on PTFE substrate, driven by an inlet airflow of 6 SLPM: a) experimentally and b,c) numerically.

Injection parameters	Time, (s)	Volume, (μL)	Exp. ASA, (deg)	Num. ASA, (deg)	Error _{ASA} , (%)	Exp. RSA, (deg)	Num. RSA, (deg)	Error _{RSA} , (%)
Water-kapton: F6-Q15	2	80	93	82	11.8	65	63	3.1
	3	95	92	85	7.6	64	65	1.6
Water-PTFE: F6-Q5	0.65	31.25	106	108	1.9	83	93	12
	1.6	55	108	115	6.5	75	78	4

Table 5.4: Dynamic contact angle vs volume of injected drop, experimental vs. numerical, for water drop injected on kapton and PTFE substrates. ASA and RSA stand for advancing and receding sliding angles, respectively.



(a)



(b)

Figure 5.12: Dynamic contact angle vs volume of injected drop, experimental vs. numerical, for : (a) water injected on kapton at flow rates of F6-Q15 and (b) PTFE substrates at flow rates of F6-Q25.

The simulation results are in good agreement with the experimental data with an average error of 5%, considering both hydrophilic and hydrophobic substrates as shown in Table 5.4 and Fig. 5.12. Injected water forms a drop that spreads on the hydrophilic kapton substrate (Fig. 5.8). The drop does not detach due to the high adhesion force between the drop and hydrophilic substrate. We stopped the simulation when the water drop came in contact with the sidewalls during the experiment. This evolution in the out-of-plane direction can not be simulated in 2D. On the PTFE substrate, however, the injected water forms a drop. The water drop leaves the PTFE substrate at an inlet airflow rate of 6 SLPM ($Re \sim 1000$), contact angle hysteresis of 30° , and drop-to-channel height ratio of ~ 0.65 (Fig. 5.10 and 5.11).

Our injection and detachment analysis match the experimental results found by Cho *et al.* [49, 50]. In their work, water was injected on a hydrophobic surface inside a 1 mm (H) x 1.6 mm (W) x 40 mm (L) fuel cell channel, and driven by varying inlet airflow rates. The range of Reynolds numbers of their inlet airflows was between ~ 450 and ~ 900 . Under equilibrium condition, the drop rests on the substrate with an equilibrium contact angle of $\theta_e = 128^\circ$. Considering twelve drop-to-channel height ratios that vary between 0.63 and 0.97, Cho *et al.* reported the required air velocity to detach each drop. They concluded that the detachment velocity is inversely proportional to the droplet diameter. At the highest and lowest values of Reynolds numbers, i.e., $Re \sim 900$ and 450 , the drop detached at drop-to-channel height ratios of ~ 0.64 and 0.96 , respectively. The detachment occurred when the contact angle hysteresis was found to be $\sim 40^\circ$.

For our detached drop on the PTFE substrate, Fig. 5.11 shows its sliding profile. Once the drop has detached, we switch off the injection simulation. The contact angle hysteresis is found to be $\sim 30^\circ$, both experimentally and numerically, with an advancing sliding angle value of $\sim 110^\circ$ and a receding contact angle value of $\sim 80^\circ$. The average sliding velocity of the liquid drop after detachment is tracked using imageJ software. Experimentally, it is found to be $\sim 0.015 \text{ m s}^{-1}$. In 2D simulation, the value of the sliding velocity is found to be 0.005 m s^{-1} (see Fig. 5.11(b)). Though the experimental and numerical sliding profiles are found to be in very good agreement, the sliding velocity obtained numerically is found

to be under-predicted by a factor of ~ 3 . This variation in the sliding velocity is expected, as both values of the water injection rate and the pressure drop along the channel are found to be scaled by a factor of ~ 3 (see Secs. 2.9.3 and 5.7, respectively).

5.8.2 3D embedded flow simulations: water drop ejection from a PEMFC channel

In this second study, we conduct 3D simulation of liquid drop motion along channels of rectangular cross-section under the effect of gas injection. Note that we are not modeling the drop injection into the channel. This should be the object of future work as suggested in Sec. 6.7.2. Once again, we wish to duplicated the work performed by the Berkeley group for water drop detachment in a PEMFC gas flow channel of 6.5 mm (H) x 6.5 mm (W) x 120 mm (L). Under equilibrium condition, the drop rests on the hydrophobic PTFE substrate with a contact angle of 107° at the center of the channel. Two experimental scenarios are considered as follows: i) drop-to-channel height ratio of 0.65 with an inlet airflow of 6 SLPM (case #1), and ii) drop-to-channel height ratio of 0.53 with an inlet airflow of 10 SLPM (case #2).

As the drop immediately slides along the channel, its experimental sliding profile and average sliding velocity are tracked using imageJ software. The sliding profiles for both cases are shown in Fig. 5.13. For a drop with drop-to-channel height ratio of 0.65 and driven by an inlet airflow of 6 SLPM, the values of the advancing and receding sliding angles are found to be $\sim 110^\circ$ and $\sim 85^\circ$, respectively. These values are found to be $\sim 113^\circ$ and $\sim 80^\circ$ in the case of a drop-to-channel height ratio of 0.53 and driven by an inlet airflow of 10 SLPM. The average sliding velocities are found to be $\sim 0.015 \text{ m s}^{-1}$ and $\sim 0.0028 \text{ m s}^{-1}$ for the first and the second cases, respectively.

Two simulations are performed to reproduce these two experimental scenarios, i.e., case #1 and case #2 above. The physical properties of the gas phase are set as $\rho = 1.2 \text{ kg m}^{-3}$ and $\mu = 1.81 \times 10^{-5} \text{ kg m}^{-1} \text{ s}^{-1}$. The physical properties of the liquid phase are $\rho = 1000 \text{ kg m}^{-3}$ and $\mu = 8.9 \times 10^{-4} \text{ kg m}^{-1} \text{ s}^{-1}$. The mesh size of the Lagrangian domain is chosen to be $4 \times 10^{-4} \text{ m}$ and the time step was set to $1 \times 10^{-5} \text{ s}$ for both cases.

The pressure fields along the channel and the average sliding velocities for case #1

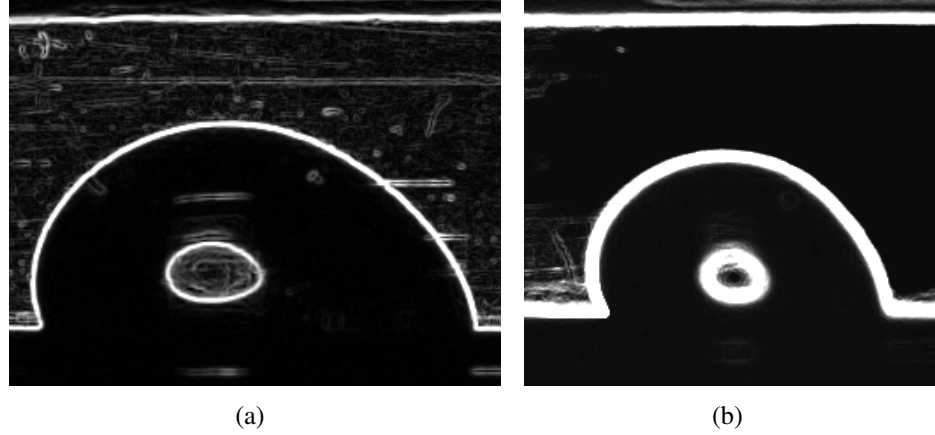


Figure 5.13: Profiles of sliding water drops on PTFE substrate: a) a drop with drop-to-channel height ratio of 0.65 driven by airflow of 6 SLPM, and b) a drop with drop-to-channel height ratio of 0.53 driven by airflow of 10 SLPM.

and case #2 are shown in Figs. 5.14 and 5.15, respectively. The drop profiles obtained numerically (see Figs. 5.14(d) and 5.15(d)) are found to be in good agreement with the experimental profiles (Fig. 5.13). The average sliding velocities are found to be $\sim 0.0163 \text{ m s}^{-1}$ and $\sim 0.0025 \text{ m s}^{-1}$ for the first and the second cases, respectively (see Figs. 5.14(f) and 5.15(f)). The relative errors between the experimental and numerical average sliding velocities are found to be 8.7% and 10.0% for the first and the second cases, respectively. For the first case, the values of the advancing and receding sliding angles are found numerically to be $\sim 109^\circ$ and $\sim 92^\circ$, respectively. These values are found numerically to be $\sim 112^\circ$ and $\sim 90^\circ$ for the second case, respectively. The average relative error between the experimental and numerical contact angle measurements is found to be $\sim 6\%$ for both cases.

The presence of the drop increases the pressure drop along the channel. For case #1, Figs 5.5(b) and 5.14(b) show that the pressure drop increased by $\sim 6.5 \text{ Pa}$. The pressure drop for the second case was found to be $\sim 9 \text{ Pa}$ (Figs 5.6(b) and 5.15(b)). The pressure drop across the drop was found to be $\sim 7 \text{ Pa}$ and $\sim 11 \text{ Pa}$ for the first and the second cases, respectively (Figs. 5.14(c) and 5.15(c)). This indicates that the drop size and the inlet air flow rate both play important roles in affecting the pressure drop along the channel.

The evolution of the average sliding velocity for both cases shows physical oscillations (Figs. 5.14(f) and 5.15(f)). These oscillations are hypothesized to be due to the minor fluctuations in the pressure evolution corresponding to the drop motion, as shown in Figs 5.14(e) and 5.15(e) for cases #1 and #2, respectively.

5.9 An embedded simulation for Reynolds number greater than 2300

This section addresses the effect of Reynolds number (Re) on the pressure drop along the channel. We will take advantage of one last experimental batch of data produced by the Berkeley and ESDLab Groups, for transitional flow inside a 6.5 mm (H) x 6.5 mm (W) x 120 mm (L) channel driven by airflow of 19 SLPM.

Practically, the fluid flow in a pipe can be i) a laminar flow, when $Re \leq 2300$, ii) a turbulent flow, when $Re > 4000$, or iii) a transitional flow, when $4000 > Re \geq 2300$. Under well-controlled conditions, i.e., smooth pipe with no external disturbances, laminar flows can be maintained for Reynolds numbers of up to a hundred thousand [42]. Hence, we aim to study the effect of the transitional flow regime on our embedded model. First, we examine the Eulerian model assuming a smooth rectangular pipe, i.e., in the absence of embedded drops. Then, we perform a two-phase flow simulation to obtain i) the evolution of the pressure drop along the channel and ii) the sliding profile of the embedded drop.

For this experimental case, air inlet the channel at a flow rate of 19 SLPM, i.e., with an inlet velocity of 7.5 m s^{-1} . Thus, the value of Re is calculated to be ~ 3250 . The drop-to-channel height ratio is 0.33. Due to high inlet speed, we could not track the sliding velocity of the drop. Instead, we obtained its sliding profile.

We first simulate the pressure evolution of a transitional flow regime inside the channel. We set the physical properties of the air as $\rho = 1.2 \text{ kg m}^{-3}$ and $\mu = 1.81 \times 10^{-5} \text{ kg m}^{-1} \text{ s}^{-1}$. The mesh size and time step are chosen to be $\sim 1.7 \times 10^{-3} \text{ m}$ and $1 \times 10^{-4} \text{ s}$, respectively. Figure 5.16 shows the numerical results for both i) steady-state pressure field along the channel and ii) pressure drop evolution at the inlet of the channel.

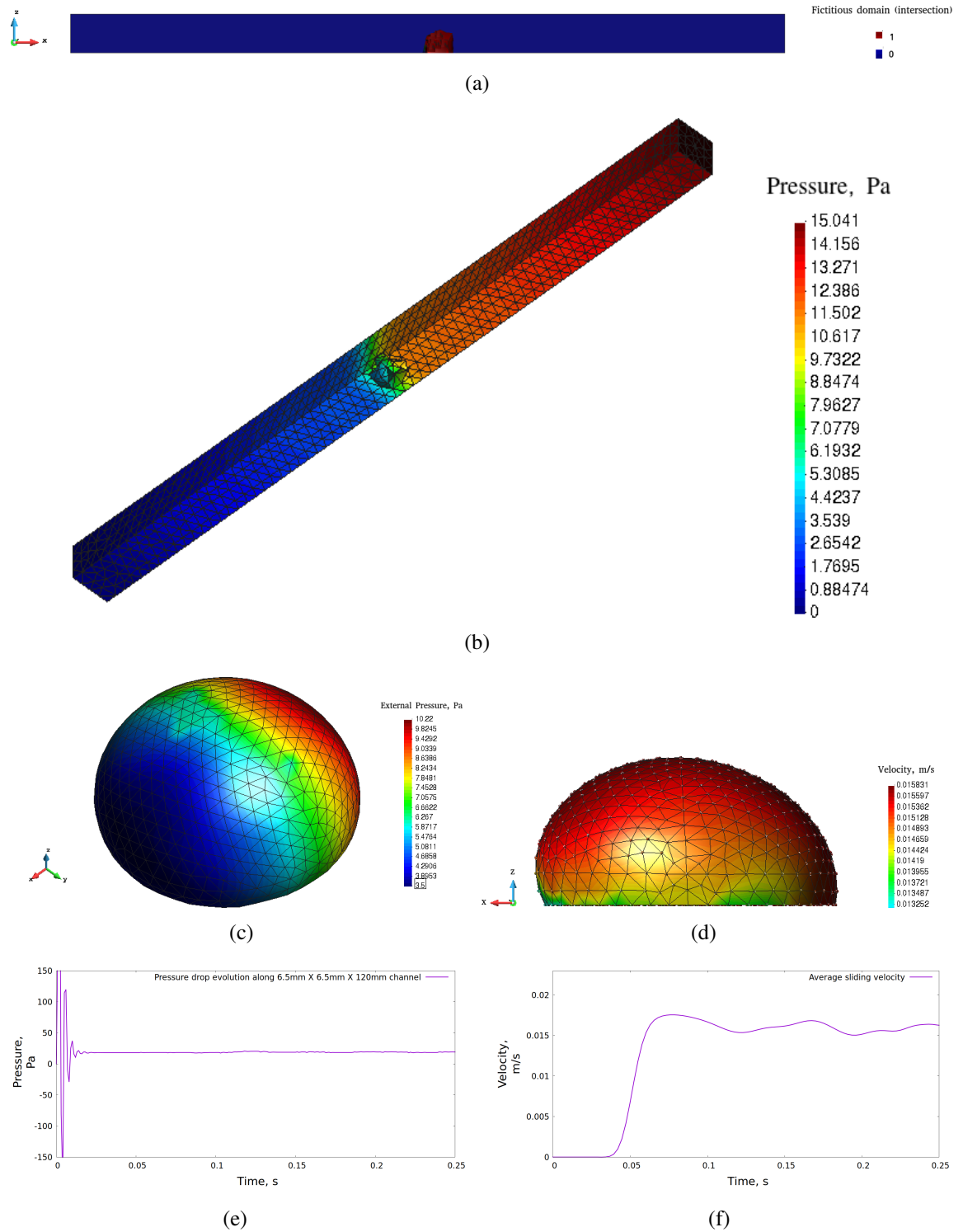


Figure 5.14: Numerical results for case #1 of the 3D embedded simulation: a) representation of the initial configuration of drop-to-channel height ratio, b) pressure field along a 6.5 mm (H) x 6.5 mm (W) x 120 mm (L) channel driven by airflow at 6 SLPM, c) external pressure acting on a water drop (Lagrangian domain), d) profile of sliding water drops on PTFE substrate, e) pressure evolution at the inlet of the channel, and f) evolution of the average sliding velocity.

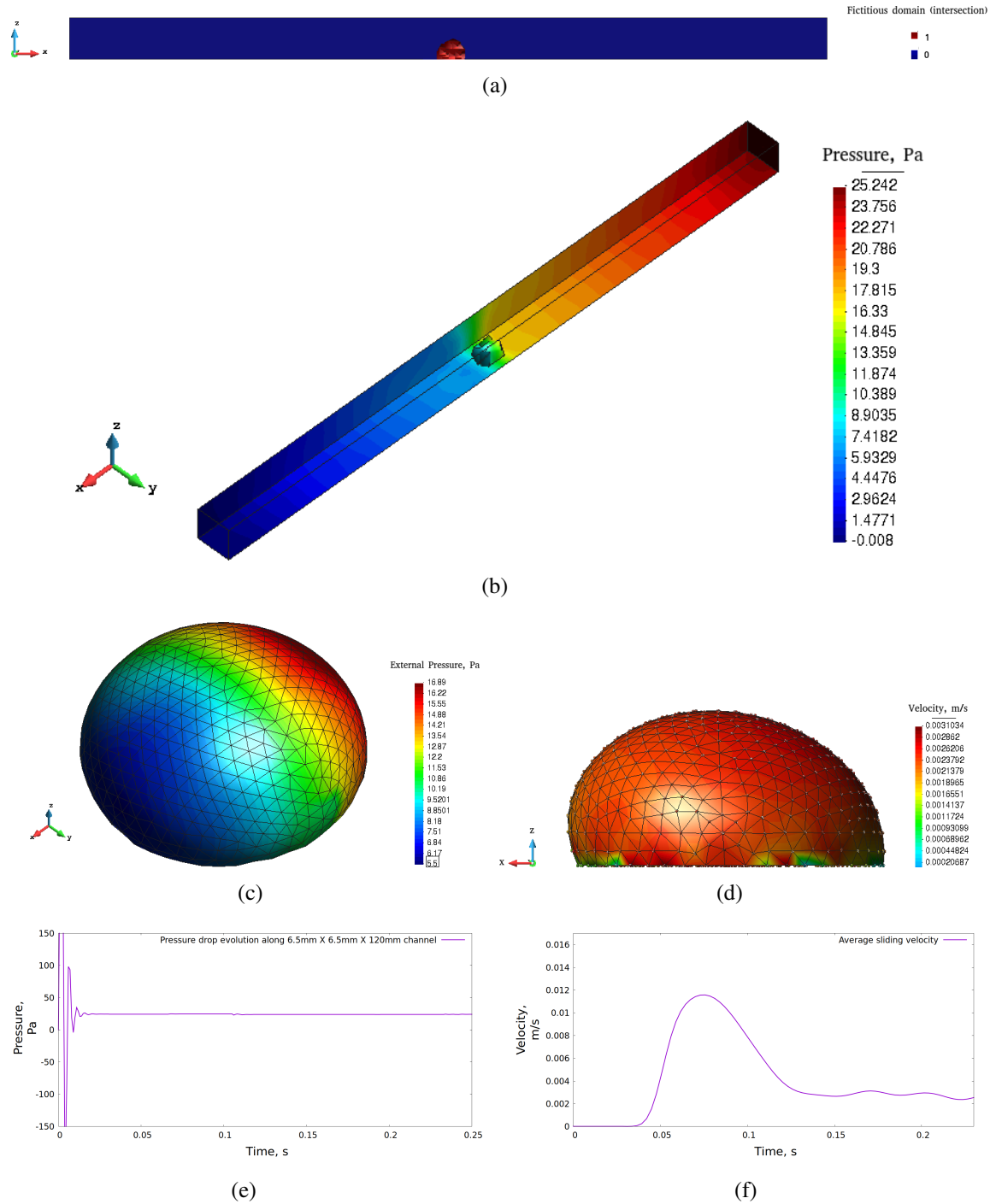
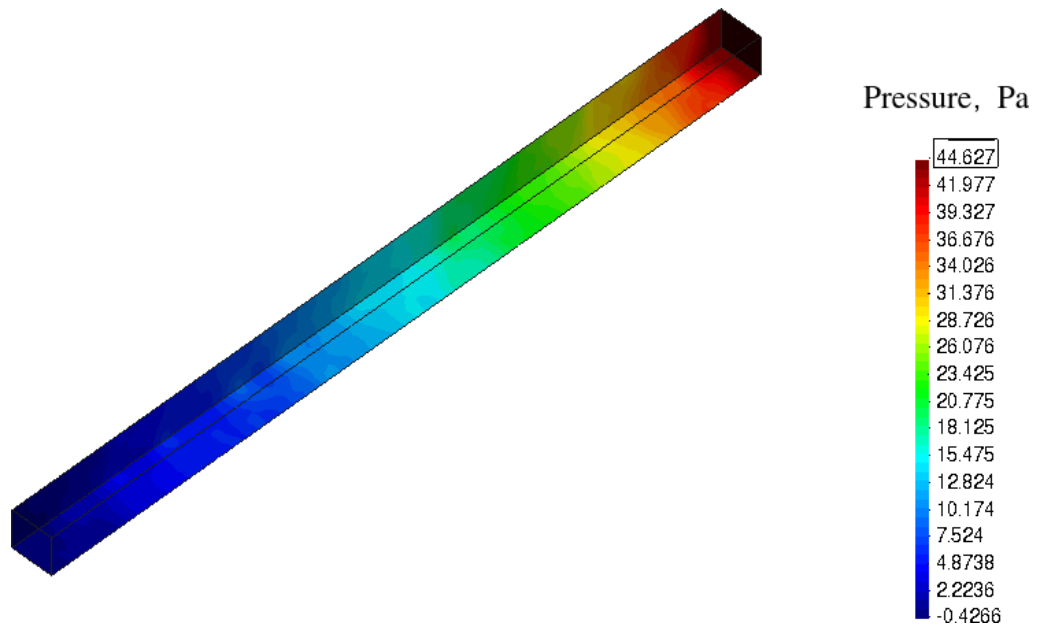


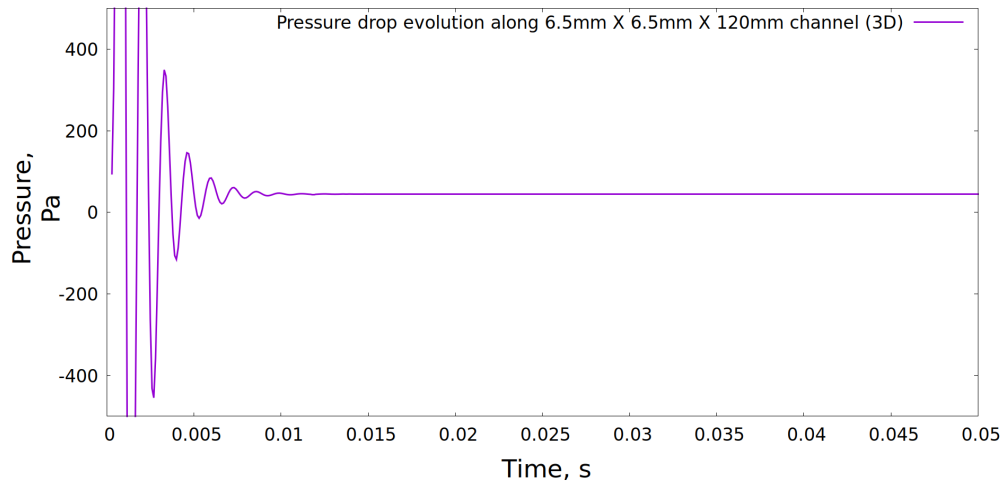
Figure 5.15: Numerical results for case #2 of the 3D embedded simulation: a) representation of the initial configuration of drop-to-channel height ratio, b) pressure field along a 6.5 mm (H) x 6.5 mm (W) x 120 mm (L) channel driven by airflow at 10 SLPM, c) external pressure acting on a water drop (Lagrangian domain), d) profile of sliding water drops on PTFE substrate, e) pressure evolution at the inlet of the channel, and f) evolution of the average sliding velocity.

Numerical oscillations are observed initially, i.e., for $0 < t < 0.015$ s. Similar oscillations were observed for laminar flow regimes (see Figs. 5.14 and 5.14), which is hypothesized to be due to the high value of the instantaneous prescribed inlet velocity. For time $t > 0.015$, the pressure field reaches its steady state of $\Delta P \sim 45$ Pa (Fig. 5.16(b)). Though the Re number of the gas flow falls in the transitional regime, the pressure field demonstrates a laminar flow behavior. It is hypothesized to be due to the smoothness of the pipe as well as the effect of the numerical stabilization, in agreement with experimental observations [42]. For laminar flow with $Re \sim 3250$, the Darcy friction factor is found to be $f_D \sim 0.063$ (Table 5.3). Thus, the analytically predicted pressure drop along the channel is calculated from eq. 5.7.3 to be ~ 40 Pa, which is in good agreement with what is found numerically (Fig. 5.16).

We then examine the effect of Re number on the embedded, two-phase flow, simulation. We set the physical properties of the drop as $\rho = 1000 \text{ kg m}^{-3}$ and $\mu = 8.9 \times 10^{-4} \text{ kg m}^{-1} \text{ s}^{-1}$. The mesh size of the Lagrangian domain is chosen to be $2.8 \times 10^{-4} \text{ m}$. Figure 5.17 shows the pressure drop evolution along the channel at different time steps. The relevant sliding profiles obtained numerically are shown in Fig. 5.18. The presence of the drop disturbs the pressure field and, thus, leads to a transitional flow regime (Fig. 5.17(d)). Thus, special attention need to be paid for $Re > 2300$. One has to include the effect of the transitional regime, which is outside the scope of this work. Though we are performing a simulation for a transitional flow regime, Fig. 5.19 shows good agreement between the experimental and numerical sliding profiles. The drop evolves in accordance with the applied forcing field (Figs. 5.18). The advancing and receding sliding angles are measured using ImageJ software. Experimentally, these angles are found to be 115° and 71° , respectively. They are numerically found to be 117° and 69° , respectively. The relative error was found to be less than 5%.



(a)



(b)

Figure 5.16: Numerical results for transitional flow inside a 6.5 mm (H) x 6.5 mm (W) x 120 mm (L) channel driven by airflow at 19 SLPM, without the drop: a) pressure field along the channel, b) pressure evolution at the inlet of the channel.

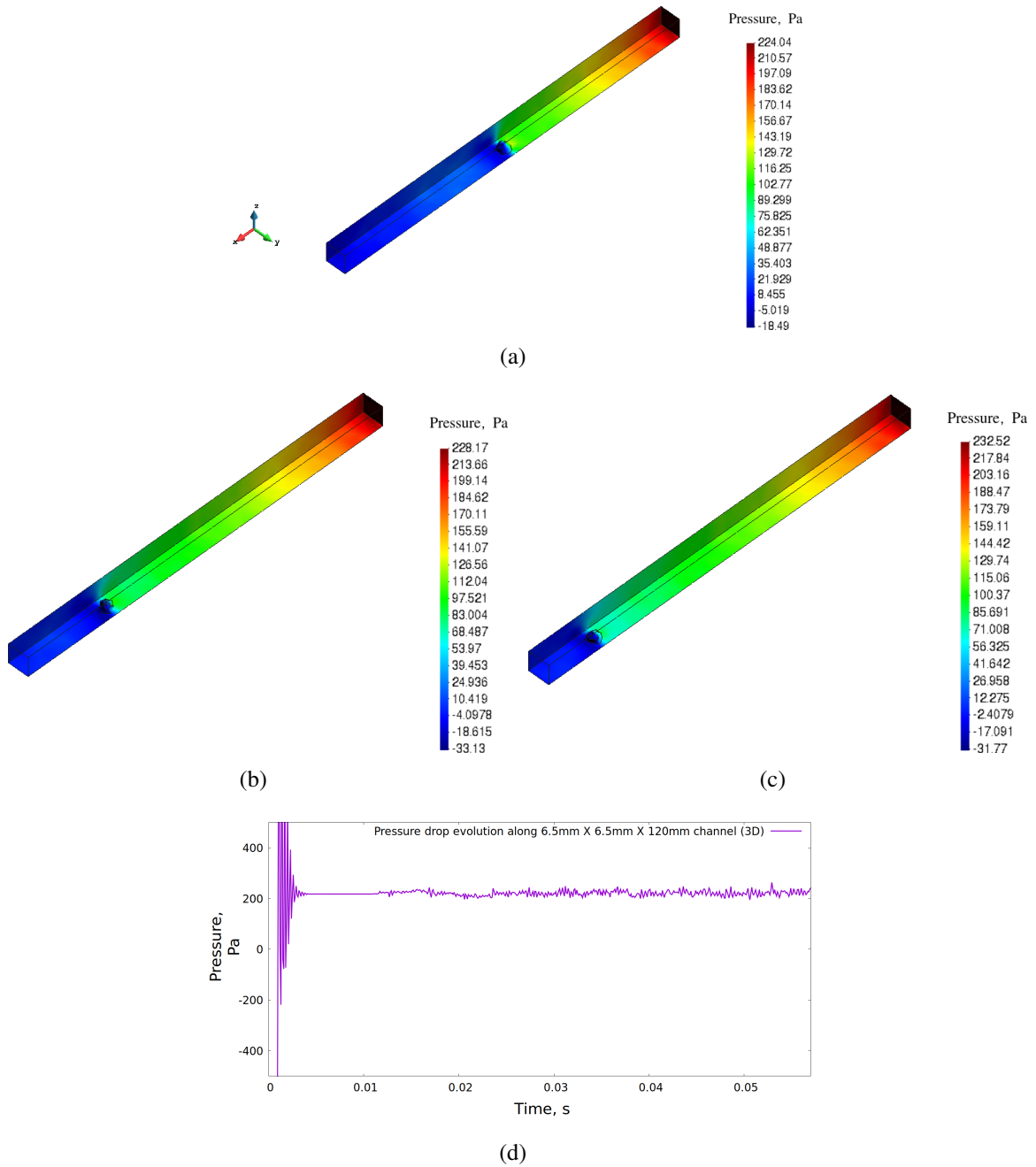


Figure 5.17: Numerical results for transitional flow in the 3D embedded simulation, pressure field along a 6.5 mm (H) x 6.5 mm (W) x 120 mm (L) channel driven by airflow at 19 SLPM: a) at $t = 0.01$ s, b) at $t = 0.055$ s, c) at $t = 0.064$ s, and d) pressure evolution at the inlet of the channel.

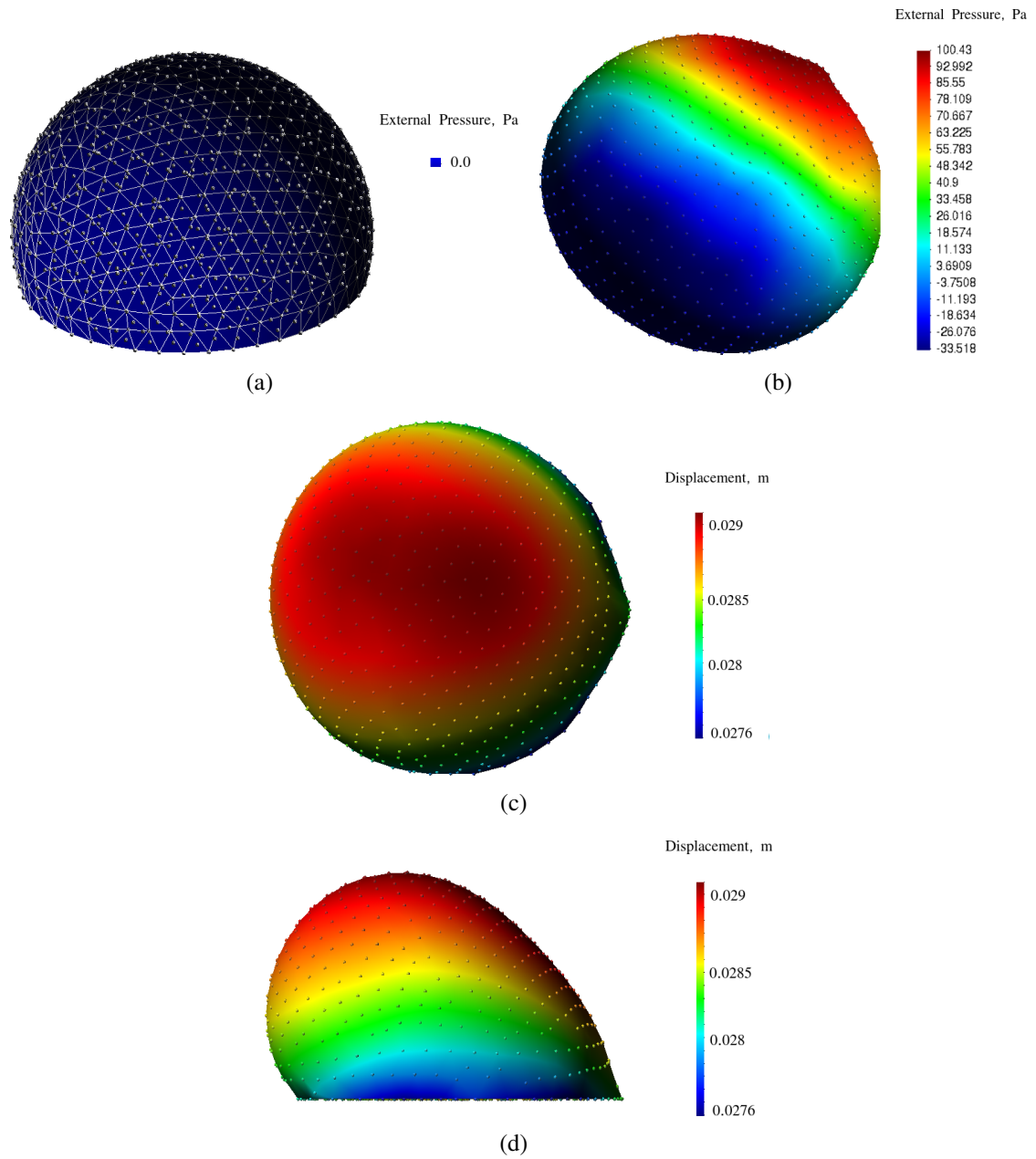
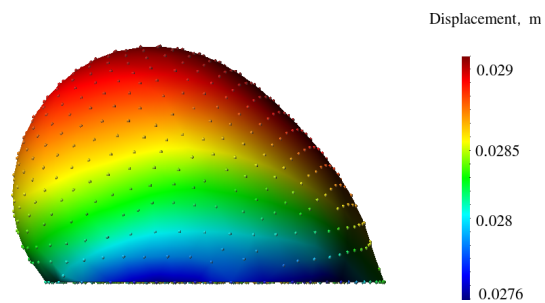


Figure 5.18: Numerical results for transitional flow in the 3D embedded simulation, drop profiles inside a 6.5 mm (H) x 6.5 mm (W) x 120 mm (L) channel driven by airflow at 19 SLPM: a) initial drop profile, b) external pressure at $t = 0.055$ s, c) top view $t = 0.055$ s, and d) side view $t = 0.055$ s.



(a)



(b)

Figure 5.19: Profile of sliding water drops on PTFE substrate, driven by an inlet airflow of 19 SLPM: a) experimentally, b) numerically.

Case number	v_{in} (m s ⁻¹)	Pressure drop along the channel in the absence of the drop, (Pa)	Pressure drop along the channel in the presence of the drop, (Pa)	Average sliding velocity of the drop (m s ⁻¹)	Advancing sliding angle (°)	Receding sliding angle (°)
1	2.37	7.3	15	0.016	109	90
2	3.35	12.5	31	0.03	155	77
3	3.95	16.7	43	0.047	160	71

Table 5.5: Numerical parametric analysis for different values of inlet air velocity (v_{in}): horizontal channel of size 6.5 mm x 6.5 mm x 12 mm, and drop-to-channel height ratio of ~ 0.65 .

5.10 Numerical experiments

In this section, we perform 3D numerical experiments to examine the effect of the inlet airflow rate on an embedded, two-phase flow. We consider the same channel of size 6.5 mm x 6.5 mm x 12 mm, and a drop-to-channel height ratio of ~ 0.65 . Three numerical scenarios are considered for an embedded drop driven by inlet air velocity of: case #1) $v_{in} = 2.37 \text{ m s}^{-1}$, which corresponds to case #1 of Sec. 5.8.2, case #2) $v_{in} = 3.35 \text{ m s}^{-1}$, and case #3) $v_{in} = 3.95 \text{ m s}^{-1}$. For each case, we obtain i) the pressure drop along the channel, ii) the average sliding velocity of the drop, and iii) the values of the advancing and receding sliding angles.

The same physical properties of the gas/liquid, i.e., air/water, are adopted. The mesh sizes of the Lagrangian and Eulerian domains are chosen to be $4 \times 10^{-4} \text{ m}$ and $1 \times 10^{-3} \text{ m}$, respectively.

Simulation results are shown in Figs. 5.14, 5.20, and 5.21. Consequently, numerical parametric analysis for different values of inlet air velocity is presented in Table. 5.5. The higher the inlet velocity of the air, the higher i) the pressure drop along the channel, ii) the average sliding velocity of the drop, and iii) the dynamic contact angle hysteresis. Figure 5.22 demonstrates the relation between the inlet air velocity and both the pressure drop along the channel and the average sliding velocity of the drop. These results show that both the pressure drop along the channel and the average sliding velocity of the drop increase nonlinearly with the inlet air velocity. The numerical profiles of the sliding drops for the three cases are shown in Fig 5.23. As expected, the higher the external pressure across the drop, the higher its dynamic contact angle hysteresis.

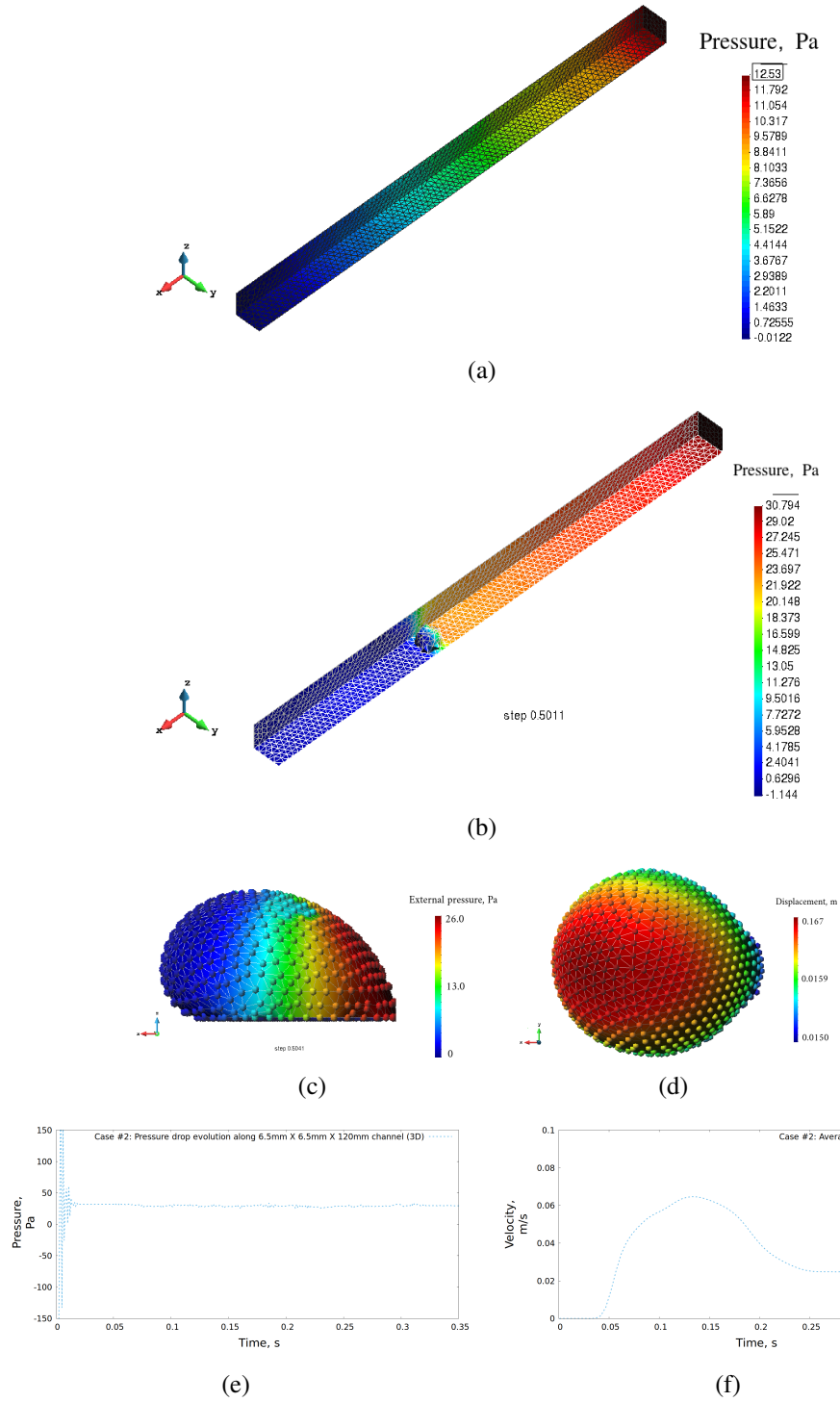


Figure 5.20: Numerical results for case #2 of the 3D embedded simulation: a) pressure field along a 6.5 mm (H) x 6.5 mm (W) x 120 mm (L) horizontal channel in the absence of the drop, b) pressure field along a 6.5 mm (H) x 6.5 mm (W) x 120 mm (L) horizontal channel in the presence of the drop, c) external pressure acting on a water drop (Lagrangian domain), d) profile of sliding water drops on PTFE substrate (top view), e) pressure evolution at the inlet of the channel, and f) evolution of the average sliding velocity.

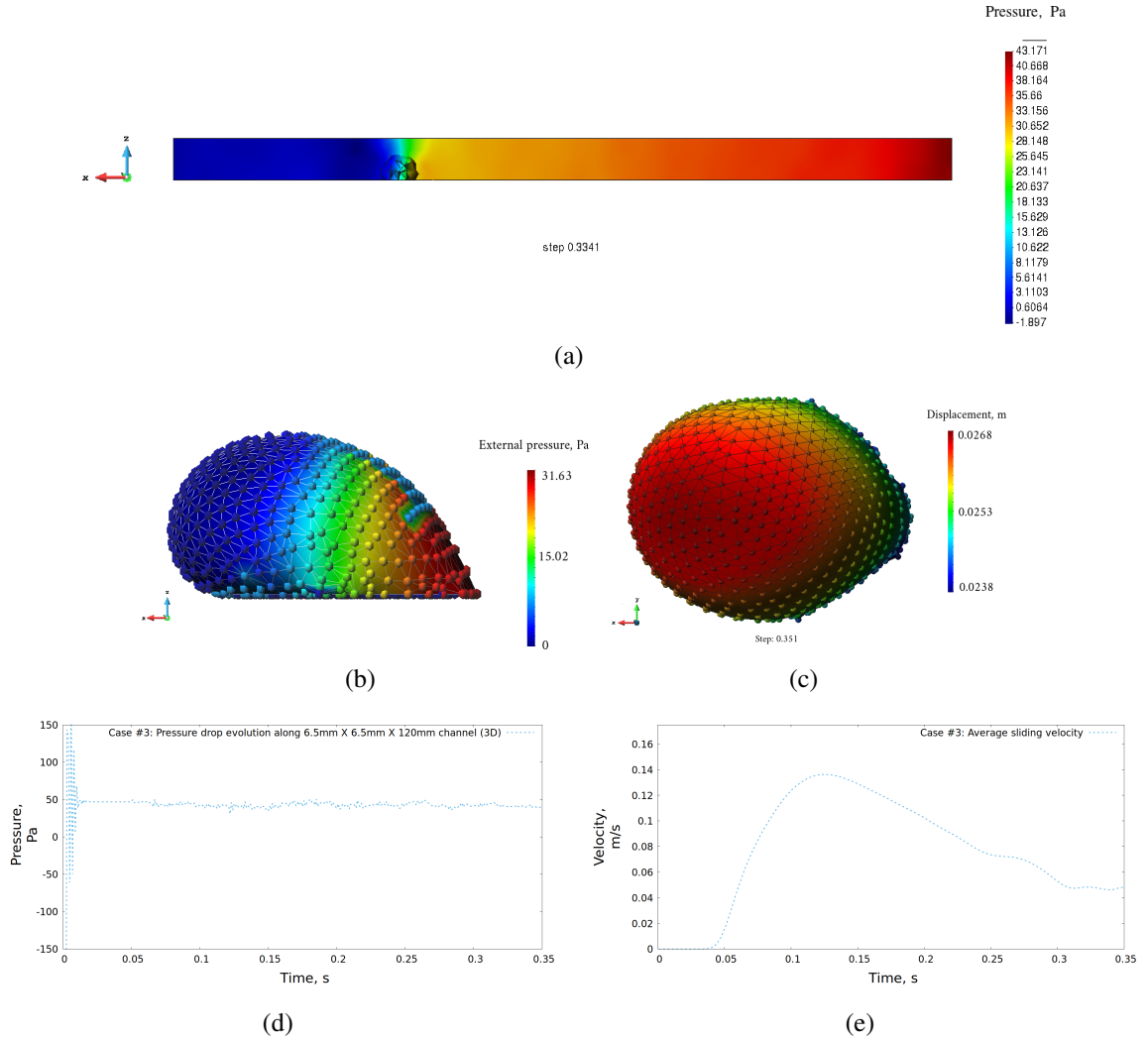
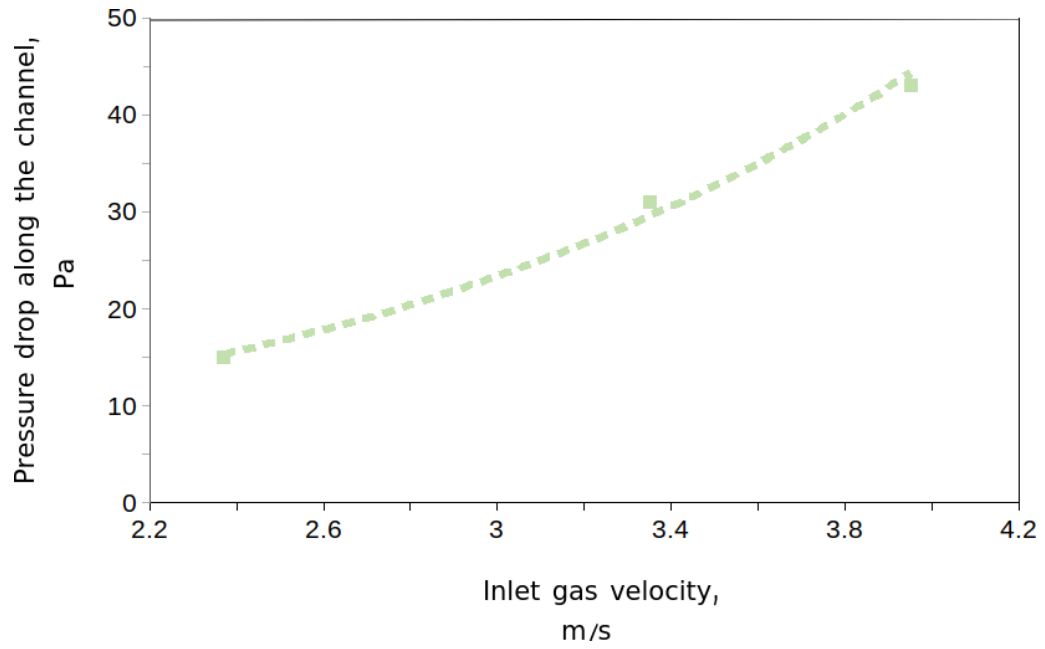
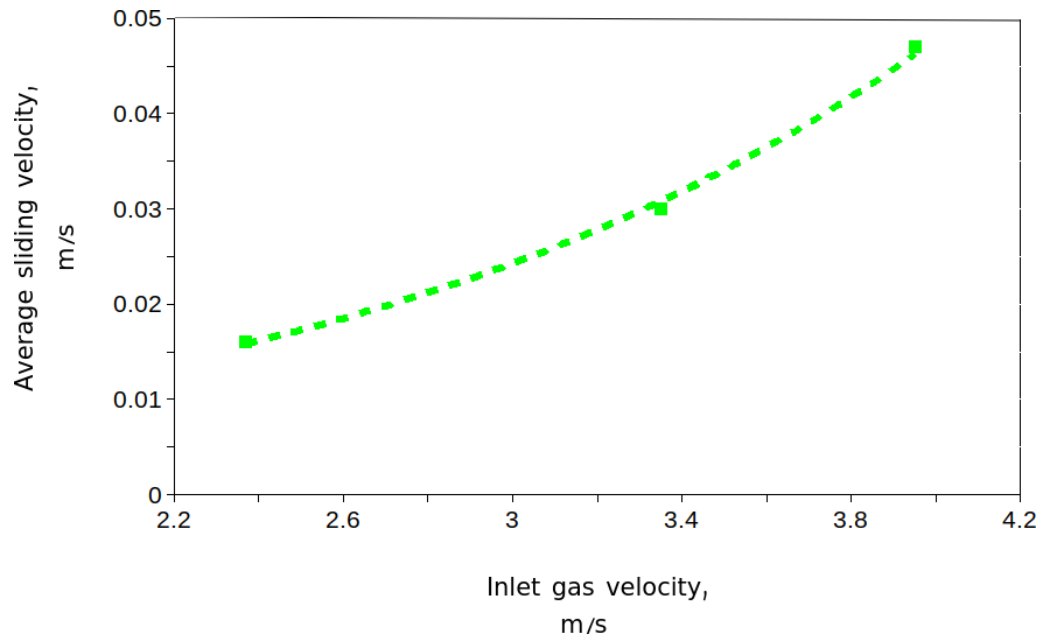


Figure 5.21: Numerical results for case #3 of the 3D embedded simulation: a) pressure field along a 6.5 mm (H) x 6.5 mm (W) x 120 mm (L) horizontal channel driven by airflow at 3.95 m s^{-1} (side view of drop-to-channel height ratio of ~ 0.65), b) external pressure acting on a water drop (Lagrangian domain), c) profile of sliding water drops on PTFE substrate (top view), d) pressure evolution at the inlet of the channel, and e) evolution of the average sliding velocity.



(a)



(b)

Figure 5.22: Numerical parametric analysis for different values of inlet air velocity (v_{in}): (a) inlet air velocity vs pressure drop along the channel (in the presence of the drop) and (b) inlet air velocity vs average sliding velocity of the drop.

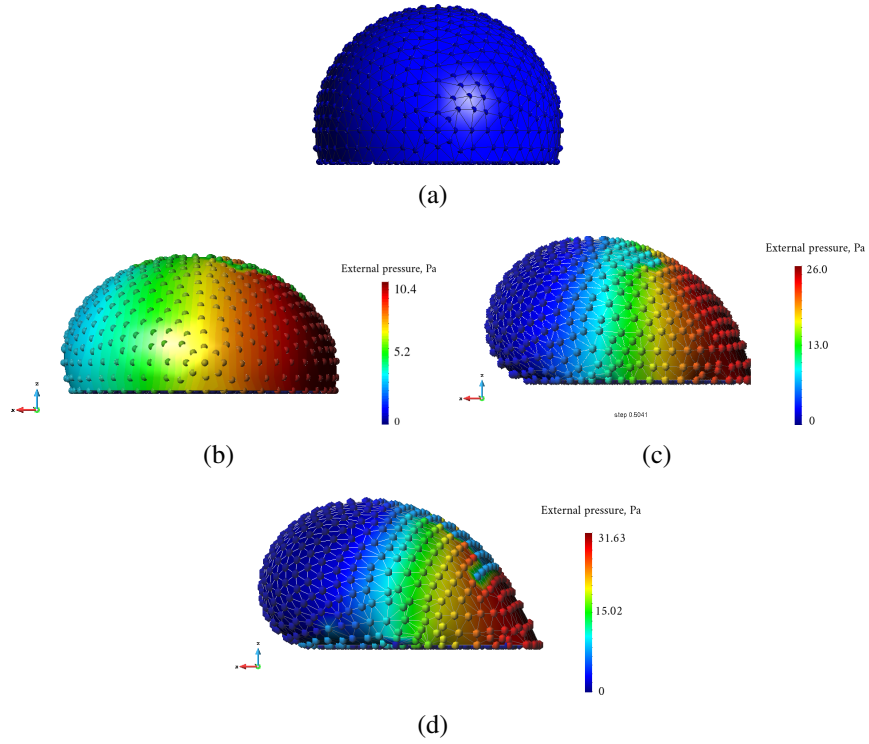


Figure 5.23: Numerical profiles of water drops on PTFE substrate: (a) initial drop configuration, (b) sliding profile for case #1, (c) sliding profile for case #2, (d) sliding profile for case #3.

5.11 Conclusion

This chapter successfully demonstrated the ability of our Eulerian-PFEM model to simulate two-phase flow of drops embedded in gas channels. The Eulerian model was validated first using an approximate analytical analysis. Following this analysis, the embedded formulation was validated using experimental data performed by the UC Berkeley group.

Our model was first examined in 2D. Simulation results were compared with two micro drop injection experiments for water on kapton (hydrophilic) and PTFE (hydrophobic) substrates. The model was able to predict the type of water formation inside the gas channel. Drop detachment was also successfully reproduced for a specific drop-to-channel height ratio (Figs. 5.9-5.11). Though the 2D model produces good qualitative outcomes and within the same order of magnitude of the experimental data, it neglects out-of-plane forces. Thus, we found numerically predicted pressure drop and drop sliding speed under predicted by a factor of about 3.

We extended the 2D Eulerian-PFEM model to 3D. The model was examined using two experiments for drop sliding at different inlet airflow rates and drop-to-channel height ratios. Numerical results of the drop profiles and average sliding velocities were found to be in good agreement with the experimental data. Our simulations showed that both airflow and drop-to-channel height ratio play major roles in drop sliding dynamics: smaller drops require higher inlet airflow rates to detach. It is worth mentioning that the GDL in real fuel cells is a porous media made with carbon fibers. Hence, the effect of surface roughness and porosity should be considered and included into the model for tracking the spatio-temporal evolution of the liquid drops/films along the GDL channel.

We demonstrated the effect of the Reynolds number on the proposed embedded, two-phase flow. In our Eulerian simulation, without considering the Lagrangian domain, laminar flow can be maintained for Re of up to 3250. However, the existence of the drop disturbs the flow, causing a transitional flow regime. This flow regime randomly switches between laminar and turbulent flows. Turbulent flow regime is highly nonlinear, stochastic, and irreversible. Thus, our two-phase flow model should be restricted to the practical laminar flow criteria of $Re < 2300$ for accurate prediction of the gas flow behavior inside the channel.

Chapter 6

CONCLUSION AND FUTURE WORK

6.1 Conclusion

Predicting the motion of liquid drops on partially wetting surfaces is of significant importance in countless natural and industrial applications. In this dissertation, we introduced novel techniques to simulate the spatio-temporal evolution of liquid drops in a motion on partially-wettable substrates and in a variety of physical conditions. We successfully developed a PFEM model for the prediction of drop dynamics in single-phase and in embedded two-phase flow, both in 2D and 3D. Our proposed drop dynamics model produced physically acceptable and mesh-independent spatio-temporal evolution of drop spreading and sliding under the effect of gravity and/or external gas flow.

For surface tension and moving contact line problems, drop dynamic models face the following challenges: i) the precise tracking of the free-surface deformation, ii) the mathematical and numerical treatment of the moving contact lines, and iii) the producing of mesh-independent solutions. The first difficulty has been resolved by Jarauta *et al.* [114]. This dissertation addressed the remaining challenges. We first studied the physical phenomena underlying drop dynamics. Accordingly, we identified the interaction forces between a drop and its surrounding. We then modeled each phenomenon by taking advantage of the PFEM Lagrangian scheme.

We presented the fundamental physical effects governing all drop spreading or sliding motions, namely, surface tension, surface forces under partial wetting conditions and gravity. Surface tension is a consequence of the cohesion between liquid molecules. It is expressed in terms of the Young-Laplace equation. Partial wetting phenomenon reflects solid-liquid-vapor interactions along the contact line. Drop spreading is caused by capillary

action, associated with the motion of the contact line (adhesive force) and the deformation of the free-surface (cohesive force). Under the effect of gravitational and/or external shear forces, the sliding motion of a liquid drop is associated with the surface forces acting on the contact line, opposing the external forcing field. In this work, we adopted the empirical concept of the retention force.

Many numerical models have been developed in the past for the prediction of the fluid flow. Among the widely used numerical approaches, we adopt the Lagrangian approach to perform hydrodynamic simulations of liquid drops. More specifically, we took advantage of the Particle Finite Element Method (PFEM) for its ability to precisely simulate the fluid boundaries. In the next sections, we summarize the novelty and the main achievements of our work.

6.2 Drop spreading dynamics

Identifying and imposing the physical interaction forces between liquids and solid substrates is one of the key factors to obtain a reliable drop spreading model. Classical Navier-Stokes equations cannot allow for the contact line motion of a liquid drop on a no-slip substrate. On one hand, the no-slip condition leads to nonphysical energy dissipation and mathematical singularity known as “Huh and Scriven’s paradox”. On the other hand, the free-slip condition, i.e., the no-penetration condition whereby the tangential component of the fluid velocity vector is unrestricted, leads to non-realistic velocity and contact angle temporal evolution. We implemented boundary conditions that resulted in physically acceptable and mesh-independent solutions. These boundary conditions include the effect of the capillary force and the normal and tangential viscous forces, both acting at the contact line, and the Navier-slip condition at the liquid-solid interface.

First, we developed a 2D PFEM based model for liquid drop spreading, using an updated Lagrangian framework. We introduced the physical model, FEM discretization, and solution strategies. The monolithic approach was adopted to solve for both velocity and pressure fields simultaneously. Algebraic Sub-Grid Scales (ASGS) stabilization method

is used to ensure numerical stability. Also, we devised mesh size and time step criteria associated with the wavelength of the capillary wave propagation at the contact line.

Detailed mesh dependence study was performed to examine the effect of our proposed boundary conditions on the spatio-temporal evolution on a spreading drop. We found that our model produces mesh-independent solutions. The model was then successfully validated experimentally on a variety of liquids and substrates, such as a water drop spreading on a hydrophobic Triethoxysilane substrate or on an omniphilic silica substrate. We were able to capture both the early spreading inertial regime and the inertial to viscous transition regimes.

The 2D model was compared with sessile-drop injection experiments, performed by the UC Berkeley and U Alberta Energy Systems Design Laboratory (ESDL) groups. To perform the injection simulation in 2D, we normalized the inlet injection rate by a factor of ~ 3 . The contact angle evolution obtained numerically was validated for each case. As the volume of the drop increased, however, the numerical profiles were found to have a discrepancy with the experimental data. This was most likely due to the fact that an axisymmetric drop geometry cannot be properly modeled in a 2D Cartesian coordinate system.

6.3 Drop sliding dynamics

Our 2D spreading model was extended to the case of liquid drops sliding down an inclined substrate under the effect of gravity. The liquid sliding model included the effect of a retention force accounted with i) the aspect ratio of the drop footprint, associated with the shape factor parameter k , ii) surface tension force, and iii) contact angle hysteresis.

The extended model was validated using six different experimental scenarios of sliding drops on inclined substrates, under a variety of wettability conditions. The first two experiments were for two ethylene glycol drops, of the same volume, sliding on an omniphilic polycarbonate substrate at different inclination angles. The third and fourth scenarios were for water drops, of different volumes, sliding on a hydrophobic PTFE substrate at the same inclination angle. The fifth case was for a water drop sliding on a hydrophilic PMMA substrate with time-varying inclination. The last validation was for a viscous Newtonian drop

sliding on an omniphilic smooth glass.

Using published experimental results, different values of the parameter k were chosen for each solid/liquid pair. With adequate choices of the parameter k , and by scaling the retention force along the contact line by a factor of π , both steady-state velocity and drop profiles were found to be in good agreement with the experiments. Similar to the drop spreading dynamic model, we performed a mesh dependency analysis and found that our choice of boundary conditions alleviates the mesh-dependency of the solution.

Parametric study was performed to examine the effect of the shape factor k on the steady-state velocity. Our simulations demonstrated that the steady-state velocity of a sliding liquid drop is inversely proportional to the scaled parameter k/π . The need of scaling the retention force indicated that the 2D model is inherently flawed, i.e., it is neither able to account for out-of-plane forces nor to replicate the full shape of a sliding drop.

2D rolling drop simulations were performed and validated. The rolling model was equipped with no-slip boundary condition at the solid-liquid interface, ignoring the effect of the retention force. The numerical results of the descent rolling velocities for two small viscous glycerol drops, of different volumes, were obtained. The numerical results were found to be in very good agreement with the experimental data. The relative error, however, increased proportionally to the volume of the drop.

6.4 3D drop dynamic model

Our 2D drop dynamic, single-phase, model was successfully extended to 3D. Our main contribution was the numerical treatment of both the contact line perimeter and the wetting area of the solid-liquid interface. We validated the extended model using experimental results obtained from the published literature, under a wide variety of liquid properties and wettability conditions.

The results showed that the 3D model was more accurate than the 2D. The spatio-temporal evolution of the contact line were found to be in very good agreement with the experiments. Our results demonstrated the success of our proposed 3D model in replicating the shape of the drops and in accounting for out-of-plane forces.

6.5 Embedded, two-phase, flow model

In this dissertation, we demonstrated the advantages of the embedded Eulerian-PFEM two-phase flow formulation in the analysis of gas-liquid interaction problems. We adopted the PFEM scheme to model the liquid phase while adopting the Eulerian scheme to model the gas phase. In addition to controlling the computation cost, this combination allows for i) precise simulation of the liquid domain boundaries and ii) accurate computation of the changes of material properties across the gas-liquid interface.

The single-phase PFEM-based drop dynamics model was further extended for two-phase flow both in 2D and 3D, where the embedded Eulerian-PFEM model was adopted. We started by presenting the governing equations for the proposed embedded numerical model, followed by the boundary and interface conditions. Both Dirichlet and Neumann boundary conditions were applied at the interface. The finite element formulation for the gas phases was introduced. The robust fractional step approach was used to solve for the Eulerian system of equations, whereas the system of equations for liquid phases was solved by the mass conservative monolithic approach. Consequently, both the coupling strategy and solution algorithms were implemented.

We started our validation process on the Eulerian domain, both in 2D and 3D, by comparing the pressure drop inside a rectangular channel with approximate analytical expression. The results of our proposed Eulerian model were found to be in good agreement with the analytical solutions.

Taking advantage of the experimental work of the UC Berkeley and ESDL groups, our 2D embedded formulation was successfully validated. Two experimental scenarios were considered: i) injection of water drop on kapton substrate, and ii) injection of water drop on PTFE substrate. In their experiment, water was injected at different flow rates from a small conduit from the bottom of the channel. The injection process was captured using two cameras, positioned perpendicular to each other.

Our injection simulation predicted film formation on kapton, whereas it predicted drop detachment on the PTFE substrate. Both the water formation rate and the contact angle evolution were found to be in a good match with the experiments. This study demonstrated

the success of the proposed mathematical model, coupling strategy, and numerical results for drop detachment analysis. However, full 3D simulations are still required to better take into consideration the effect of the geometrical effects.

The proposed Eulerian-PFEM model was extended to 3D. The model was validated using two experimental scenarios of different drop-to-channel height ratios and inlet airflow rates. Both drop profiles and average sliding velocities matched the experimental data. Our numerical results showed that the airflow rate required to eject a drop is inversely proportional to the drop-to-channel height ratio, in agreement with the experiments.

The effect of the Reynolds number on the flow regime was also demonstrated. Our numerical simulations showed that for a smooth pipe, with the absence of the drop, laminar flows can be maintained for Reynolds numbers above 2300. The presence of the drop, however, causes a disturbance in the pressure field along the channel. Therefore, a transitional flow regime, i.e., a mixture of laminar and turbulent flows, was observed. The treatment of the high non-linearity and irreversibility of the turbulent flow regime has not been addressed in our embedded model yet.

For all cases presented in Secs. 6.2-6.5, the advantage of the PFEM scheme was amply illustrated, as it allowed to precisely simulate the evolution of the domain boundaries in accordance with the computed velocity field.

6.6 Achievements and contributions

The work presented in this dissertation has led to the following publications and presentations:

- Published article:

Elaf Mahrous, R. Valéry Roy, Alex Jarauta, and Marc Secanell. “A two-dimensional numerical model for the sliding motion of liquid drops by the particle finite element method.” *Physics of Fluids*, 33(3):032117, 2021.

- Published article:

Elaf Mahrous, Alex Jarauta, Thomas Chan, Pavel Ryzhakov, Adam Z. Weber, R.

Valéry Roy, and Marc Secanell. “A particle finite element-based model for droplet spreading analysis.” *Physics of Fluids*, 32(4):042106, 2020.

- Conference contribution:

Elaf Mahrous, R. Valéry Roy, Alex Jarauta, Marc Secanell, and Pavel Ryzhakov. “Simulation of Droplet Spreading Dynamics by Particle Finite Element Method Based Model and Hydrodynamic Lubrication.” *In APS Division of Fluid Dynamics Meeting Abstracts*, pp. S21-003. 2019.

- Conference contribution:

Pavel Ryzhakov, Alex Jarauta, Elaf Mahrous, Jordi Pons, Marc Secanell, R. Valéry Roy, J. Marti et al. “Advances in the Embedded Eulerian-PFEM Modeling of Multi-phase Flows.” *By Centre Internacional de Mètodes Numèrics en Enginyeria (CIMNE), PFEM session*, 2019.

- Conference contribution:

Alex Jarauta, Elaf Mahrous, Pavel Ryzhakov, Jordi Pons-Prats, and Marc Secanell. “A transient two-phase flow model for droplets on substrates with moving contact lines.” *By Centre Internacional de Mètodes Numèrics en Enginyeria (CIMNE), coupled Problems session*, 2019.

- Numerical framework for physical modeling:

Pavel Ryzhakov, Alex Jarauta, Jordi Cotela, Elaf Mahrous. The author contributed in developing the *surface-tension* model within *Kratos Multi-Physics* [182], a C++ object oriented finite element open-source framework [57].

6.7 Future work

In this section, we propose seven promising areas for future work within the scope of the PFEM framework developed in this dissertation.

6.7.1 Rolling viscous drops simulations in 3D

Though the rolling model presented in Sec. 3.6 provides acceptable descent rolling velocity of small viscous drops, it must be extended to 3D. The transition motion between sliding and rolling should also be studied. Moreover, additional experimental work should be considered for validating the transition regime.

6.7.2 Liquid injection simulations in 3D

For the 2D injection model, we enhanced the numerical treatment of free surface flow with moving contact line by careful meshing strategies, so as to avoid element distortions during the injection process. Performing 3D liquid injection simulations should be the object of future work. Newly inserted nodes and elements must be carefully created to i) reflects the correct value of the inserted mass and ii) accurately predicts the free-surface evolution.

6.7.3 Modeling heat transport

In the context of this dissertation, the proposed numerical model developed for fuel cell channel flow can be further enhanced with additional heat and mass transfer effects. Numerical simulation can be extended to predict optimal operating conditions of fuel cells under different thermal conditions. Regarding evaporative cooling in wet cooling towers (see Sec. 1.2.2), addition of heat transfer effects will play an important role in optimizing the fill-zones design, where most of the heat transfer takes place.

The inclusion of thermal effects should be considered in the model. The main goal is to obtain an optimal heat exchange rate between the two phases by:

- Predicting the pressure drops in the channel, which depends on water and air flow rates.
- Estimating phase and temperature changes in the water, which depends on evaporation.

6.7.4 Effect of surface porosity

Our drop dynamics model was able to predict the spatio-temporal evolution of a moving drop on a smooth surface. Regarding PEMFCs applications, our model was able to

predict i) the drop-to-channel height ratio at which a drop detaches and ii) the detachment/ejection velocity. The GDL used in real fuel cells, however, is made up of a macro porous carbon fiber material. Therefore, the effect of surface porosity should be included in the model for predicting the spatio-temporal evolution of the drop after its detachment.

6.7.5 Effect of transitional and turbulent flow regimes

For smooth pipes under ideal conditions, experiments show that laminar flows can be maintained for Reynolds numbers (Re) of up to 100,000 [42]. Practically, a transitional regime starts for a flow of Reynolds number greater than 2300. The effect of the transitional flow regime on our embedded, two-phase, flow simulation was demonstrated in Sec. 5.9. Disturbance in the pressure field of the channel was observed due to the presence of the drop. Thus, our model is found to be restricted to laminar flow regime, i.e, $Re < 2300$. The effect of higher values of Reynolds numbers should be included in the model to account for both transitional and turbulent flow regimes.

6.7.6 Drop breakup and coalescence simulations

Drops, and rivulets, may breakup or coalesce in gas channels. Conducting a thorough study on drop coalescence and breakup phenomena will further enhance the capability of our proposed model.

6.7.7 Computational optimization

The remeshing requirement of the PFEM, at each time step, causes high computational cost. The computational cost can be minimized by enhancing the remeshing algorithm of the existing meshing application (within *Kratos Multi-Physics* framework [182]). In addition to the remeshing requirement, the monolithic scheme of the liquid domain (see chapter 2) results in higher computational cost compared with other numerical schemes, such as fractional step approach. The fractional step scheme, however, was found to be inefficient for modeling drop dynamics [112]. An alternative numerical scheme to solve for the liquid domain should be considered also to reduce the computational cost of our proposed model.

Appendix A

DELAUNAY TRIANGULATION AND ALPHA SHAPE METHOD

In the PFEM scheme, the initial configuration of the domain consists of mesh nodes treated as particles. Mathematical information and physical quantities are assigned to each node. The finite element mesh is generated and connected by a Delaunay triangulation/tetrahedralization. Domain boundaries are identified by the alpha shape method. An updated Lagrangian framework is used to solve the governing equations. This appendix elaborates on the most unique feature of the PFEM scheme, which is the generation of the finite element mesh. This includes both the Delaunay triangulation/tetrahedralization and the alpha shape method. More details about the PFEM can be found in [55, 185, 187].

A.1 Delaunay triangulation/tetrahedralization

Let m_i to be a set of number of points, i.e., mesh nodes, of a given domain Ω (see Fig. A.1(a) [55]). The division of the real plane \mathbb{R}^n , where $n \in \{2,3\}$, into convex cells (S_i) close to each of m_i is defined as Voronoï diagram [55] (see Fig. A.2(a) [212]). The Voronoï cell is closed for the internal domain and open at the boundaries.

The Delaunay triangulation/tetrahedralization of m_i points is the triangulation/tetrahedralization process of connecting m_i points whose S_i cells share a common edge (see Figs. A.1(b) and A.2 [55]). Vertices of the Delaunay triangulation/tetrahedralization are empty circumcircles/circumspheres, i.e, no points in the plane exist inside any triangle/tetrahedron circumcircle/circumsphere [55, 185].

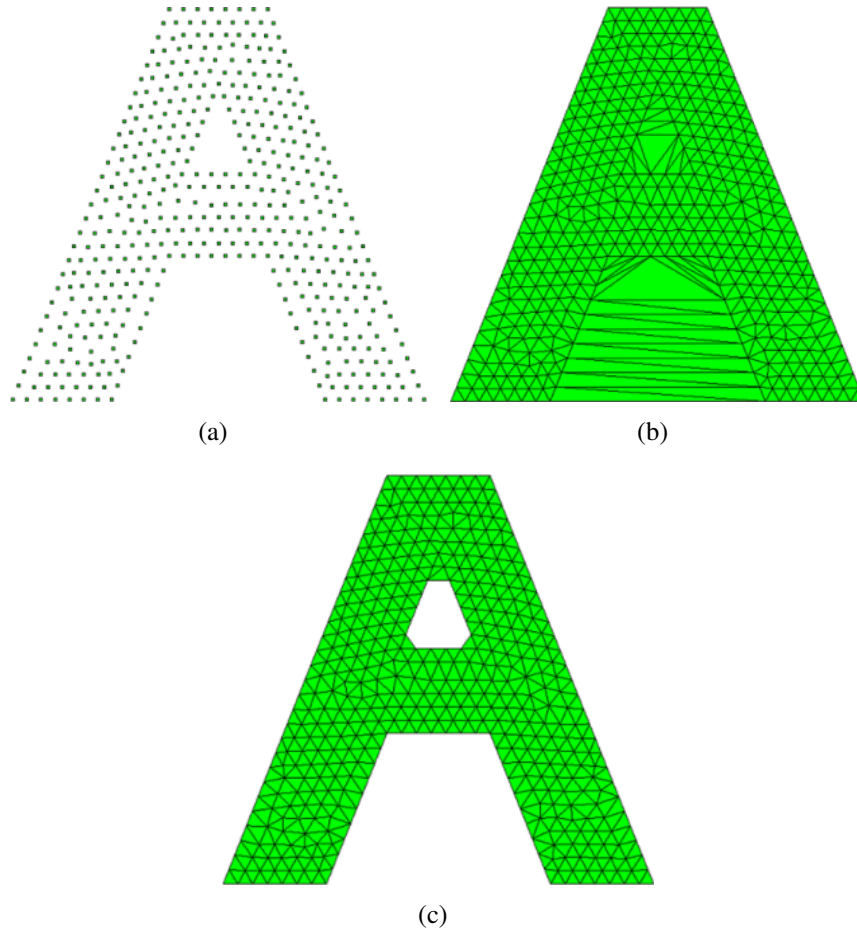


Figure A.1: Schematic representation of: a) initial mesh nodes configuration, b) mesh connectivity by Delaunay triangulation, and c) mesh nodes after implementing the alpha shape method. Figures are reproduced from [55].

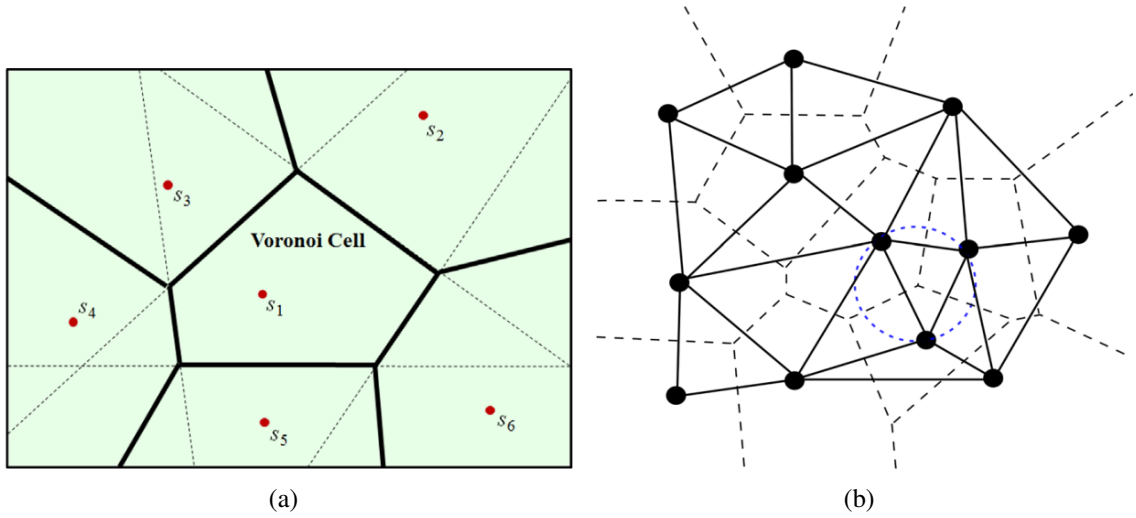


Figure A.2: Schematic representation of a) Voronoi diagram, figure is reproduced from [212] and b) Delaunay triangulation, figure is reproduced from [55].

A.2 Alpha shape method

Mesh connectivity is the main role of the Delaunay triangulation/tetrahedralization. However, the Delaunay triangulation/tetrahedralization does not recover the domain boundaries (see Fig. A.1(b)). To do so, the alpha shape technique is implemented in our PFEM scheme.

For a given domain Ω , let h represents the characteristic mesh size. Also, let α be a predefined radius of the circumcircle/circumsphere generated by the Delaunay partition, whereby the original Delaunay triangulation/tetrahedralization is fully recovered when the value of the parameter α goes to infinity [55, 185]. Accordingly, all mesh nodes on an empty circle/sphere with a radius greater than αh are identified as boundary nodes, as shown in Fig. A.1 [55]. All triangles/tetrahedrons associated with the boundary nodes are erased. In practice, the parameter α takes the value of 1.3 and 1.5 in 2D and 3D, respectively [185].

Appendix B

VISCOUS STRESS IMPLEMENTATION

This appendix introduces the viscous stress in 2D and 3D.

B.1 Viscous stress implementation in 2D

In two dimensions, the viscous stress tensor is given by [\[53, 112\]](#) :

$$\boldsymbol{\tau} = \begin{pmatrix} \tau_{xx} & \tau_{xy} \\ \tau_{yx} & \tau_{yy} \end{pmatrix} \quad (\text{B.1.1})$$

where

$$\tau_{xx} = 2\mu \frac{\partial u}{\partial x} \quad (\text{B.1.2})$$

$$\tau_{xy} = \tau_{yx} = \mu \left(\frac{\partial u}{\partial y} + \frac{\partial v}{\partial x} \right) \quad (\text{B.1.3})$$

$$\tau_{yy} = 2\mu \frac{\partial v}{\partial y} \quad (\text{B.1.4})$$

and u is the velocity component in x direction, and v is the velocity component in y direction.

The following steps give the expression of the element velocity gradient:

- First we apply the chain rule as follows:

$$\frac{\partial v}{\partial x} = \frac{\partial v}{\partial \xi} \frac{\partial \xi}{\partial x} = \frac{\partial v}{\partial \xi} J^{-1} \quad (\text{B.1.5})$$

where, ξ is the isoparametric coordinates (ξ, η) of local coordinate system, and J is the first derivative Jacobian matrix,

and the shape functions of the system coordinates are:

$$N_1 = \xi \quad (\text{B.1.6})$$

$$N_2 = \eta \quad (\text{B.1.7})$$

$$N_3 = 1 - \eta - \xi \quad (\text{B.1.8})$$

The global Cartesian coordinates (x, y) are obtained from the local isoparametric coordinates as follows:

$$x = N_1 x_1 + N_2 x_2 + N_3 x_3 = \xi x_1 + \eta x_2 + (1 - \xi - \eta) x_3 = (x_1 - x_3) \xi + (x_2 - x_3) \eta + x_3 \quad (\text{B.1.9})$$

$$y = N_1 y_1 + N_2 y_2 + N_3 y_3 = \xi y_1 + \eta y_2 + (1 - \xi - \eta) y_3 = (y_1 - y_3) \xi + (y_2 - y_3) \eta + y_3 \quad (\text{B.1.10})$$

Hence, the Jacobian matrix is found to be:

$$J = \begin{bmatrix} \frac{\partial x}{\partial \xi} & \frac{\partial y}{\partial \xi} \\ \frac{\partial x}{\partial \eta} & \frac{\partial y}{\partial \eta} \end{bmatrix} = \begin{bmatrix} x_{13} & y_{13} \\ x_{23} & y_{23} \end{bmatrix} \quad (\text{B.1.11})$$

where, $x_{ij} = x_i - x_j$. Now that Jacobian inverse is found to be:

$$J^{-1} = \frac{1}{2A} \begin{bmatrix} y_{23} & -y_{13} \\ -x_{23} & x_{13} \end{bmatrix} \quad (\text{B.1.12})$$

where A is the area of the element such that $A = \frac{1}{2} \det J$.

- Second, the velocity can be obtained at any particular location as follows:

$$u = N_1 u_1 + N_2 u_2 + N_3 u_3 = \xi u_1 + \eta u_2 + (1 - \xi - \eta) u_3 = (u_1 - u_3) \xi + (u_2 - u_3) \eta + u_3 \quad (\text{B.1.13})$$

$$v = N_1 v_1 + N_2 v_2 + N_3 v_3 = \xi v_1 + \eta v_2 + (1 - \xi - \eta) v_3 = (v_1 - v_3) \xi + (v_2 - v_3) \eta + v_3 \quad (\text{B.1.14})$$

Now, substituting equation eq. [B.1.12](#) into equation eq. [B.1.5](#) yields,

$$\begin{pmatrix} \frac{\partial u}{\partial x} \\ \frac{\partial u}{\partial y} \end{pmatrix} = J^{-1} \begin{pmatrix} \frac{\partial u}{\partial \xi} \\ \frac{\partial u}{\partial \eta} \end{pmatrix} = \frac{1}{2A} \begin{pmatrix} y_{23} u_{13} & -y_{13} u_{23} \\ -x_{23} u_{13} & x_{13} u_{23} \end{pmatrix} \quad (\text{B.1.15})$$

$$\begin{pmatrix} \frac{\partial v}{\partial x} \\ \frac{\partial v}{\partial y} \end{pmatrix} = J^{-1} \begin{pmatrix} \frac{\partial v}{\partial \xi} \\ \frac{\partial v}{\partial \eta} \end{pmatrix} = \frac{1}{2A} \begin{pmatrix} y_{23} v_{13} & -y_{13} v_{23} \\ -x_{23} v_{13} & x_{13} v_{23} \end{pmatrix} \quad (\text{B.1.16})$$

- Finally, the viscous stress discrete expression is governed by combining eqs. [B.1.15](#) and [B.1.16](#), into [B.1.2](#), [B.1.3](#), and [B.1.4](#).

B.2 Viscous stress implementation in 3D

This section introduces the viscous stress in 3D. The viscous stress tensor in three dimensions is given by [\[53, 112\]](#):

$$\boldsymbol{\tau} = \begin{pmatrix} \tau_{xx} & \tau_{xy} & \tau_{xz} \\ \tau_{yx} & \tau_{yy} & \tau_{yz} \\ \tau_{zx} & \tau_{zy} & \tau_{zz} \end{pmatrix} \quad (\text{B.2.1})$$

whose components are given by:

$$\tau_{xx} = 2\mu \frac{\partial u}{\partial x} \quad (\text{B.2.2})$$

$$\tau_{xy} = \tau_{yx} = \mu \left(\frac{\partial u}{\partial y} + \frac{\partial v}{\partial x} \right) \quad (\text{B.2.3})$$

$$\tau_{xz} = \tau_{zx} = \mu \left(\frac{\partial u}{\partial z} + \frac{\partial w}{\partial x} \right) \quad (\text{B.2.4})$$

$$\tau_{yy} = 2\mu \frac{\partial v}{\partial y} \quad (\text{B.2.5})$$

$$\tau_{yz} = \tau_{zy} = \mu \left(\frac{\partial v}{\partial z} + \frac{\partial w}{\partial y} \right) \quad (\text{B.2.6})$$

$$\tau_{zz} = 2\mu \frac{\partial w}{\partial z} \quad (\text{B.2.7})$$

The velocity gradient can be found by applying the chain rule as follows:

$$\frac{\partial \mathbf{v}}{\partial x} = \frac{\partial \mathbf{v}}{\partial \xi} \frac{\partial \xi}{\partial x} = \frac{\partial \mathbf{v}}{\partial \xi} J^{-1} \quad (\text{B.2.8})$$

where, ξ is the isoparametric coordinates (ξ, η, ζ) which map local and global coordinates, J is the first derivative Jacobian matrix,

and the shape functions of the system coordinates are:

$$N_1 = \xi \quad (\text{B.2.9})$$

$$N_2 = \eta \quad (\text{B.2.10})$$

$$N_3 = \zeta \quad (\text{B.2.11})$$

$$N_4 = 1 - \eta - \zeta - \xi \quad (\text{B.2.12})$$

The Cartesian coordinates can be obtained using the following isoparametric coordinates:

$$x = x_1 N_1 + x_2 N_2 + x_3 N_3 + x_4 N_4 = x_4 + x_{14} \xi + x_{24} \eta + x_{34} \zeta \quad (\text{B.2.13})$$

and,

$$\frac{\partial}{\partial x} = \frac{\partial}{\partial \xi} \frac{\partial \xi}{\partial x} + \frac{\partial}{\partial \eta} \frac{\partial \eta}{\partial x} + \frac{\partial}{\partial \zeta} \frac{\partial \zeta}{\partial x} \quad (\text{B.2.14})$$

Then,

$$\begin{Bmatrix} \frac{\partial}{\partial \xi} \\ \frac{\partial}{\partial \eta} \\ \frac{\partial}{\partial \zeta} \end{Bmatrix} = \begin{bmatrix} \frac{\partial x}{\partial \xi} & \frac{\partial y}{\partial \xi} & \frac{\partial z}{\partial \xi} \\ \frac{\partial x}{\partial \eta} & \frac{\partial y}{\partial \eta} & \frac{\partial z}{\partial \eta} \\ \frac{\partial x}{\partial \zeta} & \frac{\partial y}{\partial \zeta} & \frac{\partial z}{\partial \zeta} \end{bmatrix} \begin{Bmatrix} \frac{\partial}{\partial x} \\ \frac{\partial}{\partial y} \\ \frac{\partial}{\partial z} \end{Bmatrix} \quad (\text{B.2.15})$$

where,

$$[J] = \begin{bmatrix} \frac{\partial x}{\partial \xi} & \frac{\partial y}{\partial \xi} & \frac{\partial z}{\partial \xi} \\ \frac{\partial x}{\partial \eta} & \frac{\partial y}{\partial \eta} & \frac{\partial z}{\partial \eta} \\ \frac{\partial x}{\partial \zeta} & \frac{\partial y}{\partial \zeta} & \frac{\partial z}{\partial \zeta} \end{bmatrix} = \begin{bmatrix} x_{14} & y_{14} & z_{14} \\ x_{24} & y_{24} & z_{24} \\ x_{34} & y_{34} & z_{34} \end{bmatrix} \quad (\text{B.2.16})$$

and hence, the equations above yields:

$$\left\{ \frac{\partial}{\partial x} \right\} = [J^{-1}] \left\{ \frac{\partial}{\partial \xi} \right\} \quad (\text{B.2.17})$$

Finally, we obtain $[J^{-1}]$, as follows:

$$J^{-1} = \frac{1}{\det[J]} \begin{bmatrix} y_{24}z_{34} - y_{34}z_{24} & y_{34}z_{14} - y_{14}z_{34} & y_{14}z_{24} - y_{24}z_{14} \\ x_{34}z_{24} - x_{24}z_{34} & x_{14}z_{34} - x_{34}z_{14} & z_{14}x_{24} - x_{14}z_{24} \\ y_{34}x_{24} - x_{34}y_{24} & x_{34}y_{14} - y_{34}x_{14} & x_{14}y_{24} - x_{24}y_{14} \end{bmatrix} \quad (\text{B.2.18})$$

where,

$$\det[J] = x_{14}[y_{24}z_{34} - y_{34}z_{24}] + y_{14}[z_{24}x_{34} - z_{34}x_{24}] + z_{14}[x_{24}y_{34} - x_{34}y_{24}] = 6V, \text{ and}$$

V is the element volume, $V = \frac{1}{6} \det J$,

Appendix C

ELEMENTAL CONTRIBUTION TO MATRIX ENTRIES OF THE 2D LIQUID DROP SLIDING MODEL

Eqs. 2.2.1, 2.2.2, 2.5.9-2.5.12, 3.2.5, 3.2.6, 3.3.1 and 3.3.2 are assembled using the local matrices and vectors, with components defined as:

$$M^{ab} = \rho \int_{\Omega_{\mathbf{X}}} N^a N^b d\Omega_{\mathbf{X}} = \rho \int_{\Omega} N^a N^b J(\mathbf{X}) d\Omega \quad (\text{C1})$$

$$L^{ab} = \int_{\Omega_{\mathbf{X}}} \frac{\partial N^a}{\partial X_i} \frac{\partial N^b}{\partial X_i} \Omega_{\mathbf{X}} = \int_{\Omega} \frac{\partial N^a}{\partial x_i} \frac{\partial N^b}{\partial x_i} J(\mathbf{X}) d\Omega \quad (\text{C2})$$

$$G_i^{ab} = - \int_{\Omega_{\mathbf{X}}} \frac{\partial N^a}{\partial X_i} N^b d\Omega_{\mathbf{X}} = - \int_{\Omega} \frac{\partial N^a}{\partial x_i} N^b J(\mathbf{X}) d\Omega \quad (\text{C3})$$

$$f_i^a = \rho \int_{\Omega_{\mathbf{X}}} N^a g_i d\Omega_{\mathbf{X}} = \rho \int_{\Omega} N^a g_i J(\mathbf{X}) d\Omega \quad (\text{C4})$$

$$D_i^{ab} = \int_{\Omega_{\mathbf{X}}} N^a \frac{\partial N^b}{\partial X_i} d\Omega_{\mathbf{X}} = \int_{\Omega} N^a \frac{\partial N^b}{\partial x_i} J(\mathbf{X}) d\Omega \quad (\text{C5})$$

$$f_{st,i}^a = - \int_{\Gamma_{l,\mathbf{X}}} \gamma \kappa N^a n_i d\Gamma_{\mathbf{X}} = - \int_{\Gamma_l} \gamma \kappa N^a n_i J_{\Gamma}(\mathbf{X}) d\Gamma \quad (\text{C6})$$

$$f_{\partial\Gamma,i}^a = - \int_{\partial\Gamma_{\mathbf{X}}} \beta_{\partial\Gamma} u_i N^a d\partial\Gamma_{\mathbf{X}} = - \int_{\partial\Gamma} \beta_{\partial\Gamma} u_i N^a J_{\Gamma}(\mathbf{X}) d\partial\Gamma \quad (\text{C7})$$

$$f_{\Gamma_s,i}^a = - \int_{\Gamma_{s,\mathbf{X}}} \beta_{\Gamma_s} u_i N^a d\Gamma_{\mathbf{X}} = - \int_{\Gamma_s} \beta_{\Gamma_s} u_i N^a J_{\Gamma}(\mathbf{X}) d\Gamma \quad (\text{C8})$$

where N^a represents the standard finite element shape function at node a , and the index i is used for the spatial components. The model is based on the updated Lagrangian formulation. The integration domains in eqs. (C1)-(C5), $\Omega_{\mathbf{X}}$, represent to the updated configuration. The Jacobian transformation is performed between the reference configuration, Ω , and the updated one.

Appendix D

SOLUTION ALGORITHM OF THE 2D LIQUID DROP SLIDING MODEL

Assuming the current configuration X_n , velocity \bar{v}_n , and pressure \bar{p}_n , are known at time t_n , the solution algorithm for updating the values of these variables at the next time step is summarized in Algorithm 2.

Algorithm 2: Simulation algorithm of the liquid phase problem using a PFEM formulation.

```
1 for  $t = t_{n+1}$  do
2   Current configuration is the known configuration, such that:  $X_{n+1}^k = X_n$ ;
3   for nonlinear iteration  $k$  do
4     Obtain curvature at  $X_{n+1}^k$ ; Update discrete operators in eqs. (C1)-(C5);
5     Compute  $f_{st,i}^a$  using eq. (C6),
6     Compute  $f_{\partial\Gamma,i}^a$  and  $f_{\Gamma_S,i}^a$  using eq. (C7) and eq. (C8), respectively;
7     Update both velocity and pressure, such that:  $\bar{v}_{n+1}^{k+1} = \bar{v}_{n+1}^k + d\bar{v}$  and
         $\bar{p}_{n+1}^{k+1} = \bar{p}_{n+1}^k + d\bar{p}$ , respectively;
8     Update configuration, such that:  $X_{n+1}^{k+1} = X_{n+1}^k + \Delta t \cdot d\bar{v}$ ;
9     Remesh;
10  end
11   $X_{n+1} = X_n + \Delta t \cdot \bar{v}_{n+1}$ ;
12 end
```

Appendix E

GEOMETRY OF SPHERICAL DROPS

The equations which relate the volume and contact angle to the geometrical parameters of a drop in contact with an omniphilic or an omniphobic surface are presented here (see references [78, 112] for more details). The initial shape of the drop is considered as i) a spherical cap on an omniphilic substrate or ii) a spherical drop on an omniphobic substrate, as shown in Fig.E.1(a) and E.1(b), respectively. This assumption might produce up to 15% error when the gravitational force is considered for a drop size of the order of 10 μL [125].

i) Starting with a known liquid drop volume and equilibrium contact angle condition of a spherical cap, the drop height (H), drop radius (R), and wetting radius (a) are obtained using the following equations:

$$R = \left(\frac{V}{\frac{\pi}{3}(2 - 3\cos\theta + \cos^3\theta)} \right)^{\frac{1}{3}} \quad (\text{E1})$$

$$a = R \sin\theta \quad (\text{E2})$$

$$H = R(1 - \cos\theta) \quad (\text{E3})$$

ii) Starting with a known liquid drop volume and equilibrium contact angle condition, the geometrical parameters of a spherical drop are obtained as follows:

$$R = \left(\frac{V}{\frac{4\pi}{3} - \frac{\pi}{3}(1 + \cos\theta)^2(2 - \cos\theta)} \right)^{\frac{1}{3}} \quad (\text{E4})$$

$$\bar{H} = -R \cos\theta \quad (\text{E5})$$

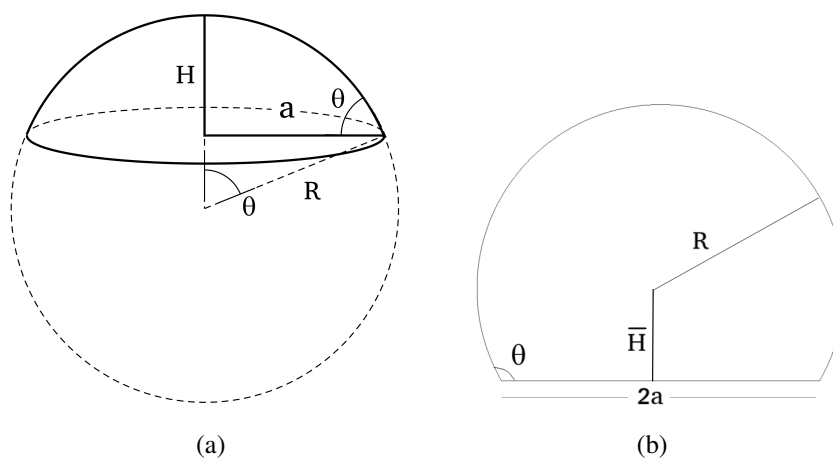


Figure E.1: Geometrical parameters of a drop (a) on an omniphilic substrate and (b) on an omniphobic substrate.

Appendix F

ELEMENTAL CONTRIBUTION TO MATRIX ENTRIES OF THE 3D LAGRANGIAN MODEL

Eqs. 4.2.26, 4.2.27, 4.2.22, and 4.2.15 are assembled using the local matrices and vectors, with components defined as:

$$M^{ab} = \rho \int_{\Omega_{\mathbf{X}}} N^a N^b d\Omega_{\mathbf{X}} = \rho \int_{\Omega} N^a N^b J(\mathbf{X}) d\Omega \quad (\text{F1})$$

$$L^{ab} = \int_{\Omega_{\mathbf{X}}} \frac{\partial N^a}{\partial X_i} \frac{\partial N^b}{\partial X_i} \Omega_{\mathbf{X}} = \int_{\Omega} \frac{\partial N^a}{\partial x_i} \frac{\partial N^b}{\partial x_i} J(\mathbf{X}) d\Omega \quad (\text{F2})$$

$$G_i^{ab} = - \int_{\Omega_{\mathbf{X}}} \frac{\partial N^a}{\partial X_i} N^b d\Omega_{\mathbf{X}} = - \int_{\Omega} \frac{\partial N^a}{\partial x_i} N^b J(\mathbf{X}) d\Omega \quad (\text{F3})$$

$$f_i^a = \rho \int_{\Omega_{\mathbf{X}}} N^a g_i d\Omega_{\mathbf{X}} = \rho \int_{\Omega} N^a g_i J(\mathbf{X}) d\Omega \quad (\text{F4})$$

$$D_i^{ab} = \int_{\Omega_{\mathbf{X}}} N^a \frac{\partial N^b}{\partial X_i} d\Omega_{\mathbf{X}} = \int_{\Omega} N^a \frac{\partial N^b}{\partial x_i} J(\mathbf{X}) d\Omega \quad (\text{F5})$$

$$f_{st,i}^a = - \int_{\Gamma_{I,\mathbf{X}}} \gamma \kappa N^a n_i d\Gamma_{\mathbf{X}} = - \int_{\Gamma_I} \gamma \kappa N^a n_i J_{\Gamma}(\mathbf{X}) d\Gamma \quad (\text{F6})$$

$$f_{\partial\Gamma,i}^a = - \int_{\partial\Gamma_{\mathbf{X}}} \beta_{\partial\Gamma} \mathbf{v} \cdot (\mathbf{v} \cdot (\mathbf{e}_x + \mathbf{e}_y))_i N^a d\partial\Gamma_{\mathbf{X}} = - \int_{\partial\Gamma} \beta_{\partial\Gamma} (\mathbf{v} \cdot (\mathbf{e}_x + \mathbf{e}_y))_i N^a J_{\Gamma}(\mathbf{X}) d\partial\Gamma \quad (\text{F7})$$

$$f_{\Gamma_s,i}^a = - \int_{\Gamma_{S,\mathbf{X}}} \beta_{\Gamma_s} (\mathbf{v} \cdot (\mathbf{e}_x + \mathbf{e}_y))_i N^a d\Gamma_{\mathbf{X}} = - \int_{\Gamma_S} \beta_{\Gamma_s} (\mathbf{v} \cdot (\mathbf{e}_x + \mathbf{e}_y))_i N^a J_{\Gamma}(\mathbf{X}) d\Gamma \quad (\text{F8})$$

where N^a represents the standard finite element shape function at node a , and the index i is used for the spatial components. The present model is based on the updated Lagrangian formulation (ULF), and therefore the integration domains in eqs. (F1)-(F5), $\Omega_{\mathbf{X}}$, correspond to the updated configuration. The transformation between the reference configuration, Ω , and the updated one is performed using the Jacobians $J(\mathbf{X})$ and $J_{\Gamma}(\mathbf{X})$.

Appendix G

SOLUTION ALGORITHM OF THE 3D LAGRANGIAN MODEL

Given a known configuration X_n , velocity \bar{v}_n , and pressure \bar{p}_n , at time t_n , the procedure for obtaining the values of these variables at the next time step t_{n+1} is summarized in Algorithm 3.

Algorithm 3: Simulation algorithm of the liquid phase problem using a PFEM formulation.

```

1 for  $t = t_{n+1}$  do
2   Current configuration is the known configuration, such that:  $X_{n+1}^k = X_n$ ;
3   for nonlinear iteration  $k$  do
4     Obtain curvature at  $X_{n+1}^k$ ;
5     Update discrete operators in eqs. (F1)-(F5);
6     Compute  $f_{st,i}^a$ ,  $f_{\partial\Gamma,i}^a$ , and  $f_{\Gamma_S,i}^a$  using eq. (F6), eq. (F7), and eq. (F8),
       respectively;
7     Solve system of equations for liquid phase, eq. (4.2.30);
8     Update both velocity and pressure, such that:  $\bar{v}_{n+1}^{k+1} = \bar{v}_{n+1}^k + \delta\bar{v}$  and
        $\bar{p}_{n+1}^{k+1} = \bar{p}_{n+1}^k + \delta\bar{p}$ , respectively;
9     Update configuration, such that:  $X_{n+1}^{k+1} = X_{n+1}^k + \Delta t \cdot \delta\bar{v}$ ;
10    Remesh;
11  end
12   $X_{n+1} = X_n + \Delta t \cdot \bar{v}_{n+1}$ ;
13 end

```

Appendix H

PERMISSION

The author has the publisher’s permission to include the following published articles in this dissertation (see Fig. [H.1](#)):

- The main concepts, figures, and outcomes of chapter [2](#) are reproduced from [Elaf Mahrous, Alex Jarauta, Thomas Chan, Pavel Ryzhakov, Adam Z Weber, R Valéry Roy, and Marc Secanell. A particle finite element-based model for droplet spreading analysis. *Physics of Fluids*, 32(4):042106, 2020.], with the permission of AIP Publishing. “<https://aip.scitation.org/doi/abs/10.1063/5.0006033>”.
- The main concepts, figures, and outcomes of chapter [3](#) are reproduced from [Elaf Mahrous, R Valéry Roy, Alex Jarauta, and Marc Secanell. A two-dimensional numerical model for the sliding motion of liquid drops by the particle finite element method. *Physics of Fluids*, 33(3):032117, 2021.], with the permission of AIP Publishing. “<https://aip.scitation.org/doi/10.1063/5.0039517>”.

More information about the publisher’s regulation can be found in the link below:
“<https://publishing.aip.org/resources/researchers/rights-and-permissions/permissions/>”.

On Tue, Jun 29, 2021 at 1:56 PM AIPRights Permissions <Rights@aip.org> wrote:

Dear Dr. Mahrous:

You are permitted to include your published articles in your thesis, provided you also include a credit line referencing the original publication.

Our preferred format is (please fill in the citation information):

"Reproduced from [FULL CITATION], with the permission of AIP Publishing."

If the thesis will be available electronically, please include a link to the version of record on AIP Publishing's site.

Please let us know if you have any questions.

Sincerely,

Susann LoFaso

Manager, Rights & Permissions

AIP Publishing

1305 Walt Whitman Road | Suite 300 | Melville NY 11747-4300 | USA

t +1.516.576.2268

rights@aip.org | publishing.aip.org

Follow us: [Facebook](#) | [Twitter](#) | [LinkedIn](#)

From: Elaf Mahrous <elaf.mahrous@gmail.com>

Sent: Monday, June 28, 2021 4:06 PM

To: AIPRights Permissions <Rights@aip.org>

Subject: Could you please provide me with the "Rights Link" for my dissertation

Greetings dear and very good day to you,

I am Elaf Mahrous, a Ph.D. student at the University of Delaware. Currently, I am working on my dissertation.

I am honored that I published two articles in Physics of Fluids,

As requested from our graduate office that I need to include an Appendix titled Permissions and include the "Rights Link"; from the journal that it is okay to copyright these articles in the dissertation.

Could you please support by providing the required documents or link for my two articles published in Physics of Fluids:

1. Mahrous, Elaf, et al. "A particle finite element-based model for droplet spreading analysis." *Physics of Fluids* 32.4 (2020): 042106.
2. Mahrous, Elaf, et al. "A two-dimensional numerical model for the sliding motion of liquid drops by the particle finite element method." *Physics of Fluids* 33.3 (2021): 032117.

Thanks and best regards,

Figure H.1: Permission to include the published articles in this dissertation.

BIBLIOGRAPHY

- [1] Advancing and receding contact angles. <https://www.nanoscience.com/techniques/tensiometry/advancing-and-receding-contact-angles/>. [Online; accessed 2021-06-5].
- [2] ANSYS Fluent. <http://www.ansys.com/Products/Fluids/ANSYS-Fluent>.
- [3] Chapter 5 - saudi aramco; processing petroleum. <https://abcdocz.com/doc/767545/chapter-5---saudi-aramco>. Accessed: April 2021.
- [4] Gerris flow solver. http://gfs.sourceforge.net/wiki/index.php/Main_Page.
- [5] STAR-CCM+. <https://mdx.plm.automation.siemens.com/star-ccm-plus>.
- [6] Level Set Methods: An initial value formulation. https://math.berkeley.edu/~sethian/2006/Explanations/level_set_explain.html, 2019. [Online; accessed 2021-05-26].
- [7] Capillary action and water. https://www.usgs.gov/special-topic/water-science-school/science/capillary-action-and-water?qt-science_center_objects=0#qt-science_center_objects, 2021. [Online; accessed 2021-06-5].
- [8] Doe technical targets for polymer electrolyte membrane fuel cell components. <https://www.energy.gov/eere/fuelcells/doe-technical-targets-polymer-electrolyte-membrane-fuel-cell-components>, 2021. [Online; accessed 2021-02-25].
- [9] Two-phase gas-liquid flow discussion. <https://fluidflowinfo.com/two-phase-gas-liquid-flow-discussion/>, 2021. [Online; accessed 2021-06-5].
- [10] Mehran Abolghasemibizaki, Connor J Robertson, Christian P Fergusson, Robert L McMasters, and Reza Mohammadi. Rolling viscous drops on a non-wettable surface containing both micro-and macro-scale roughness. *Physics of Fluids*, 30(2):023105, 2018.
- [11] Robert A Adams and John JF Fournier. *Sobolev spaces*. Elsevier, 2003.

- [12] S Afkhami, Stephane Zaleski, and Markus Bussmann. A mesh-dependent model for applying dynamic contact angles to VOF simulations. *Journal of computational physics*, 228(15):5370–5389, 2009.
- [13] Maher Al-Baghdadi. Can CFD analysis help PEM fuel cell design and operation? 2020. DOI:10.32545/encyclopedia202004.0023.v1. *scholar community encyclopedia*, <https://encyclopedia.pub/1092>, 2020.
- [14] Martin Andersson, SB Beale, U Reimer, Werner Lehnert, and D Stolten. Interface resolving two-phase flow simulations in gas channels relevant for polymer electrolyte fuel cells using the volume of fluid approach. *International journal of hydrogen energy*, 43(5):2961–2976, 2018.
- [15] Martin Andersson, V Vukčević, S Zhang, Y Qi, H Jasak, SB Beale, and Werner Lehnert. Modeling of droplet detachment using dynamic contact angles in polymer electrolyte fuel cell gas channels. *International Journal of Hydrogen Energy*, 44(21):11088–11096, 2019.
- [16] S Ravi Annapragada, Jayathi Y Murthy, and Suresh V Garimella. Prediction of droplet dynamics on an incline. *International Journal of Heat and Mass Transfer*, 55(5-6):1466–1474, 2012.
- [17] John Argyris, Ioannis St Doltsinis, and Heinz Friz. Studies on computational reentry aerodynamics. *Computer Methods in Applied Mechanics and Engineering*, 81(3):257–289, 1990.
- [18] M. Ashrafi, M. Shams, A. Bozorgnezhad, and G. Ahmadi. Simulation and experimental validation of droplet dynamics in microchannels of PEM fuel cells. *Heat and Mass Transfer*, 52(12):2671–2686, 2016.
- [19] R Aubry, SR Idelsohn, and Eugenio Oñate. Particle finite element method in fluid-mechanics including thermal convection-diffusion. *Computers & structures*, 83(17-18):1459–1475, 2005.
- [20] Anahita Fathi Azarbayjani, Abolghasem Jouyban, and Sui Yung Chan. Impact of surface tension in pharmaceutical sciences. *Journal of pharmacy & pharmaceutical sciences*, 12(2):218–228, 2009.
- [21] Kevin Bartlet, Sanli Movafaghi, Arun Kota, and Ketul C Popat. Superhemophobic titania nanotube array surfaces for blood contacting medical devices. *RSC advances*, 7(56):35466–35476, 2017.
- [22] Ilker S Bayer and Constantine M Megaridis. Contact angle dynamics in droplets impacting on flat surfaces with different wetting characteristics. *Journal of Fluid Mechanics*, 558:415–449, 2006.

- [23] John C Berg. *An introduction to interfaces & colloids: the bridge to nanoscience*. World Scientific, 2010.
- [24] Bharat Bhushan. Roughness-induced superomniphobic surfaces: Lessons from nature. In *Biomimetics*, pages 11–18. Springer, 2012.
- [25] Bharat Bhushan. *Biomimetics: bioinspired hierarchical-structured surfaces for green science and technology*. Springer, 2016.
- [26] Anne-Laure Biance, Christophe Clanet, and David Quéré. First steps in the spreading of a liquid droplet. *Physical Review E*, 69(1):016301, 2004.
- [27] José Bico, Uwe Thiele, and David Quéré. Wetting of textured surfaces. *Colloids and Surfaces A: Physicochemical and Engineering Aspects*, 206(1-3):41–46, 2002.
- [28] James C Bird, Shreyas Mandre, and Howard A Stone. Short-time dynamics of partial wetting. *Physical review letters*, 100(23):234501, 2008.
- [29] Arnout MP Boelens and Juan J de Pablo. Generalised Navier boundary condition for a volume of fluid approach using a finite-volume method. *Physics of Fluids*, 31(2):021203, 2019.
- [30] Daniel Bonn, Jens Eggers, Joseph Indekeu, Jacques Meunier, and Etienne Rolley. Wetting and spreading. *Reviews of modern physics*, 81(2):739, 2009.
- [31] J.U. Brackbill, D.B. Kothe, and C. Zemach. A continuum method for modeling surface tension. *Journal of Computational Physics*, 100:335–354, 1992.
- [32] M Bracke, F De Voeght, and P Joos. The kinetics of wetting: the dynamic contact angle. In *Trends in Colloid and Interface Science III*, pages 142–149. Springer, 1989.
- [33] Philip S Brown and Bharat Bhushan. Bioinspired materials for water supply and management: water collection, water purification and separation of water from oil. *Philosophical Transactions of the Royal Society A: Mathematical, Physical and Engineering Sciences*, 374(2073):20160135, 2016.
- [34] RA Brown, FM Orr Jr, and LE Scriven. Static drop on an inclined plate: analysis by the finite element method. *Journal of Colloid and Interface Science*, 73(1):76–87, 1980.
- [35] Brad Buecker. Cooling tower heat transfer fundamentals. <https://www.power-eng.com/articles/print/volume-121/issue-7/features/cooling-tower-heat-transfer-fundamentals.html>, 2017. [Online; accessed 2019-02-01].
- [36] Brad Buecker and Rich Aull. Cooling tower heat transfer 201. *Power Engineering*, 114(11):94–98, 2010.

- [37] G.C. Buscaglia and R.F. Ausas. Variational formulations for surface tension, capillarity and wetting. *Computer Methods in Applied Mechanics and Engineering*, 200(45-46):3011–3025, 2011.
- [38] MG Cacace, EM Landau, and JJ Ramsden. The hofmeister series: salt and solvent effects on interfacial phenomena. *Quarterly reviews of biophysics*, 30(3):241–277, 1997.
- [39] Y.H. Cai, J. Hu, H.P. Ma, B.L. Yi, and H.M. Zhang. Effects of hydrophilic/hydrophobic properties on the water behavior in the micro-channels of a proton exchange membrane fuel cell. *Journal of Power Sources*, 161(2):843–848, 2006.
- [40] John Canning, Hadrien Weil, Masood Naqshbandi, Kevin Cook, and Matthieu Lancry. Laser tailoring surface interactions, contact angles, drop topologies and the self-assembly of optical microwires. *Optical Materials Express*, 3(2):284–294, 2013.
- [41] J.G. Carton, V. Lawlor, A.G. Olabi, C. Hochenauer, and G. Zauner. Water droplet accumulation and motion in PEM (Proton Exchange Membrane) fuel cell mini-channels. *Energy*, 39(1):63–73, 2012.
- [42] Yunus A Çengel and John M Cimbala. Flow in pipes. *Fluid mechanics: fundamentals and applications*, pages 321–398, 2006.
- [43] Amrit Chandan, Mariska Hattenberger, Ahmad El-Kharouf, Shangfeng Du, Aman Dhir, Valerie Self, Bruno G Pollet, Andrew Ingram, and Waldemar Bujalski. High temperature (ht) polymer electrolyte membrane fuel cells (PEMFC)—a review. *Journal of Power Sources*, 231:264–278, 2013.
- [44] K.S. Chen, M.A. Hickner, and D.R. Noble. Simplified models for predicting the onset of liquid water droplet instability at the gas diffusion layer/gas flow channel interface. *International Journal of Energy Research*, 29(12):1113–1132, 2005.
- [45] L. Chen, Y.L. He, and W.Q. Tao. Effects of surface microstructures of gas diffusion layer on water droplet dynamic behaviors in a micro gas channel of proton exchange membrane fuel cells. *International Journal of Heat and Mass Transfer*, 60:252–262, 2013.
- [46] Longquan Chen, Günter K Auernhammer, and Elmar Bonaccorso. Short time wetting dynamics on soft surfaces. *Soft Matter*, 7(19):9084–9089, 2011.
- [47] Longquan Chen, Elmar Bonaccorso, and Martin ER Shanahan. Inertial to viscoelastic transition in early drop spreading on soft surfaces. *Langmuir*, 29(6):1893–1898, 2013.
- [48] Shiyi Chen and Gary D Doolen. Lattice boltzmann method for fluid flows. *Annual review of fluid mechanics*, 30(1):329–364, 1998.

- [49] S. C. Cho, Y. Wang, and K.S. Chen. Droplet dynamics in a polymer electrolyte fuel cell gas flow channel: Forces, deformation, and detachment. II: Comparisons of analytical solution with numerical and experimental results. *Journal of Power Sources*, 210:191–197, 2012.
- [50] Sung Chan Cho, Yun Wang, and Ken S Chen. Droplet dynamics in a polymer electrolyte fuel cell gas flow channel: Forces, deformation, and detachment. I: Theoretical and numerical analyses. *Journal of power sources*, 206:119–128, 2012.
- [51] Alexandre Joel Chorin. A numerical method for solving incompressible viscous flow problems. *Journal of computational physics*, 135(2):118–125, 1997.
- [52] Manisha Chowdhury and BV Rathish Kumar. On subgrid multiscale stabilized finite element method for advection-diffusion-reaction equation with variable coefficients. *Applied Numerical Mathematics*, 150:576–586, 2020.
- [53] Ramon Codina. A stabilized finite element method for generalized stationary incompressible flows. *Computer Methods in Applied Mechanics and Engineering*, 190(20-21):2681–2706, 2001.
- [54] Laurent Courbin, James C Bird, Mathilde Reyssat, and Howard A Stone. Dynamics of wetting: from inertial spreading to viscous imbibition. *Journal of Physics: Condensed Matter*, 21(46):464127, 2009.
- [55] Massimiliano Cremonesi, Alessandro Franci, Sergio Idelsohn, and Eugenio Oñate. A state of the art review of the particle finite element method (PFEM). *Archives of Computational Methods in Engineering*, 27(5):1709–1735, 2020.
- [56] RM Curr, Devraj Sharma, and DG Tatchell. Numerical predictions of some three-dimensional boundary layers in ducts. *Computer Methods in Applied Mechanics and Engineering*, 1(2):143–158, 1972.
- [57] P. Dadvand, R. Rossi, and E. Oñate. An object-oriented environment for developing finite element codes for multi-disciplinary applications. *Archives of Computational Methods in Engineering*, 17/3:253–297, 2010.
- [58] John Tasman Davies. *Interfacial phenomena*. Elsevier, 2012.
- [59] B-J De Gans, Paul C Duineveld, and Ulrich S Schubert. Inkjet printing of polymers: state of the art and future developments. *Advanced materials*, 16(3):203–213, 2004.
- [60] Pierre-Gilles De Gennes, Françoise Brochard-Wyart, and David Quéré. *Capillarity and wetting phenomena: drops, bubbles, pearls, waves*. Springer Science & Business Media, 2013.
- [61] B Delaunay. Sur la sphère vide, izvestia akademii nauk sssr, otdelenie matematicheskikh i estestvennykh nauk. 1934.

- [62] E Delnoij, JAM Kuipers, and Willibrordus Petrus Maria van Swaaij. Dynamic simulation of gas-liquid two-phase flow: effect of column aspect ratio on the flow structure. *Chemical Engineering Science*, 52(21-22):3759–3772, 1997.
- [63] Fabian Denner and Berend GM van Wachem. Numerical time-step restrictions as a result of capillary waves. *Journal of Computational Physics*, 285:24–40, 2015.
- [64] BV Derjaguin. Theory of the capillary condensation and other capillary phenomena taking into account the disjoining effect of long-chain molecular liquid films. *Zh. Fiz. Khim*, 14:137, 1940.
- [65] Hang Ding and Peter DM Spelt. Inertial effects in droplet spreading: a comparison between diffuse-interface and level-set simulations. *Journal of fluid mechanics*, 576:287–296, 2007.
- [66] Jean Donea and Antonio Huerta. *Finite element methods for flow problems*. John Wiley & Sons, 2003.
- [67] Jaroslaw Drelich, Emil Chibowski, Dennis Desheng Meng, and Konrad Terpilowski. Hydrophilic and superhydrophilic surfaces and materials. *Soft Matter*, 7(21):9804–9828, 2011.
- [68] Jiayu Du, Nikolaos T Chamakos, Athanasios G Papathanasiou, and Qi Min. Initial spreading dynamics of a liquid droplet: The effects of wettability, liquid properties, and substrate topography. *Physics of Fluids*, 33(4):042118, 2021.
- [69] Jean-Baptiste Dupont and Dominique Legendre. Numerical simulation of static and sliding drop with contact angle hysteresis. *Journal of Computational Physics*, 229(7):2453–2478, 2010.
- [70] Franz Durst. *Fluid mechanics: an introduction to the theory of fluid flows*. Springer Science & Business Media, 2008.
- [71] EB Dussan. On the spreading of liquids on solid surfaces: static and dynamic contact lines. *Annual Review of Fluid Mechanics*, 11(1):371–400, 1979.
- [72] E.B. Dussan and R.T. Chow. On the ability of drops or bubbles to stick to non-horizontal surfaces of solids. *Journal of Fluid Mechanichs*, 137:1–29, 1983.
- [73] M Ebner, T Miranda, and A Roth-Nebelsick. Efficient fog harvesting by stipagrostis sabulicola (namib dune bushman grass). *Journal of arid environments*, 75(6):524–531, 2011.
- [74] Frank D Egitto and Luis J Matienzo. Plasma modification of polymer surfaces for adhesion improvement. *IBM Journal of Research and Development*, 38(4):423–439, 1994.

- [75] AI ElSherbini and AM Jacobi. Retention forces and contact angles for critical liquid drops on non-horizontal surfaces. *Journal of colloid and interface science*, 299(2):841–849, 2006.
- [76] HB Eral, JM Oh, et al. Contact angle hysteresis: a review of fundamentals and applications. *Colloid and polymer science*, 291(2):247–260, 2013.
- [77] MH Eres, LW Schwartz, and RV Roy. Fingering phenomena for driven coating films. *Physics of Fluids*, 12(6):1278–1295, 2000.
- [78] Angelo Esposito, Pierpaolo Polverino, Cesare Pianese, and Yann G Guezennec. A lumped model of single droplet deformation, oscillation and detachment on the gdl surface of a PEM fuel cell. In *International Conference on Fuel Cell Science, Engineering and Technology*, volume 44045, pages 581–592, 2010.
- [79] Izhak Etsion. State of the art in laser surface texturing. *J. Trib.*, 127(1):248–253, 2005.
- [80] Charles W Extrand and Y Kumagai. Liquid drops on an inclined plane: the relation between contact angles, drop shape, and retentive force. *Journal of colloid and interface science*, 170(2):515–521, 1995.
- [81] CW Extrand and AN Gent. Retention of liquid drops by solid surfaces. *Journal of Colloid and Interface Science*, 138(2):431–442, 1990.
- [82] Robert Finn. Capillary surface interfaces. *Notices AMS*, 46(7):770–781, 1999.
- [83] AN Frumkin. On the phenomena of wetting and sticking of bubbles (in russian). *Zh. Fiz. Khim.*, 12:337, 1938.
- [84] Lichao Gao and Thomas J McCarthy. Contact angle hysteresis explained. *Langmuir*, 22(14):6234–6237, 2006.
- [85] Sydney Goldstein. *Modern developments in fluid dynamics: an account of theory and experiment relating to boundary layers, turbulent motion and wakes*. Number 58. Dover publications, 1965.
- [86] A. Golpaygan and N. Ashgriz. Effects of oxidant fluid properties on the mobility of water droplets in the channels of PEM fuel cell. *International journal of energy research*, 29(12):1027–1040, 2005.
- [87] A. Golpaygan and N. Ashgriz. Multiphase flow model to study channel flow dynamics of PEM fuel cells: deformation and detachment of water droplets. *International Journal of Computational Fluid Dynamics*, 22(1-2):85–95, 2008.
- [88] Douglas JC Gomes, Nara C de Souza, and Josmary R Silva. Using a monocular optical microscope to assemble a wetting contact angle analyser. *Measurement*, 46(9):3623–3627, 2013.

- [89] Vinay R Gopala and Berend GM van Wachem. Volume of fluid methods for immiscible-fluid and free-surface flows. *Chemical Engineering Journal*, 141(1-3):204–221, 2008.
- [90] Jibrán Haider. Numerical modelling of evaporation and condensation phenomena-numerische modellierung von verdampfungs-und kondensationsphänomenen. Master’s thesis, Universität Stuttgart, 2013.
- [91] LS Han. Hydrodynamic entrance lengths for incompressible laminar flow in rectangular ducts. *Journal of Applied Mechanics*, 27(3):403, 1960.
- [92] Jafar Hasan and Kaushik Chatterjee. Recent advances in engineering topography mediated antibacterial surfaces. *Nanoscale*, 7(38):15568–15575, 2015.
- [93] Ghassan Hassan, Bekir Sami Yilbas, Abdullah Al-Sharafi, and Hussain Al-Qahtani. Self-cleaning of a hydrophobic surface by a rolling water droplet. *Scientific reports*, 9(1):1–14, 2019.
- [94] Tsuyoshi Hattori, Masaharu Sakai, Shigeru Akaike, and Seiichi Koshizuka. Numerical simulation of droplet sliding on an inclined surface using moving particle semi-implicit method. *Computational Particle Mechanics*, 5(4):477–491, 2018.
- [95] Donald J Hayes, Weldon Royall Cox, and David B Wallace. Printing systems for mems packaging. In *Reliability, Testing, and Characterization of MEMS/MOEMS*, volume 4558, pages 206–215. International Society for Optics and Photonics, 2001.
- [96] Robert A Hayes and John Ralston. The molecular-kinetic theory of wetting. *Langmuir*, 10(1):340–342, 1994.
- [97] H Hervet and P-G De Gennes. Dynamique du mouillage: films précurseurs sur solides sec. *Comptes-rendus des séances de l’Académie des sciences. Série 2, Mécanique-physique, chimie, sciences de l’univers, sciences de la terre*, 299(9):499–503, 1984.
- [98] C.W. Hirt and B.D. Nichols. Volume of Fluid (VOF) method for the dynamics of free boundaries. *Journal of Computational Physics*, 39:201–225, 1981.
- [99] LM Hocking. A moving fluid interface on a rough surface. *Journal of Fluid Mechanics*, 76(4):801–817, 1976.
- [100] PJ Holloway, MC Butler Ellis, DA Webb, NM Western, CR Tuck, AL Hayes, and PCH Miller. Effects of some agricultural tank-mix adjuvants on the deposition efficiency of aqueous sprays on foliage. *Crop Protection*, 19(1):27–37, 2000.
- [101] KKB Hon, L Li, and IM Hutchings. Direct writing technology—advances and developments. *CIRP annals*, 57(2):601–620, 2008.
- [102] Robert W Hornbeck. Laminar flow in the entrance region of a pipe. *Applied Scientific Research, Section A*, 13(1):224–232, 1964.

- [103] Y. Hou, G. Zhang, Y. Qin, Q. Du, and K. Jiao. Numerical simulation of gas liquid two-phase flow in anode channel of low-temperature fuel cells. *International Journal of Hydrogen Energy*, 42(5):3250–3258, 2017.
- [104] Chun Huh and LE Scriven. Hydrodynamic model of steady movement of a solid/liquid/fluid contact line. *Journal of colloid and interface science*, 35(1):85–101, 1971.
- [105] Tae Myung Huh, Hojung Choi, Simone Willcox, Stephanie Moon, and Mark R Cutkosky. Dynamically reconfigurable tactile sensor for robotic manipulation. *IEEE Robotics and Automation Letters*, 5(2):2562–2569, 2020.
- [106] Tommi Huhtamäki, Xuelin Tian, Juuso T Korhonen, and Robin HA Ras. Surface-wetting characterization using contact-angle measurements. *Nature protocols*, 13(7):1521–1538, 2018.
- [107] Sergio R Idelsohn, Eugenio Oñate, and F Del Pin. The particle finite element method: a powerful tool to solve incompressible flows with free-surfaces and breaking waves. *International journal for numerical methods in engineering*, 61(7):964–989, 2004.
- [108] SR Idelsohn, J Marti, Antonio Souto-Iglesias, and Eugenio Oñate. Interaction between an elastic structure and free-surface flows: experimental versus numerical comparisons using the PFEM. *Computational Mechanics*, 43(1):125–132, 2008.
- [109] Mamoru Ishii and Takashi Hibiki. *Thermo-fluid dynamics of two-phase flow*. Springer Science & Business Media, 2010.
- [110] Daulet Izbassarov and Metin Muradoglu. A front-tracking method for computational modeling of viscoelastic two-phase flow systems. *Journal of Non-Newtonian Fluid Mechanics*, 223:122–140, 2015.
- [111] Alka Jaggesar, Hesam Shahali, Asha Mathew, and Prasad KDV Yarlagaadda. Biomimicking nano and micro-structured surface fabrication for antibacterial properties in medical implants. *Journal of nanobiotechnology*, 15(1):64, 2017.
- [112] A Jarauta. *Modeling of droplet dynamics in a proton exchange fuel cell electrode channel*. PhD thesis, Ph. D. Thesis, Universitat Politècnica de Catalunya, 2016.
- [113] Alex Jarauta and Pavel Ryzhakov. Challenges in computational modeling of two-phase transport in polymer electrolyte fuel cells flow channels: A review. *Archives of Computational Methods in Engineering*, 25(4):1027–1057, 2018.
- [114] Alex Jarauta, Pavel Ryzhakov, Jordi Pons-Prats, and Marc Secanell. An implicit surface tension model for the analysis of droplet dynamics. *Journal of Computational Physics*, 374:1196–1218, 2018.

- [115] Alex Jarauta, Pavel Ryzhakov, Marc Secanell, Prashant R Waghmare, and Jordi Pons-Prats. Numerical study of droplet dynamics in a polymer electrolyte fuel cell gas channel using an embedded Eulerian-Lagrangian approach. *Journal of Power Sources*, 323:201–212, 2016.
- [116] Alex Jarauta, Marc Secanell, Jordi Pons-Prats, Pavel Ryzhakov, Sergio R Idelsohn, and Eugenio Onate. A semi-analytical model for droplet dynamics on the gdl surface of a pefc electrode. *international journal of hydrogen energy*, 40(15):5375–5383, 2015.
- [117] Tsung-Shann Jiang, OH Soo-Gun, and John C Slattery. Correlation for dynamic contact angle. *Journal of Colloid and Interface Science*, 69(1):74–77, 1979.
- [118] K. Jiao and B. Zhou. Innovative gas diffusion layers and their water removal characteristics in PEM fuel cell cathode. *Journal of Power Sources*, 169(2):296–314, 2007.
- [119] K. Jiao, B. Zhou, and P. Quan. Liquid water transport in parallel serpentine channels with manifolds on cathode side of a PEM fuel cell stack. *Journal of Power Sources*, 154(1):124–137, 2006.
- [120] K. Jiao, B. Zhou, and P. Quan. Liquid water transport in straight micro-parallel-channels with manifolds for PEM fuel cell cathode. *Journal of Power Sources*, 157(1):226–243, 2006.
- [121] J.H. Jo and W.T. Kim. Numerical simulation of water droplet dynamics in a right angle gas channel of a polymer electrolyte membrane fuel cell. *International Journal of Hydrogen Energy*, 40(26):8368–8383, 2015.
- [122] Alexander Kamyshny, Joachim Steinke, and Shlomo Magdassi. Metal-based inkjet inks for printed electronics. *The Open applied physics journal*, 4(1), 2011.
- [123] Joseph B Keller, Paul A Milewski, and Jean-Marc Vanden-Broeck. Merging and wetting driven by surface tension. *European Journal of Mechanics-B/Fluids*, 19(4):491–502, 2000.
- [124] H.I. Kim, J.H. Nam, D. Shin, T.Y. Chung, and Y.G. Kim. Computational fluid dynamics simulations for hydrogen dispersion and exhaust in residential fuel cell systems. *Current Applied Physics*, 10(2):S81–S85, 2010.
- [125] Ho-Young Kim, Heon Ju Lee, and Byung Ha Kang. Sliding of liquid drops down an inclined solid surface. *Journal of Colloid and Interface Science*, 247(2):372–380, 2002.
- [126] A. Klimanek. Numerical modelling of natural draft wet-cooling towers. *Archives of Computational Methods in Engineering*, 20(1):61–109, 2013.

- [127] Adam Klimanek, Ryszard A Białecki, and Ziemowit Ostrowski. Cfd two-scale model of a wet natural draft cooling tower. *Numerical Heat Transfer, Part A: Applications*, 57(2):119–137, 2010.
- [128] K Komvopoulos. Adhesion and friction forces in microelectromechanical systems: mechanisms, measurement, surface modification techniques, and adhesion theory. *Journal of adhesion science and technology*, 17(4):477–517, 2003.
- [129] Margaritis Kostoglou and Thodoris D Karapantsios. An analytical two-dimensional linearized droplet shape model for combined tangential and normal body forces. *Colloids and Interfaces*, 4(3):35, 2020.
- [130] Sunil Kumar and Ajay Mandal. Studies on interfacial behavior and wettability change phenomena by ionic and nonionic surfactants in presence of alkalis and salt for enhanced oil recovery. *Applied Surface Science*, 372:42–51, 2016.
- [131] E.C. Kumbur, K.V. Sharp, and M.M. Mench. Liquid droplet behavior and instability in a polymer electrolyte fuel cell flow channel. *Journal of Power Sources*, 161:333–345, 2006.
- [132] Nathan Matthew Lane. *Numerical studies of flow in porous media using an unstructured approach*. PhD thesis, Ph. D. Thesis, Louisiana State University., 2011.
- [133] Kock-Yee Law. Definitions for hydrophilicity, hydrophobicity, and superhydrophobicity: getting the basics right, 2014.
- [134] S Edward Law. Agricultural electrostatic spray application: a review of significant research and development during the 20th century. *Journal of Electrostatics*, 51:25–42, 2001.
- [135] L Leger and JF Joanny. Liquid spreading. *Reports on Progress in Physics*, 55(4):431, 1992.
- [136] PF Li, SF Wang, and WL Dong. Capillary wave and initial spreading velocity at impact of drop onto a surface. *Journal of Applied Fluid Mechanics*, 12(4), 2019.
- [137] Zhe Li, Jennifer Marlana, Dicky Pranantyo, Ba Loc Nguyen, and Choon Hwai Yap. A porous superhydrophobic surface with active air plastron control for drag reduction and fluid impalement resistance. *Journal of Materials Chemistry A*, 7(27):16387–16396, 2019.
- [138] Ming Liu and Xiao-Peng Chen. Numerical study on the stick-slip motion of contact line moving on heterogeneous surfaces. *Physics of Fluids*, 29(8):082102, 2017.
- [139] Z Lu, SG Kandlikar, C Rath, M Grimm, W Domigan, AD White, M Hardbarger, JP Owejan, and TA Trabold. Water management studies in PEM fuel cells, part ii: Ex situ investigation of flow maldistribution, pressure drop and two-phase flow pattern in gas channels. *International Journal of Hydrogen Energy*, 34(8):3445–3456, 2009.

- [140] L Mahadevan and Yves Pomeau. Rolling droplets. *Physics of fluids*, 11(9):2449–2453, 1999.
- [141] Elaf Mahrous, Alex Jarauta, Thomas Chan, Pavel Ryzhakov, Adam Z Weber, R Valéry Roy, and Marc Secanell. A particle finite element-based model for droplet spreading analysis. *Physics of Fluids*, 32(4):042106, 2020.
- [142] Elaf Mahrous, R Valéry Roy, Alex Jarauta, and Marc Secanell. A two-dimensional numerical model for the sliding motion of liquid drops by the particle finite element method. *Physics of Fluids*, 33(3):032117, 2021.
- [143] S. Manservigi and R. Scardovelli. A variational approach to the contact angle dynamics of spreading droplets. *Computers & Fluids*, 38(2):406–424, 2009.
- [144] Marcia HB Mantelli. Development of porous media thermosyphon technology for vapor recovering in cross-current cooling towers. *Applied Thermal Engineering*, 108:398–413, 2016.
- [145] Jason Marcinkoski, Jacob Spendelow, Adria Wilson, and Dimitrios Papageorgopoulos. Fuel cell system cost-2015. www.hydrogen.energy.gov/pdfs/15015_fuel_cell_system_cost_2015.pdf, 2015. [Online; accessed 2021-02-25].
- [146] J. Marti, P. Ryzhakov, S. Idelsohn, and E. Oñate. Combined Eulerian-PFEM approach for analysis of polymers in fire situations. *International Journal for Numerical Methods in Engineering*, 92:782–801, 2012.
- [147] J Marti and PB Ryzhakov. An explicit–implicit finite element model for the numerical solution of incompressible navier–stokes equations on moving grids. *Computer Methods in Applied Mechanics and Engineering*, 350:750–765, 2019.
- [148] Julio Marti and Pavel Ryzhakov. An explicit/implicit Runge–Kutta-based PFEM model for the simulation of thermally coupled incompressible flows. *Computational Particle Mechanics*, 7(1):57–69, 2020.
- [149] Mathieu Massinon, Nicolas De Cock, W Alison Forster, Justin J Nairn, Scott W McCue, Jerzy A Zabkiewicz, and Frédéric Lebeau. Spray droplet impaction outcomes for different plant species and spray formulations. *Crop Protection*, 99:65–75, 2017.
- [150] Giorgio Mattana and Danick Briand. Recent advances in printed sensors on foil. *Materials Today*, 19(2):88–99, 2016.
- [151] Thomas Maurer, Axel Mebus, and Uwe Janoske. Water droplet motion on an inclining surface. In *Proceedings of the 3rd International Conference on Fluid Flow, Heat and Mass Transfer (FFHMT’16), Ottawa, Canada–May*, pages 2–3, 2016.
- [152] Mark Meyer, Mathieu Desbrun, Peter Schröder, and Alan H Barr. Discrete differential-geometry operators for triangulated 2-manifolds. In *Visualization and mathematics III*, pages 35–57. Springer, 2003.

- [153] Mónica de Mier Torrecilla. *Numerical simulation of multi-fluid flows with the Particle Finite Element Method*. Universitat Politècnica de Catalunya, 2010.
- [154] Athanasios Milionis, K Ghokulla Krishnan, Eric Loth, and Michael Lawrence. Dynamic wetting of human blood and plasma on various surfaces. *Colloids and Surfaces B: Biointerfaces*, 166:218–223, 2018.
- [155] AK Mohanty and Reeta Das. Laminar flow in the entrance region of a parallel plate channel. *AIChE Journal*, 28(5):830–833, 1982.
- [156] B. Mondal, K. Jiao, and X. Li. Three-dimensional simulation of water droplet movement in PEM fuel cell flow channels with hydrophilic surfaces. *International Journal of Energy Research*, 35(13):1200–1212, 2011.
- [157] Elvira Moreno, Antonia Larese, and Miguel Cervera. Modelling of Bingham and Herschel–Bulkley flows with mixed P1/P1 finite elements stabilized with orthogonal subgrid scale. *Journal of Non-Newtonian Fluid Mechanics*, 228:1–16, 2016.
- [158] NM Natarajan and SM Lakshmanan. Analytical method for the determination of the pressure drop in rectangular ducts. *Indian Chem. Eng*, 12:68–69, 1970.
- [159] CLMH Navier. Mémoire sur les lois du mouvement des fluides. *Mémoires de l’Académie Royale des Sciences de l’Institut de France*, 6(1823):389–440, 1823.
- [160] Z. Niu, L. Fan, Z. Bao, and K. Jiao. Numerical investigation of innovative 3D cathode flow channel in proton exchange membrane fuel cell. *International Journal of Energy Research*.
- [161] John O’Donnell, Myungsun Kim, and Hwan-Sik Yoon. A review on electromechanical devices fabricated by additive manufacturing. *Journal of Manufacturing Science and Engineering*, 139(1), 2017.
- [162] Cassio M Oishi, Fernando P Martins, and Roney L Thompson. Gravitational effects in the collision of elasto-viscoplastic drops on a vertical plane. *Fluids*, 5(2):61, 2020.
- [163] Eugenio Oñate, Sergio R Idelsohn, Facundo Del Pin, and Romain Aubry. The particle finite element method—an overview. *International Journal of Computational Methods*, 1(02):267–307, 2004.
- [164] Eugenio Oñate, Sergio Rodolfo Idelsohn, Miguel Angel Celigueta, Riccardo Rossi, J Marti, Josep Maria Carbonell, Pavel Ryzhakov, and Benjamín Suárez. Advances in the particle finite element method (PFEM) for solving coupled problems in engineering. In *Particle-Based Methods*, pages 1–49. Springer, 2011.
- [165] Daniel K Owens and RC Wendt. Estimation of the surface free energy of polymers. *Journal of applied polymer science*, 13(8):1741–1747, 1969.

- [166] John F Padday. *Wetting, spreading, and adhesion: comprising papers (with discussions) presented to a symposium, organised by the Colloid and Surface Chemistry Group of the Society of Chemical Industry, held on 27-29 September 1976 at Loughborough University, Leicestershire*. Academic Press, 1978.
- [167] Eung Seok Park. *Application of Inkjet-Printing Technology to Micro-Electro-Mechanical Systems*. PhD thesis, UC Berkeley, 2013.
- [168] Jun Kwon Park and Kwan Hyoung Kang. Numerical analysis of moving contact line with contact angle hysteresis using feedback deceleration technique. *Physics of Fluids*, 24(4):042105, 2012.
- [169] Andrew R Parker and Chris R Lawrence. Water capture by a desert beetle. *Nature*, 414(6859):33–34, 2001.
- [170] J Pellicer, V Garcia-Morales, and MJ Hernandez. On the demonstration of the young-laplace equation in introductory physics courses. *Physics Education*, 35(2):126, 2000.
- [171] Charles S Peskin. The immersed boundary method. *Acta numerica*, 11:479–517, 2002.
- [172] DW Pilat, P Papadopoulos, D Schaffel, Doris Vollmer, Rüdiger Berger, and H-J Butt. Dynamic measurement of the force required to move a liquid drop on a solid surface. *Langmuir*, 28(49):16812–16820, 2012.
- [173] Mihail Nicolae Popescu, G Oshanin, S Dietrich, and AM Cazabat. Precursor films in wetting phenomena. *Journal of Physics: Condensed Matter*, 24(24):243102, 2012.
- [174] P. Quan, B. Zhou, A. Sobiesiak, and Z. Liu. Water behavior in serpentine micro-channel for proton exchange membrane fuel cell cathode. *Journal of Power Sources*, 152:131–145, 2005.
- [175] Peng Quan and Ming-Chia Lai. Numerical study of water management in the air flow channel of a PEM fuel cell cathode. *Journal of Power Sources*, 164(1):222–237, 2007.
- [176] K.A. Raman, B. Mondal, and X. Li. Water droplet transport in single gas flow channel of PEM fuel cell. *International Journal of Advances in Thermal Sciences and Engineering*, 2(1):27–33, 2011.
- [177] Norbert Rasenack, Helge Hartenhauer, and Bernd W Müller. Microcrystals for dissolution rate enhancement of poorly water-soluble drugs. *International journal of pharmaceutics*, 254(2):137–145, 2003.
- [178] Weiqing Ren and Weinan E. Boundary conditions for the moving contact line problem. *Physics of fluids*, 19(2):022101, 2007.

- [179] Michael Renardy, Yuriko Renardy, and Jie Li. Numerical simulation of moving contact line problems using a volume-of-fluid method. *Journal of Computational Physics*, 171(1):243–263, 2001.
- [180] Yuriko Renardy, Stéphane Popinet, Laurent Duchemin, Michael Renardy, Stéphane Zaleski, Christophe Josserand, MA Drumright-Clarke, D Richard, Christophe Clanet, and David Quéré. Pyramidal and toroidal water drops after impact on a solid surface. *Journal of Fluid Mechanics*, 484:69–83, 2003.
- [181] Riccardo Rossi, A Larese, Pooyan Dadvand, and E Oñate. An efficient edge-based level set finite element method for free surface flow problems. *International Journal for Numerical Methods in Fluids*, 71(6):687–716, 2013.
- [182] Riccardo Rossi, Pavel B Ryzhakov, and Eugenio Oñate. A monolithic FE formulation for the analysis of membranes in fluids. *International Journal of Space Structures*, 24(4):205–210, 2009.
- [183] A Roth-Nebelsick, M Ebner, T Miranda, V Gottschalk, D Voigt, S Gorb, T Stegmaier, J Sarsour, M Linke, and W Konrad. Leaf surface structures enable the endemic namib desert grass stipagrostis sabulicola to irrigate itself with fog water. *Journal of the Royal Society interface*, 9(73):1965–1974, 2012.
- [184] P. Ryzhakov, R. Rossi, S. Idelsohn, and E. Oñate. A monolithic Lagrangian approach for fluid-structure interaction problems. *Journal of Computational Mechanics*, 46/6:883–399, 2010.
- [185] Pavel Ryzhakov, Riccardo Rossi, and Sergio Rodolfo Idelsohn Barg. *Lagrangian FE methods for coupled problems in fluid mechanics*. International Centre for Numerical Methods in Engineering (CIMNE), 2010.
- [186] Pavel B Ryzhakov and Alex Jarauta. An embedded approach for immiscible multi-fluid problems. *International Journal for Numerical Methods in Fluids*, 81(6):357–376, 2016.
- [187] Pavel B Ryzhakov, Alex Jarauta, Marc Secanell, and Jordi Pons-Prats. On the application of the PFEM to droplet dynamics modeling in fuel cells. *Computational Particle Mechanics*, 4(3):285–295, 2017.
- [188] P.B. Ryzhakov, E. Oñate, R. Rossi, and S.R. Idelsohn. Improving mass conservation in simulation of incompressible flows. *International Journal for Numerical Methods in Engineering*, 90:1435–1451, 2012.
- [189] M. Sabharwal, J.T. Gostick, and M. Secanell. Virtual liquid water intrusion in fuel cell gas diffusion media. *Journal of The Electrochemical Society*, 165(7):F553–F563, 2018.

- [190] Wolfram Saenger and Anke Müller-Fahrnow. Cyclodextrins increase surface tension and critical micelle concentrations of detergent solutions. *Angewandte Chemie International Edition in English*, 27(3):393–394, 1988.
- [191] Tomomi Sakata, Hiromu Ishii, Norio Sato, Kei Kuwabara, Toshishige Shimamura, Kazuhisa Kudou, and Katsuyuki Machida. Prevention of sticking in mems devices by electrodeposition. In *Meeting Abstracts*, number 26, pages 1274–1274. The Electrochemical Society, 2006.
- [192] Matts-Ola Samuelsson and David L Kirchman. Degradation of adsorbed protein by attached bacteria in relationship to surface hydrophobicity. *Appl. Environ. Microbiol.*, 56(12):3643–3648, 1990.
- [193] A.D. Santamaria, P.K. Das, J.C. MacDonald, and A.Z. Weber. Liquid-water interactions with gas-diffusion-layer surfaces. *Journal of The Electrochemical Society*, 161(12):F1184–F1193, 2014.
- [194] Robert Schlapak, Patrick Pammer, David Armitage, Rong Zhu, Peter Hinterdorfer, Matthias Vaupel, Thomas Frühwirth, and Stefan Howorka. Glass surfaces grafted with high-density poly (ethylene glycol) as substrates for dna oligonucleotide microarrays. *Langmuir*, 22(1):277–285, 2006.
- [195] C.A. Schneider, W.S. Rasband, and K.W. Eliceiri. NIH Image to ImageJ: 25 years of image analysis. *Nature methods*, 9(7):671, 2012.
- [196] Leonard W Schwartz. Hysteretic effects in droplet motions on heterogeneous substrates: direct numerical simulation. *Langmuir*, 14(12):3440–3453, 1998.
- [197] M. Secanell, A. Jarauta, A. Kosakian, M. Sabharwal, and J. Zhou. PEM fuel cells, modeling. In Robert A. Meyers, editor, *Encyclopedia of Sustainability Science and Technology*, pages 1–61, New York, NY, 2017. Springer New York.
- [198] M Secanell, J Wishart, and P Dobson. Computational design and optimization of fuel cells and fuel cell systems: a review. *Journal of Power Sources*, 196(8):3690–3704, 2011.
- [199] Jill E Seebergh and John C Berg. Dynamic wetting in the low capillary number regime. *Chemical Engineering Science*, 47(17-18):4455–4464, 1992.
- [200] D. Seveno, A. Vaillant, R. Rioboo, H. Adao, J. Conti, and J. De Coninck. Dynamics of wetting revisited. *Langmuir*, 25(22):13034–13044, 2009.
- [201] Ramesh K Shah and Alexander Louis London. *Laminar flow forced convection in ducts: a source book for compact heat exchanger analytical data*. Academic press, 2014.

- [202] Yulii D Shikhmurzaev. Singularities at the moving contact line. Mathematical, physical and computational aspects. *Physica D: Nonlinear Phenomena*, 217(2):121–133, 2006.
- [203] Ebrahim Shirani and Shila Masoomi. Deformation of a droplet in a channel flow. *Journal of fuel cell science and technology*, 5(4):041008, 2008.
- [204] P.D.M Spelt. A level-set approach for simulations of flows with multiple moving contact lines with hysteresis. *Journal of Computational Physics*, 207(2):389–404, 2005.
- [205] Colleen Spiegel. *Designing and building fuel cells*, volume 87. Citeseer, 2007.
- [206] A.F. Stalder, G. Kulik, D. Sage, L. Barbieri, and P. Hoffmann. A snake-based approach to accurate determination of both contact points and contact angles. *Colloids And Surfaces A: Physicochemical And Engineering Aspects*, 286(1-3):92–103, 2006.
- [207] Aurélien F Stalder, Tobias Melchior, Michael Müller, Daniel Sage, Thierry Blu, and Michael Unser. Low-bond axisymmetric drop shape analysis for surface tension and contact angle measurements of sessile drops. *Colloids and Surfaces A: Physicochemical and Engineering Aspects*, 364(1-3):72–81, 2010.
- [208] Victor M Starov and Manuel G Velarde. *Wetting and spreading dynamics*, volume 12. CRC press, 2019.
- [209] Howard A Stone, Abraham D Stroock, and Armand Ajdari. Engineering flows in small devices: microfluidics toward a lab-on-a-chip. *Annu. Rev. Fluid Mech.*, 36:381–411, 2004.
- [210] Di Sun and Karl F Böhringer. An active self-cleaning surface system for photovoltaic modules using anisotropic ratchet conveyors and mechanical vibration. *Microsystems & Nanoengineering*, 6(1):1–12, 2020.
- [211] Xinwei Sun, Stian Christopher Simonsen, Truls Norby, and Athanasios Chatzitakis. Composite membranes for high temperature PEM fuel cells and electrolyzers: a critical review. *Membranes*, 9(7):83, 2019.
- [212] Tien-Wen Sung and Chu-Sing Yang. Voronoi-based coverage improvement approach for wireless directional sensor networks. *Journal of Network and Computer Applications*, 39:202–213, 2014.
- [213] Mark Sussman and Mitsuhiro Ohta. A stable and efficient method for treating surface tension in incompressible two-phase flow. *SIAM Journal on Scientific Computing*, 31(4):2447–2471, 2009.
- [214] Robert B Suter and Jessica Gruenwald. Spider size and locomotion on the water surface (araneae, pisauridae). *Journal of Arachnology*, pages 300–308, 2000.

- [215] Rafael Tadmor. Line energy and the relation between advancing, receding, and young contact angles. *Langmuir*, 20(18):7659–7664, 2004.
- [216] LH Tanner. The spreading of silicone oil drops on horizontal surfaces. *Journal of Physics D: Applied Physics*, 12(9):1473, 1979.
- [217] Italo VM Tasso, Diego S Rodrigues, and Gustavo C Buscaglia. Assessment of curvature approximation methods in the simulation of viscous biological membranes.
- [218] Sumesh P Thampi, Ronojoy Adhikari, and Rama Govindarajan. Do liquid drops roll or slide on inclined surfaces? *Langmuir*, 29(10):3339–3346, 2013.
- [219] A. Theodorakakos, T. Ous, M. Gavaises, J.M. Nouri, N. Nikolopoulos, and H. Yanagihara. Dynamics of water droplets detached from porous surfaces of relevance to PEM fuel cells. *Journal of Colloid and Interface Science*, 300:673–687, 2006.
- [220] Yu Tian, Yangyang Tian, Guoxin Shi, Bo Zhou, Chunying Zhang, and Limin He. Experimental study on oil droplet breakup under the action of turbulent field in modified concentric cylinder rotating device. *Physics of Fluids*, 32(8):087105, 2020.
- [221] Kurian J Vachaparambil and Kristian Etienne Einarsrud. Comparison of surface tension models for the volume of fluid method. *Processes*, 7(8):542, 2019.
- [222] PK Valavala and GM Odegard. Modeling techniques for determination of mechanical properties of polymer nanocomposites. *Reviews on Advanced Materials Science*, 9(1):34–44, 2005.
- [223] S Van Mourik, AEP Veldman, and ME Dreyer. Simulation of capillary flow with a dynamic contact angle. *Microgravity-Science and Technology*, 17(3):87, 2005.
- [224] Subhashini Vashisth and KDP Nigam. Prediction of flow profiles and interfacial phenomena for two-phase flow in coiled tubes. *Chemical Engineering and Processing: Process Intensification*, 48(1):452–463, 2009.
- [225] Dominic Vella and Paul D Metcalfe. Surface tension dominated impact. *Physics of Fluids*, 19(7):072108, 2007.
- [226] Jagannath Venkatesan and Sashikumaar Ganesan. On the Navier-slip boundary condition for computations of impinging droplets. In *2015 IEEE 22nd International Conference on High Performance Computing Workshops*, pages 2–11. IEEE, 2015.
- [227] Jagannath Venkatesan and Sashikumaar Ganesan. Computational modeling of impinging viscoelastic droplets. *Journal of Non-Newtonian Fluid Mechanics*, 263:42–60, 2019.
- [228] Meng-Jiy Wang, Fang-Hsing Lin, Yi-Lin Hung, and Shi-Yow Lin. Dynamic behaviors of droplet impact and spreading: water on five different substrates. *Langmuir*, 25(12):6772–6780, 2009.

- [229] A. Z. Weber, R. L. Borup, R. M. Darling, P. K. Das, T. J. Dursch, W. Gu, D. Harvey, A. Kusoglu, S. Litster, M. M. Mench, R. Mukundan, J. P. Owejan, J. G. Pharoah, M. Secanell, and I. V. Zenyuk. A critical review of modeling transport phenomena in Polymer-Electrolyte fuel cells. *Journal of the Electrochemical Society*, 161(12):F1254–F1299, 2014.
- [230] DE Weidner, LW Schwartz, and RR Eley. Role of surface tension gradients in correcting coating defects in corners. *Journal of colloid and interface science*, 179(1):66–75, 1996.
- [231] Edward B White and Jason A Schmucker. Wind-and gravity-forced drop depinning. *Physical Review Fluids*, 6(2):023601, 2021.
- [232] Robin T White, Sebastian H Eberhardt, Yadvinder Singh, Tylynn Haddow, Monica Dutta, Francesco P Orfino, and Erik Kjeang. Four-dimensional joint visualization of electrode degradation and liquid water distribution inside operating polymer electrolyte fuel cells. *Scientific reports*, 9(1):1–12, 2019.
- [233] Kyle Wilke. *Tailoring wetting behavior at extremes*. PhD thesis, Massachusetts Institute of Technology, 2019.
- [234] Martin Wörner. Numerical modeling of multiphase flows in microfluidics and micro process engineering: a review of methods and applications. *Microfluidics and nanofluidics*, 12(6):841–886, 2012.
- [235] Hsuan-Chung Wu, Huey-Jiuan Lin, Yung-Chi Kuo, and Weng-Sing Hwang. Simulation of droplet ejection for a piezoelectric inkjet printing device. *Materials Transactions*, 45(3):893–899, 2004.
- [236] T.C. Wu and N. Djilali. Experimental investigation of water droplet emergence in a model polymer electrolyte membrane fuel cell microchannel. *Journal of Power Sources*, 208:248–256, 2012.
- [237] Jian Xie, Jinliang Xu, Wei Shang, and Kai Zhang. Mode selection between sliding and rolling for droplet on inclined surface: Effect of surface wettability. *International Journal of Heat and Mass Transfer*, 122:45–58, 2018.
- [238] H Xu, A Clarke, JP Rothstein, and RJ Poole. Viscoelastic drops moving on hydrophilic and superhydrophobic surfaces. *Journal of colloid and interface science*, 513:53–61, 2018.
- [239] Takuya Yamamoto, Yasunori Okano, and Sadik Dost. Validation of the S-CLSVOF method with the density-scaled balanced continuum surface force model in multiphase systems coupled with thermocapillary flows. *International Journal for Numerical Methods in Fluids*, 83(3):223–244, 2017.

- [240] Toshiaki Yamamoto, Masaaki Okubo, Norikazu Imai, and Yasunao Mori. Improvement on hydrophilic and hydrophobic properties of glass surface treated by nonthermal plasma induced by silent corona discharge. *Plasma Chemistry and Plasma Processing*, 24(1):1–12, 2004.
- [241] Chun-Wei Yao, Sirui Tang, Divine Sebastian, and Rafael Tadmor. Sliding of water droplets on micropillar-structured superhydrophobic surfaces. *Applied Surface Science*, 504:144493, 2020.
- [242] Bekir Sami Yilbas, Abudllah Al-Sharafi, Haider Ali, and Nasser Al-Aqeeli. Dynamics of a water droplet on a hydrophobic inclined surface: influence of droplet size and surface inclination angle on droplet rolling. *Rsc Advances*, 7(77):48806–48818, 2017.
- [243] Bekir Sami Yilbas, Ghassan Hassan, Hussain Al-Qahtani, Naser Al-Aqeeli, Abdullah Al-Sharafi, Abdulrahman S Al-Merbati, Turki N Baroud, and Johnny Adukwu Ebaika Adukwu. Stretchable hydrophobic surfaces and self-cleaning applications. *Scientific reports*, 9(1):1–13, 2019.
- [244] KW Yong, Poo Balan Ganesan, Md Salim Newaz Kazi, Sathyadeepak Ramesh, Irfan Anjum Badruddin, and Nabisab Mujawar Mubarak. Sliding behavior of droplet on a hydrophobic surface with hydrophilic cavities: A simulation study. *Physics of Fluids*, 30(12):122006, 2018.
- [245] Youngsam Yoon, Daeyoung Kim, and Jeong-Bong Lee. Hierarchical micro/nano structures for super-hydrophobic surfaces and super-lyophobic surface against liquid metal. *Micro and Nano Systems Letters*, 2(1):3, 2014.
- [246] Yuehua Yuan and T Randall Lee. Contact angle and wetting properties. In *Surface science techniques*, pages 3–34. Springer, 2013.
- [247] Z. Zhan, J. Xiao, M. Pan, and R. Yuan. Characteristics of droplet and film water motion in the flow channels of polymer electrolyte membrane fuel cells. *Journal of Power Sources*, 160(1):1–9, 2006.
- [248] Jun Zhang, Matthew K Borg, and Jason M Reese. Multiscale simulation of dynamic wetting. *International Journal of Heat and Mass Transfer*, 115:886–896, 2017.
- [249] J. Zhou, D. Stanier, A. Putz, and M. Secanell. A mixed wettability pore size distribution based mathematical model for analyzing two-phase flow in porous electrodes II. Model validation and analysis of micro-structural parameters. *Journal of The Electrochemical Society*, 164(6):F540–F556, 2017.
- [250] X. Zhu, Q. Liao, P.C. Sui, and N. Djilali. Numerical investigation of water droplet dynamics in a low-temperature fuel cell microchannel: Effect of channel geometry. *Journal of Power Sources*, 195:801–812, 2010.

- [251] X. Zhu, P.C. Sui, and N. Djilali. Three-dimensional numerical simulations of water droplet dynamics in a PEMFC gas channel. *Journal of Power Sources*, 181:101–115, 2008.
- [252] Xun Zhu, PC Sui, and Ned Djilali. Numerical simulation of emergence of a water droplet from a pore into a microchannel gas stream. *Microfluidics and Nanofluidics*, 4(6):543–555, 2008.
- [253] Zhi-Qiang Zhu, Yang Wang, Qiu-Sheng Liu, and Jing-Chang Xie. Influence of bond number on behaviors of liquid drops deposited onto solid substrates. *Microgravity Science and Technology*, 24(3):181–188, 2012.
- [254] Olek C Zienkiewicz and Robert L Taylor. *The finite element method for solid and structural mechanics*. Elsevier, 2005.